

# Carbon and nutrient fluxes in the North Atlantic Ocean

Dissertation zur Erlangung des Doktorgrades  
der Mathematisch-Naturwissenschaftlichen Fakultät  
der Christian-Albrechts-Universität  
zu Kiel

vorgelegt von

**Tobias Steinhoff**

Kiel

2010

Referent/in: Prof. Dr. A. Körtzinger

Koreferent/in: Prof. Dr. D. W. R. Wallace

Tag der mündlichen Prüfung: 29.11.2010

Zum Druck genehmigt: Kiel 08.12.2010

gez. Prof. Dr. rer. nat. Lutz Kipp  
- Dekan -

# Contents

<b>1. Introduction</b>	<b>9</b>
1.1. Scientific background . . . . .	9
1.2. Study regions . . . . .	12
1.3. Underway measurements . . . . .	14
1.4. Oceanic carbonate system . . . . .	16
1.5. Global carbon cycle . . . . .	18
1.6. Air-sea gas exchange of $\text{CO}_2$ . . . . .	20
1.7. Large scale $p\text{CO}_2$ observation and estimation . . . . .	22
1.8. Thesis outline . . . . .	23
<b>2. Data and Methods</b>	<b>25</b>
2.1. Underway measurements . . . . .	26
2.2. Discrete water samples . . . . .	31
2.3. Data reduction of $p\text{CO}_2$ measurements . . . . .	33
<b>3. Autonomous <math>p\text{CO}_2</math> measurements in the North Atlantic</b>	<b>39</b>
3.1. Data . . . . .	39
3.2. Results . . . . .	42
3.3. Discussion . . . . .	53
<b>4. Tracking the Variable North Atlantic Sink for Atmospheric <math>\text{CO}_2</math></b>	<b>59</b>
<b>5. Estimating the monthly <math>p\text{CO}_2</math> distribution in the North Atlantic using a self-organizing neural network</b>	<b>65</b>
<b>6. Climatological mean and decadal change in surface ocean <math>p\text{CO}_2</math>, and net sea-air <math>\text{CO}_2</math> flux over the global oceans</b>	<b>85</b>
<b>7. Estimating mixed layer nitrate in the North Atlantic Ocean</b>	<b>111</b>
<b>8. Production estimates in the Mauritanian upwelling</b>	<b>127</b>
8.1. Methods . . . . .	127
8.2. Results and Discussion . . . . .	134
8.3. Conclusions . . . . .	139
<b>9. Conclusions and future outlook</b>	<b>141</b>
<b>References</b>	<b>148</b>
<b>A. Abbreviations</b>	<b>156</b>
<b>B. Cruises</b>	<b>158</b>



# Zusammenfassung

Die vorliegende Dissertation wurde im Rahmen des von der EU geförderten Projektes CARBOOCEAN erstellt. Das Ziel von CARBOOCEAN war es den  $\text{CO}_2$  Fluss im Nordatlantik und Südpolarmeer mit großer Genauigkeit zu bestimmen und die bestehenden Unsicherheiten der Bestimmung zu verringern. Unter anderem sollte dafür ein Netzwerk von Handelsschiffen etabliert werden, die mit Messgeräten zur Messung des Partialdrucks von  $\text{CO}_2$  ( $p\text{CO}_2$ ) im Oberflächenwasser ausgestattet sind. Daher wurde im Rahmen dieser Arbeit ein solches Gerät 2005 auf einem Frachtschiff installiert, das regelmäßig zwischen Europa und Nordamerika verkehrt. Über mehr als ein Jahr konnten so kontinuierliche Daten ( $p\text{CO}_2$ , Temperatur, Salzgehalt) und diskrete Proben (Nährstoffe, diverse Kohlenstoffparameter) gewonnen werden. Die Daten dieser Arbeit wurden mit Daten verglichen, die 2002/2003 im Rahmen des Projektes "CARbon VARIability Studies by Ships of Opportunity" (CAVASSOO) auf einem anderen Handelsschiff erhoben wurden, das auch in dieser Region verkehrte. Der Vergleich zeigt, dass der Nordatlantik zwar eine Nettosenke für atmosphärisches  $\text{CO}_2$  ist, dass der  $\text{CO}_2$ -Fluss aber von Jahr zu Jahr stark variiert. Diese hohe Variabilität wurde besonders im westlichen Teil (westlich von  $35^\circ\text{W}$ ) beobachtet:  $48.4 \text{ g C m}^{-2} \text{ yr}^{-1}$  in 2002/2003 und  $32.0 \text{ g C m}^{-2} \text{ yr}^{-1}$  in 2006/2007. Außerdem waren die Daten dieser Arbeit Teil weiterer Studien, die  $p\text{CO}_2$ -Daten verschiedener Handelsschiffe benutzt haben um mittels eines neuronalen Netzes (NN) oder multipler linearer Regression (MLR) beckenweite Abschätzungen des  $\text{CO}_2$ -Flusses zu machen. Der Nettofluss in den Ozean über die gesamte Region wurde für das Jahr 2005 auf  $0.25 \pm 0.5 \text{ Pg C}$  bestimmt. Außerdem flossen die Daten dieser Arbeit in eine neue weltweite Klimatologie von Oberflächen- $p\text{CO}_2$  ein. Diese basiert auf über 3 Millionen Messungen zwischen 1974 und 2007.

Die Nährstoff-Daten dieser Arbeit und des CAVASSOO-Projektes wurden benutzt, um mittels MLR eine Gleichung aufzustellen mit der sich die Nährstoffkonzentrationen in der durchmischten Deckschicht des Nordatlantiks (zwischen  $40^\circ\text{N}$  und  $52^\circ\text{N}$ ) mit einer Unsicherheit von  $\pm 1.4 \mu\text{mol L}^{-1}$  abschätzen lässt. Mit den berechneten Nitrat-Konzentrationen lassen sich beobachtete langjährige  $p\text{CO}_2$  Anstiege im Nordatlantik teilweise erklären.

Im Rahmen dieser Arbeit wurden auch  $p\text{CO}_2$  Messungen auf Forschungsschiffen während drei Reisen in das Auftriebsgebiet vor Mauretania (Nordwest-Afrika,  $16^\circ\text{N}$  -  $21^\circ\text{N}$ ) durchgeführt. Das Gebiet vor Mauretania ist bekannt für seine hohe biologische Produktivität; hohe Nährstoffkonzentrationen und warme Wassertemperaturen sorgen für starke Planktonblüten. In den frisch aufgetriebenen Wassermassen nahe der Küste sind  $\text{CO}_2$  und  $\text{N}_2\text{O}$  in Bezug auf die Atmosphäre stark übersättigt, in Richtung des offenen Ozeans fallen die Konzentrationen allerdings schnell ab. Das Abklingen der hohen  $\text{CO}_2$  Konzentration wird hauptsächlich vom Gasaustausch und biologischer Aktivität getrieben, wobei es schwierig ist den Anteil der beiden Prozesse zu quantifizieren. Das Abklingen der hohen  $\text{N}_2\text{O}$ -Konzentrationen hingegen wird nur vom Gasaustausch bestimmt. Mittels dieser Gasaustauschraten kann jeder Wassermasse eine Zeit zugeordnet werden, die seit dem Auftrieb vergangen ist und durch die Kombination der beiden Datensätze von  $\text{CO}_2$  und  $\text{N}_2\text{O}$  können nun der Gasaustausch-Anteil und der biologische Anteil ("net community production", NCP) vom  $\text{CO}_2$  Abfall quantifiziert werden. Der Auftrieb vor Mauretania ist zeitlich und räumlich sehr variabel. Im Frühjahr ist er am stärksten ausgeprägt und  $p\text{CO}_2$  Werte um  $750 \mu\text{atm}$  wurden im Oberflächenwasser beobachtet. Die berechneten NCP Werte reichen von  $0.4 \pm 0.1 \text{ g C m}^{-2} \text{ d}^{-1}$  während schwachen Auftriebs bis zu  $2.8 \pm 0.9 \text{ g C m}^{-2} \text{ d}^{-1}$  während starken Auftriebs. Außerdem zeigen die NCP-Werte eine starke Korrelation mit einem (aus Winddaten erstellten) Auftriebsindex. Mittels dieser empirischen Beziehung wurden jährliche NCP Werte berechnet, die eine hohe Variabilität zwischen den Jahren zeigen.

# Abstract

This Ph.D. thesis was part of the European project CARBOOCEAN. The aim of CARBOOCEAN was to significantly reduce the uncertainty of air-sea CO<sub>2</sub> fluxes in the North Atlantic and Southern Ocean. One part was the establishment of a network of "Volunteer Observing Ships" (VOS) equipped with instruments to measure the partial pressure of CO<sub>2</sub> ( $p\text{CO}_2$ ) in the surface water of the North Atlantic. Therefore an autonomously working  $p\text{CO}_2$  instrument was installed on a commercial vessel which crossed the North Atlantic between Europe and Canada from 2005 until 2007.

The data obtained during this thesis were compared with data from a VOS that covered nearly the same region in 2002/2003 during the project "CARbon VARIability Studies by Ships of Opportunity" (CAVASSOO). It was shown that the North Atlantic is a net CO<sub>2</sub> sink on an annual basis but that the CO<sub>2</sub> fluxes into the ocean are highly variable especially in the western part (48.4 g C m<sup>-2</sup> yr<sup>-1</sup> in 2002/2003 and 32.0 g C m<sup>-2</sup> yr<sup>-1</sup> in 2006/2007). Furthermore the obtained data were part of studies that used data from several VOS lines to estimate basinwide CO<sub>2</sub> fluxes using a neural network approach or multiple linear regression (MLR). The integrated net flux into the ocean (between 10°N and 65°N) across the North Atlantic in 2005 was estimated to be  $0.25 \pm 0.5$  PgC. The data were also part of a new surface ocean  $p\text{CO}_2$  climatology containing more than 3 million measurements between 1974 and 2007.

Furthermore discrete nutrient samples obtained during this work and the CAVASSOO era were used to derive an equation for the estimation of nitrate in the mixed layer of the North Atlantic between 40°N and 51°N. The equation was derived by multiple linear regression (MLR) from nitrate, sea surface temperature (SST) observational data and model mixed layer depth (MLD) data. With the proposed equation it is possible to estimate nitrate concentration with an uncertainty of  $1.4 \mu\text{mol L}^{-1}$  in the study region.

During this thesis surface  $p\text{CO}_2$  and N<sub>2</sub>O data were also obtained during three research cruises in the upwelling region off Mauritania (Northwest Africa, 16°N - 21°N). The region is known as a very productive region since the upwelled water has high nutrient concentrations which

---

together with rapid warming triggers intensive blooms. High supersaturation (with respect to atmosphere) of  $\text{CO}_2$  and  $\text{N}_2\text{O}$  is observed in the fresh upwelled water masses close to the coast, while a fast decay of supersaturation of  $\text{CO}_2$  and  $\text{N}_2\text{O}$  is observed towards the open ocean. The decay of  $\text{CO}_2$  supersaturation is mainly driven by air-sea gas exchange (ASE) and biological production which are hard to separate quantitatively. In contrast the  $\text{N}_2\text{O}$  supersaturation decreases only due to ASE. Using  $\text{N}_2\text{O}$  ASE rates the time elapsed since upwelling can be assigned to a water mass. Through combination of the saturation patterns of  $\text{CO}_2$  and  $\text{N}_2\text{O}$  this time information can be used to separate the ASE and biological (net community production, NCP) components of the  $\text{CO}_2$  decay. The upwelling shows strong variability but is most pronounced in early spring with highest observed values of  $p\text{CO}_2$  of  $750 \mu\text{atm}$ . NCP values ranges from  $0.4 \pm 0.1 \text{ g C m}^{-2} \text{ d}^{-1}$  during times of weak upwelling to  $2.8 \pm 0.9 \text{ g C m}^{-2} \text{ d}^{-1}$  during a strong upwelling situation, which is comparable with other studies in this region. The estimated NCP values show a strong relationship with a wind derived upwelling index. This empirical relationship was used to estimate annual NCP, which is characterized by high interannual variability.



# 1. Introduction

This thesis was prepared within the framework of the European project CARBOOCEAN. The aim of CARBOOCEAN was to determine the ocean's role (focusing on the North Atlantic and Southern Ocean) for uptake of CO<sub>2</sub> very precisely, i.e. reducing the uncertainties of air-sea CO<sub>2</sub> flux by a factor of 2. The consortium consisted of 47 international groups that have started this integrated research. The reduction of uncertainties of CO<sub>2</sub> fluxes provides an optimal basis for further CO<sub>2</sub> predictions. The work of this thesis was part of CARBOOCEAN's work package 4 ("North Atlantic Observing system"): together with colleagues from France, Norway, Great Britain, Spain and USA an integrated observing network for surface ocean-atmosphere fluxes of CO<sub>2</sub>, based on voluntary observing ships (VOS), was established. Therefore autonomous instruments for measurement of partial pressure of CO<sub>2</sub> ( $p\text{CO}_2$ ) were installed on commercial vessels operating in the North Atlantic.

Another part of this thesis deals with autonomous  $p\text{CO}_2$  measurements that were conducted onboard research vessels. These measurements were done in the framework of the German project "Surface Ocean Processes in the Anthropocene" (SOPRAN, <http://sopran.pangaea.de/>). In contrast to measurements onboard the commercial vessels the research vessels provide the opportunity to study surface processes on smaller time scales and in specified regions. The underway  $p\text{CO}_2$  measurements of three research cruises to the Mauritanian upwelling region were used to study biological production rates in this region.

## 1.1. Scientific background

Since the 18<sup>th</sup> century the concentration of atmospheric greenhouses gases has increased steadily due to human activities. The most important gas is CO<sub>2</sub> and its concentration rose from 280 ppm to values exceeding 380 ppm at present (Forster *et al.*, 2007). Due to improving economies in emerging countries the emissions increased by 29% from 2000 to 2008 (Le Quéré *et al.*, 2009). Fig. 1.1 shows the (famous) atmospheric CO<sub>2</sub> concentration record from the Mauna Loa Observatory

in Hawaii. In addition to the increasing CO<sub>2</sub> signal a seasonal amplitude is observed, that corresponds to the terrestrial biosphere net carbon drawdown during spring/summer and net respiration during autumn/winter. Since 1800 the ocean removed (until 1994) about  $118 \pm 19$

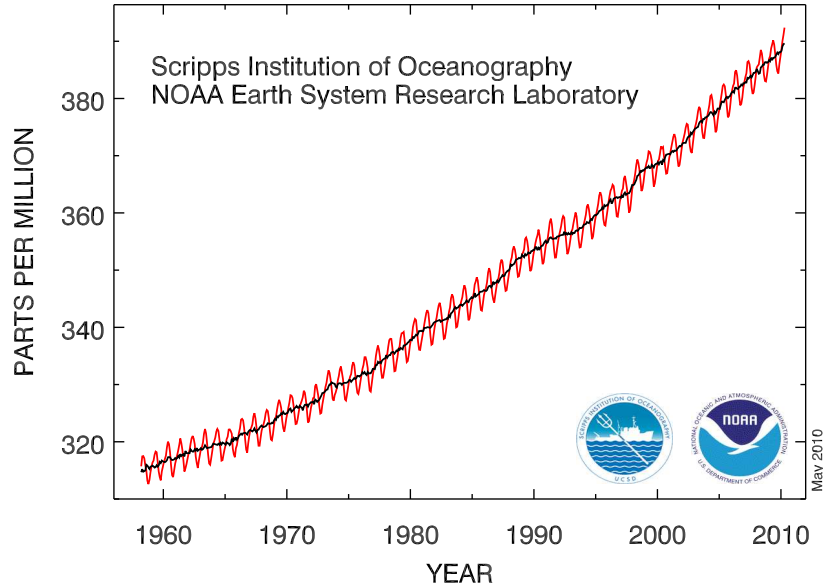


Figure 1.1.: Monthly mean (red) of atmospheric CO<sub>2</sub> concentration as measured at Mauna Loa Observatory in Hawaii, USA. The black line denote the annual mean. The figure is taken from GLOBALVIEW-CO<sub>2</sub> (2009).

PgC from the atmosphere (Sabine *et al.*, 2004) which is approximately one-third of the amount of CO<sub>2</sub> that were emitted to the atmosphere during this period. Thus the ocean is an important net sink for anthropogenic CO<sub>2</sub> and hence slows the anthropogenically driven climate change. The ocean's net uptake is superimposed on the natural CO<sub>2</sub> sink source pattern which is variable both in space and time. Consequently a detailed knowledge of the magnitude and distribution of the source and sink areas is crucial for further climate predictions.

Generally the tropics serve as a CO<sub>2</sub> source and the midlatitudes as a strong sink (Gruber *et al.*, 2009). The high latitudes (north of 50°) show lower net fluxes into the ocean. In the northern hemisphere the North Atlantic has been shown to be the largest CO<sub>2</sub> ocean sink (e.g. Gloor *et al.*, 2003; Takahashi *et al.*, 2009). The CO<sub>2</sub> fluxes in the North Atlantic are highly variable on seasonal and interannual time scales (Corbière *et al.*, 2007; Gruber *et al.*, 2002; Lüger *et al.*, 2004; Schuster *et al.*, 2009; Watson *et al.*, 2009) and consequently large scale observations of the North Atlantic are needed to document and understand the driving forces of the observed variability to constrain further climate predictions (Hegerl *et al.*, 2007). The strength of the North Atlantic carbon sink depends very much on the difference of seawater and atmospheric  $p\text{CO}_2$  ( $\Delta p\text{CO}_2$ ).

Numerous studies investigated in the long term observation of  $\Delta p\text{CO}_2$  in the North Atlantic (e.g. Bates, 2007; Corbière *et al.*, 2007; Omar and Olsen, 2006; Schuster and Watson, 2007; Takahashi *et al.*, 2009) and some studies report a decreasing  $\Delta p\text{CO}_2$  (Corbière *et al.*, 2007; Lefèvre *et al.*, 2004; Omar and Olsen, 2006; Schuster and Watson, 2007; Schuster *et al.*, 2009) in the North Atlantic which results in a decreasing sink for atmospheric  $\text{CO}_2$ .

One major driving force of the  $p\text{CO}_2$  variability in the North Atlantic is the biological productivity (Lüger *et al.*, 2004; Takahashi *et al.*, 2002). The North Atlantic shows one of the largest greening events of the global surface (Siegel *et al.*, 2002) extending several hundreds of kilometers. Fig. 1.2 shows three-monthly averaged data of chlorophyll-a concentration (chl-a).

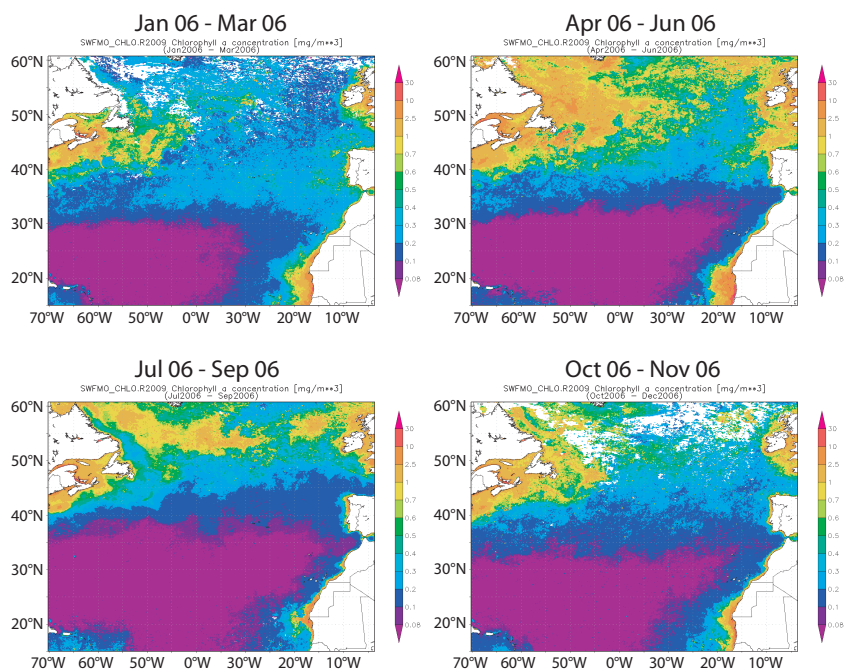


Figure 1.2.: Seasonally averaged chlorophyll-a concentration in the North Atlantic. The figure was produced with the Giovanni online data system, developed and maintained by the NASA GES DISC.

North of  $40^\circ\text{N}$  the start of the spring bloom in March/April can be clearly observed. The coherent  $\text{CO}_2$  drawdown counteracts the  $\text{CO}_2$  outgassing due to warming of the surface waters in spring/summer. The resulting monthly Net Primary Production (NPP) as estimated with a chlorophyll based model (Behrenfeld *et al.*, 2005) and varies between 0.1 Pg C during winter (January) and 0.5 Pg C in July in the North Atlantic.

Among the great ocean basins with their high productivities, Eastern Boundary Upwelling Ecosystems (EBUE) are known as some of the most productive regions in the ocean. In combination with the Coriolis force trade winds drive a coastal upwelling along the continental

west coasts. The observed upwelling patterns are in some regions seasonal phenomena while there are also coastal regions with a constant upwelling during the year. Freon *et al.* (2009) recently compiled available evidence documenting the importance of EBUEs with respect to ocean productivity and air sea gas exchange (ASE). Upwelling injects nutrients into the euphotic zone inducing plankton blooms. Approximately 11% of global new production are generated in EBUEs although they account for only 1% of the surface area of the world ocean (Chavez and Toggweiler, 1995). This high productivity is accompanied by a strong CO<sub>2</sub> drawdown and uptake of atmospheric CO<sub>2</sub>. On the other hand, upwelling transports water enriched in dissolved inorganic carbon (DIC) and nitrous oxide (N<sub>2</sub>O) to the surface. This results in supersaturation of these gases in freshly upwelled waters and consequently in outgassing. For CO<sub>2</sub>, outgassing to the atmosphere and concurrent net primary production will both lead to a rapid decline of CO<sub>2</sub> supersaturation. A separation of these two processes is not straight forward (Service *et al.*, 1998).

Lueker *et al.* (2003) estimated the ASE for various gases in a coastal upwelling region using high precision atmospheric observations. Primary production in upwelling areas has also been estimated by different methods using remotely sensed data as proxies (e.g., Behrenfeld *et al.*, 2005; Demarcq, 2009; Hoepffner *et al.*, 1999; Messié *et al.*, 2009) and by incubation measurements (Dugdale and Goering, 1967). The latter provide local instantaneous productivity estimates with potential artefacts due to the incubation whereas remotely sensed estimates cover larger areas but have other sources of bias (Chavez and Messié, 2009). Minas *et al.* (1986) derived production estimates for the Mauritanian upwelling by direct measurements of nutrients and their subsequent decrease. They estimated Net Community Production (NCP) on a daily basis for a single cruise in spring 1974. During our cruises both CO<sub>2</sub> and N<sub>2</sub>O were measured and N<sub>2</sub>O was used as an inert tracer of ASE in the mixed layer providing a means to assess time elapsed since the upwelling. In the study region, changes in N<sub>2</sub>O are only caused by ASE, because nitrification is inhibited by light (Horrigan *et al.*, 1981). In contrast CO<sub>2</sub> changes in the surface water are mediated by both, ASE and biology. This distinctive behavior was used to separate the two processes (ASE and biology) for CO<sub>2</sub> and calculate NCP.

## 1.2. Study regions

The North Atlantic Ocean between 40°N and 55°N is divided into four major basins (Labrador, European, North American and North African basin (Wright and Worthington, 1970)). The

Mid-Atlantic ridge, which runs approximately along  $30^{\circ}\text{W}$  -  $35^{\circ}\text{W}$ , separates the western from the eastern basins. It divides the surface water into the "Eastern North Atlantic Central Water" (ENACW) and the "Western North Atlantic Central Water" (WNAC) which differ both in physical and biological properties (Emery and Meincke, 1986; Tomczak and Godfrey, 2002). The western part is dominated by the north-eastwards flowing "Gulf Stream" (GFST) which dissipates approximately east of  $55^{\circ}\text{W}$  into the "North Atlantic Drift" (NADR) which is flowing further north-eastward and into the "North Atlantic Subtropical Gyre" (NAST). Fig. 1.3 shows

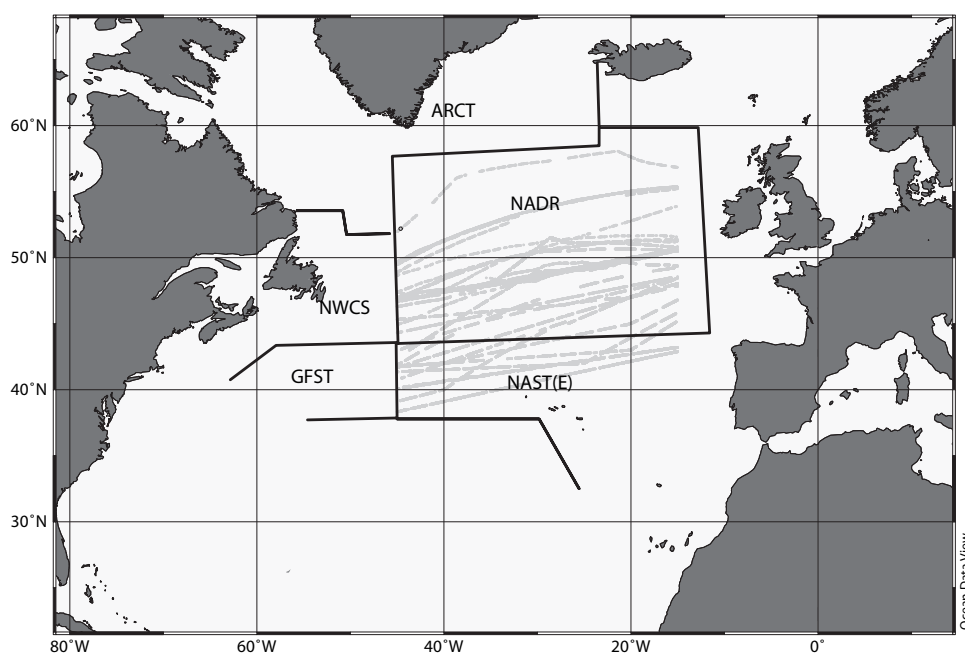


Figure 1.3.: The biogeochemical provinces in the North Atlantic as defined by Longhurst (2007). The grey dots denote the  $p\text{CO}_2$  underway data recorded onboard the VOS (only data between  $10^{\circ}\text{W}$   $45^{\circ}\text{W}$  are shown). ARCT: Atlantic Arctic Province, GFST: Gulf Stream Province, NADR: North Atlantic Drift Province, NAST(E): North Atlantic Subtropical Gyral Province (eastern), NWCS: Northwest Atlantic Shelves Province.

cruise tracks of the VOS lines and the partitioning of the North Atlantic into different biogeochemical provinces as defined by Longhurst (2007). The main part of the data lies in the NADR and NAST provinces. The ecological processes in these provinces are primarily driven by the same physical processes (i.e. winter advection) that transport nutrients into the euphotic zone. At the north-west boundary of the study region the Labrador current (LC) transports nutrient rich water into the GFST and NADR. As mentioned above nutrient supply to the euphotic zone is crucial for a phytoplankton bloom in the whole study area. In the western part this supply is mainly driven by wind stirring and eddies. Together with sufficient light conditions this promotes phytoplankton growth. In the eastern part winter convection plays a major role for the nutrient

supply (Cianca *et al.*, 2007). During summer the strong stratification prevents further nutrient supply to the surface and the phytoplankton growth stops.

The Mauritanian upwelling region reaches from approximately  $18^{\circ}\text{N}$  to  $21^{\circ}\text{N}$  along the coast of northwest Africa and shows the highest spatial and temporal variability compared to the other main EBUEs (Peru, Benguela, California) (Carr and Kearns, 2003). The study region is known as a transition zone between constant upwelling during the year (north of  $20^{\circ}\text{N}$ ) to seasonal upwelling with the strongest upwelling in spring (Schemainda *et al.*, 1975; Wooster *et al.*, 1976) south of  $20^{\circ}\text{N}$ . This phenomenon can be observed in the surface chl-a concentration shown in Fig. 1.2: Low chl-a concentration during summer and highest chl-a concentration in spring.

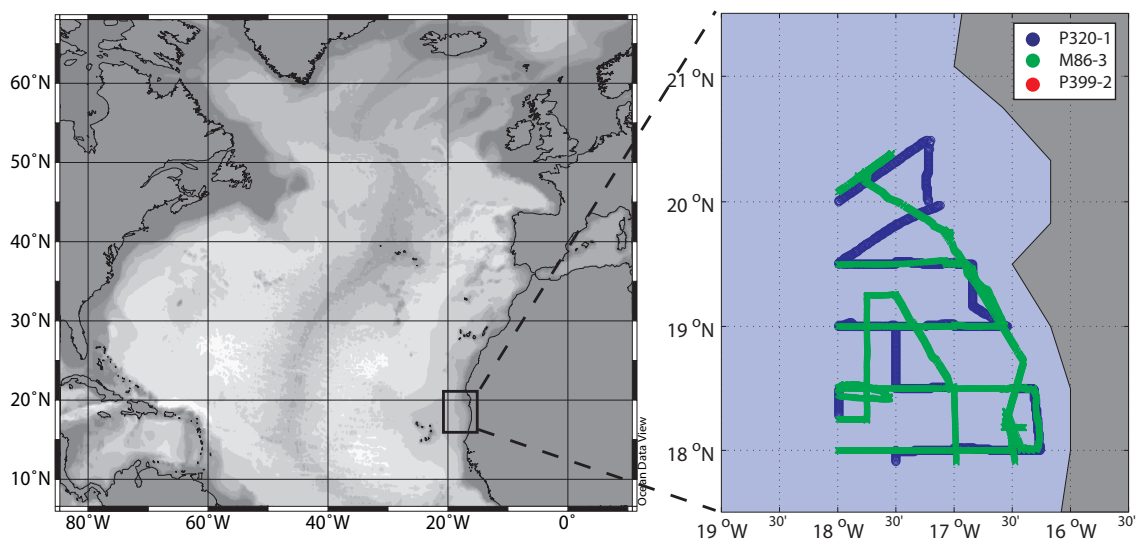


Figure 1.4.: The Mauritanian upwelling region and the cruise tracks of the three cruises.

### 1.3. Underway measurements

This thesis is mostly based on data obtained from underway measurements performed both on research vessels and commercial vessels. A detailed description of the used instruments is provided in Chapter 2.

Seafarers originally made meteorological observations to aid efficient and safe navigation. During the last decades the use of commercial vessels as VOS became more and more common because they provide a great opportunity for ocean observation (Goni *et al.*, 2010; Monteiro *et al.*, 2010; Kent *et al.*, 2010) as they often operate on regular routes (studying seasonal and interannual

variations) and provide a low-cost research platform. At present, observations on VOS are not limited to meteorological observations. The use of technical equipment allows high resolution datasets of various parameters: Takahashi *et al.* (2009, see also Chapter 6) published a global climatological mean seawater  $p\text{CO}_2$  dataset that is based on about 3 million datapoints recorded since 1970 onboard VOS and research vessels. Fig. 1.5 shows the VOS lines presently measuring

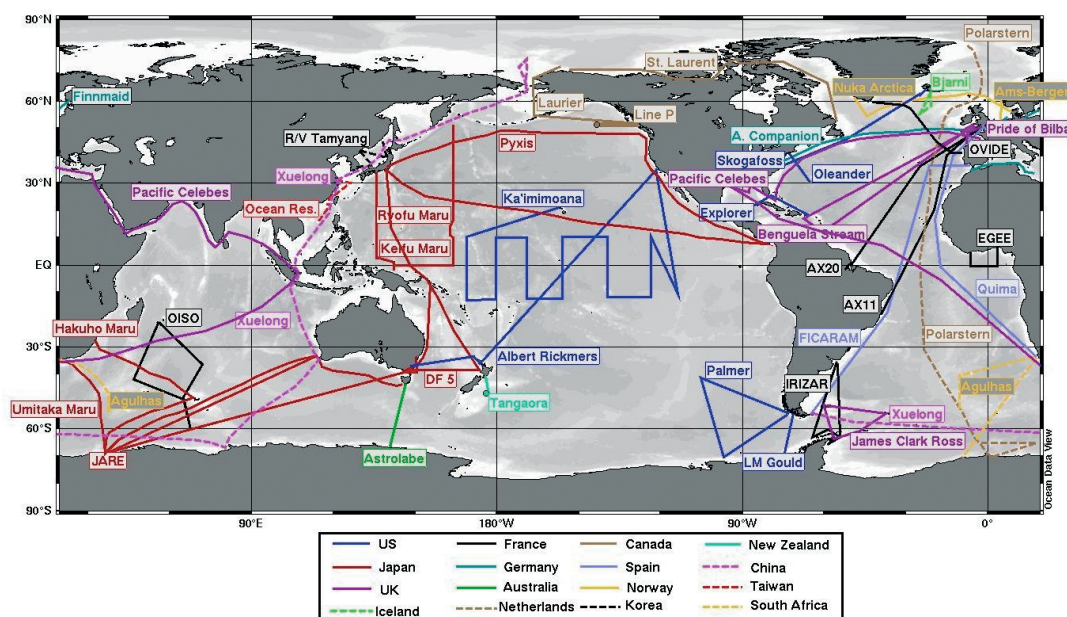


Figure 1.5.: Map of the global ocean showing locations where routine surface carbon measurements are presently undertaken. (<http://ioccp.org>)

surface carbon parameters. During the era of CARBOOCEAN a coordinated network of several VOS produced a high-quality dataset that was used to define the annual  $\text{CO}_2$  flux in the North Atlantic to a precision of about 10% (Watson *et al.*, 2009, see also Chapter 4).

However,  $p\text{CO}_2$  measurements onboard commercial vessels are a metastable enterprise for several reasons: (1) The installation onboard commercial vessels remain often improved because one has to find the best compromise between the ship's and the scientist's needs with limited funding. (2) Ship routes are subject to change and it can happen that the vessel with the equipment onboard suddenly changes its route. (3) Intercomparison of the data from different VOS lines is difficult due to different installations onboard. Furthermore a variety of systems for  $p\text{CO}_2$  measurements are used. (4) Sometimes it is hard to argue with the shipping companies to allow shipriders onboard. But joining the ship is a good opportunity to supervise the instruments and adjust them in order to obtain and secure high-quality datasets.

Also onboard research vessels underway measurements were done. In contrast to commercial

vessels research vessels go to areas where the scientist want them to go. But in general it is difficult to obtain ship time and the costs for a day of ship time are high in comparison with VOS ship time. Measurements in small areas with high data resolution are possible and thus basic mechanisms of the surface biogeochemistry can be studied. Furthermore onboard research vessels it is possible to conduct reference measurements and a variety of ancillary parameter can be measured. Thus detailed biogeochemical interpretations of the dataset are possible and research vessels provide a good basis to intercompare and test instruments before installing on VOS.

## 1.4. Oceanic carbonate system

For the understanding of the variability of  $p\text{CO}_2$  the oceanic carbonate system has to be taken into account. The oceanic carbonate system is responsible for about 95% of the acid-base buffering over the normal pH range of seawater (7.8 - 8.2). The exchange of  $\text{CO}_2$  across the seawater-atmosphere interface is the fundamental process where atmospheric  $\text{CO}_2$  can dissolve into the ocean or is released from the ocean to the atmosphere:



where K is the equilibrium solubility constant which varies with temperature, pressure and salinity. In contrast to other gases that are dissolved in the ocean  $\text{CO}_2$  chemically reacts with the water and forms carbonic acid:



Due to the different rate constants of the forward and backward reaction the concentration of  $\text{CO}_2(\text{aq})$  is about 670 times higher than the concentration of  $\text{H}_2\text{CO}_3$ . Furthermore the two species are hard to differentiate (by analytical means) and thus they were summarized to  $\text{CO}_2^*$ :

$$[\text{CO}_2^*] = [\text{CO}_2(\text{aq})] + [\text{H}_2\text{CO}_3] \quad (1.3)$$

Consequently equation 1.1 has to be rewritten as:





Since  $\text{H}_2\text{CO}_3$  is an acid it dissociates in water as follows:



$K_1^*$  and  $K_2^*$  are the corresponding dissociation constants. They depend on temperature, salinity and pressure and were precisely determined by various authors (e.g. Goyet and Poisson, 1989; Hansson, 1973; Lueker *et al.*, 2000; Mehrbach *et al.*, 1973; Mojica Prieto and Millero, 2002; Roy *et al.*, 1993).

The individual carbonate species can not be analytically determined but a full characterisation of the oceanic carbonate system is based on the following suite of four measurable parameter:

- pH
- Total alkalinity ( $A_T$ )
- Dissolved inorganic carbon (DIC)
- partial pressure of  $\text{CO}_2$  ( $p\text{CO}_2$ )

Knowing two of these parameters (and the equilibrium constants involved) the other two and the full speciation of the  $\text{CO}_2$  systems concentration can be calculated. In the following paragraph the parameters itself are described:

**pH** The pH is the negative common logarithm of the  $\text{H}^+$ -ion concentration. For quantitative considerations in the marine environment only concentration based scales are used (total scale, seawater scale, free scale). The different scales reflect the composition of the buffer solutions used and can be converted among each other.

**DIC** This is the sum of all inorganic carbon species dissolved in water:

$$\text{DIC} = [\text{CO}_2^*] + [\text{HCO}_3^-] + [\text{CO}_3^{2-}] \quad (1.7)$$

**$A_T$**  Total alkalinity is defined as the number of moles of  $\text{H}^+$ -ions equivalent to the excess of proton acceptors (corresponding bases from weak acids,  $K \leq 10^{-4.5}$  @ 25°C) over proton donors

(acids with  $K > 10^{-4.5}$ ) per kg sample (Dickson, 1981):

$$\begin{aligned}
 A_T = & [\text{HCO}_3^-] + 2[\text{CO}_3^{2-}] + [\text{B}(\text{OH})_4^-] + [\text{OH}^-] + [\text{HPO}_4^{2-}] \\
 & + 2[\text{PO}_4^{3-}] + [\text{SiO}(\text{OH})_3^-] + [\text{NH}_3] + [\text{HS}^-] + \dots \\
 & - [\text{H}^+] - [\text{HSO}_4^-] - [\text{HF}] - [\text{H}_3\text{PO}_4] - \dots
 \end{aligned} \tag{1.8}$$

Thus the alkalinity is a measure for the buffer capacity of a seawater sample.

**$p\text{CO}_2$**  The partial pressure of any gas (G) is the product of its mole fraction ( $x_G$ ) and the total pressure ( $P$ ) of the gas phase. For  $\text{CO}_2$  this results in Eq. 1.9:

$$p\text{CO}_2 = x\text{CO}_2 \times P \tag{1.9}$$

Consequently the  $p\text{CO}_2$  of seawater is only measurable in a gas phase that is in thermodynamical equilibrium with the sample. There occurs a net flux of  $\text{CO}_2$  via the air-sea interface as long as the two phases are in disequilibrium. More correctly the fugacity of  $\text{CO}_2$  ( $f\text{CO}_2$ ) should be used instead of  $p\text{CO}_2$  which takes into account the slight non-ideal behavior of  $\text{CO}_2$ . The difference between  $f\text{CO}_2$  and  $p\text{CO}_2$  is about 0.4% at 1 atm.

The  $p\text{CO}_2$  is connected with  $\text{CO}_2(\text{aq})$  by the Henry's law constant  $K_H$ :

$$K_H \times p\text{CO}_2 = [\text{CO}_2^*(\text{aq})] \tag{1.10}$$

## 1.5. Global carbon cycle

$\text{CO}_2$  plays an important role in cycling of carbon between the different pools, i.e. atmosphere, terrestrial biosphere and ocean. Atmospheric  $\text{CO}_2$  is converted to biomass by terrestrial plants via photosynthesis where soils, animals and respiration return carbon to the atmosphere. Fig. 1.6 shows the global carbon cycle including the anthropogenic perturbation which is caused by burning of fossil fuel, cement production and changed land use. Furthermore  $\text{CO}_2$  is continuously exchanged with the ocean. Once  $\text{CO}_2$  enters the ocean it reacts with water and forms carbonate and bicarbonate. The fate of  $\text{CO}_2$  in seawater is governed by various (physical and biological) processes (e.g. Sarmiento and Gruber, 2006). Since these processes "transport" the  $\text{CO}_2$  against a concentration gradient through the ocean they are called "pumps". Fig. 1.7 shows the three main pumps.

If  $\text{CO}_2$  is dissolved in the surface waters it can be transported to any region and depth of the

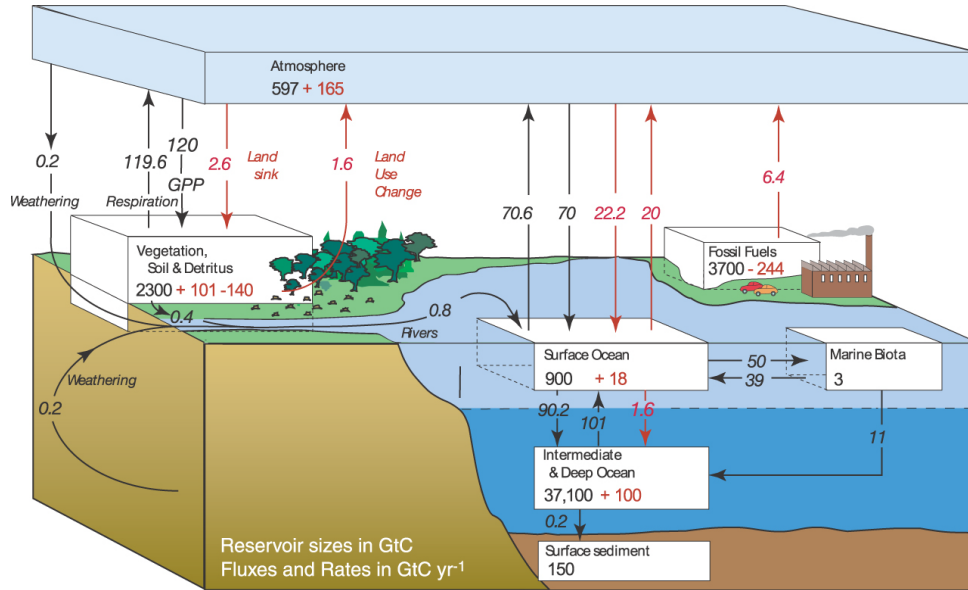
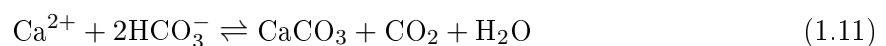


Figure 1.6.: The global carbon cycle during the 1990's. The annual fluxes are in  $\text{Gt C yr}^{-1}$  and the reservoirs in  $\text{Gt C}$ . Preindustrial values are shown in black while the anthropogenic perturbation is shown in red numbers. (Figure is taken from the 4<sup>th</sup> IPCC report, Denman *et al.* (2007)).

ocean by advective and convective mixing.  $\text{CO}_2$  dissolves into surface waters when they cool during transit from warm to cold regions where they can sink in deep water forming regions. When surface water sinks down following the ocean conveyor belt (Broecker, 1991) it takes along also the dissolved  $\text{CO}_2$  and brings it to the deep ocean where it is transported through until it reaches the surface again. This effect is called the "solubility pump" or "physical pump"

The "biological pump" is separated into the "organic pump" and the "calcium carbonate pump". The first one (also called "soft tissue pump") runs on photosynthesis, which can be visualized as the fixation of dissolved inorganic carbon into organic particles. These particles partly sink out of the sunlit zone into deeper waters where they are remineralized and thus carbon is removed from the interface between ocean and atmosphere until the water reaches the surface again. The efficiency of the pump is controlled by the amount of nutrients available to drive the process. The second one (also called the "hard tissue pump") runs in the reverse direction and is driven by the precipitation and dissolution of calcium carbonate:



In the surface  $\text{CaCO}_3$  is produced mainly by biological processes (Sarmiento and Gruber, 2006). The  $\text{CaCO}_3$  sinks and dissolves partly in the deep ocean which transports carbon to the depth.

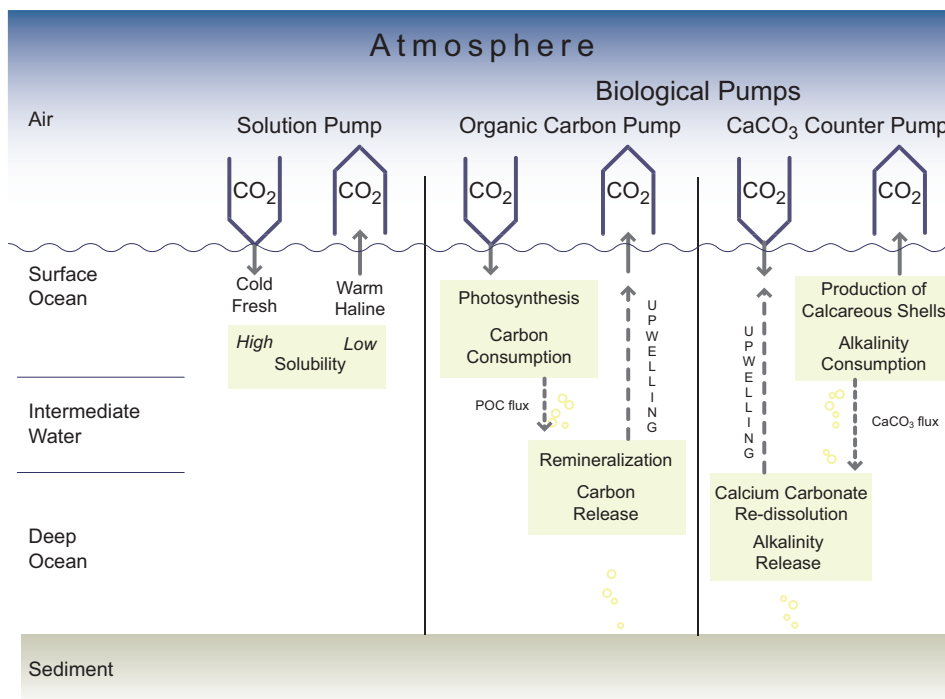


Figure 1.7.: The three oceanic carbon pumps: solubility pump, organic pump and  $\text{CaCO}_3$  pump. (Figure is taken from the 4<sup>th</sup> IPCC report, Denman *et al.* (2007)).

The production of  $\text{CaCO}_3$  in surface waters drives  $\text{CO}_2$  out of the ocean and therefore constitutes a counter effect to the soft tissue pump. This production and dissolution of  $\text{CaCO}_3$  influences both the DIC and the  $A_T$  and can thus have a large influence on the carbon cycle.

## 1.6. Air-sea gas exchange of $\text{CO}_2$

The net flux of  $\text{CO}_2$  across the air-sea interface is mainly driven by the difference of partial pressures of  $\text{CO}_2$  in seawater and atmosphere:

$$\Delta p\text{CO}_2 = p\text{CO}_{2,\text{seawater}} - p\text{CO}_{2,\text{atmosphere}} \quad (1.12)$$

In contrast to the atmospheric  $p\text{CO}_2$  ( $p\text{CO}_{2,\text{atm}}$ ) the seawater  $p\text{CO}_2$  ( $p\text{CO}_{2,\text{sw}}$ ) typically shows higher spatial and temporal variability. The factors driving  $p\text{CO}_{2,\text{sw}}$  are

- temperature changes,
- advective and convective mixing,
- biological production and respiration,

- air-sea gas exchange.

The effect of temperature was quantified by Takahashi *et al.* (1993) and the variations of  $p\text{CO}_{2,\text{sw}}$  that are only mediated by temperature changes can be quantified using their proposed empiric equation (Eq. 1.13). Fig. 1.8 shows the exponential relationship between temperature and  $p\text{CO}_2$ . They used an Atlantic surface water sample with constant chemical composition (i.e. DIC,  $A_T$ ) during the whole experiment.

$$p\text{CO}_2(T_1) = p\text{CO}_2(T_2) \times \exp(0.0423 \times (T_1 - T_2)) \quad (1.13)$$

$$p\text{CO}_2(T_1) = p\text{CO}_2(T_2) \times \exp[0.0433 \times ((T_1 - T_2) - 4.35 \times 10^{-5}(T_1^2 - T_2^2))] \quad (1.14)$$

where  $p\text{CO}_2(T_x)$  denote  $p\text{CO}_2$  at temperature  $x$ . Recently Takahashi *et al.* (2009) updated

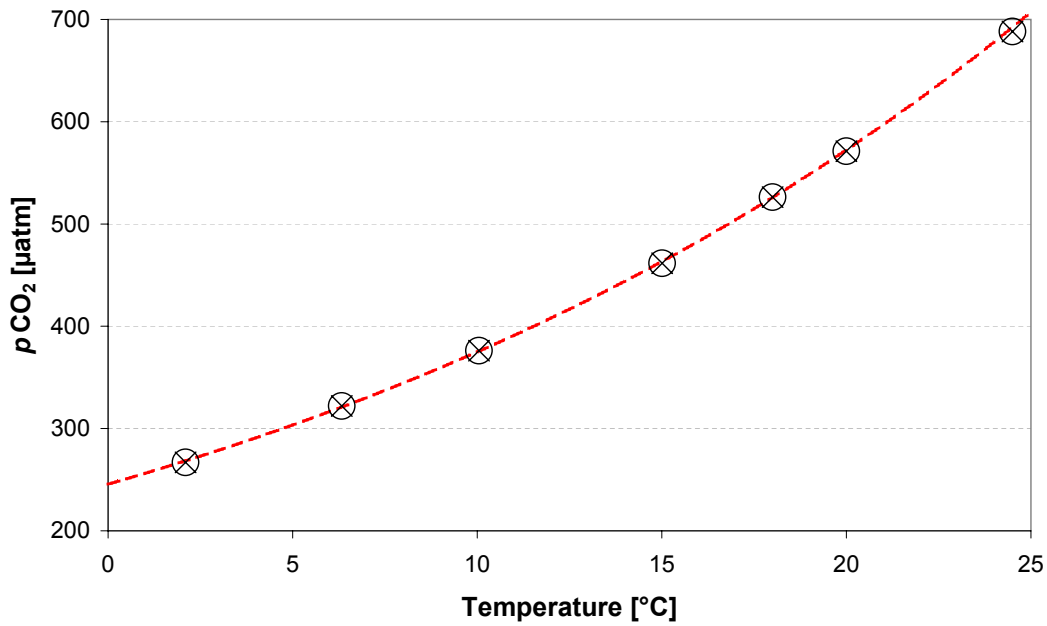


Figure 1.8.: Temperature effect on  $p\text{CO}_2$ . Data were taken from Takahashi *et al.* (1993). They used an Atlantic surface water sample with constant chemical composition. The circled crosses denote the measurements and the dashed line is the exponential fit to the data.

the proposed relationship (Eq. 1.14). However, if the temperature difference is less than  $2^\circ\text{C}$  Eq. 1.13 and Eq. 1.14 are virtually indistinguishable. Thus, both versions of the temperature correction were used in this study.

Advection and mixing processes are difficult to determine, whereas convective mixing can be addressed if the deepening and shoaling of the mixed layer depth (MLD) is estimated from models

or observations. The nutrient supply in the study area is mainly driven by winter convection (Longhurst, 2007). Thus knowledge about the variation of MLD results in knowledge of nutrient supply to the surface ocean. The variability of the nitrate concentrations can be used to estimate the biological driven component of  $p\text{CO}_{2,sw}$ . One part of this thesis deals with the estimation of nitrate concentration in the mixed layer from remotely sensed or modeled data (Chapter 7).

The air-sea gas flux of  $\text{CO}_2$  ( $F_{\text{CO}_2}$ ) is difficult to determine directly but can be estimated from  $\Delta p\text{CO}_2$  (Liss, 1983):

$$F_{\text{CO}_2} = k \times K_0 \times \Delta p\text{CO}_2 \quad (1.15)$$

where  $K_0$  is the solubility of  $\text{CO}_2$  which can be calculated following Weiss (1974) and  $k$  is the transfer velocity which is generally expressed as a power function of wind speed at 10 m height ( $k \propto u_{10}$ ). Numerous formulations can be found (e.g. Liss, 1983; Liss and Merlivat, 1986; Nightingale *et al.*, 2000; Wanninkhof, 1992; Wanninkhof *et al.*, 2009). There are other factors affecting the  $F_{\text{CO}_2}$  across the air-sea interface (waves, bubbles, surfactants) and thus the parameterization of  $k$  is still matter of debate. Consequently the determination of  $k$  is probably the part of the flux calculation that introduces the largest error.

## 1.7. Large scale $p\text{CO}_2$ observation and estimation

Next to a  $p\text{CO}_2$  climatology based on seawater measurements of 37 years (Takahashi *et al.* (2009), Chapter 6) many studies dealt with the feasibility to estimate seawater  $p\text{CO}_2$  from proxy data (Friedrich and Oschlies, 2009; Gruber *et al.*, 2009; Jamet *et al.*, 2007; Lüger *et al.*, 2006; Olsen *et al.*, 2004; Telszewski *et al.*, 2009). The chosen methods range from multiple linear regression (MLR) over neural networks (NN) to advanced model studies. Various parameters (e.g. sea surface temperature (SST), sea surface salinity (SSS), chl-a) were used to estimate seawater  $p\text{CO}_2$ . Since the NN found its way into geoscience during the last decade it is now also used in oceanography for mapping biogeochemical parameter (Friedrich and Oschlies (2009); Lefèvre *et al.* (2005); Telszewski *et al.* (2009), Chapter 5).

However, to accurately determine annually changing  $\text{CO}_2$  fluxes into the ocean a comprehensive network of observations is needed for several years. In Chapter 3,  $p\text{CO}_2$  data from two VOS lines obtained in 2002/2003 and 2006/2007 are presented. It becomes clear that the interpretation of two single years in this highly variable region of the North Atlantic is limited. Furthermore the observation of such a huge ocean basin needs more than one VOS line. Watson *et al.* (2009) have shown the capability of a network of VOS equipped with  $p\text{CO}_2$  instruments. During

the "OceanObs'09" conference several "community white papers" documented the capability of VOS for earth observation programs (e.g. Goni *et al.*, 2010; Hydes *et al.*, 2009). Furthermore the new European research structure "Integrated Carbon Observation System" (ICOS; [www.icos-infrastructure.eu](http://www.icos-infrastructure.eu)) will form a good basis to continue the oceanic  $p\text{CO}_2$  measurements beyond the duration of research projects.

## 1.8. Thesis outline

In Chapter 3 a full annual cycle of  $p\text{CO}_2$  data obtained onboard VOS during this thesis is presented and compared with data obtained during the project "CARbon VARIability Studies by Ships Of Opportunity" (CAVASSOO) in 2002/2003 (Lüger *et al.*, 2004, 2006). Even if both datasets do not cover exactly the same region interannual differences and similarities are observed.

Chapter 4 estimates the North Atlantic sink for atmospheric  $\text{CO}_2$  using measurements from 6 different VOS lines covering the North Atlantic. The potential of an integrated approach for underway  $p\text{CO}_{2,\text{sw}}$  measurements is shown.

In Chapter 5 the data from the CARBOOCEAN VOS network are used for basin-wide  $p\text{CO}_{2,\text{sw}}$  estimates on a monthly basis with a NN approach. The root mean square error (RMSE) of the NN fit to the data is  $11.6 \mu\text{atm}$ .

A climatological mean distribution of  $p\text{CO}_{2,\text{sw}}$  data is presented in Chapter 6 that is based upon 3 million  $p\text{CO}_2$  measurements between 1974 and 2007. All data were referenced to a single year (2000) and seasonal changes in different regions of the world ocean are presented.

In Chapter 7 nitrate data obtained during CAVASSOO and CARBOOCEAN era were used to estimate nitrate in the mixed layer for the North Atlantic. The equation was derived by MLR from nitrate, SST observational data and model MLD data. The nitrate estimates for different years were used to explain the observed  $p\text{CO}_{2,\text{sw}}$  variability in parts of the North Atlantic.

In Chapter 8 surface measurements of  $p\text{CO}_{2,\text{sw}}$  and  $\text{N}_2\text{O}$  in the Mauritanian upwelling region are presented. These data were obtained during 3 research cruises. The data were used to separate the biological driven  $\text{CO}_2$  drawdown from the air-sea gas exchange. With the resulting biological driven  $\text{CO}_2$  change NCP was calculated for different seasons and a relation between NCP and the strength of upwelling was observed.





## 2. Data and Methods

The main part of this thesis deals with data from two VOS: the car carrier M/V Falstaff and the combined container/car carrier M/V Atlantic Companion. Both ships crossed the North Atlantic between Europe and North America approximately on a monthly basis. Fig 2.1 shows the areas of the typical cruise tracks of these two ships. The area covered by M/V Falstaff is located south to the area covered by the M/V Atlantic Companion. The data were obtained during two European projects: CAVASSOO in 2002/2003 and CARBOOCEAN in 2005 - 2007. The M/V Falstaff was used in 2002/2003 and in 2005. Since 2005 the ship was no longer operated on a North Atlantic service but was switched to an around-the-world-route. As a consequence, the ship crossed the North Atlantic only three times a year which was considered inadequate so that a new ship had to be found. The new ship was the M/V Atlantic Companion was found which crossed the North Atlantic twice on a 5 week rounding. Due to leakage problems in our measurement system, the first good data from M/V Atlantic Companion were obtained since June 2006. On both ships, instruments were installed to measure seawater and atmospheric  $p\text{CO}_2$ , SST, SSS and chlorophyll-a. Up to seven times a year shipriders participated in trans-Atlantic crossings in order to take discrete water samples for DIC,  $A_T$  and nutrients.

For the studies in the Mauritanian upwelling region, underway data of three research cruises were used: March 2005 (R/V Poseidon, P320-1), July 2006 (R/V Meteor, M68-3) and June 2010 (R/V Poseidon, P399-2). The measured parameters were seawater and atmospheric  $p\text{CO}_2$ , SST, SSS and chl-a.

As the analytical setup on research and commercial vessels is very different a detailed description of the setup and data follows below. Table B (see appendix) lists all cruises (research cruises as well as cruises of commercial vessels) used in this study.

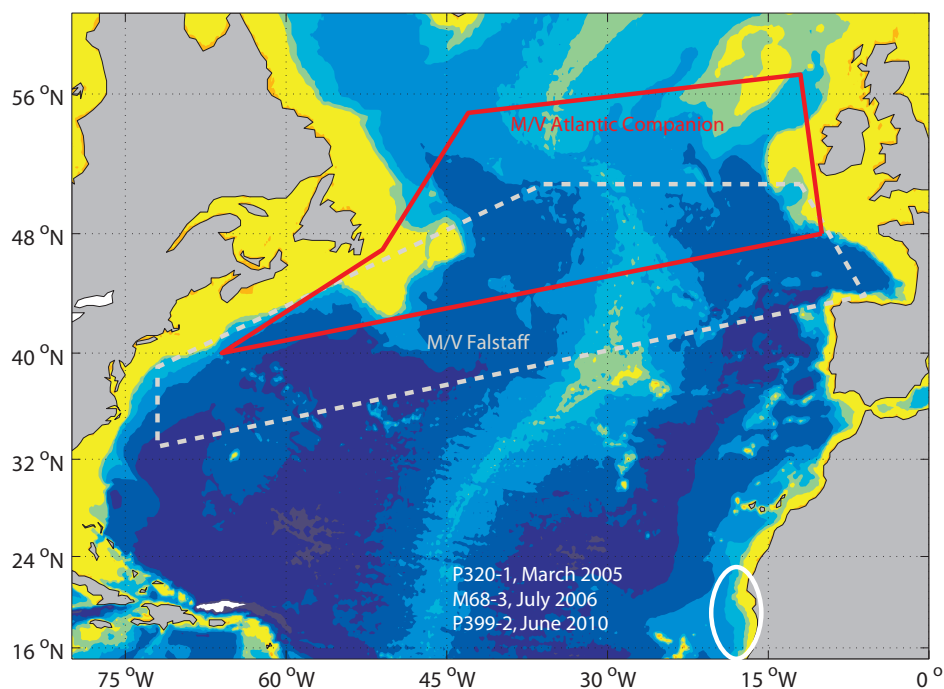


Figure 2.1.: Location of dataset acquired by the different ships/studies: Shown are the three areas of the North Atlantic that were used for this study. The red polygon shows the area that was covered by the M/V Atlantic Companion since 2006, the white polygon shows the area covered by the M/V Falstaff in 2002/2003 and 2005. The ellipse denotes the Mauritanian upwelling region, where the three research cruises took place.

## 2.1. Underway measurements

### M/V Falstaff

The instruments were installed inside the engine room next to a sea chest (approximately 6 m below the water line) that was used for the ships evaporator. A 4 m long insulated pipe was connecting the seachest with the thermosalinograph (SBE21, Seabird Electronics, Seattle, USA) which was also used to divide the water flow. To acquire unbiased in situ SST measurements an external temperature sensor (SBE38) was installed in the piping directly in the intake at the seachest. Both temperature sensors were calibrated every 6 month at the Federal Maritime Hydrographic Agency of Germany (BSH) or directly at Seabird Electronics. The  $p\text{CO}_2$  instrument used during 2002/2003 has been described in detail by Lüger *et al.* (2004).

In 2005, a new system also known as "Neill- $p\text{CO}_2$ system" was installed onboard M/V Falstaff. This system was explicitly developed for underway  $p\text{CO}_2$  measurements on commercial vessels and is designed to work autonomously for several weeks. Fig. 2.2 shows a schematic drawing of

the instrument. This new instrument has only small diameter internal tubing and it turned out that the water hydrostatic pressure was too low to ensure high enough water flow ( $3 \text{ L min}^{-1}$ ) to the instrument. Therefore a pump had to be installed between the seachest and the SBE21. Since we also wanted to sample for particulate matter we opted for a so called "torque flow" pump where the impeller is set back to allow particles to pass without being destroyed.

After passing the thermosalinograph the seawater enters the  $p\text{CO}_2$  instrument at a flow rate of  $2\text{-}3 \text{ L min}^{-1}$ . The seawater is equilibrated with an air sample using a spray head equilibrator and the air is pumped via two drying stages (thermoelectric cooler and Nafion<sup>®</sup> tubes) to the measurement unit inside a dry box where the dry  $\text{CO}_2$  mole fraction ( $x\text{CO}_2$ ) is determined via infrared measurement using a LICOR<sup>®</sup> NDIR analyzer (model 6262 or 7000). The temperature inside the equilibrator is measured as the water warms on its way from the inlet to the equilibrator and the  $p\text{CO}_2$  data have to be corrected for this warming. This temperature probe was regularly calibrated against the intake thermometer in order to ensure an accurate record of the seawater warming.

Since the system is operated at atmospheric pressure, the equilibrator vent is connected to a "pre-equilibrator" which prevents the system from aspirating engine room air with elevated  $\text{CO}_2$  concentrations inside the main equilibrator. Every three hours atmospheric  $x\text{CO}_2$  was determined. An air intake installed at a contamination free location on the ship's superstructure was connected to the instrument via a long tube. The air was pumped to the instrument and after drying the  $x\text{CO}_2$  was determined. Furthermore a small unit was installed at the upper deck of the vessel that contains a barometer for measurements of atmospheric pressure, a GPS receiver for geolocation and a modem that is connected to an Iridium antenna for data telemetry. Recorded data were sent to shore once every day, so that it was possible to check the data quality and - in case of problems - the ships crew was contacted so that they could possibly solve the problem.

The analysis cycle involves a calibration cycle every three hours during which a suite of three standard gases (nominal concentrations: 250, 350, and 450 ppm  $\text{CO}_2$  in natural air) was measured. These working standard gases were calibrated against NOAA primary standards (accuracy: 0.1 ppm (Kitzis and Zhao, 1999)) with similar concentration ranges using a LICOR NDIR analyzer (model 6262). The achieved accuracy was 0.13 ppm. Once a day the analyzer was flushed with nitrogen and the highest standard gas to correct for small instrument drift.

One big advantage of this type of instruments are the numerous housekeeping variables that are also recorded (e.g. water flow, condensation inside the air stream, ...) which strongly enhance

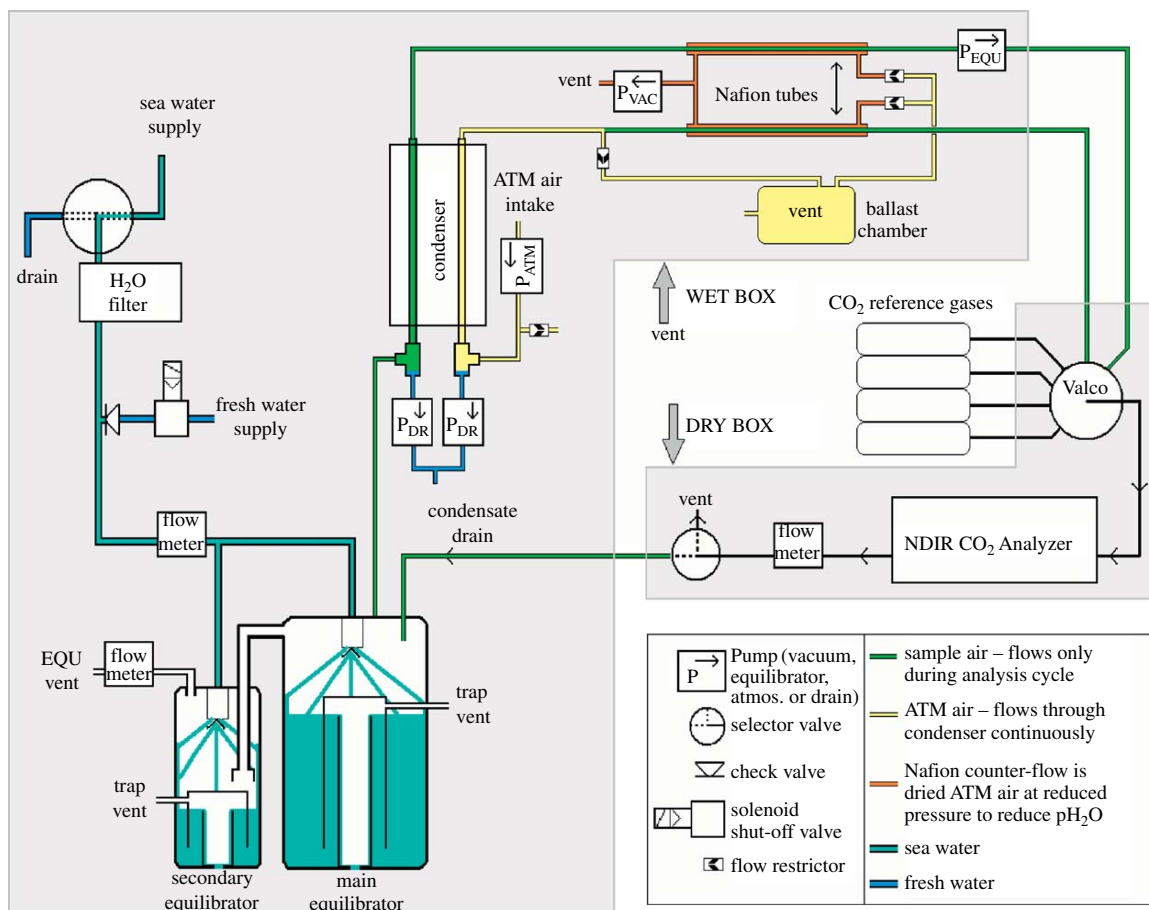


Figure 2.2.: Autonomous  $p\text{CO}_2$  instrument onboard M/V Falstaff and M/V Atlantic Companion. The wet box and dry box are indicated by the shaded areas. Inside the wet box is the equilibrator and the drying unit, while the NDIR  $\text{CO}_2$  analyzer, PC and gas valves are located in the dry box. The figure is taken from Pierrot *et al.* (2009)

the data reduction as bad data can be identified more easily by routine algorithms and flagged accordingly.

### M/V Atlantic Companion

In January 2006, a similar  $p\text{CO}_2$  instrument was installed onboard the M/V Atlantic Companion. Again the engine room was chosen for the installation of the equipment. Fig. 2.3 shows the general scheme of the installation onboard. Seawater was drawn from a sea chest approximately

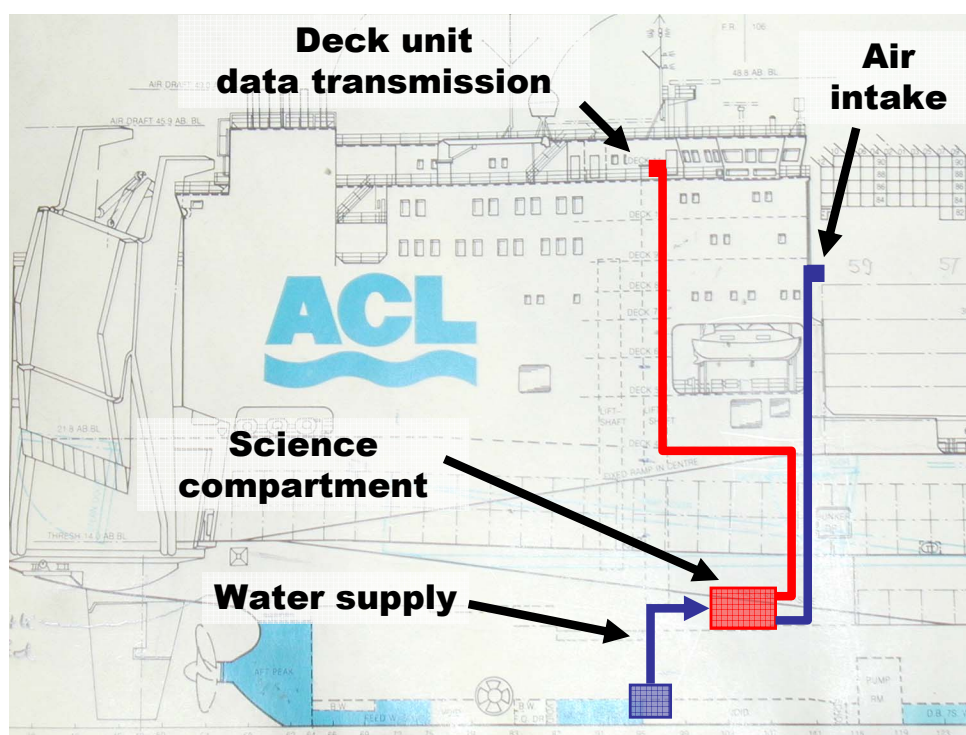


Figure 2.3.: Overview drawing of the installation onboard M/V Atlantic Companion.

7 m below the water line. The instruments were installed in a small compartment next to the main engine and a 15 m long steel pipe was installed between the seachest and the compartment. Directly at the seachest SST was measured using a SBE38 external temperature sensor (cf. paragraph above) and the same pump as described above was installed downstream of it. A stainless steel manifold was installed at the end of the pipe inside the compartment to divide the water flow into four pathways:  $p\text{CO}_2$ , chlorophyll-probe, thermosalinograph (SBE45) and a sampling spot for discrete samples. It turned out that the salinity data measured by the SBE45 were too low by approximately 1 PSU due to miscalibration by the owner (NOAA AOML, Miami, USA). For the period from January 2006 to October 2006 the measured salinity data could not be used and data from the World Ocean Atlas 2005 (Antonov *et al.*, 2006) were in

further calculations.

There was also an air inlet installed outside the ship that provided clean air to the instrument to determine atmospheric  $x\text{CO}_2$ . Again a deck unit was installed next to the bridge for the GPS antenna, Iridium antenna and barometric pressure sensor.

In October 2006 the installation was changed: The  $p\text{CO}_2$  instrument that was installed onboard M/V Falstaff was moved to M/V Atlantic Companion. At the same time the SBE21 thermosalinograph was installed onboard M/V Atlantic Companion and replaced also the manifold.

All calibration procedures (e.g. standard gas runs, temperature sensors) were the same as described for the M/V Falstaff.

## R/V Poseidon

**P320-1, March 2005** A submersible impeller pump was installed in the ship's moon pool at approximately 5 m depth. The water was pumped to the laboratory and a manifold was used to supply the water to different instruments and to take discrete samples from the underway line. A small CTD probe (ECO-probe, ME-Grisard, Germany) was installed next to the pump in the moon pool.

The  $p\text{CO}_2$  system used onboard R/V Poseidon is described in Körtzinger *et al.* (1996). The measurement principle is the same as described for the VOS: seawater is pumped through an equilibrator (2-stage equilibrator with laminar flow and bubble stage), subsequently dried and measured via a LICOR NDIR gas analyzer. The calibration procedure of the LICOR was the same as described above but the highest  $\text{CO}_2$  standard gases had higher concentration for P320-1 (510 ppm) and the zero and span settings were done manually every two days. Air was drawn from the compass platform and pumped to the laboratory to measure atmospheric  $x\text{CO}_2$ . The temperature sensors (CTD and equilibrator) were compared, but during the P320-1 cruise it turned out, that the initial calibration of the temperature probe was faulty and the CTD temperature readings of P320-1 were not usable. For further calculation SST and SSS were used from the ship's thermosalinograph. The atmospheric pressure and wind data were taken from the ship's weather stations and the wind data were corrected to 10 m height following Eq. 2.1:

$$u_{10} = \frac{u_z \times \kappa}{\sqrt{c_d} \times \log\left(\frac{z}{z_0}\right)} \quad (2.1)$$

where  $z$  is the height of wind measurements,  $u_z$  is the wind speed at height  $z$ ,  $\kappa$  the Kármán

constant ( $=0.4$ ),  $c_d$  the Drag coefficient ( $=0.0013$ ) and  $z_0$  ( $=0.0005$  m) is the roughness length.

**P399-2, June 2010** During P399-2 a commercially available  $p\text{CO}_2$  system was used (General Oceanics, USA) that is virtually identical with the Neill- $p\text{CO}_2$  system. A submersible pump was installed in the ship's moon pool at approximately 5 m depth. The water was pumped to the laboratory and a manifold was used to supply the water to different instruments and to take discrete samples from the underway line. SST and SSS were used from the ship's thermosalinograph. The temperature probe of the equilibrator was calibrated against international standards. A pipe was drawn from the compass platform to the instrument to provide uncontaminated air for measurement of atmospheric  $x\text{CO}_2$ . The atmospheric pressure and wind data were taken from the ship's weather stations and the wind data were corrected to 10 m height as described above.

## R/V Meteor

The setup onboard R/V Meteor was nearly the same as onboard R/V Poseidon (same instruments and same calibration methods). The Eco-probe CTD was recalibrated and the temperature readings were of good quality. But the salinity readings were still inadequate. The data of the ship's thermosalinograph were also useless as there were only a few days with data. Therefore all salinity data of the upper 6 m from the CTD that was used for the deep profiles were matched with salinity data from the ECO-probe. 117 matching data points were found. Fig. 2.4 shows the resulting difference between the salinity measurements from the profiling CTD and the ECO-probe. These data were divided into 3 groups and polynomial functions were fitted to the data. Note that these functions were empirical as it is not clear what caused the observed drift of the salinity readings. These functions were used to correct the recorded salinity data from the ECO-probe and the residuals (calculated - measured) is 0.014 PSU. The atmospheric pressure and wind data were taken from the ship's weather stations and the wind data were corrected to 10 m height as described above.

## 2.2. Discrete water samples

In addition to the underway measurements discrete water samples were taken. Onboard the research vessels a large number of discrete samples were obtained from deep water profiles by means of a CTD -rosette sampling system. For this study only data from the upper few meters

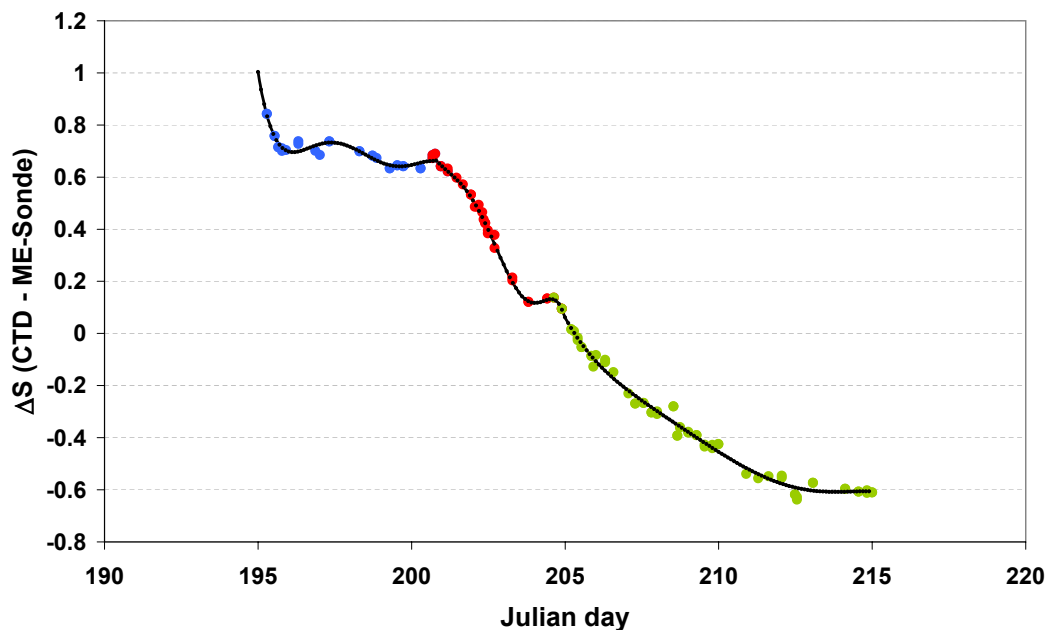


Figure 2.4.: Difference of the salinity data from the upper 6 meter of the profiling CTD from the salinity data of the ECO-probe, which was installed in the ship’s moonpool. The different colour denote the grouping of the data. For details please refer to the text.

(between 4 and 8 m depth) were used. Discrete samples were also drawn from the water lines that supplied water to the underway instruments. Onboard the commercial vessels this was the only way to take discrete samples.

Onboard the research vessels the samples were measured within several hours of collection, so that sample conservation was not necessary, whereas onboard the commercial vessels the samples had to be conserved. The sample handling is described below.

## DIC and $A_T$

Following the recommendations of Dickson *et al.* (2007) seawater was drawn into 500 mL glass bottles using a tube to fill them from the bottom to the top. Approximately half of the bottle volume were overflowed and a small head-space (approximately 1% of the bottle volume) was left to allow for water expansion. The samples onboard M/V Falstaff and M/V Atlantic Companion were poisoned by adding 100  $\mu\text{L}$  saturated mercuric chloride ( $\text{HgCl}_2$ ) solution thus preventing further biological activity. These samples were stored in the dark at room temperature and were measured within four month at the IFM-GEOMAR. The DIC measurements were performed (ashore and onboard) using a coulometric technique with a SOMMA system (Johnson *et al.*, 1993, 1998). The determination of  $A_T$  was performed by potentiometric titration using a VINDTA



system (Mintrop *et al.*, 2000).

In order to assess the precision and accuracy, certified seawater samples (Dickson, 2001) and duplicate samples were routinely measured. The accuracy was estimated to  $2.2 \mu\text{mol kg}^{-1}$  for DIC and  $4.7 \mu\text{mol kg}^{-1}$  for  $A_T$ .

## Nutrients

Seawater was drawn into 60 mL plastic bottles that were either immediately measured (P320, M68-3, P399-2) or frozen at  $-18^\circ\text{C}$  (VOS). The latter were kept frozen until measurement in the shore-based laboratory at the IFM-GEOMAR, Kiel. All samples were measured with the same continuous-flow-autoanalyzer following the method of Hansen and Koroleff (1999). The overall accuracy for nutrient analysis was approximately 1 %. The precision was determined by duplicate measurements and resulted in  $0.12 \pm 0.10 \mu\text{mol L}^{-1}$  for nitrate.

### 2.3. Data reduction of $p\text{CO}_2$ measurements

Data reduction and quality check of all  $p\text{CO}_2$  data was done by numerous Matlab scripts, that were written following Pierrot *et al.* (2009). No data were deleted but flagged as good, questionable and bad according to various criteria and only good data were used for this study. The following procedure was applied to the data obtained since 2005 onboard the VOS and onboard the research vessels:

1. The daily data files were plotted for visual data inspection and all daily files of one cruise were merged into one data file per cruise.
2. Sometimes auxiliary data (e.g. pressure) were not saved for a datapoint. If the data gap was not more than 5 minutes the data were linearly interpolated using the surrounding data.
3. The seawater needed a long time (up to 6 minutes) from the intake to the instrument. Consequently the equilibrator temperature ( $T_{\text{EQU}}$ ) at a certain point is connected to an intake temperature of seawater that was measured a few minutes later. Most of the time this would not cause serious problems, but in case of high temperature variability this introduces additional errors. Therefore the time difference between the seawater intake and the instrument itself was determined cruise by cruise and the corresponding data were

shifted in time for better temporal match. Then the temperature difference between  $T_{\text{EQU}}$  and SST was determined ( $\Delta T = T_{\text{EQU}} - SST$ ).

4. A range check and weak flagging algorithm was applied in order to flag clear outliers.
5. The  $x\text{CO}_2$  data were calibrated against the  $x\text{CO}_2$  data of the standard gases using the linear least squares method. The calculated coefficients were interpolated linearly over time between calibrations to correct for the small drift and provide the most appropriate calibration function for any single point. Any data before the first and after the last calibration were flagged as questionable.

Since each standard gas was measured three times consecutively the mean and standard deviation were calculated. If the standard deviation was higher than a threshold value (0.5 ppm) the according  $x\text{CO}_2$  data were also flagged as "questionable".

6. Afterwards all data were visually inspected for outliers and unusual features and flagged if necessary.
7. Running means were applied to atmospheric  $x\text{CO}_2$  (500 minutes) and  $\Delta T$  (3 minutes) data. The latter was done to remove any bias from the data that was introduced by electronic noise.
8. Following the procedures of Dickson *et al.* (2007) the  $p\text{CO}_2$  and  $f\text{CO}_2$  data were calculated: The water vapor pressure in atm was calculated after Weiss (1974):

$$p(\text{H}_2\text{O}) = \exp\left(24.4543 - 67.4509 \times \frac{100}{T + 273.15} - 4.8489 \times \log\left(\frac{273.15 + T}{100}\right) - 0.000544 \times SSS\right) \quad (2.2)$$

where  $T$  is the  $T_{\text{EQU}}$  or  $SST$  in  $^{\circ}\text{C}$ . Using the calibrated  $x\text{CO}_2$  ( $x\text{CO}_{2,\text{corr}}$ ) the  $p\text{CO}_2$  at 100% humidity was calculated:

$$p\text{CO}_2 = x\text{CO}_{2,\text{corr}} \times \left(\frac{P}{1013.25} - p\text{H}_2\text{O}\right) \quad (2.3)$$

$P$  is the pressure inside the equilibrator ( $P_{\text{EQU}}$ ) or  $P_{\text{atm}}$  and  $p\text{H}_2\text{O}$  the according water vapor pressure. To calculate  $f\text{CO}_2$  the first virial coefficient of  $\text{CO}_2$   $B$  (in  $\text{cm}^3 \text{mol}^{-1}$ ) and

the cross virial coefficient  $\delta(\text{CO}_2 - \text{air})$  (in  $\text{cm}^3 \text{mol}^{-1}$ ) have to be calculated:

$$B = -1636.75 + 12.0408 \times T_{\text{abs}} - 3.27957 \times 10^{-2} \times T_{\text{abs}}^2 + 3.16528 \times 10^{-5} \times T_{\text{abs}}^3 \quad (2.4)$$

$$\delta(\text{CO}_2 - \text{air}) = 57.5 - 0.118 \times T_{\text{abs}} \quad (2.5)$$

where  $T_{\text{abs}}$  is the thermodynamic temperature in K. Then follows:

$$f\text{CO}_2 = x\text{CO}_{2,\text{corr}} \times (P - p\text{H}_2\text{O}) \times \exp\left(\frac{\left[B + 2 \times (1 - x\text{CO}_2)^2 \times \delta(\text{CO}_2 - \text{air})\right] \times P}{R \times T_{\text{abs}}}\right) \quad (2.6)$$

where  $P$  is  $P_{\text{EQU}}$  or  $P_{\text{atm}}$  (in atm),  $p\text{H}_2\text{O}$  the appropriate water vapor pressure (in atm) and  $R$  is the universal gas constant (in  $\text{J K}^{-1} \text{mol}^{-1}$ ). Both  $p\text{CO}_2$  and  $f\text{CO}_2$  were corrected with Eq. 1.13 to  $SST$ .

9. Only data flagged as "good" were compiled and were visually inspected day by day in order to achieve highest quality.

The data from 2002/2003 (Lüger *et al.*, 2004, 2006) had to be recalculated because inconsistencies in the procedure for the correction of  $p\text{CO}_2$  to  $SST$  were identified. New Matlab routines were written for the data reduction of this dataset based on the routines used for the dataset since 2005.

1. First the data from the  $p\text{CO}_2$  instrument and data from GPS and thermosalinograph data were merged by time.
2. The input data were checked for obvious outliers and flagged where necessary.
3. The seawater flowed only by hydrostatic pressure to the instrument. Thus the flow rate was highly variable between 10 and 20  $\text{L min}^{-1}$ . Therefore the time the water needed from the intake to the equilibrator varied significantly (between 1 and 7 minutes). Analogous to point 3 from the scheme above data had to be shifted in time for appropriate temporal matching. Due to the huge range of the flowrate and the fact that the flowrate was not recorded it was not suitable to use a fixed time step to correct a whole cruise. Therefore new Matlab routine was written:

- The dataset was searched for local minima of SST.
- The subsequent 10 minutes of the dataset were searched for the corresponding local minimum of  $T_{\text{EQU}}$ .
- The time difference  $\Delta t$  at this time was calculated and stored.

This produced between 50 and 100  $\Delta t$  values per cruise. Linear interpolation between these pairs resulted in a  $\Delta t$  value for each datapoint. While crossing regions of the Atlantic with low temperature variability fewer minima were found to constrain this approach but the temperature correction in this regions was not critical. Crossing regions with high

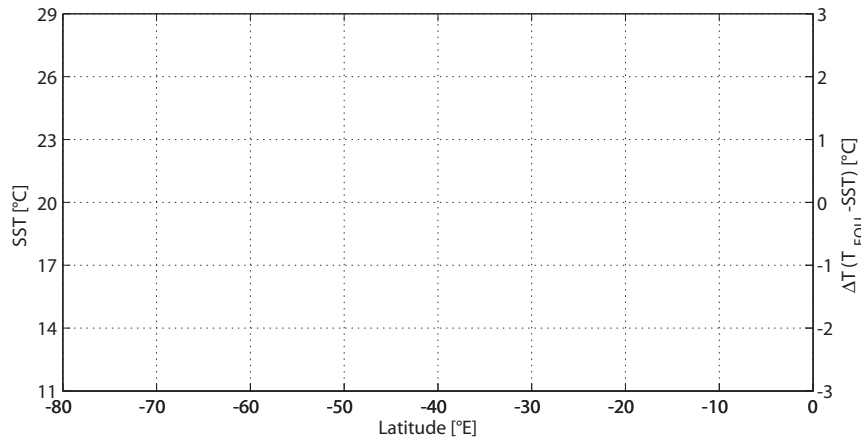


Figure 2.5.: Temperature difference  $\Delta T$  of raw data (red) and shifted (and calibrated) data (blue). The standard deviation is  $0.27^{\circ}\text{C}$  for the raw data and  $0.03^{\circ}\text{C}$  for the shifted data. Also shown are the  $SST$  data in grey.

variability (e.g. Labrador Current) the number of minima found is high and ensures a robust determination of  $\Delta t$ . Fig. 2.5 shows the  $\Delta T$  before the data were shifted and after determination of  $\Delta t$  and shifting.  $\Delta T$  calculated from raw data increases when the variability of SST increases and the need for a correct time shift of the data is clearly shown.

4. The resulting data showed a variable cruise-averaged  $\Delta T$  that changed from negative (FAL01 - FAL04, cf. Tab. B) to positive values (Fig. 2.6). Temperature calibration of the equilibrator temperature probe (i.e. temperature comparison of intake and equilibrator temperature) was done for cruises after FAL04. For the first four cruises (FAL01 - FAL04) no temperature calibration was available and measured  $T_{\text{EQU}}$  had to be considered faulty (Fig. 2.6, black dots). The temperature differences between the calibrated  $T_{\text{EQU}}$  and

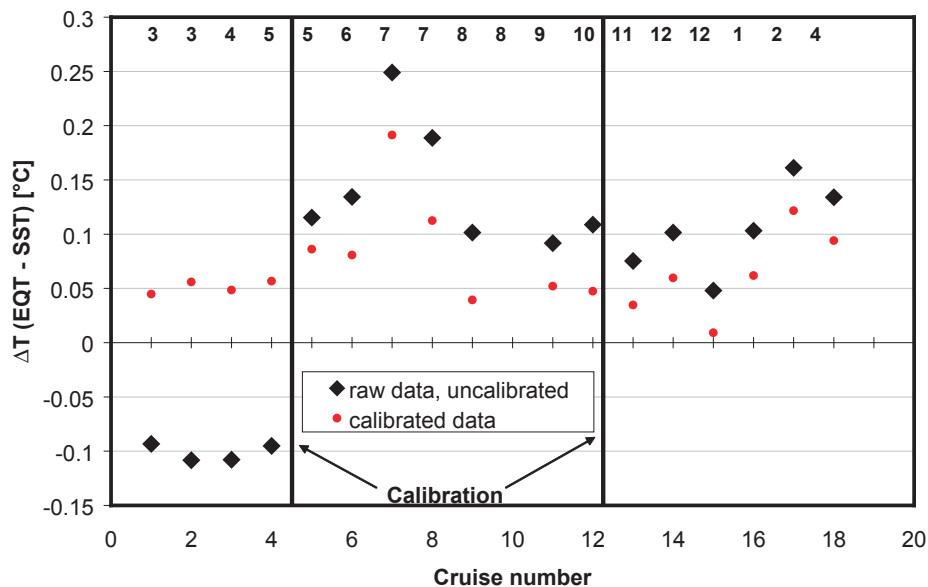


Figure 2.6.: Difference between seawater SST and  $T_{\text{EQU}}$  onboard M/V Falstaff in 2002/2003. Shown are the mean temperature differences for each cruise before correction and after correction. The numbers at the top of the figure denote the month of the cruises. The bars denote the time of calibration.

$SST$  of the cruises FAL05 - FAL18 were used to establish a relationship between average  $SST$  ( $\overline{SST}$ ) and the cruise-averaged temperature difference ( $\overline{\Delta T}$ ):

$$\overline{\Delta T} = 0.0168 \times \exp(0.0723 \times \overline{SST}) \quad (2.7)$$

Using Eq. 2.7 an average temperature difference was calculated for each of the first four cruises (FAL01 - FAL04). This  $\overline{\Delta T}$  was added to the  $SST$  data from intake temperature and thus equilibrator temperature for these cruises was calculated:

$$T_{\text{EQU}} = SST + \overline{\Delta T} \quad (2.8)$$

5. The calibration of the raw  $x\text{CO}_2$  was done as described in Lüger *et al.* (2004).

Afterwards the data were treated as described above in steps 6-9 for the data after 2005. Both instruments (GO and the custom-built) were run in parallel on another cruise and agreed within  $\pm 3 \mu\text{atm}$ . Therefore we estimate the overall accuracy of the resulting  $p\text{CO}_2$  to  $\pm 3 \mu\text{atm}$ .



## 3. Autonomous $p\text{CO}_2$ measurements in the North Atlantic

### 3.1. Data

Fig. 3.1 shows the study area and the cruise tracks of the VOS lines from which  $p\text{CO}_2$  data were used in this study. A direct comparison of these two periods is limited because of their different latitudinal extent. Particularly data from the western part of the study area are not comparable because the lack of significant overlap. The region west of  $40^\circ\text{W}$  and south of  $45^\circ\text{N}$  is predominantly influenced by the warm and salty North Atlantic Current (NAC) while the region north of  $45^\circ\text{N}$  is governed by the cold and fresher Labrador Current (LC) (Tomczak and Godfrey, 2002). Both water masses show rather different biogeochemical properties (cf. section 1.2).

In 2005,  $p\text{CO}_2$  data were obtained only during three cruises. In the following comparison these data are excluded. Furthermore the cruise track of the cruise in February 2007 was exceptionally far north due to severe weather conditions and therefore this cruise was also excluded from the analysis. Thus the remaining data span full seasonal cycles during 2002/2003 (February 2002 - April 2003) and 2006/2007 (June 2006 - October 2007), respectively.

For better interpretability, the data were averaged within bands of  $5^\circ$  longitude for each of the two periods (Fig 3.1). The temperature range from the lower to the upper border of each band is on the order of  $5^\circ\text{C}$ . Thus the temperature effect itself can introduce  $p\text{CO}_2$  variability of about 20% within a single box. Therefore the  $p\text{CO}_2$  data were corrected to the monthly mean SST per box. Using the measured SST would introduce a systematic error because cruises may be crossing a box in one month at the southern end with the maximum SST at this month and at another month at the northern end with the minimum SST. To avoid this systematic error, SST from the Advanced Microwave Scanning Radiometer (AMSR-E) on NASA EOS Aqua satellite (<ftp://ftp.ssmi.com/>) were used. For each month of the study period, all  $\text{SST}_{\text{AMSR-E}}$  data were

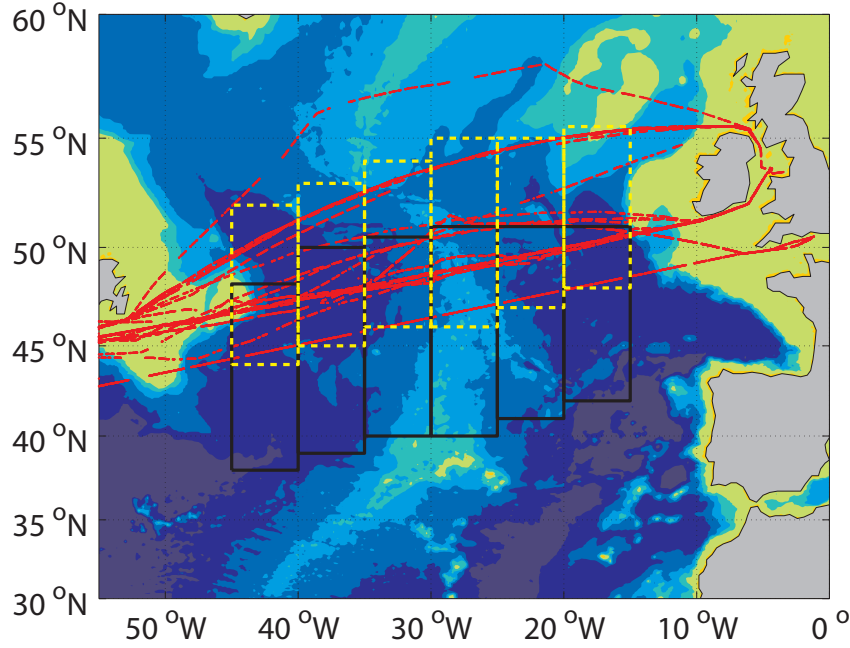


Figure 3.1.: Map of the North Atlantic showing the cruise tracks from 2002/2003 (white) and since 2005 (red). The black and yellow boxes denote the areas that were used for data analysis of the 2002/2003 dataset and the 2006/2007 dataset, respectively.

averaged for each box. This assures a representative monthly mean  $\overline{\text{SST}_{\text{AMSR-E}}}$  ( $\overline{\text{SST}_{\text{AMSR-E}}}$ ) for each box.

The  $p\text{CO}_2$  data measured at SST ( $p\text{CO}_{2,\text{in-situ}}$ ) were corrected to the  $\overline{\text{SST}_{\text{AMSR-E}}}$  ( $p\text{CO}_{2,\text{AMSR-E}}$ ) using Eq. 1.14 following Takahashi *et al.* (2009). In the case of correcting to the  $\overline{\text{SST}_{\text{AMSR-E}}}$  the temperature difference can be up to several degrees and thus the correction with Eq. 1.14 provides more precise results.

Fig. 3.2(a) shows the resulting difference between monthly  $\overline{\text{SST}_{\text{AMSR-E}}}$  and the observed in situ SST. Most data were corrected within a temperature range of  $\pm 3^\circ\text{C}$ . In 2002/2003 the temperature was corrected mainly to lower values in early spring and summer and to higher values in late spring and fall. In 2006/2007 it lead to higher values in fall 2006 in the whole study area. The largest temperature difference was observed in the area of the influence of the cold LC. In Fig. 3.2(b) the difference between  $p\text{CO}_{2,\text{in-situ}}$  and the resulting  $p\text{CO}_{2,\text{AMSR-E}}$  is shown. Consequently, the observed pattern is the same as in Fig. 3.2(a).

The temperature corrected data were used to calculate the  $p\text{CO}_2$  difference between seawater and atmosphere  $\Delta p\text{CO}_2$ :

$$\Delta p\text{CO}_2 = p\text{CO}_{2,\text{AMSR-E}} - p\text{CO}_{2,\text{atm}} \quad (3.1)$$



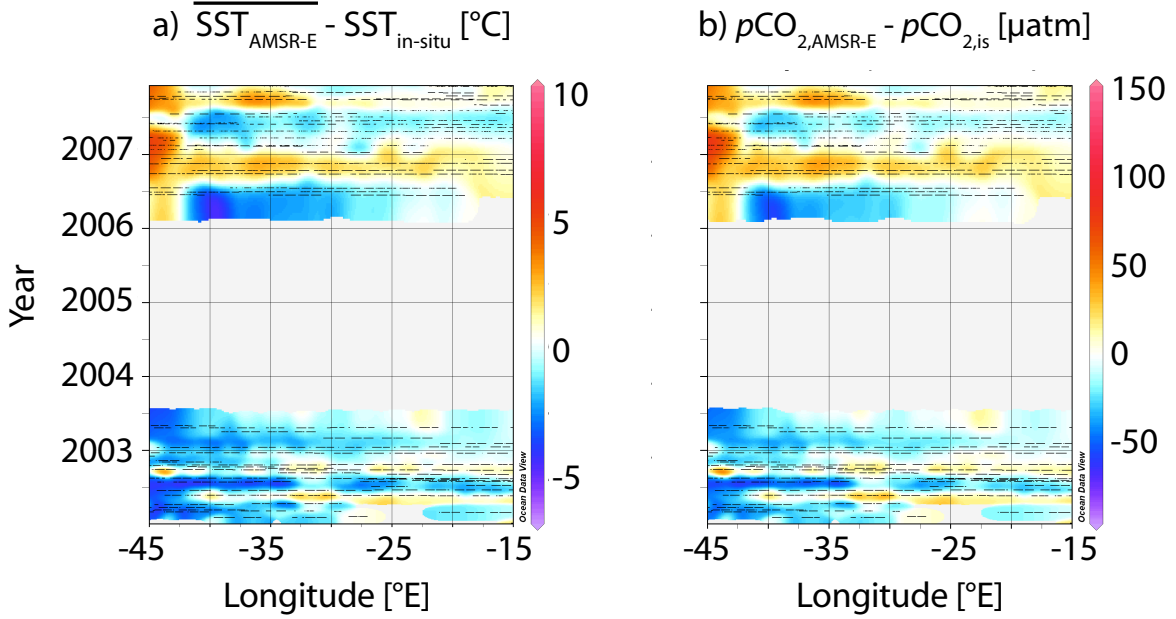


Figure 3.2.: Difference of (a)  $\overline{\text{SST}}_{\text{AMSR-E}} - \text{SST}_{\text{in-situ}}$  and (b)  $p\text{CO}_{2,\text{AMSR-E}} - p\text{CO}_{2,\text{in-situ}}$ . Reddish (bluish) colours denote areas where the temperature correction lead to higher (smaller) values, i.e. the mean  $\text{SST}_{\text{AMSR-E}}$  was higher (lower) than  $\text{SST}_{\text{is}}$ .

where  $p\text{CO}_{2,\text{atm}}$  is the atmospheric  $p\text{CO}_2$  and consequently positive  $\Delta p\text{CO}_2$  corresponds to  $\text{CO}_2$  supersaturation which results in a  $\text{CO}_2$  flux from the ocean to the atmosphere and vice versa. The  $p\text{CO}_{2,\text{atm}}$  was calculated using Eq. 3.2 with  $x\text{CO}_2$  measurements from GLOBALVIEW- $\text{CO}_2$  (2009) and the observed atmospheric pressure ( $p_{\text{atm}}$ ):

$$p\text{CO}_{2,\text{atm}} = x\text{CO}_{2,\text{atm}} \times p_{\text{atm}} \quad (3.2)$$

The  $x\text{CO}_2$  data from GLOBALVIEW- $\text{CO}_2$  (2009) were used because they do not show short term fluctuation that can result from weather events and/or changing air mass signatures. Since atmospheric  $x\text{CO}_2$  shows a strong latitudinal dependence data from three stations were used to establish a linear function in order to estimate  $x\text{CO}_2$  for every datapoint ( $x\text{CO}_2 = f(\text{Latitude})$ ): Mace Head (MHD:  $53.33^\circ\text{N}$ ,  $9.90^\circ\text{W}$ ), Begur (BGU:  $41.83^\circ\text{W}$ ,  $3.33^\circ\text{W}$ ) and Azores (AZR:  $38.77^\circ\text{N}$ ,  $27.38^\circ\text{W}$ ).

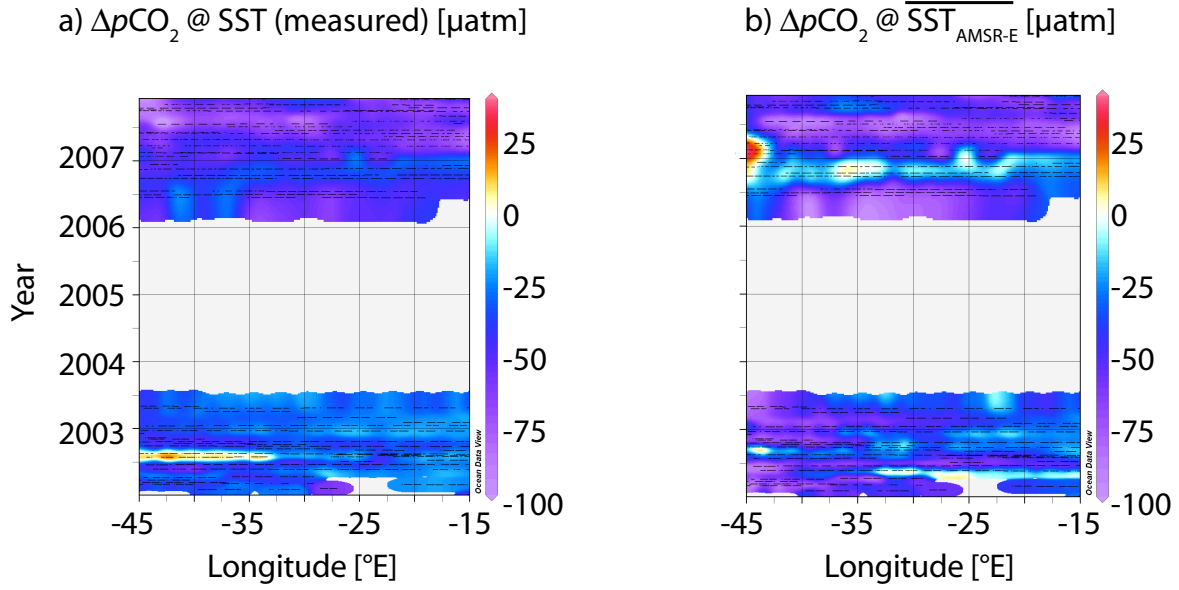


Figure 3.3.: Hovmoeller plots of observed  $\Delta p\text{CO}_2$  @ SST (a) and  $\Delta p\text{CO}_2$  @  $\overline{\text{SST}}_{\text{AMSR-E}}$  (b). Blue colours denote undersaturation and red values supersaturation with respect to the atmosphere.

## 3.2. Results

Fig. 3.3(a) shows  $\Delta p\text{CO}_2$  values calculated with  $p\text{CO}_{2,\text{in-situ}}$ . In 2002/2003 a difference between the western and eastern part was observed. In the eastern part, the Atlantic is undersaturated with respect to the atmosphere during the whole year and has a minimum in late summer due to biological drawdown. In the western part the minimal values appear earlier in the year and are followed by supersaturation in summer. This maximum is largely due to warming (Lüger *et al.*, 2004). Another minimum follows in autumn and may be indicative of a fall bloom. The situation is different in 2006/2007 and the whole study area is undersaturated during the whole year. Here two  $p\text{CO}_2$  minima are observed (one in spring and one in autumn) in the eastern part. In the western part exists only one minimum. This minimum is reached in early summer and lasts until autumn. The observed pattern of  $\Delta p\text{CO}_2$  in both datasets are  $\Delta p\text{CO}_2$  mainly triggered by temperature changes of the seawater and by biological activity (Lüger *et al.*, 2004, 2006). As mentioned above the latitudinal spread of the cruises for each annual cycle itself is huge and two cruises in two consecutive month could differ by 20% in  $p\text{CO}_2$  only due to temperature differences. Fig 3.3(b) shows  $\Delta p\text{CO}_2$  calculated using  $p\text{CO}_{\text{AMSR-E}}$ . Again two minima were observed in the western part in 2002/2003 but only a small part shows supersaturation during summer. The minimum of the eastern part is now observed in late spring while during the rest of the year the  $p\text{CO}_2$  is

nearly uniform. The data from 2006/2007 show values around zero in fall 2006 which is an effect of the large temperature correction (compare Fig. 3.2). The minimal values in spring/summer 2007 remain nearly unchanged after the temperature correction. Furthermore highest values were observed in the western most area from late summer 2006 to late spring 2007. This is again an effect of the temperature correction since the area is influenced by the cold water of the LC.

This overview over the data show the limitations for the interpretation of the two datasets. It is not clear if the observed pattern are due to interannual variability or even decadal changes or if it is more a pattern of spatial variability.

**Comparison with  $p\text{CO}_2$  climatology** The  $p\text{CO}_2$  seasonality for the two annual cycles was compared to the climatology of Takahashi *et al.* (2009) (Fig. 3.4). The  $p\text{CO}_{2,in-situ}$  data were averaged per month and box. Analoguouse to Zeng *et al.* (2002) a sigmoidal function was applied to the averaged data:

$$\chi = c_0 + c_1 \sin(2\pi t) + c_2 \cos(2\pi t) + c_3 \sin(4\pi t) + c_4 \cos(4\pi t) \quad (3.3)$$

where  $\chi$  is the seasonally varying quantity,  $t$  is the day of the year and  $c_0$  to  $c_4$  are the coefficients that were determined by MLR.

The  $p\text{CO}_{2,AMSR-E}$  data were averaged per box and the sigmoidal function was applied, too.

In addition the climatological  $p\text{CO}_2$  data from Takahashi *et al.* (2009) were used ( $p\text{CO}_{2,clim-00}$ ): For each  $p\text{CO}_{2,in-situ}$  measurement the nearest  $p\text{CO}_{2,clim-00}$  value was searched and corrected to the specific year adding  $1.8 \mu\text{atm yr}^{-1}$ , what is the mean seawater  $p\text{CO}_2$  increase in the North Atlantic (Takahashi *et al.*, 2009). The resulting time corrected  $p\text{CO}_2$  data ( $p\text{CO}_{2,clim-act}$ ) were corrected to  $\overline{SST_{AMSR-E}}$ , averaged (per box and month) and the sigmoidal function was applied.

Fig. 3.4 show the resulting seasonal cycles. With the exception of July all months in 2002/2003 show a standard deviation smaller than 5%. This gives confidence in the calculated seasonal cycles. The high standard deviation of the July value might be due to the cruises that were used for averaging: two cruises were used of which one took place at the beginning of July and the second one at the end of July. Furthermore one of this cruises was the southernmost cruise in 2002/2003 (cf. Fig. 3.1). The rather large spatial and temporal spread may also explain the higher standard deviations in the 2006/2007 dataset. During 2002/2003, the M/V Falstaff made a round trip between Europe and North America in approximately 6 weeks and the M/V Atlantic Companion in 2006/2007 took 5 weeks. Thus there are more month including two

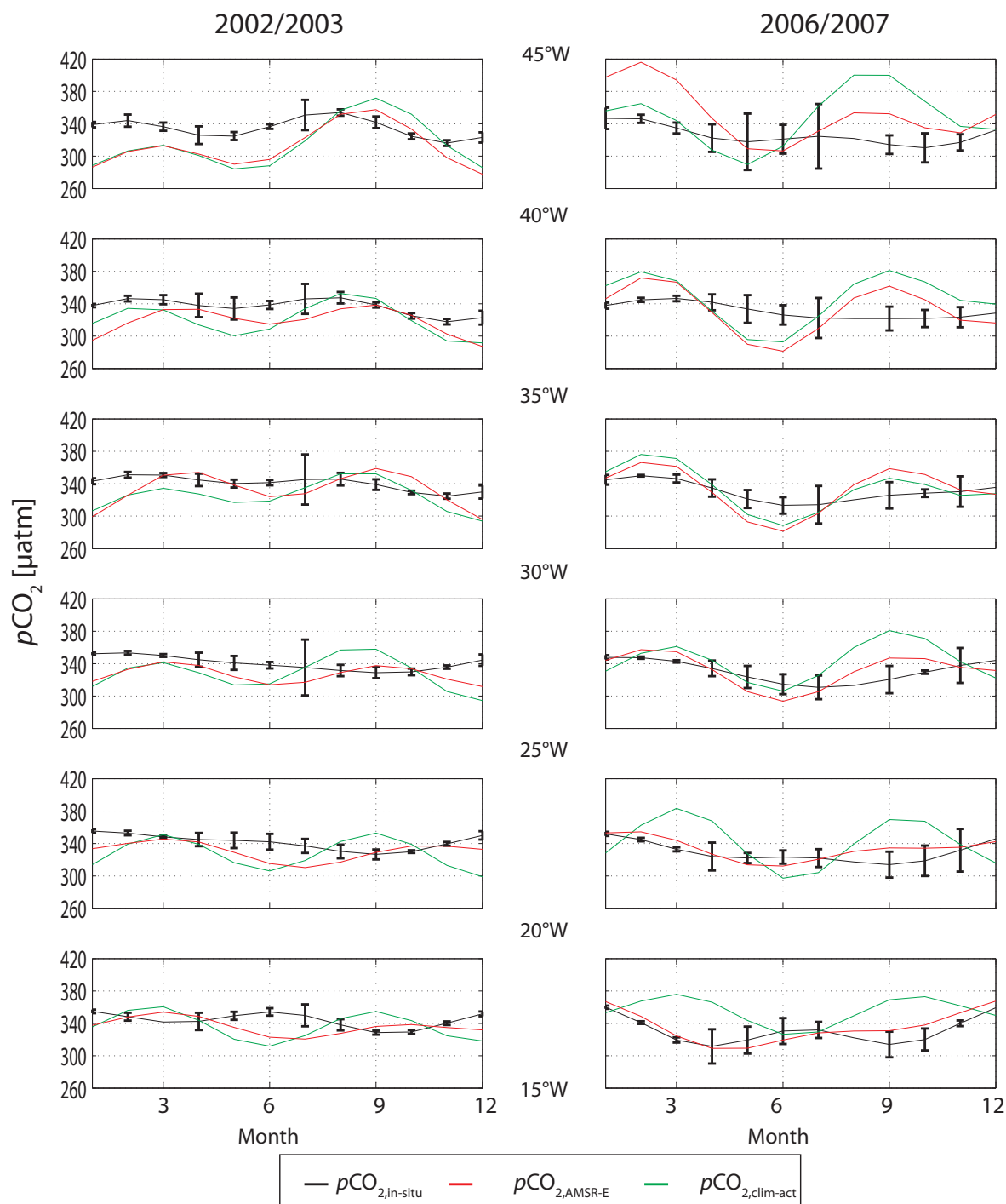


Figure 3.4.: Sigmoidal functions fitted to the seasonal cycle of seawater  $p\text{CO}_2$ . The left panels show data from 2002/2003 and the right panels data from 2006/2007. The data correspond from top to bottom to the boxes from 45°W to 15°W (Fig. 3.1).

different cruises for the dataset in 2006/2007.

The seasonality of the in-situ data is smaller than the seasonality of the data after correction to  $\overline{\text{SST}_{\text{AMSR-E}}}$  as well as the data derived from the climatology. This might be due the superposition of the thermodynamical and biological effects and will be discussed later. The 2002/2003  $p\text{CO}_{2,\text{in-situ}}$  data west of  $30^\circ\text{W}$  show two minima, one in spring (April/May) and one in autumn (November). These minima are due to two annual blooms in the western part of the North Atlantic (see also Lüger *et al.*, 2004). In the boxes between  $30^\circ\text{W}$  and  $20^\circ\text{W}$  there is only a minimum during late summer and in the most eastern box the same seasonality showing two minima is observed as in the western boxes. The dataset from 2006/2007 show a different seasonality. Only the box between  $15^\circ\text{W}$  and  $20^\circ\text{W}$  has two minima. The boxes west of  $20^\circ\text{W}$  exhibit only one minimum in late fall. Correcting the  $p\text{CO}_{2,\text{in-situ}}$  to  $\overline{\text{SST}_{\text{AMSR-E}}}$  results in different seasonal cycles. The only difference to the in situ measured data should be small scale variability on timescales of days and with a spatial extension smaller than  $5^\circ$  longitude. However, all  $p\text{CO}_{2,\text{AMSR-E}}$  data show a minimum during summer but a different seasonal amplitude. The amplitude in the 2006/2007 dataset is more pronounced than in the 2002/2003 dataset. Especially in the boxes west of  $40^\circ\text{W}$  the  $p\text{CO}_{2,\text{AMSR-E}}$  data diverge from  $p\text{CO}_{2,\text{in-situ}}$ . These boxes are influenced by the LC with its cold surface water. This may increase the uncertainty that is introduced by the temperature corrections.

In Fig. 3.4 the corrected values from the climatology of Takahashi *et al.* (2009) are also shown (green line). They agree rather well with the 2002/2003  $p\text{CO}_{2,\text{AMSR-E}}$  data. This is an interesting finding especially since the data from M/V Falstaff were not used in the establishment of the climatology. In the 2006/2007 dataset there are boxes with good agreement ( $25^\circ\text{W}$ - $40^\circ\text{W}$ ) and boxes where the climatology shows a huge offset ( $>40 \mu\text{atm}$ ) or even an inverted seasonal cycle ( $15^\circ\text{W}$  -  $20^\circ\text{W}$ ).

The data from the climatology and the measured  $p\text{CO}_{2,\text{in-situ}}$  data of this study were also used to estimate the mean annual change in seawater  $p\text{CO}_2$  ( $\overline{dp\text{CO}_2}$ ) since 2000. Therefore,  $p\text{CO}_{2,\text{clim-00}}$  was corrected to observed SST according to Eq. 1.14 leading to  $p\text{CO}_{2,\text{clim-00,SST}}$ . Furthermore the  $p\text{CO}_{2,\text{in-situ}}$  can be corrected to the year 2000 following Eq. 3.4:

$$p\text{CO}_{2,\text{in-situ},2000} = p\text{CO}_{2,\text{in-situ}} - n \times \overline{dp\text{CO}_2} \quad (3.4)$$

where  $n$  is the number of years since 2000. In an ideal case (i.e. the measurements matches

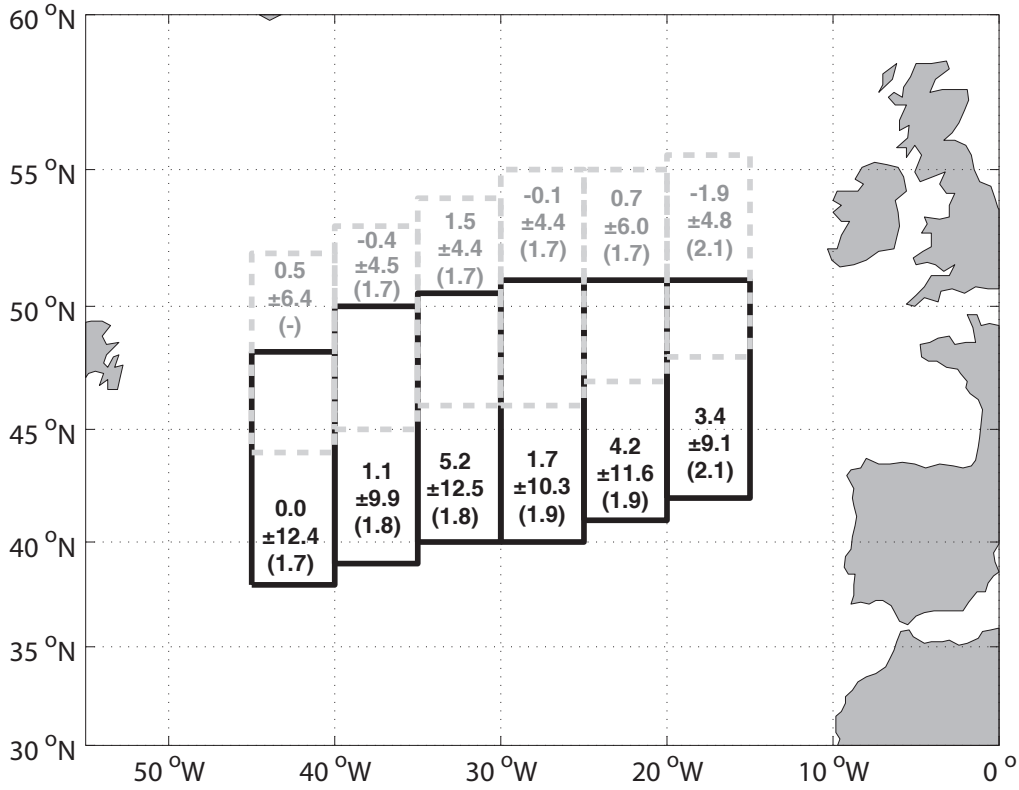


Figure 3.5.: Boxwise mean annual increase of seawater  $p\text{CO}_2$  in  $\mu\text{atm yr}^{-1}$  with standard deviation. Data were calculated as the difference between climatological and in situ data after correction to the same corresponding SST. The numbers in parentheses are the values estimated by Takahashi *et al.* (2009). Black boxes denote the 2002/2003 dataset and grey boxes data from 2006/2007.

perfectly with the climatology) the following equation must be valid:

$$p\text{CO}_{2,\text{in-situ},2000} = p\text{CO}_{2,\text{clim-00,SST}} \quad (3.5)$$

Substituting Eq. 3.4 into Eq. 3.5 and solving for  $\overline{dp\text{CO}_2}$  results in the mean annual increase between the year 2000 and the observations of 2002/2003 or 2006/2007, respectively.  $\overline{dp\text{CO}_2}$  was calculated for every datapoint and the results were averaged within the boxes. Fig. 3.5 shows the resulting mean increase and standard deviation per box and dataset. The data from the 2002/2003 dataset show a faster increase than the 2006/2007 data. The latter one show even a decrease in some boxes. These data are not comparable to the data estimated by Takahashi *et al.* (2009) because they used deseasonalized data over a period of 37 years. Thus the results

are more indicative of the interannual variability of the North Atlantic.

**Thermal and non-thermal effects on  $p\text{CO}_2$**  There are several processes that can drive seasonal  $p\text{CO}_2$  variability: thermodynamic effects, biological activity, air-sea gas exchange, advective and convective mixing processes. These effects can be divided into thermal and non-thermal components, where the latter includes anything except the direct thermodynamic effect of temperature. These effects on  $p\text{CO}_2$  can be separated following Takahashi *et al.* (1993) (cf. Eq. 1.13):

Thermal effect

$$p\text{CO}_{2,t} = p\text{CO}_{2,\text{mean}} \times \exp[0.0423(T_{\text{obs}} - T_{\text{mean}})] \quad (3.6)$$

Non-thermal effect

$$p\text{CO}_{2,\text{non-t}} = p\text{CO}_{2,\text{obs}} \times \exp[0.0423(T_{\text{mean}} - T_{\text{obs}})] \quad (3.7)$$

where  $p\text{CO}_{2,\text{mean}}$  and  $T_{\text{mean}}$  are the average  $p\text{CO}_{2,\text{AMSR-E}}$  and  $\text{SST}_{\text{AMSR-E}}$  for each box and dataset, respectively, and  $p\text{CO}_{2,\text{obs}}$  and  $T_{\text{obs}}$  are the observed values. The data were first corrected and subsequently averaged per box. Eq. 3.6 thus modulates the mean observed  $p\text{CO}_2$  at  $T_{\text{mean}}$  to the seasonal cycle of SST thereby not allowing for any effect of air-sea exchange on the  $p\text{CO}_2$ . In contrast, in Eq. 3.7 the observed  $p\text{CO}_2$  is corrected from  $T_{\text{obs}}$  to the annual mean SST thereby removing the thermodynamic effect of temperature. Fig. 3.6 show the results. The deconvolution of the thermal and non-thermal components are the same in all boxes for both datasets. The thermal component shows the effect of the seasonal SST cycle with a minimum during spring and a maximum in late summer. The non-thermal component, i.e. the remaining  $p\text{CO}_2$  variability after removal of the effect of temperature, rises at the beginning of the year until it reaches a maximum during spring time. This increase corresponds well with the deepening of the mixed layer (see Fig. 5 in Steinhoff *et al.* (2010); Chapter 7, this thesis). The decrease of the non-thermal component starts in late spring and is driven mostly by the biological carbon drawdown during the spring bloom. The sole exception from this pattern is the most eastern box: During 2006/2007 the maximum of  $p\text{CO}_{2,\text{non-t}}$  appears during December. Steinhoff *et al.* (2010) (cf. section 7) report a faster increase of MLD than usual which results also in a deeper MLD during winter 2006/2007. Also in the remaining boxes ( $20^\circ\text{W} - 45^\circ\text{W}$ ) the minimum of  $p\text{CO}_{2,\text{non-t}}$  and the point of intersection of  $p\text{CO}_{2,\text{non-t}}$  and  $p\text{CO}_{2,t}$  occurs one or two months earlier in 2006/2007 than in 2002/2003. With the present dataset it is not clear if this is due to interannual variability or the spatial difference of the datasets. However, this means that the

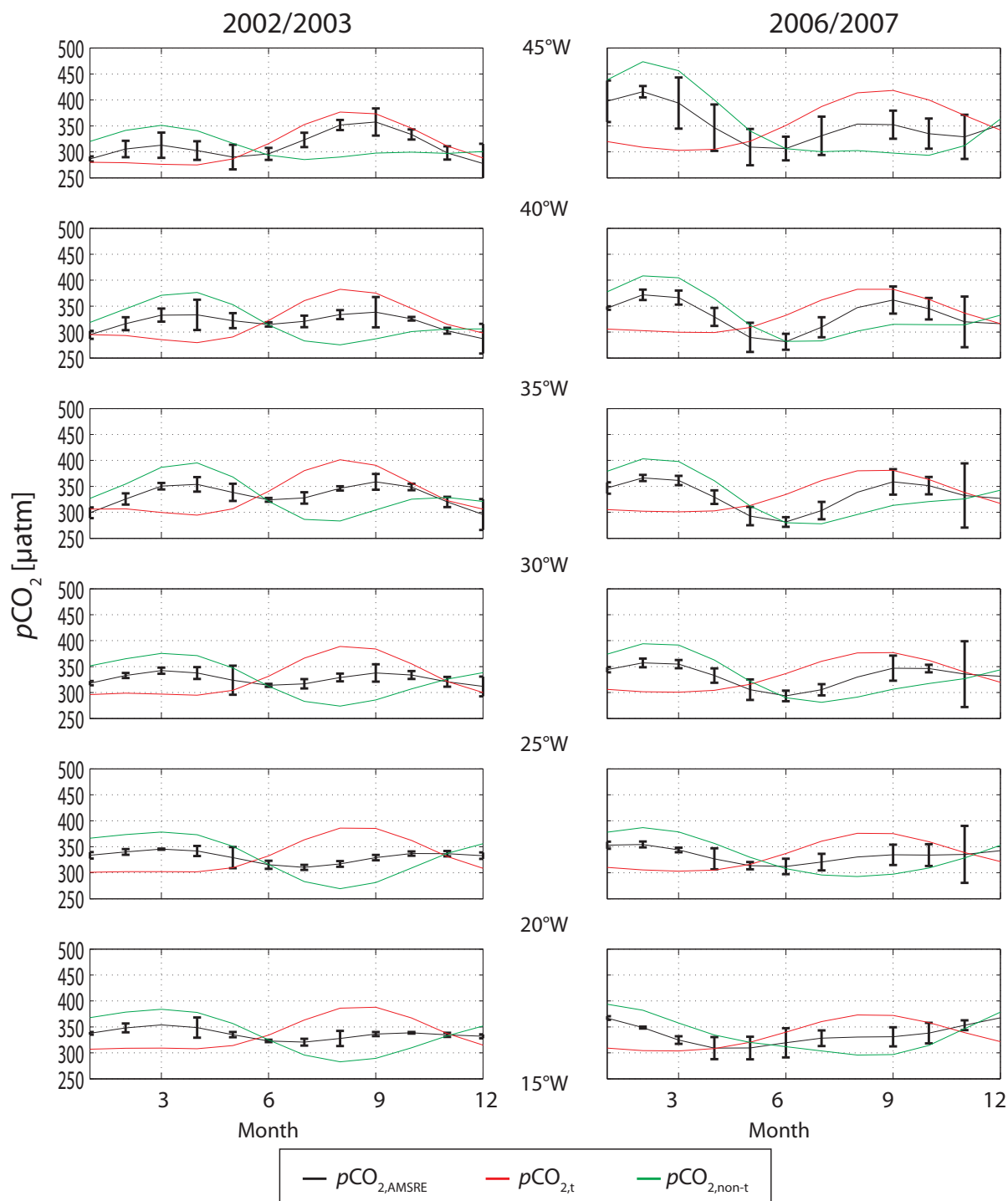


Figure 3.6.: Annual cycle of  $p\text{CO}_{2,\text{AMSRE}}$  and its thermal and non-thermal components. The errorbars are the standard deviation from averaging per box. Periods where one of the component is above the black line means that this component increases the seawater  $p\text{CO}_2$  and vice versa.



non-thermal drawdown of the  $p\text{CO}_2$  starts earlier in 2006/2007 dataset. Analogous to Takahashi

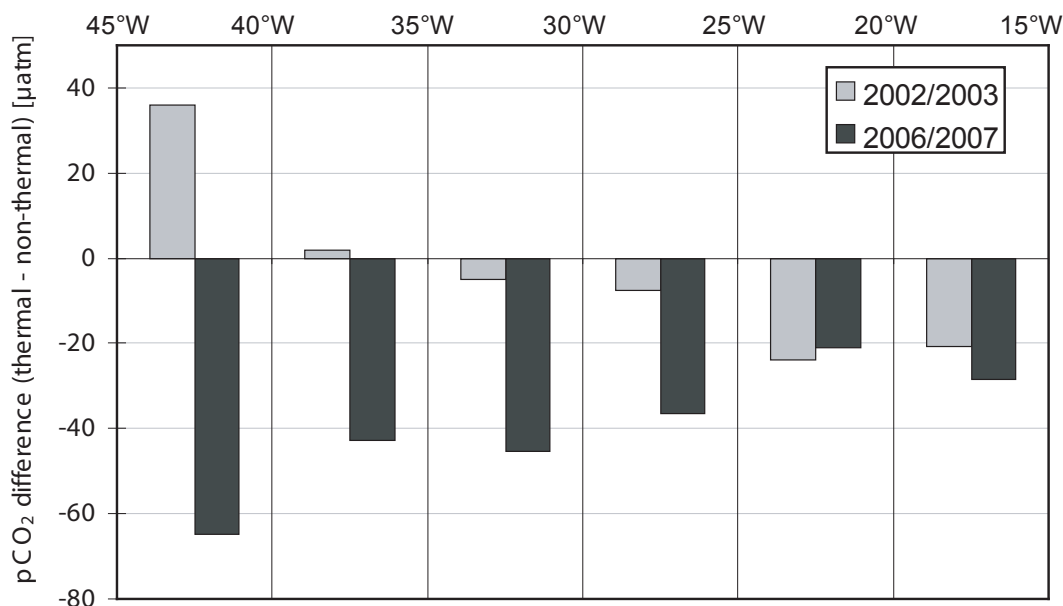


Figure 3.7.: Difference between the annual amplitude of  $p\text{CO}_{2,t}$  and  $p\text{CO}_{2,\text{non-t}}$ .

*et al.* (2002) the difference between the peak-to-peak amplitude of  $p\text{CO}_{2,t}$  and  $p\text{CO}_{2,\text{non-t}}$  was calculated (Fig. 3.7). Positive values denote areas where the thermal effect exceeds the non-thermal effects and vice versa. Fig. 3.7 show that only the boxes west of 35°W in the 2002/2003 study region show positive values. This show the influence of the subtropical gyre within these two boxes. The 2002/2003 dataset at 35°W appears to be at the border between the eastern and western part of the North Atlantic. This observation agrees well with the study of Lüger *et al.* (2004) (their Fig. 6) even if the numbers are of different order (which is a result of the temperature correction (cf. Chapter 2.3 that was applied to the 2002/2003 data). They show a different trend from west to east. During 2006/2007 the amplitude difference is negative in all boxes that is to say the non-thermal effect on  $p\text{CO}_2$  exceeds the thermal effect and the magnitude of the non-thermal effect decreases from west to east. In 2002/2003 the thermal effect is larger than the non-thermal effect in the boxes west of 35°W and the non-thermal effect increases from west to east.

The biological component of the non-thermal effect was estimated as follows. Steinhoff *et al.* (2010) present an equation for estimating nitrate concentration in the mixed layer for the study region as a function of time, latitude, MLD and SST. The French assimilation model MERCATOR ([www.mercator.eu.org](http://www.mercator.eu.org)) provides good MLD estimates (Steinhoff *et al.*, 2010). Thus MLD from MERCATOR and  $\text{SST}_{\text{AMSR-E}}$  were used to calculate nitrate. The nitrate data were

averaged within the boxes and the same sigmoidal function was applied. The nitrate amplitude was determined as the difference between the maximum and minimum nitrate value within each box. Using a C/N ratio of 7.2 (Körtzinger *et al.*, 2001) the nitrate amplitude was converted to a DIC drawdown ( $\Delta\text{DIC}_{\text{bio}}$ ). The corresponding  $p\text{CO}_2$  drawdown by biology was estimated from Eq. 3.8:

$$\Delta p\text{CO}_{2,\text{bio}} = RF \times \Delta\text{DIC}_{\text{bio}} \times \frac{p\text{CO}_{2,\text{mean}}}{\text{DIC}_{\text{mean}}} \quad (3.8)$$

where RF is the Revelle factor,  $p\text{CO}_{2,\text{mean}}$  and  $\text{DIC}_{\text{mean}}$  are the mean values per box and dataset. Following Sabine *et al.* (2004) a value of  $RF=11$  was used and  $\text{DIC}_{\text{mean}}$  was estimated from discrete samples to be  $2050 \mu\text{mol kg}^{-1}$ . Fig. 3.8 shows the  $p\text{CO}_2$  amplitude derived from the

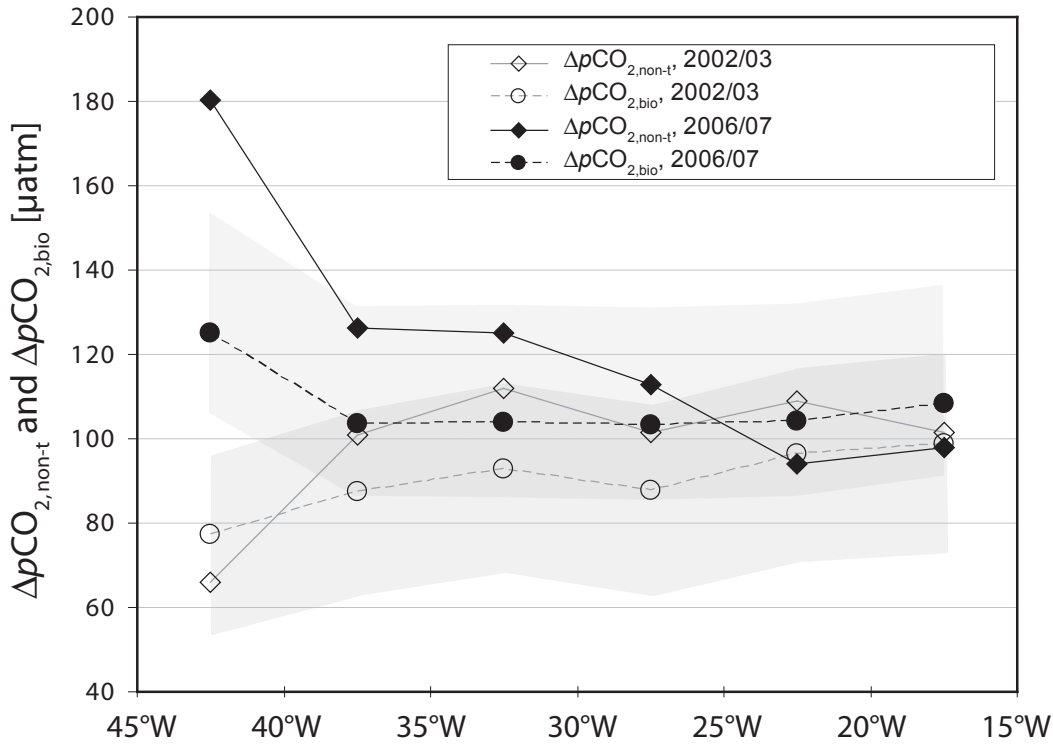


Figure 3.8.:  $p\text{CO}_2$  drawdown as calculated from nitrate drawdown and as the non-thermal component of the observed seawater  $p\text{CO}_2$ . The grey shaded area denote the uncertainty in the calculation of  $\Delta p\text{CO}_{2,\text{bio}}$  arising from uncertainties in nitrate estimation and standard deviations of  $\text{DIC}_{\text{mean}}$  and  $p\text{CO}_{2,\text{mean}}$ .

non-thermal component ( $\Delta p\text{CO}_{2,\text{non-t}}$ ) and  $\Delta p\text{CO}_{2,\text{bio}}$ . If the non-thermal component was driven purely by biology both values should coincide. For the study region one can speculate that if there were other factors than biology or temperature that drive the  $p\text{CO}_2$  the  $\Delta p\text{CO}_{2,\text{bio}}$  should be lower than the value derived from the non-thermal amplitude. Fig. 3.8 show that all values east

of  $35^\circ\text{W}$  are nearly of the same magnitude and that most of the non-thermal component is driven by biology. However, west of  $35^\circ\text{W}$  the values decrease for the 2002/2003 dataset and increase for the 2006/2007 dataset. These observations agree with Fig. 3.7 where the values west  $35^\circ\text{W}$  are positive in 2002/2003 and negative in 2006/2007. The positive values in Fig. 3.7 denote areas where the thermal component exceeded the non-thermal and vice versa. The observed amplitude in this region (Fig. 3.4) is not smaller than in the other regions and thus the low values of both,  $\Delta p\text{CO}_{2,\text{bio}}$  and  $\Delta p\text{CO}_{2,\text{non-t}}$ , indicate that this region is mostly driven by temperature changes. The regions west of  $35^\circ\text{W}$  in 2006/2007 have also nearly the same  $p\text{CO}_2$  amplitude as the other regions. The increased values in Fig. 3.8 west of  $35^\circ\text{W}$  consequently indicate an increased non-thermal effect with respect to the regions east of  $35^\circ\text{W}$ . The  $\Delta p\text{CO}_{2,\text{bio}}$  is significantly lower than  $\Delta p\text{CO}_{2,\text{non-t}}$ , i.e. there are other effects than biology that drive the  $p\text{CO}_2$ . This observation agrees with the fact that the regions west of  $35^\circ$  are strongly influenced by the LC.

**CO<sub>2</sub> fluxes** The CO<sub>2</sub> flux was calculated using Eq. 1.15. In order to make our results comparable to the data from Takahashi *et al.* (2009) we used the parameterization for the wind speed dependent transfer velocity  $k$  as in their study:

$$k = 0.26 \times u_{10}^2 \times \sqrt{\left(\frac{Sc}{660}\right)} \quad (3.9)$$

where  $Sc$  is the Schmidt number of CO<sub>2</sub> and  $u_{10}$  is the model derived wind speed at 10 m height above sea surface (FNMOC, model derived wind speed on a 6 hourly  $1^\circ \times 1^\circ$  grid, <http://las.pfeg.noaa.gov/>). The calculated fluxes were averaged per month and box and the sigmoidal function (Eq. 3.3) was applied. Fig. 3.9 shows the resulting seasonal CO<sub>2</sub> flux for all grid boxes. The values are all in the same range although there are boxes with better agreement (boxes east from  $30^\circ\text{W}$ ) and boxes where significant differences are observed (boxes west of  $30^\circ\text{W}$ ). In the boxes west of  $30^\circ\text{W}$  the 2002/2003 data show an intense CO<sub>2</sub> flux into the ocean during winter. During the warmer seasons (April - October) the CO<sub>2</sub> flux is nearly zero with even short periods of outgassing. The flux data from 2006/2007 have a smaller seasonal amplitude. They also show a flux into the ocean during most of the year but the time with lowest flux (or even outgassing) is found in winter. In the boxes east of  $30^\circ\text{W}$  both datasets have a lower seasonal amplitude and they agree well with small differences during winter.

For comparison the flux data from Takahashi *et al.* (2009) for the year 2000 are also shown in Fig. 3.9. The measured data show a higher amplitude than the climatological values but the

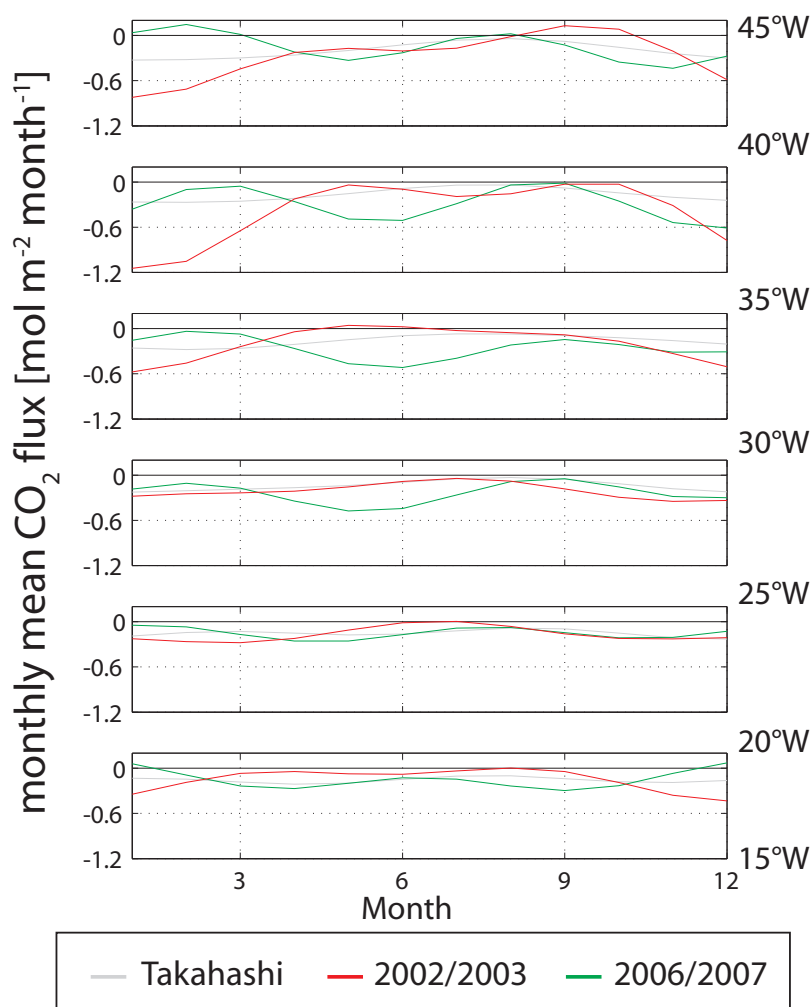


Figure 3.9.:  $\text{CO}_2$  flux as calculated from  $p\text{CO}_{2,\text{AMSR-E}}$ . The red line denotes the data from 2002/2003 and the GREEN line the 2006/2007 data. For comparison the  $\text{CO}_2$  fluxes from Takahashi *et al.* (2009) are shown in grey. Note, that the latter represent climatological fluxes.

fluxes are of rather similar magnitude. The observations east of  $35^\circ\text{W}$  agree very well with the climatological data and the data west of  $35^\circ\text{W}$  show larger differences especially during winter.

From the monthly values an annual flux was calculated for each box (Fig. 3.10). Note, that the data were not corrected to a single year and thus the climatological data show the flux for 2000. However, the North Atlantic between  $40^\circ\text{N}$  and  $55^\circ\text{N}$  acts as a perennial sink for  $\text{CO}_2$ . The annual fluxes agree remarkably well east of  $25^\circ\text{W}$ . Only the climatological data for the 2006/2007 dataset show a higher flux into the ocean. This difference results from the location of the cruise tracks. Mostly the ship was sailing south of Ireland but some cruise tracks lead north of Ireland. Thus the box had to be chosen to cover the whole region and all climatological data went into the averaging process while most observations are from the southern end of the box.

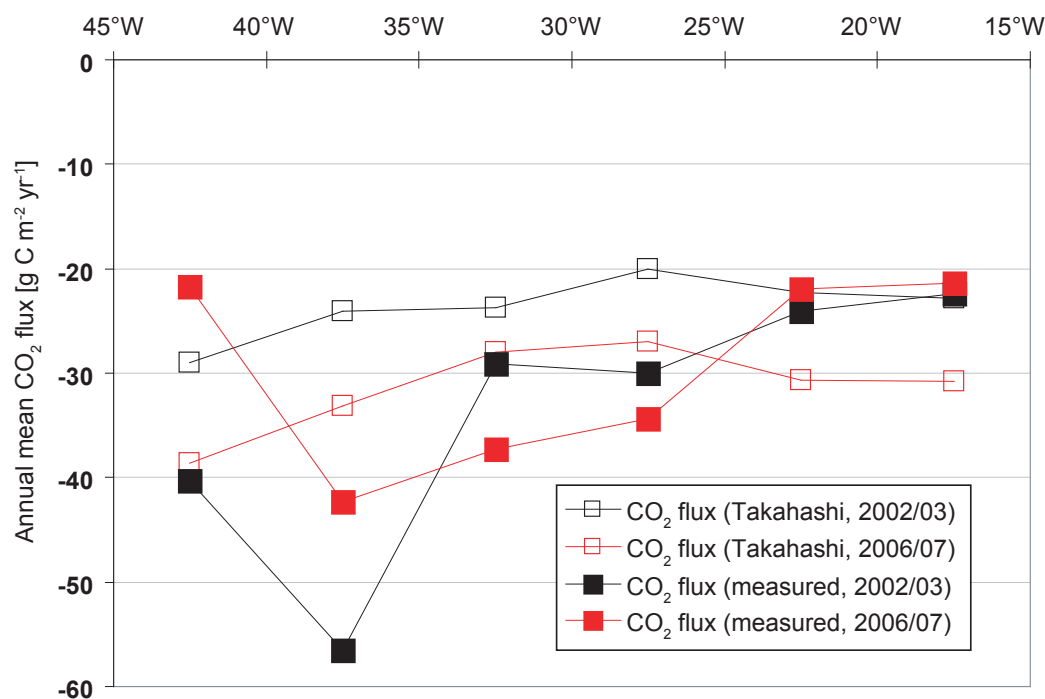


Figure 3.10.: Annual mean  $\text{CO}_2$  flux for 2002/2003 and 2006/2007 data. Shown are the fluxes derived from measurements and fluxes taken from Takahashi *et al.* (2009). All flux data were not corrected to a single year, thus the flux data from Takahashi *et al.* (2009) show the flux in 2000 for the particular boxes. The differences between their  $\text{CO}_2$  fluxes arise from the different regional coverage.

The data from 2002/2003 are generally lower than the climatological values and the highest measured annual  $\text{CO}_2$  flux into the ocean was observed in the area between  $35^\circ\text{W}$  and  $40^\circ\text{W}$ . The same was observed for the data from 2006/2007 but they show lower fluxes in the region west of  $45^\circ\text{W}$ . Table 3.1 shows the annual  $\text{CO}_2$  flux calculated with the observed data with the data from Takahashi *et al.* (2009). The 2002/2003 dataset results in a higher  $\text{CO}_2$  flux into the ocean than the climatology while the value resulting from the 2006/2007 dataset is virtually the same as calculated from the climatology.

### 3.3. Discussion

The dataset of this study is located in a critical region of the North Atlantic. First this region acts as the major sink for atmospheric  $\text{CO}_2$  (e.g. Gruber *et al.*, 2009; Takahashi *et al.*, 2009) which make it a key region for investigation of interannual and decadal changes of  $\text{CO}_2$  fluxes. Second, the dataset covers a region encompassing different oceanic regimes. Following the classification of Longhurst (2007) the dataset includes the following provinces: the southern part (and thus

	CO <sub>2</sub> flux in $\text{g C m}^{-2} \text{yr}^{-1}$	
	West	East
Lüger <i>et al.</i> (2006)		
2002/2003	-41.9	-38.9
Takahashi <i>et al.</i> (2009)		
2002/2003	-26.4	-22.0
2006/2007	-35.9	-28.9
this study		
2002/2003	-48.4	-26.4
2006/2007	-32.0	-28.9

Table 3.1.: Annual CO<sub>2</sub> fluxes for the study area from different studies. The data from Takahashi *et al.* (2009) are calculated for the same area but for the year 2000. West denotes the study region west of 35°W and east the study region east of 35°W. Lüger *et al.* (2006) used the same data for 2002/2003 but the data had had to be slightly corrected because of an inconsistent temperature correction. The western part from the study of Lüger *et al.* (2006) reaches until 70°W.

most of the 2002/2003 dataset) covers the GFST and North Atlantic drift region (NADR). These cruises may be also influenced by the subtropical gyre (NAST, west and east) region. The northern part (most of the 2006/2007 dataset) is located in the NADR and partly covers the Atlantic Arctic province (ARCT). This classification is not exclusive for one of the datasets since both cover more or less all provinces, except the ARCT province which is only covered by a few cruises of the 2006/2007 dataset. Furthermore the study area is highly variable on seasonal and interannual timescales (e.g. Corbière *et al.*, 2007; Olsen *et al.*, 2003; Schuster *et al.*, 2009) and thus a direct comparability of the two datasets is limited.

The distribution of  $\Delta p\text{CO}_2$  (Fig. 3.3c) shows the differences between the two datasets clearly: The 2002/2003 dataset has local minima in the western part in spring and autumn and a maximum in summer while the situation for the 2006/2007 dataset is reversed. Given that our results are representative for the study area these observation might be due to the fact that the NADR is an extension of the GFST and consequently both regions show the same pattern of  $\Delta p\text{CO}_2$ . An early bloom triggers the CO<sub>2</sub> drawdown in spring. As a consequence of the warming of the surface water during summer the solubility of CO<sub>2</sub> decreases and  $p\text{CO}_2$  increases (i.e.  $\Delta p\text{CO}_2$  decreases in an undersaturated situation). During autumn the water cools again and a late bloom causes another CO<sub>2</sub> drawdown both of which result in the second observed minimum. The deepening of the MLD during winter brings respired CO<sub>2</sub> to the surface and thus increases the  $p\text{CO}_2$ .

The annual cycle of seawater  $p\text{CO}_2$  in the different boxes and datasets is also shown in Fig. 3.4 where the observed data are also compared to the data from the climatology of Takahashi *et al.* (2009). The  $p\text{CO}_{2,\text{AMSR-E}}$  and  $p\text{CO}_{2,\text{clim-act}}$  agree well for most of the boxes but especially in the 2006/2007 dataset differences are observed. The differences in the box between  $40^\circ\text{W}$  and  $45^\circ\text{W}$  are likely due to the seasonally varying influence of the LC. The climatological data show the long-term mean value while even the data corrected to  $\overline{\text{SST}_{\text{AMSR-E}}}$  are highly variable in this region. The differences in the eastern part of the study region cannot be explained by the influence of different water masses. Furthermore the cruises in this part are distributed over a narrower latitudinal range than in the western part. Consequently the differences between the climatological and observed data can be explained by the large interannual variability of the North Atlantic.

The partitioning of the observed  $p\text{CO}_2$  into a thermal and non-thermal component helps to understand the processes driving the annual cycle (Fig. 3.6). The thermal component mirrors the annual cycle of SST with lowest  $p\text{CO}_2$  values during late winter/early spring and maximum values towards the end of summer. The non-thermal component represents the remainder of the variability and is largely driven by biological processes, i.e. net community production. The latter was calculated in section 3.2 using the nitrate parameterization of Steinhoff *et al.* (2010). The corresponding part of the amplitude of the non-thermal component (cf. Fig. 3.8) should be less or equal to the non-thermal component. In case it is less there should be other factors driving the non-thermal component of  $p\text{CO}_2$ . Otherwise the biological drawdown would be the only effect (in addition to the thermal effect) that drives the annual  $p\text{CO}_2$  cycle.

In 2002/2003 the seasonal  $p\text{CO}_{2,\text{non-t}}$  amplitude is lower in the box between  $40^\circ\text{W}$  and  $45^\circ\text{W}$  and nearly uniform in the residual boxes. The two westernmost boxes are also the boxes where the thermal effect exceeds the non-thermal effect (Fig. 3.7). Even if the non-thermal component is not the major driver of observed  $p\text{CO}_2$  in the western part, Fig. 3.8 shows that the biological drawdown is the major component of the non-thermal component in all boxes. In the western- and easternmost boxes one can speculate that it is nearly the only part driving the non-thermal component, while in the boxes between  $20^\circ\text{W}$  and  $40^\circ\text{W}$  there are additional factor that drive  $p\text{CO}_{2,\text{non-t}}$  (e.g. advective processes, MLD variations,...). In 2006/2007, again the most western box is different from the residual boxes, but this time the values are increased. This coincides with the findings shown in Fig. 3.7 where the non-thermally mediated amplitude exceeds the thermally mediated one. Biology accounts only for 2/3 of the observed amplitude. This shows again that the variability of the LC is a main driver of the observed  $p\text{CO}_2$  variability in this

part of the study area. Between  $25^\circ\text{W}$  and  $40^\circ\text{W}$  the values are nearly stable and the biology accounts for approximately 80% of the amplitude. East of  $25^\circ\text{W}$ , the values decrease again and the biology term accounts for nearly all of the observed amplitude. The amplitude data in the western part agree very well between the two datasets and are more or less on the same level. Only the westernmost box is different and the data are decreased (higher influence of  $p\text{CO}_{2,t}$ ) for 2002/2003 and increased (higher influence of  $p\text{CO}_{2,\text{non-t}}$ ) for 2006/2007. These observations indicate that the driving forces in the eastern part (east of  $35^\circ\text{W}$ ) of the North Atlantic are relatively stable on interannual time scales. The huge differences in the most western box are due to the different watermasses (or provinces) that were observed in this part: the 2002/2003 dataset is located in GFST and the 2006/2007 dataset in ARCT.

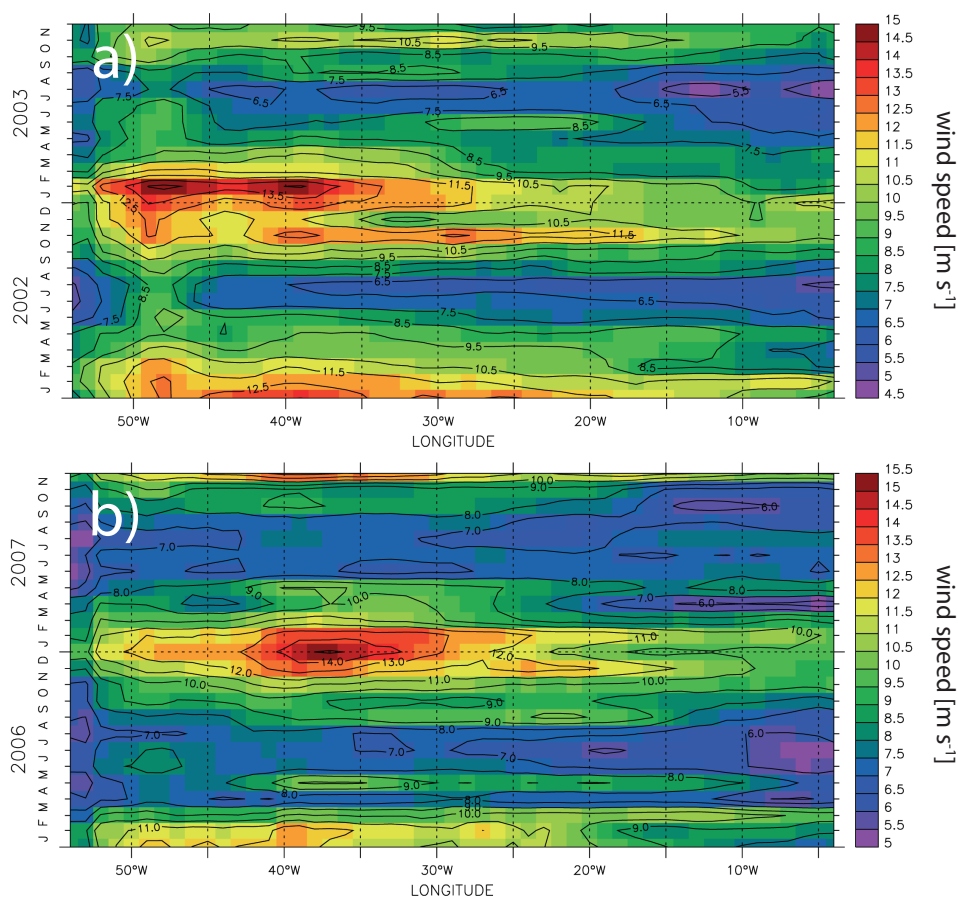


Figure 3.11.: Wind speed along  $47^\circ\text{N}$  for (a) 2002/2003 and (b) 2006/2007. The figures were generated using FNMOC wind data from the Live Access Server (<http://las.pfeg.noaa.gov/>).

The same pattern can be observed in the  $\text{CO}_2$  fluxes (Fig. 3.9): no large differences between the two datasets were observed in the eastern part. The data east of  $30^\circ\text{W}$  agree also well with



the values from the climatology. The differences increase west of  $30^\circ\text{W}$  which can be explained with the different pattern of  $\Delta p\text{CO}_2$  shown in Fig. 3.3c). The residual differences must be due to different wind conditions between the two observed years. However, the resulting annual fluxes are shown in Fig. 3.10. Again there is no interannual variability observed in the eastern part, but strong interannual changes in the western part. The fluxes are also lower in the eastern part than in the western part. The box between  $35^\circ\text{W}$  and  $40^\circ\text{W}$  shows the most intense  $\text{CO}_2$  flux into the ocean in both datasets. This huge flux is mediated by the strong winter winds that occur in this region (Fig. 3.11). This strong wind events explain also the deviations during winter in Fig. 3.9.



## 4. Tracking the Variable North Atlantic Sink for Atmospheric CO<sub>2</sub>

A.J. Watson, U. Schuster, D.C.E. Bakker, N.R. Bates, A. Corbière, M. González-Dávila, T. Friedrich, J. Hauck, C. Heinze, T. Johannessen, A. Körtzinger, N. Metzl, J. Olafsson, A. Olsen, A. Oschlies, X. A. Padin, B. Pfeil, J.M. Santana-Casiano, **T. Steinhoff**, M. Telszewski, A.F. Rios, D.W.R. Wallace, and R. Wanninkhof (2009), *Science*, 326 (5958), doi:10.1126/science.1177394.

My contribution:

- Operating  $p\text{CO}_2$  instrument onboard M/V Falstaff.
- Processing, quality control and evaluation of  $p\text{CO}_2$  data from IFM-GEOMAR VOS line.



# Tracking the Variable North Atlantic Sink for Atmospheric CO<sub>2</sub>

Andrew J. Watson,<sup>1\*</sup> Ute Schuster,<sup>1</sup> Dorothee C. E. Bakker,<sup>1</sup> Nicholas R. Bates,<sup>2</sup> Antoine Corbière,<sup>3</sup> Melchor González-Dávila,<sup>4</sup> Tobias Friedrich,<sup>5</sup> Judith Hauck,<sup>1†</sup> Christoph Heinze,<sup>6</sup> Truls Johannessen,<sup>6</sup> Arne Körtzinger,<sup>5</sup> Nicolas Metzler,<sup>3</sup> Jon Olafsson,<sup>7</sup> Are Olsen,<sup>6,8</sup> Andreas Oschlies,<sup>5</sup> X. Antonio Padin,<sup>9</sup> Benjamin Pfeil,<sup>6</sup> J. Magdalena Santana-Casiano,<sup>4</sup> Tobias Steinhoff,<sup>5</sup> Maciej Telszewski,<sup>1</sup> Aida F. Rios,<sup>9</sup> Douglas W. R. Wallace,<sup>5</sup> Rik Wanninkhof<sup>10</sup>

The oceans are a major sink for atmospheric carbon dioxide (CO<sub>2</sub>). Historically, observations have been too sparse to allow accurate tracking of changes in rates of CO<sub>2</sub> uptake over ocean basins, so little is known about how these vary. Here, we show observations indicating substantial variability in the CO<sub>2</sub> uptake by the North Atlantic on time scales of a few years. Further, we use measurements from a coordinated network of instrumented commercial ships to define the annual flux into the North Atlantic, for the year 2005, to a precision of about 10%. This approach offers the prospect of accurately monitoring the changing ocean CO<sub>2</sub> sink for those ocean basins that are well covered by shipping routes.

The natural sinks for atmospheric carbon dioxide have been of great importance in slowing the rate of anthropogenic climate change. Currently, humans emit ~8.5 Pg C year<sup>-1</sup> from fossil fuel and cement production, with another ~1.5 Pg C year<sup>-1</sup> produced by land use change (1). However, the net increase of the atmospheric concentration is only about half what it would be if all this CO<sub>2</sub> remained in the atmosphere. The remainder is taken up by land vegetation and the ocean in roughly equal measure, as evidenced by simultaneous observations of atmospheric oxygen and CO<sub>2</sub> (2). The ocean uptake of anthropogenically produced CO<sub>2</sub> is reducing the pH of surface waters, an acidification that is expected to have appreciable effects on the marine biota over this century (3).

Both ocean and land uptake is variable in space and time. Estimates of the magnitude and causes of temporal variations averaged over large areas have come from atmospheric observations in inverse models (4–6) and from ocean carbon models (7, 8). The atmospheric inver-

sions suggest that ocean regions such as the North Atlantic and Pacific, as well as continental land regions, exhibit variations in their annual fluxes that are a substantial fraction of their means. Ocean carbon cycle models usually suggest much smaller yearly and decadal changes (7), so it is not clear how much the ocean sinks actually vary. Neither is it clear whether the overall ocean sink is increasing or decreasing: Most models suggest that it should increase with time as atmospheric CO<sub>2</sub> continues to grow, but recent studies have suggested a “saturation” of the sink in the Southern Ocean (5). For the North Atlantic, observations suggest a decrease dating from ~1990 (9), especially between 1995–1996 and 2002–2005 (10). It has been suggested that such variation is linked to the dominant climate mode over the region, the North Atlantic Oscillation (NAO) (8, 10), but the heterogeneous

pattern of CO<sub>2</sub> in the surface ocean has made it difficult to unambiguously identify the nature of this connection. Ocean models forced with atmospheric variation are able to reproduce some of the observational trends, although usually at lower amplitude, and suggest complex patterns of variability within the basins (8).

Although the actual air-sea flux of CO<sub>2</sub> is difficult to measure directly, observations of sea-surface fugacity of CO<sub>2</sub> (fCO<sub>2</sub>) can be used to infer it. In recent years, volunteer observing ships (VOS) plying regular routes have been instrumented to make such measurements, and there has been a rapid increase in the quantity of data available (10–14). Figure 1 presents annual flux estimates for the longest-running VOS, for the period 2002 to 2007, between northwestern Europe and the Caribbean [for details of flux calculations, see (10), modified as we describe in (15)]. A substantial variation in the annual fluxes is seen, more than a factor of two over this time period. The observations show decadal rather than interannual variability, with the flux rising and falling over several years. The variation is presumably climatically forced (8, 16), although a relationship with the NAO is not immediately obvious.

The North Atlantic and Pacific are well covered by shipping, and networks of VOS in these oceans might form the backbone of an observing system to continuously monitor the air-sea exchange of carbon dioxide. In 2005, a trial of such a network in the North Atlantic was initiated under CarboOcean, a European Union-funded project, and here we use a year of observations to map the air-sea flux of the region and to evaluate the performance of the network. Figure 2A shows the location of the observations in 2005 on which our evaluation is based. These include VOS routes established specifically for the project (e.g., 1 and 4) and other routes and time series stations of longer establishment.

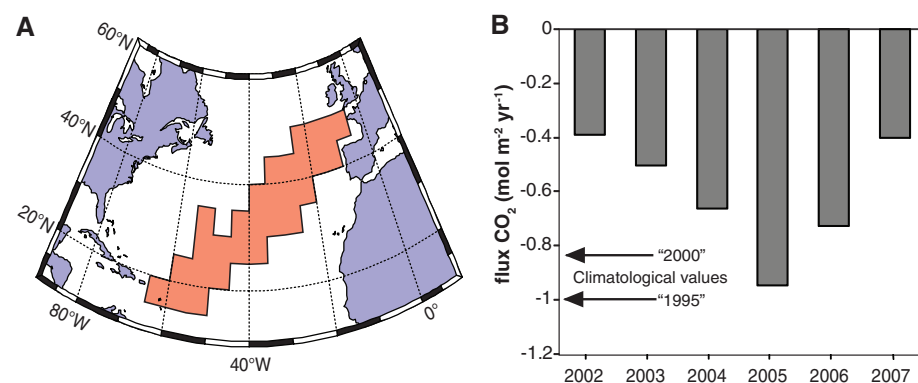


**Fig. 1.** Annual sea-air fluxes of CO<sub>2</sub> calculated from data on a shipping route between the United Kingdom and the Caribbean. Details of the data collection and the methods of calculating averages and fluxes are given in (10), modified as we describe in (15). (A) Mosaic of 5° by 5° tiles in which data coverage of the UK-Caribbean route is sufficient to calculate annual fluxes over the years 2002 to 2007. (B) Annual average fluxes for the enclosed area. The fluxes are negative (e.g., from air to sea), not only for the region as a whole but for every individual tile within it. Fluxes calculated using “climatological” values of air-sea fCO<sub>2</sub> gradient in this region, referenced to 2000 (14) or 1995 (23), are also indicated. Although these may be indicative of fluxes at these earlier times, they are not strictly applicable to any given year.

<sup>1</sup>School of Environmental Sciences, University of East Anglia, Norwich NR4 7TJ, UK. <sup>2</sup>Bermuda Biological Station for Research, Ferry Reach, GE01, Bermuda. <sup>3</sup>Laboratoire d’Océanographie et du Climat: Expérimentation et Approches Numériques Institut Pierre Simon Laplace, CNRS, Université Pierre et Marie Curie, Case 100, 4 Pl Jussieu, 75252 Paris, France. <sup>4</sup>Universidad de Las Palmas de Gran Canaria, Faculty of Marine Science, Department of Chemistry, Las Palmas, Gran Canaria, Spain. <sup>5</sup>Leibniz Institut für Meereswissenschaften, D-24105 Kiel, Germany. <sup>6</sup>University of Bergen, Geophysical Institute and Bjerknes Centre for Climate Research, Allégaten 55, N5007, Bergen, Norway. <sup>7</sup>Marine Research Institute and University of Iceland, Reykjavik, Iceland. <sup>8</sup>Department of Chemistry, University of Gothenburg, 41296, Göteborg, Sweden. <sup>9</sup>Consejo Superior de Investigaciones Científicas, Instituto de Investigaciones Marinas, Eduardo Cabello 6, Vigo 36208, Spain. <sup>10</sup>National Oceanic and Atmospheric Administration, Atlantic Oceanographic and Meteorological Laboratory, Miami, FL 33149, USA.

\*To whom correspondence should be addressed. E-mail: a.watson@uea.ac.uk

†Present address: Alfred Wegener Institute for Polar and Marine Research, Postfach 12 01 61, 27515 Bremerhaven, Germany.

In total, about 125,000 measurements taken in 2005 have gone into this study. Figure 2B shows the locations of observations divided into 2-month periods, to indicate temporal coverage through 2005 (15).

To estimate basinwide fluxes, we constructed maps of sea-surface  $f\text{CO}_2$  across the region and through time, by the method of developing relationships between the observed  $f\text{CO}_2$  and independent variables, for which data products

were available covering the entire domain. The variables chosen were sea surface temperature (SST) and mixed layer depth (MLD) (15). To obtain a data set of matched parameters from which to begin mappings, these fields were averaged or interpolated onto a  $1^\circ$  by  $1^\circ$  by once-per-day grid, and matched with  $f\text{CO}_2$  measurements binned to the same grid, wherever they existed. Observations taken over shelf or shelf-break waters (water depth  $< 1000$  m) were excluded. The rationale for the choice of SST and MLD is that  $f\text{CO}_2$  is strongly influenced by temperature change and mixing with subsurface waters, which should be well captured by these variables. Satellite-derived chlorophyll was also initially included (as a proxy for biological activity), but it was found to be of limited utility in predicting  $f\text{CO}_2$  and was finally dropped from the analysis. Two different mapping techniques were tested, one based on conventional multivariate linear regressions (MLR) applied after dividing the domain into subregions, and the other based on a self-organizing map (17) covering the entire spatial domain and year with a single map (15).

Fluxes were calculated from the mappings using the gas exchange equation  $F = K\alpha\Delta f\text{CO}_2$ . Here,  $\Delta f\text{CO}_2 = f\text{CO}_{2\text{surface}} - f\text{CO}_{2\text{atm}}$  is the difference between sea-surface and atmospheric  $f\text{CO}_2$ ,  $K$  is the gas transfer velocity (parameterized as a function of wind speed and temperature), and  $\alpha$  is the solubility of  $\text{CO}_2$  in the surface seawater. This approach has historically suffered from a lack of agreement between parameterizations of  $K$  derived from in situ measurements and those calibrated for agreement with the global bomb-derived  $^{14}\text{C}$  budget. However, recent reanalysis of the  $^{14}\text{C}$  budget has largely resolved these discrepancies (18, 19), leading to increased confidence in estimates of  $\text{CO}_2$  fluxes by this method. Parameterization of  $K$  used National Centers for Environmental Prediction/National

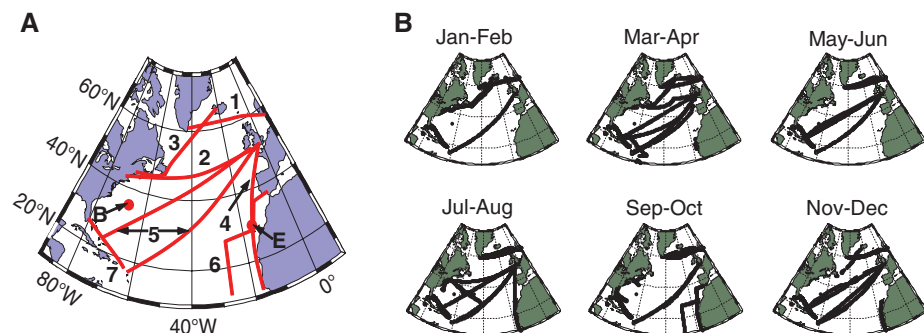


**Fig. 2.** (A) Location of regular VOS routes supplying data to the Carbo-Ocean network in 2005. Also shown are the locations of time series stations (B, Bermuda Atlantic time series station; E, European station for time series in the ocean, Canary Islands). (B) Post-plot of data binned into 2-month intervals through the year 2005.

**Table 1.** Integrated net ocean-to-atmosphere flux ( $10^\circ$  to  $65^\circ\text{N}$ ) across the North Atlantic in 2005. Values in the table are normalized to an area of  $3.1$  by  $10^{13}$   $\text{m}^2$  for comparison (15).  $P_{\text{CO}_2}$ , partial pressure of  $\text{CO}_2$ .

Method of interpolation	Value ( $\text{Pg C year}^{-1}$ )	Area average ( $\text{mol m}^{-2} \text{ year}^{-1}$ )
MLR in $10^\circ$ latitude bands	-0.274	-0.737
MLR in $20^\circ$ latitude bands	-0.251	-0.675
MLR in $30^\circ$ latitude bands	-0.246	-0.661
Self-organizing mapping	-0.238	-0.640
Mean	-0.252	-0.677
Standard deviation	0.015 (6.1%)	0.040
Using 1995 climatological $\Delta P_{\text{CO}_2}$ values*	-0.340	-0.914
Using 2000 climatological $\Delta P_{\text{CO}_2}$ values*	-0.300	-0.806

\*Estimates made using climatological maps of ocean-atmosphere  $\text{CO}_2$  gradient, which are based on analysis of observations spanning many decades, adjusted to 1995 or 2000 using assumptions described by Takahashi *et al.* (14, 23). These flux estimates used identical gas transfer velocities (e.g., calculated using 2005 winds and temperatures) to the upper rows, so that the differences are due to the different  $\Delta f\text{CO}_2$  fields only. For methodological reasons (14), the 1995 climatological value may have overestimated the magnitude of the flux into regions north of  $45^\circ\text{N}$ . Both climatological estimates are based on compilations of data collected over decades and are therefore not precise estimates for a given year.

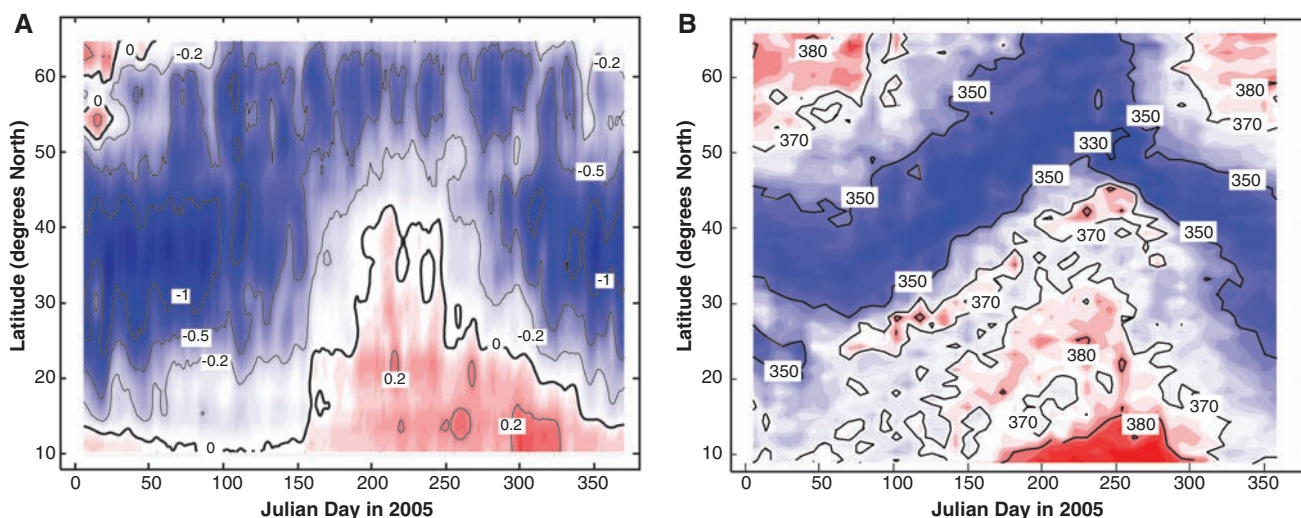


**Fig. 3.** Contours of ocean-atmosphere flux of  $\text{CO}_2$  [(A), in  $\text{Tmol year}^{-1}$  per degree of latitude] and surface ocean  $f\text{CO}_2$  [(B), in  $\mu\text{atm}$ ] in the North Atlantic in 2005, as a function of latitude and time. Fluxes are positive from sea to air.

The color scheme shades regions of strong positive fluxes and high  $f\text{CO}_2$  red, strong negative fluxes and low  $f\text{CO}_2$  blue, and near-neutral regions white. The zero flux contour is shown thicker than the others.

Center for Atmospheric Research (NCEP/NCAR) 6-hour winds and surface temperatures (20) and the wind-speed relationship of Nightingale *et al.* (21). The use of winds with 6-hour time resolution captures the great majority of the short-term variation in gas flux (15, 22).

Table 1 shows values of the flux integrated across the North Atlantic throughout the year 2005, for several different methods of mapping. The stability of the calculation gives us some confidence that the overall flux is well constrained by the observations, so is relatively insensitive to the details of the mapping technique. Shown for comparison are flux estimates using climatological values of  $f\text{CO}_2$  referenced to 1995 (23) and to 2000 (14), but for the same area and using the identical 2005 gas transfer velocities as the observations, so that differences compared to the observations are entirely due to the  $\Delta f\text{CO}_2$  distribution. For the region as a whole, these both show substantially higher sink strengths. Within the restricted area of the time series in Fig. 1, the climatological values are similar to those of 2005 but considerably larger than other years. Taken together, therefore, these comparisons suggest a decline in sink strength from the 1990s to the present decade, but one which is nonuniform with location.

We used two methods to more formally estimate uncertainties: (i) application of geostatistical techniques, proceeding from semivariograms of the residual  $f\text{CO}_2$  fields (24) and (ii) application of our methods to  $f\text{CO}_2$  fields generated by an eddy-resolving biogeochemical ocean model of the North Atlantic (25). These two techniques have very different underlying assumptions. The second method, in particular, explicitly tests for bias introduced by the mapping techniques. Although the uncertainty on the flux at any given point is in general large (26), it decreases with integration over larger domains. Both our methods of estimating uncertainty indicate that, integrated over the North Atlantic from  $10^\circ\text{N}$  to  $65^\circ\text{N}$ , the  $1-\sigma$  error on the annual mean  $f\text{CO}_2$  is  $\sim 10\%$  of  $\Delta f\text{CO}_2$ , with somewhat smaller errors propagating through to the derived flux (15). The broad agreement between two uncertainty analyses having very different underlying assumptions gives us additional confidence in these estimates.

Year-to-year differences are dominated by variability in  $\Delta f\text{CO}_2$  (10). Hence, annual flux estimates from different years may also be compared with a precision of  $\sim 10\%$ . The absolute values, however, have larger uncertainty because of the systematic error arising from the parameterization of gas transfer. Recent estimates for the global gas transfer rate appropriate to  $\text{CO}_2$  span a range from  $14.6$  to  $17.1 \text{ cm hour}^{-1}$  (18, 19, 27) and suggest that there remains a  $\sim 20\%$  uncertainty here. We therefore quote a flux of  $0.25 \pm 0.05 \text{ Pg C}$  for the  $10^\circ\text{N}$  to  $65^\circ\text{N}$  region for 2005, where the uncertainty is approximately  $1 \sigma$ . Our errors compare favorably with previous attempts to observationally constrain surface-atmosphere fluxes over continents or oceans. For example, the recent North American net “natural” sink,

calculated from land use analyses, is believed to be  $0.49 \text{ Pg C year}^{-1}$ , with  $95\%$  confidence limits ( $\sim 2 \sigma$ ) of  $50\%$ , where, however, the estimate is the average over 5- to 10-year periods (28), so that interannual variability cannot be addressed. Estimates made by a dense network of atmospheric observations to provide a “top-down” constraint place this sink in the range of  $0.4$  to  $1.0 \text{ Pg C year}^{-1}$  (29). The VOS network is thus capable of defining the North Atlantic sink to substantially better precision, and somewhat better absolute accuracy, than is currently possible on the land surface.

Figure 3 shows both  $f\text{CO}_2$  and air-sea flux integrated across the North Atlantic, as a function of latitude and time through the year (15). The figures show a major sink area in winter due to low  $f\text{CO}_2$ , extending from  $20^\circ$  to  $50^\circ\text{N}$ , which migrates northward through the subpolar gyre during the year. In 2005, it reached a maximum flux into the ocean in March and April, and then weakened through the summer. This  $\text{CO}_2$  sink is maintained year-round by the cooling, northward transport of surface waters and is accentuated by the unfolding spring and summer phytoplankton bloom. Also prominent is the subtropical gyre annual cycle driven by temperature increase and strongest in the west. In 2005, the subtropical gyre was a net sink during the winter months but developed into a source as the summer progressed.

These broad features are repeated each year and are seen in climatological estimates of the flux (14, 23), but, it now seems clear, they have substantial interannual and decadal variability around the climatology. Recent work using data before 2005 from some of the Atlantic VOS lines indicates that in 2002 to 2004, the net flux into some areas was only  $\sim 50\%$  of mid-1990s values (10, 13). Repeating the flux calculation, but replacing the 2005  $\Delta f\text{CO}_2$  observations with climatological air-sea  $\text{CO}_2$  gradients referenced to 2000 (14) or 1995 (23), yields annual sinks of respectively  $0.30$  or  $0.34 \text{ Pg C}$  (Table 1). Although the climatological values cannot be unambiguously related to the actual situation in any given year, this suggests that  $\Delta f\text{CO}_2$  was on the order of  $20\%$  or more lower in 2005 than 5 to 10 years earlier.

Our work demonstrates that an observing network based on commercial VOS is able to constrain the atmosphere-ocean flux of  $\text{CO}_2$  into the North Atlantic with good precision. VOS networks are very cost-efficient because the ships are already in place. VOS also operates in the North Pacific and South Atlantic, and a similar approach should in principle be applicable in these oceans, too. An increasing number of moorings in the equatorial Pacific and Atlantic are also now equipped with instrumentation to observe surface  $f\text{CO}_2$ , so that a greatly improved precision of in situ observation of at least the Northern Hemisphere oceans is now possible. Such an observing system will greatly aid in understanding the ocean sink for atmospheric carbon dioxide and the progress of ocean acidification. It will also provide

a valuable “top-down” constraint on the land sinks, which are more heterogeneous and thus more difficult to observe directly.

#### References and Notes

1. J. G. Canadell *et al.*, *Proc. Natl. Acad. Sci. U.S.A.* **104**, 18866 (2007).
2. A. C. Manning, R. F. Keeling, *Tellus* **58B**, 95 (2006).
3. J. C. Orr *et al.*, *Nature* **437**, 681 (2005).
4. P. Bousquet *et al.*, *Science* **290**, 1342 (2000).
5. C. Le Quéré *et al.*, *Science* **316**, 1735 (2007).
6. P. K. Patra *et al.*, *Global Biogeochem. Cycles* **19**, GB4013 (2005).
7. C. Le Quéré *et al.*, *Tellus* **55B**, 649 (2003).
8. H. Thomas *et al.*, *Global Biogeochem. Cycles* **22**, GB4027 (2008).
9. U. Schuster *et al.*, *Deep Sea Res. Part II Top. Stud. Oceanogr.* **56**, 620 (2009).
10. U. Schuster, A. J. Watson, *J. Geophys. Res.* **112**, C11006 (2007).
11. H. Lüger, D. W. R. Wallace, A. Körtzinger, Y. Nojiri, *Global Biogeochem. Cycles* **18**, GB3023 (2004).
12. A. Olsen, J. A. Trinanes, R. Wanninkhof, *Remote Sens. Environ.* **89**, 309 (2004).
13. A. Corbière, N. Metzl, G. Reverdin, C. Brunet, T. Takahashi, *Tellus* **59B**, 168 (2007).
14. T. Takahashi *et al.*, *Deep Sea Res. Part II Top. Stud. Oceanogr.* **56**, 554 (2009).
15. Materials and methods are available as supporting material on Science Online.
16. N. Gruber, *Nature* **458**, 155 (2009).
17. T. Kohonen, *Self-Organizing Maps*. Series in Information Sciences, vol. 30 (Springer, Heidelberg, ed. 2, 1995).
18. S. A. Müller, F. Joos, G. K. Plattner, N. R. Edwards, T. F. Stocker, *Global Biogeochem. Cycles* **22**, GB3011 (2008).
19. C. Sweeney *et al.*, *Global Biogeochem. Cycles* **21**, GB2015 (2007).
20. E. Kalnay *et al.*, *Bull. Am. Met. Soc.* **77**, 437 (1996).
21. P. D. Nightingale *et al.*, *Global Biogeochem. Cycles* **14**, 373 (2000).
22. H. Lüger, R. Wanninkhof, D. W. R. Wallace, A. Körtzinger, *J. Geophys. Res.* **111**, C06024 (2006).
23. T. Takahashi *et al.*, *Deep Sea Res. Part II Top. Stud. Oceanogr.* **49**, 1601 (2002).
24. R. Webster, M. A. Oliver, *Geostatistics for Environmental Scientists* (Wiley, Chichester, UK, 2001).
25. C. Eden, A. Oschlies, *Global Biogeochem. Cycles* **20**, GB2008 (2006).
26. T. Friedrich, A. Oschlies, *J. Geophys. Res.* **114**, C03020 (2009).
27. T. Naegler, P. Ciais, K. Rodgers, I. Levin, *Geophys. Res. Lett.* **33**, L11802 (2006).
28. A. W. King *et al.*, “North American carbon budget and implications for the global carbon cycle”; [www.climateaction.gov/Library/sap/sap2-2/final-report/default.htm](http://www.climateaction.gov/Library/sap/sap2-2/final-report/default.htm) (NOAA, 2008).
29. W. Peters *et al.*, *Proc. Natl. Acad. Sci. U.S.A.* **104**, 18925 (2007).
30. We thank Seatrade Reefer Chartering, Belgium; Geest Line Ltd, UK; Royal Arctic Line, Denmark; Royal Caribbean International, USA; Atlantic Container Lines Inc., USA; Eimskip Company, Iceland; and Wallenius Lines, Sweden, as well as the captains, officers, and crew of all ships for support of our projects. We acknowledge funding from the European Commission under CarboOcean [project 511176 (GOCE)]; Intercambio de Carbono entre Canarias y Barcelona CTM2005-03893/MAR and CTM2006-27116-E/MAR in Spain; the Natural Environment Research Council’s Centre for Observation of Air-Sea Interactions and Fluxes and the National Centre for Earth Observation in the United Kingdom; and Institut National des Sciences de l’Univers and Institut Paul Emile Victor in France.

#### Supporting Online Material

[www.sciencemag.org/cgi/content/full/326/5958/1391/DC1](http://www.sciencemag.org/cgi/content/full/326/5958/1391/DC1)  
Materials and Methods

Figs. S1 to S3

Table S1

References

8 June 2009; accepted 7 October 2009

10.1126/science.1177394





## 5. Estimating the monthly $p\text{CO}_2$ distribution in the North Atlantic using a self-organizing neural network

M. Telszewski, A. Chazottes, U. Schuster, A. J. Watson, C. Moulin, D. C. E. Bakker, M. González-Dávila, T. Johannessen, A. Körtzinger, H. Lüger, A. Olsen, A. Omar, X. A. Padin, A. F. Rios, **T. Steinhoff**, M. Santana-Casiano, D. W. R. Wallace, and R. Wanninkhof (2009), *Biogeosciences*, 6, 1405-1421.

My contribution:

- Operating  $p\text{CO}_2$  instrument onboard M/V Falstaff and M/V Atlantic Companion.
- Processing, quality control and evaluation of  $p\text{CO}_2$  data from IFM-GEOMAR VOS line.



## Estimating the monthly $p\text{CO}_2$ distribution in the North Atlantic using a self-organizing neural network

M. Telszewski<sup>1</sup>, A. Chazottes<sup>2</sup>, U. Schuster<sup>1</sup>, A. J. Watson<sup>1</sup>, C. Moulin<sup>2</sup>, D. C. E. Bakker<sup>1</sup>, M. González-Dávila<sup>3</sup>, T. Johannessen<sup>4</sup>, A. Körtzinger<sup>5</sup>, H. Lüger<sup>6</sup>, A. Olsen<sup>4,8,9</sup>, A. Omar<sup>4</sup>, X. A. Padin<sup>7</sup>, A. F. Ríos<sup>7</sup>, T. Steinhoff<sup>5</sup>, M. Santana-Casiano<sup>3</sup>, D. W. R. Wallace<sup>5</sup>, and R. Wanninkhof<sup>6</sup>

<sup>1</sup>School of Environmental Sciences, University of East Anglia, Norwich, UK

<sup>2</sup>L'Institut Pierre-Simon Laplace/Laboratoire des Sciences du Climat et de l'Environnement, Centre National de la Recherche Scientifique – Commissariat à l'Énergie Atomique, Gif-sur-Yvette, France

<sup>3</sup>Department of Marine Chemistry, Universidad de Las Palmas de Gran Canaria, Las Palmas, Gran Canaria, Spain

<sup>4</sup>Geophysical Institute, University of Bergen, Bergen, Norway

<sup>5</sup>Leibniz Institute of Marine Sciences, Kiel, Germany

<sup>6</sup>Atlantic Oceanographic and Meteorological Laboratory, National Oceanic and Atmospheric Administration, Miami, Florida, USA

<sup>7</sup>Instituto de Investigaciones Marinas, Consejo Superior de Investigaciones Científicas (CSIC), Vigo, Spain

<sup>8</sup>Bjerknes Centre for Climate Research, UNIFOB AS, Bergen, Norway

<sup>9</sup>Marine Chemistry, Department of Chemistry, University of Göteborg, Göteborg, Sweden

Received: 10 March 2009 – Published in Biogeosciences Discuss.: 30 March 2009

Revised: 21 July 2009 – Accepted: 31 July 2009 – Published: 5 August 2009

**Abstract.** Here we present monthly, basin-wide maps of the partial pressure of carbon dioxide ( $p\text{CO}_2$ ) for the North Atlantic on a  $1^\circ$  latitude by  $1^\circ$  longitude grid for years 2004 through 2006 inclusive. The maps have been computed using a neural network technique which reconstructs the non-linear relationships between three biogeochemical parameters and marine  $p\text{CO}_2$ . A self organizing map (SOM) neural network has been trained using 389 000 triplets of the SeaWiFS-MODIS chlorophyll-*a* concentration, the NCEP/NCAR reanalysis sea surface temperature, and the FOAM mixed layer depth. The trained SOM was labelled with 137 000 underway  $p\text{CO}_2$  measurements collected in situ during 2004, 2005 and 2006 in the North Atlantic, spanning the range of 208 to 437  $\mu\text{atm}$ . The root mean square error (RMSE) of the neural network fit to the data is 11.6  $\mu\text{atm}$ , which equals to just above 3 per cent of an average  $p\text{CO}_2$  value in the in situ dataset. The seasonal  $p\text{CO}_2$  cycle as well as estimates of the interannual variability in the major biogeochemical provinces are presented and discussed. High resolution combined with basin-wide coverage makes the maps a useful tool

for several applications such as the monitoring of basin-wide air-sea  $\text{CO}_2$  fluxes or improvement of seasonal and interannual marine  $\text{CO}_2$  cycles in future model predictions. The method itself is a valuable alternative to traditional statistical modelling techniques used in geosciences.

### 1 Introduction

Globally, the oceans have absorbed around 30 per cent of the total anthropogenic carbon dioxide ( $\text{CO}_2$ ) emissions to the atmosphere since the beginning of the industrial era (Sabine et al., 2004). This natural buffer slows the effects of anthropogenic interference with the global carbon cycle. The North Atlantic Ocean, being a highly biogeochemically dynamic basin and one of the strongest sinks of carbon in the world's oceans (Takahashi et al., 2002), plays an important role in the world's carbon cycle. Understanding the future behaviour of the global carbon sinks and sources, as well as related effects on the planet's climate, can only be obtained given a robust understanding of the current distribution of carbon sink and source regions.

The magnitude of the ocean sink can be determined using air-sea flux estimates based on in situ measurements of



Correspondence to: M. Telszewski  
(m.telszewski@uea.ac.uk)

the sea surface partial pressure of  $\text{CO}_2$  ( $p\text{CO}_2$ ). However, while atmospheric  $p\text{CO}_2$  shows relative homogeneity, marine  $p\text{CO}_2$  varies strongly both temporarily and spatially (Sarmiento and Gruber, 2002). Monitoring the marine  $p\text{CO}_2$  distribution on monthly to interannual time-scales is thus crucial for further understanding of the global carbon cycle in the context of current climate dynamics. Due to technical as well as financial restrictions, in situ measurements of marine  $p\text{CO}_2$  are sparse even in the relatively well sampled North Atlantic Ocean. However, over the last decade, technical improvements and cooperation with the shipping industry have allowed for the installation of several autonomous underway systems on board commercial vessels routinely crossing the ocean basin. Those instruments perform quasicontinuous measurements, offering temporal and spatial coverage which allows for regional analysis of the highly variable spatial and temporal distribution of  $p\text{CO}_2$  (e.g. Cooper et al., 1998; Lefèvre et al., 2004; Lüger et al., 2004 and 2006; Corbière et al., 2007; Schuster and Watson, 2007; Olsen et al., 2004 and 2008; Schuster et al., 2009). Most of these authors suggest that the strength of the North Atlantic sink has decreased over the last decade, with the decline especially significant (up to 50%) in the northern part of the basin. This change indicates that an increasing fraction of the anthropogenic emissions remains in the atmosphere, which is consistent with some recent modelling results. For instance, Canadell et al. (2007) suggest that around 10 per cent of the recent (2000–2006) rise in the atmospheric  $\text{CO}_2$  concentrations can be attributed to the weakening of the ocean sink.

Despite the huge community effort to increase the network of in situ  $p\text{CO}_2$  measurements in the North Atlantic, the coverage still remains unevenly distributed in time and space. The regional character of the existing estimates poses difficulties for extrapolation to the entire basin; therefore a robust and reliable method to spatially and temporarily interpolate available measurements of marine  $p\text{CO}_2$  has been long sought (e.g. Lefèvre et al., 1999 and 2005; Takahashi et al., 2002 and 2009; Olsen et al., 2003; Jamet et al., 2007; Chierici et al., 2009).

In the work presented here, we seek to map oceanic  $p\text{CO}_2$  in the North Atlantic at a monthly timescale. We use an artificial neural network (NN), a powerful non-linear modelling tool for mapping performance (Dreyfus, 2005). Neural networks were first used extensively by the pattern recognition community 20–30 years ago (Kohonen, 2001). Since then NN have made their way into geosciences and over the last decade there has been a significant increase in their application to environmental problems. They are now commonly used in atmospheric science (Cavazos, 1999; Hewitson et al., 2002; Niang et al., 2006), oceanography (Richardson et al., 2003; Liu et al., 2005 and 2006a; Reusch et al., 2007) and meteorology (e.g. Ali et al., 2007).

The term *artificial neural network* reflects a mechanistic connection to the processes found in the human brain and therefore generates some confusion. At present their data-

processing algorithms are well understood and may be used in parallel with traditional statistical tools. Among the numerous NN types, the Self Organizing Map (SOM) seems to gain the most attention as being well suited to study empirical relationships in geosciences. It is a particularly powerful tool for the extraction and classification of features, such as trends, in (and between) input variables. The SOM is a “black-box” type of model. While its restrictions and limitations need to be considered, it has an essential advantage over more commonly used knowledge-based models which are based on equations describing the physical, chemical and biological phenomena that control the quantity to be modelled. As opposed to the latter, the SOM technique is based solely on observations. The SOM uses an unsupervised (no need for a priori, empirical or theoretical description of the input – output relationships) learning algorithm, enabling us to identify relationships among the state variables of the phenomena under analysis, where our understanding of these is insufficient to be fully described using mathematical equations, and where applications of knowledge-based models are therefore limited.

The SOM technique has been successfully used to synthesise regional marine  $p\text{CO}_2$  maps from in situ measurements. Lefèvre et al. (2005) have constructed a monthly climatology for years 1995–1997 using the reanalyzed SST fields as the SOM input. Their estimates cover the North Atlantic sub-polar gyre ( $50^\circ\text{N}$  to  $70^\circ\text{N}$  and  $10^\circ\text{W}$  to  $60^\circ\text{W}$ ). Lefèvre et al. were able to capture a more complex distribution in the northern North Atlantic using SOM than they could using multiple linear regressions. Also the residuals determined through the validation against an independent subset of the data were smaller for the SOM.

In this study, we construct basin-wide ( $10.5^\circ\text{N}$  to  $75.5^\circ\text{N}$  and  $9.5^\circ\text{E}$  to  $75.5^\circ\text{W}$ ), monthly  $p\text{CO}_2$  maps for three consecutive years with a  $1^\circ$  latitude by  $1^\circ$  longitude resolution. We use 137 000 in situ  $p\text{CO}_2$  measurements collected in the North Atlantic throughout 2004, 2005 and 2006 as part of CarboOcean (<http://www.carboocean.org/>), an EU-funded Integrated Project, and parallel US projects. The  $p\text{CO}_2$  data are combined with 389 000 satellite, reanalysis and assimilation data of chlorophyll-*a*, sea surface temperature, and mixed layer depth, which allows basin-wide, continuous mapping over extended periods of time.

We show the capacity of the method to synthesize coherent, spatial and temporal distribution patterns of marine  $p\text{CO}_2$  fields in the North Atlantic, and propose the method to be used in conjunction with in situ data collection during future oceanic  $p\text{CO}_2$  monitoring programs.

## 2 Data and methods

We hypothesise that sea surface  $p\text{CO}_2$  can be estimated through the SOM based multiple non-linear regression with three parameters (Eq. 1): sea surface temperature (SST),

wind-mixed layer depth (MLD) and the abundance of photosynthesizing organisms in the surface ocean represented by the chlorophyll-*a* concentration (CHL).

$$p\text{CO}_2 = \text{SOM}(\text{SST}, \text{MLD}, \text{CHL}) \quad (1)$$

Lefèvre et al. (2005) and Friedrich and Oschlies (2009) used position and time as additional training parameters for their SOM-based mapping. The different training scheme (compared to that used by Friedrich and Oschlies, 2009) applied in this study allows for improved determination of the statistical structure of the basin-wide input data (discussed in Sect. 3.1). However, the patterns found are more strongly implemented in the resulting maps. The maps obtained using position and time are unrealistic (not shown), as also reported by Jamet et al. (2007) who compared three different combinations of parameters needed to generate  $p\text{CO}_2$  maps in the North Atlantic. Using latitude or longitude causes concentration of similar values along east-west or north-south lines, respectively. Using both causes clustering of similar  $p\text{CO}_2$  values in patches, with surprisingly equal distances between one another. Finally, using time increases the influence of seasonality on the  $p\text{CO}_2$  maps. Thus, whereas using position and time can be sufficient to work with small regions (e.g. Lefèvre et al., 2005), they are definitely not applicable as a basin-wide training parameters.

During our SOM analysis three steps are taken in order to estimate basin-wide  $p\text{CO}_2$  fields: first, an unsupervised training takes place without  $p\text{CO}_2$  data; second, in situ  $p\text{CO}_2$  data is used to label the preconditioned SOM neurons; third, the trained and labelled SOM neurons are used to assign  $p\text{CO}_2$  values to the (geographical) grid points of the North Atlantic.

## 2.1 An overview of the SOM setup

The SOM, introduced by Kohonen (2001), is a competitive learning method in which an algorithm learns to classify the samples by recognizing and extracting patterns from the statistical structure of the multivariate dataset. It performs a non-linear projection from the highly dimensional input data onto a usually two-dimensional (2-D) grid, as described by Niang et al. (2003). The SOM analysis was carried out using the SOM Toolbox Version 2 (Vesanto, 2000) for Matlab, developed by the Laboratory of Information and Computer Science at the Helsinki University of Technology and freely available from <http://www.cis.hut.fi/projects/somtoolbox> (visualizations of the resulting North Atlantic  $p\text{CO}_2$  maps were done using additional procedures in Matlab). For general SOM procedures and parameter settings consult Liu et al. (2006b) and Vesanto et al. (2000). The SOM procedure adopted in this study is outlined below.

Our SOM-map consists of 2220 *i* units (often referred to as neurons) organized on a regular 2D grid. Moderately sized maps (in relation to the training data set) are found to be the most efficient. Too many neurons do not reduce the

data enough for extracting characteristic patterns. Too few neurons do not provide sufficient representation of patterns underlying the in situ observations. A flat sheet map shape ( $60 \times 37$ ) with a hexagonal regional lattice structure was chosen. Each neuron is represented by a three-dimensional weight vector  $y_i$ , with one component for each input variable (SST, MLD and CHL). All the values are linearly normalized to acquire an even weight distribution between the input variables. Additionally CHL and MLD values are  $\log_{10}$  normalized to minimize the influence which their spread throughout four and three orders of magnitude, respectively, would otherwise have on the weight distribution. Linear initialization (performed in this study) of the components of weight vectors applied prior to the training process decreases the computing time required for the SOM to converge with the input data (Kohonen, 2001).

## 2.2 Training data set (SST, MLD, CHL)

The training data set consists of three subsets, one for each parameter. Basin-scale SST data were obtained from the NCEP/NCAR Reanalysis Project (<http://www.cdc.noaa.gov/cdc/data.ncep.reanalysis.html>) at daily frequency and  $2.5^\circ$  latitude  $\times$   $2.5^\circ$  longitude resolution. The SST data (used in this study) contain the values as described in Kalnay et al. (1996). As such, over open water the temperature is fixed at its initial weekly value and linearly interpolated to daily frequency in the NCEP data product.

Basin-wide MLD estimates were obtained from the Forecasting Ocean Assimilation Model (FOAM, Meteorological Office, Exeter, UK; <http://www.nerc-essc.ac.uk/godiva>) at daily frequency and  $1^\circ$  latitude  $\times$   $1^\circ$  longitude resolution. The FOAM model assimilates both in situ and remotely sensed ocean observations in near real-time including: vertical temperature and salinity profiles from sea stations and research vessels, Argo profiling floats and PIRATA moored arrays, as well as sea surface temperature from Voluntary Observing Ships (VOS), buoys, and the satellite mounted Advanced Very High Resolution Radiometer (AVHRR). The mixed layer depth used in this study is determined by the FOAM model using the density based criterion as the depth where a density increase of  $0.05 \text{ kg m}^{-3}$  from the surface value occurs (Chunlei Liu, Environmental Systems Science Centre of the UK National Environmental Research Council, personal communication, 2007).

CHL data were obtained from Aqua-MODIS/SeaWiFS merged Level-3 Standard maps provided by NASA/GFSC/DAAC at weekly frequency and 9 km resolution (<http://oceancolor.gsfc.nasa.gov>). The use of the merged product was dictated by considerable improvement in coverage in relation to the single mission products (20% and 24% for SeaWiFS and MODIS 8-daily product, respectively).

All three products (SST, MLD, CHL) offer almost full basin-wide coverage for the years 2004 to 2006. All

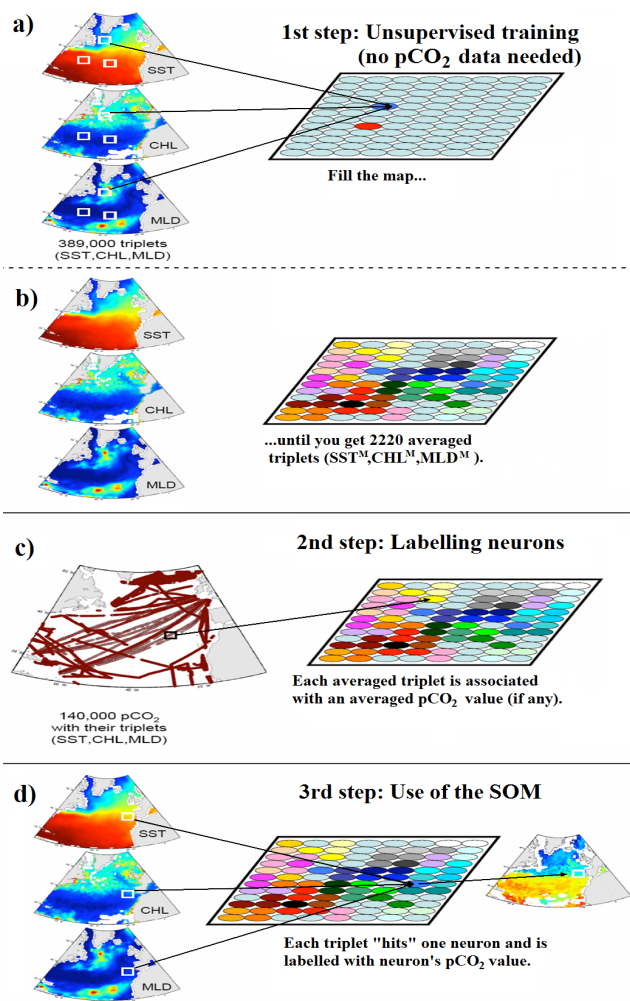


**Fig. 1.** Visualization of the procedures for the self organizing map (SOM). Three main steps are necessary: first (a and b), an unsupervised training takes place, and no  $p\text{CO}_2$  data is used; second (c) preconditioned neurons are labelled with  $p\text{CO}_2$  data measured in situ; third (d) the trained and labelled SOM is used to assign  $p\text{CO}_2$  values to the geographical map for the whole basin.

parameters were re-gridded onto a 8-daily frequency and  $1^\circ$  latitude  $\times$   $1^\circ$  longitude resolution. The study area stretches from  $10.5^\circ$  N to  $75.5^\circ$  N and from  $9.5^\circ$  E to  $75.5^\circ$  W and is hereafter called the North Atlantic.

We have excluded coastal (water column  $<500$  m) and ice covered (SST  $<-1.8^\circ\text{C}$ ) waters from the training data set, which consists of 389 000 pixels (training vectors) each containing normalized SST, MLD and CHL values (used in training) as well as additional information such as month and year, position, bottom-depth and other ancillary information which is used during mapping and analysis of the results.

Seasons are as follows: winter includes December, January and February, spring includes March, April and May, summer includes June, July and August and fall includes September, October and November.

### 2.3 The self organizing process – training the SOM

During the self-organizing process, 389 000 training vectors  $x_i$ , are presented to the SOM (Fig. 1a). The activation of each neuron's weight vector,  $y_i$ , is computed for the presented training vector. For a given training vector, the "winning" neuron (the one with the highest activation) is the one whose weight vector is the closest to the presented training vector in Euclidean distance  $D(x_i, y_i)$ , defined as:

$$D(x_i, y_i) = \left[ (x_{i\text{SST}} - y_{i\text{SST}})^2 + (x_{i\text{MLD}} - y_{i\text{MLD}})^2 + (x_{i\text{CHL}} - y_{i\text{CHL}})^2 \right]^{0.5} \quad (2)$$

The weight vector of the winning neuron is updated by adjusting it towards the training vector by a certain fraction of the difference between the two, as indicated by a linear, monotonically time-decreasing learning rate function  $\alpha$ . Thus the winner's activation will be even higher the next time a similar input vector is presented. In addition to the winning-neuron, the weight vectors of neurons in the neighbourhood of the winner are also stretched towards the input vector, according to a neighbourhood function,  $H$ , which decreases with each neuron away from the winner:

$$H_{ci}(t) = \alpha(t) \times \exp(d_{ci}^2 / 2(\sigma(t))^2) \quad (3)$$

where  $\sigma(t)$  is the neighbourhood radius at time  $t$ , and  $d_{ci}$  is the distance between map units  $c$  (winner) and  $i$  on the map grid. The neighbourhood radius  $\sigma(t)$  decreases as a function of time along with the learning rate  $\alpha(t)$ . The neighbourhood radius and also the shape of the neighbourhood function have to be decided before the training starts. In this study the neighbourhood radius decreases from 8 to 2 neurons during the rough training and further to 0 during the fine-tuning phase. The shape of the neighbourhood function dictates the extent to which the neighbours of the winning-neuron are updated, and how it changes with increasing distance from the winning-neuron. A Gaussian shape has been used in this study. The learning rule which incorporates such a neighbourhood function leads to a topologically ordered mapping of the input vectors and distinguishes the SOM from other vector quantization algorithms (Kohonen, 2001). By virtue of the neighbourhood function, the winning-neuron is not a mean of the data it accounts for, but rather an expression of the local ordination of patterns extracted from the input data set (Dreyfus et al., 2005). Similar patterns are mapped onto neighbouring regions on the SOM-map, while dissimilar patterns are mapped further apart.

After the training, each neuron becomes a synthetic sample with an associated weight vector (Fig. 1b). Every weight vector has a different combination of components, therefore the SOM estimates are based on 2220 relationships between the three training parameters. To account for strong nonlinearities in the real system it is important that the frequency

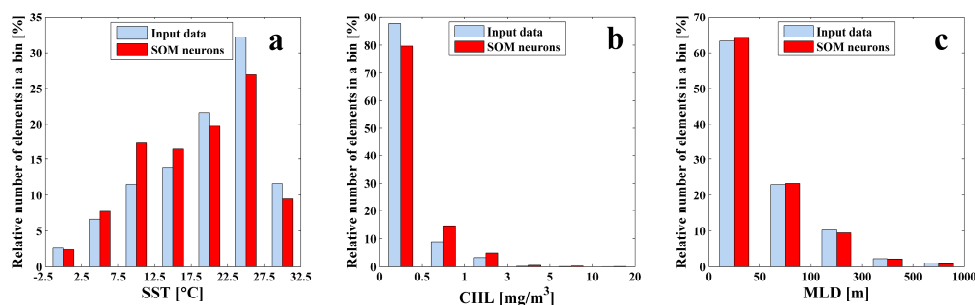


**Fig. 2.** The frequency distribution of each training parameter in the input data and the SOM neurons. Note that scales in the x-axes in (b) and (c) are not increasing monotonically.

distribution of each parameter in the input data is well represented by the SOM neurons (Fig. 2). Mean values of parameters ( $SST_{\text{SOM}}=18.1$ ,  $SST_{\text{INPUT}}=19.4$ ;  $MLD_{\text{SOM}}=63.6$ ,  $MLD_{\text{INPUT}}=66.3$ ;  $CHL_{\text{SOM}}=0.37$ ,  $CHL_{\text{INPUT}}=0.27$ ) and their ranges are also similar in the training data and SOM neurons. More importantly, neurons follow highly non-linear relationships between each pair of components in the training data set (Fig. 3a–c) visualizing how well the SOM is equipped for such a complicated setup. The distribution of neurons generally follows the training data distribution, even in such an extreme case as MLD versus SST (Fig. 3b).

## 2.4 Labelling the trained SOM with the $p\text{CO}_2$ data

In order to estimate  $p\text{CO}_2$  fields in the North Atlantic, the trained SOM neurons need to be labelled with the  $p\text{CO}_2$  values. In the labelling set, in situ  $p\text{CO}_2$  measurements are used, all accompanied by corresponding SST, MLD and CHL values (according to their time and space coordinates). For the purpose of this work, we used a subset of the North Atlantic data set compiled under auspices of CarboOcean, an EU-funded Integrated Project (<http://www.carboocean.org>). A total of 137 000  $p\text{CO}_2$  data points were collected on several vessels routinely crossing the North Atlantic between June 2004 and October 2006.

### 2.4.1 Distribution of the in situ measurements

The data in the labelling set is not evenly distributed in time and space (Fig. 4). More measurements are available in spring and summer than in fall and winter (Fig. 5) as a result of difficulties related to sampling in stormy winter waters. For the three years there are less than 3500 measurements between November and January. Few data are available for 2004: a major contribution in June, 2 days in July and 7 days in October make that year's input rather imbalanced.

Such an uneven distribution would make this data very difficult to analyse using traditional statistical techniques. Most linear methods would be biased towards summer waters, and the exceptionally high volume of data from June 2004 would create mapping discrepancies. In contrast, the

ranges of input parameters captured in the labelling data set ( $p\text{CO}_2$ , SST, MLD, CHL) are more relevant for SOM estimates than their temporal and spatial distribution. This is one of the advantages that the SOM has over the other interpolation techniques. However, the variability in the labelling data set should not be significantly smaller than that of the training set in order for the SOM to give optimal mapping results (Kohonen, 2001).

The training data set (as introduced in Sect. 2.2) offers wide ranges for all parameters, providing sufficient information about their variability as summarized in Table 1. The SST varies between  $-1.8^\circ\text{C}$  and  $30^\circ\text{C}$ , the depth of the mixed layer ranges from  $\sim 10$  m to more than 1000 m (in total, 0.15% of data has MLD values greater than 1000 m) and chlorophyll-*a* concentrations vary from 0 to  $\sim 10$   $\text{mg}/\text{m}^3$  (0.04% of data has CHL values greater than  $10$   $\text{mg}/\text{m}^3$ ). The labelling data set captures most of the variability in the training data set (Table 1). The temperature ranges are  $2.8^\circ\text{C}$  to  $8.2^\circ\text{C}$  smaller than those in the training data set. Most of this difference is due to the fact that there are few in situ measurements from ice-melting zones, where water temperature drops below  $0^\circ\text{C}$ . Those regions are negligible in terms of the area covered, and the number of below  $0^\circ\text{C}$  measurements accounts for less than 1% of the training data. Hence the lack of the lowest temperature labels in the labelling data set is unlikely to have a significant effect on the basin-wide  $p\text{CO}_2$  maps.

The mixed layer depth is well represented in the labelling data set. In winter however, the maximum mixed layer depth in the labelling set is substantially lower than that in the training set. This has two causes, firstly commercial vessels avoid storm regions and therefore measurements in deep vertical mixing areas are rare, especially in winter when the ocean is generally under-sampled (Fig. 5); secondly, the highest MLD's in the training data occur in two very specific regions (Labrador Sea and the Greenland-Norwegian Sea), where deep water formation takes place. Those two relatively small basins are not extensively sampled, and the deepest MLDs are not measured. As a result the SOM output is potentially biased towards shallower mixed layer depths in all regions

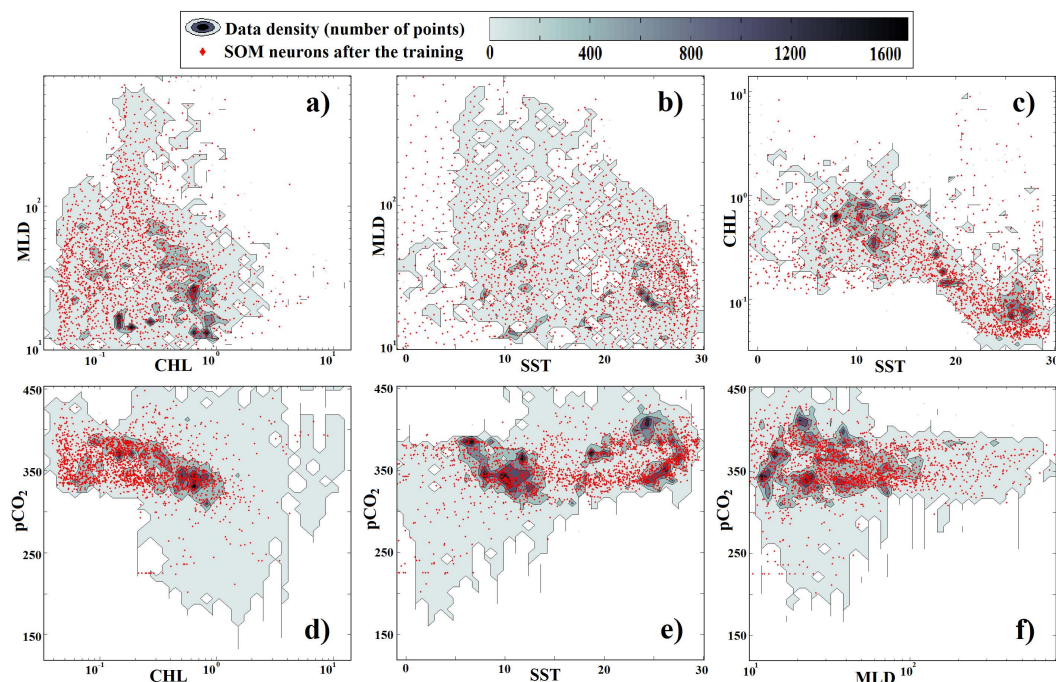


**Fig. 3.** (a–c) property – property plots for MLD, CHL and SST. The distribution of the density of the 389 000 training data points within each two-dimensional data space is shown in grey. Overlaid in red is the distribution of 2220 SOM neurons after the training. (d–f) property – property plots for  $p\text{CO}_2$  and CHL, SST and MLD. The distribution of the density of the 137 000 labelling data points within each 2-dimensional data space is shown in grey. Overlaid in red is the distribution of 2220 SOM neurons after the training.

**Table 1.** Ranges of sea surface temperature, mixed layer depth and chlorophyll- $a$  in the training (T) and labelling (L) data sets by season. Percentage of the training data within the range of the labelling data set is given for each parameter (L cover).

Season	Data	Temperature ( $^{\circ}\text{C}$ )			Mixed Layer Depth (m)			Chlorophyll $a$ ( $\text{mg}/\text{m}^3$ )		
		Min	Max	L cover(%) <sup>a</sup>	Min	Max	L cover(%) <sup>a</sup>	Min	Max	L cover(%) <sup>a</sup>
WINTER (Dec–Feb)	T	–1.80	29.2	99.7	10.0	>1000 <sup>b</sup>	98.2	0.04	>10 <sup>c</sup>	98.5
	L	0.45	28.5		17.9	571.9		0.05	2.0	
SPRING (Mar–May)	T	–1.80	29.7	97.8	10.0	>1000 <sup>b</sup>	99.2	0.02	>10 <sup>c</sup>	99.8
	L	0.17	28.9		10.0	834.5		0.03	9.6	
SUMMER (Jun–Aug)	T	–1.80	30.3	95.7	8.4	387.5	99.5	0.02	>10 <sup>c</sup>	99.6
	L	1.92	29.1		10.0	337.7		0.03	12.7	
FALL (Sep–Nov)	T	–1.80	30.7	97.9	9.0	484.9	99.6	0.02	>10 <sup>c</sup>	99.1
	L	5.85	30.1		12.0	360.4		0.04	26.8	

<sup>a</sup> Percentage of the training data within the range of the labelling data set.

<sup>b</sup> 0.15% of the training data has MLD values greater than 1000 m.

<sup>c</sup> 0.04% of the training data has CHL values greater than  $10 \text{ mg}/\text{m}^3$ .

and seasons where the actual depth of the mixed layer is greater than  $\sim 850$  m. This affects a small fraction (between 0.4% and 1.8%) of the training data as indicated in Table 1. The exponential character of the relationship between sea surface  $p\text{CO}_2$  and MLD in the subpolar North Atlantic (Olsen et al., 2008) suggests that MLDs deeper than 500 m have little influence on sea surface  $p\text{CO}_2$  (their Fig. 9a). A

similar relationship was found for the subtropical North Atlantic in our labelling data set (not shown) with a threshold value of 200 m.

The chlorophyll- $a$  concentrations in the labelling data capture most of the variability between 2004 and 2006. The seasonal maxima between  $2 \text{ mg}/\text{m}^3$  in winter and  $27 \text{ mg}/\text{m}^3$  in fall suggest that even the strongest blooms are represented.



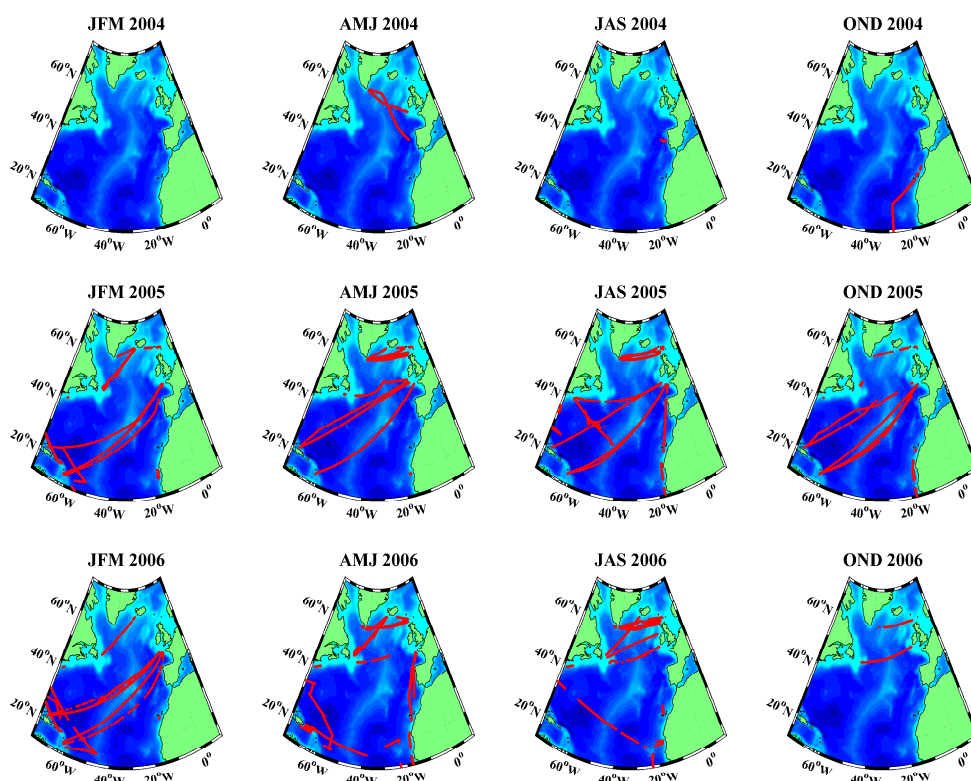


**Fig. 4.** The spatial distribution of the  $p\text{CO}_2$  measurements used in this study. Data constitute the subset of the CarboOcean dataset for 2004 through 2006. Quarterly plots show data for January to March (JFM), April to June (AMJ), July to September (JAS) and October to December (OND).

More than 99% of the training data falls within the range of the labelling data (Table 1), meaning that the SOM is labelled with a sufficient fraction of the observed variability. Additionally, chlorophyll  $a$  data in both data sets are affected by the lack of satellite coverage north of  $\sim 45^\circ\text{N}$  in December and January.

#### 2.4.2 The labelling procedure

Each data point from the labelling set is presented to the already trained SOM as an input vector (Fig. 1c). The winning neuron is found according to Eq. (2). Instead of updating the winning neuron and its neighbourhood, such input vector labels the winning neuron with its  $p\text{CO}_2$  value. Consequently each  $p\text{CO}_2$  measurement is assigned to one of the neurons. Most of the neurons are labelled more than once and the ultimate  $p\text{CO}_2$  value of the neuron is an average of all the labels it accounts for. Relationships between the in situ  $p\text{CO}_2$  measurements and each individual component (SST, MLD and CHL) of the associated vectors are strongly non-linear from the basin-wide, year-long perspective. Figure 3d–f shows how the density distribution of the SOM neurons follows the density distribution of the  $p\text{CO}_2$  data. Neurons concentrate where data density is highest and there is little data space

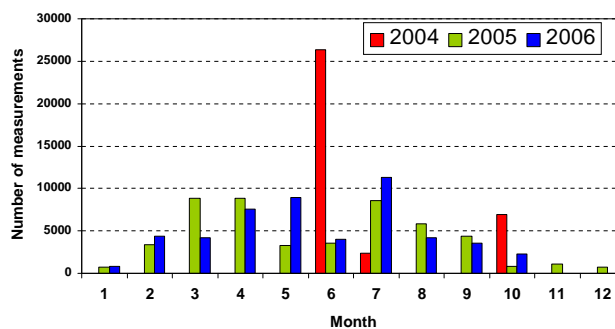


**Fig. 5.** Number of in situ  $p\text{CO}_2$  measurements in the North Atlantic used for labelling the preconditioned SOM versus month for 2004, 2005 and 2006.

(grey colour) not accounted for during the labelling (red diamonds), meaning that SOM produces a highly discriminative representation of the data. Neurons outside the data cloud mean that for a certain value of the property (x axis) the SOM will estimate a  $p\text{CO}_2$  value other than that measured (y axis). This could suggest that parameters additional to those considered in this study control the distribution of  $p\text{CO}_2$  in the North Atlantic.

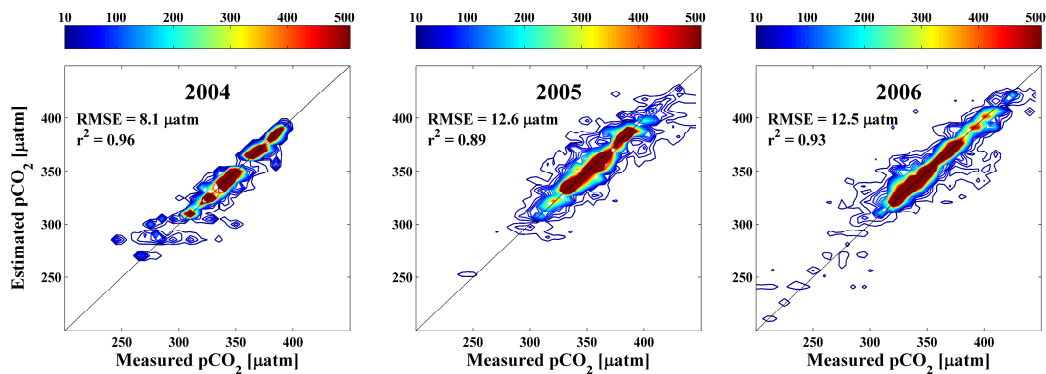


**Fig. 6.** Comparison of the SOM estimates with the measured  $p\text{CO}_2$  for 2004, 2005 and 2006 as data density contours.

## 2.5 Estimating basin-wide $p\text{CO}_2$ fields

In order to estimate the geographical distribution of  $p\text{CO}_2$  for a certain time period, the training input data are used. Each of the 389 000 input vectors has a time coordinate and two space coordinates. June 2005 has been chosen to visualize this step, and is shown in Fig. 1d. All the input vectors from June 2005 are presented to the preconditioned (trained and labelled) SOM. Each input vector is labelled with the  $p\text{CO}_2$  label of the winning-neuron. Using the space coordinates of the input vector, this  $p\text{CO}_2$  value is then associated with the appropriate pixel on the geographical map. As a final result, each pixel used as SOM input data has an estimated  $p\text{CO}_2$  value assigned to it. In this study we produce 36 monthly, basin-wide  $p\text{CO}_2$  maps between January 2004 and December 2006.

## 3 Results and discussion

### 3.1 Uncertainty estimate

For each in situ  $p\text{CO}_2$  measurement, the corresponding SOM  $p\text{CO}_2$  estimate was found based on spatial ( $1^\circ$  longitude  $\times$   $1^\circ$  latitude grid) and temporal (8 day intervals between 1 January 2004 and 31 December 2006) coordinates. The residual  $r$  value was calculated as a difference between the two. The Root mean-square error (RMSE) of the residuals calculated as:

$$\text{RMSE} = \sqrt{\frac{\sum_{i=1}^n r_i^2}{n}} \quad (4)$$

for the whole dataset ( $n$ ), provides an estimate of the uncertainty of the method in reproducing the available in situ measurements, and equals  $11.6 \mu\text{atm}$ , or 3.2% of average  $p\text{CO}_2$  in the in situ dataset.

Contour plots (one for each year) of estimated values, versus measured  $p\text{CO}_2$  are shown in Fig. 6. The RMSE varies

from  $8.1 \mu\text{atm}$  in 2004 to  $12.6 \mu\text{atm}$  in 2005 and  $12.5 \mu\text{atm}$  in 2006. The distribution of the data density in all three years indicates that no systematic bias exists in the method. The values are scattered around the identity line for which the correlation coefficient is 1.

In a recent study, Friedrich and Oschlies (2009) derived the basin-wide monthly maps of  $p\text{CO}_2$  in the North Atlantic for 2005 from modelled  $p\text{CO}_2$  distribution using the SOM approach (they call it KFM). These authors report the basin-wide RMSE of  $21.1 \mu\text{atm}$ . Such a relatively high error results mainly from the employed SOM training procedure, which is fundamentally different to that used in our study. As described in Sect. 2.3 we use three years of the whole grid data (SST, MLD and CHL) to train the SOM. This way the SOM “sees” the relationships between the training parameters in every grid point in the North Atlantic, with weekly frequency for the three years. This enables maximum SOM efficiency, regardless of the spatio-temporal cover of the in situ measurements used for labelling, and ensures that the SOM has been preconditioned with comprehensive, basin-wide training knowledge with regards to the relevant biogeochemical processes. Friedrich and Oschlies (2009) decided to train the SOM only with values (SST, CHL) collected along the VOS lines in 2005 (2005 VOS coverage metadata was used to extract the values from the model output). Such a small data set carries limited training knowledge, despite the very successful data gathering campaign in 2005. Processes occurring in the vast extent of the basin are never sampled (and therefore not included in the training), and when they are sampled, it very often happens only a few times during the year (Friedrich and Oschlies, 2009; their Fig. 2 for monthly cover and Fig. 6 for seasonal cover). It is not surprising that such trained SOM produces poor estimates for regions biogeochemically different than those sampled for the training data (their Fig. 6).

Moreover, our RMSE of  $11.6 \mu\text{atm}$  relates the SOM estimates to data points along the  $p\text{CO}_2$  sampling network (VOS lines), whereas in Friedrich and Oschlies (2009), the basin-wide  $p\text{CO}_2$  distribution in the North Atlantic is known

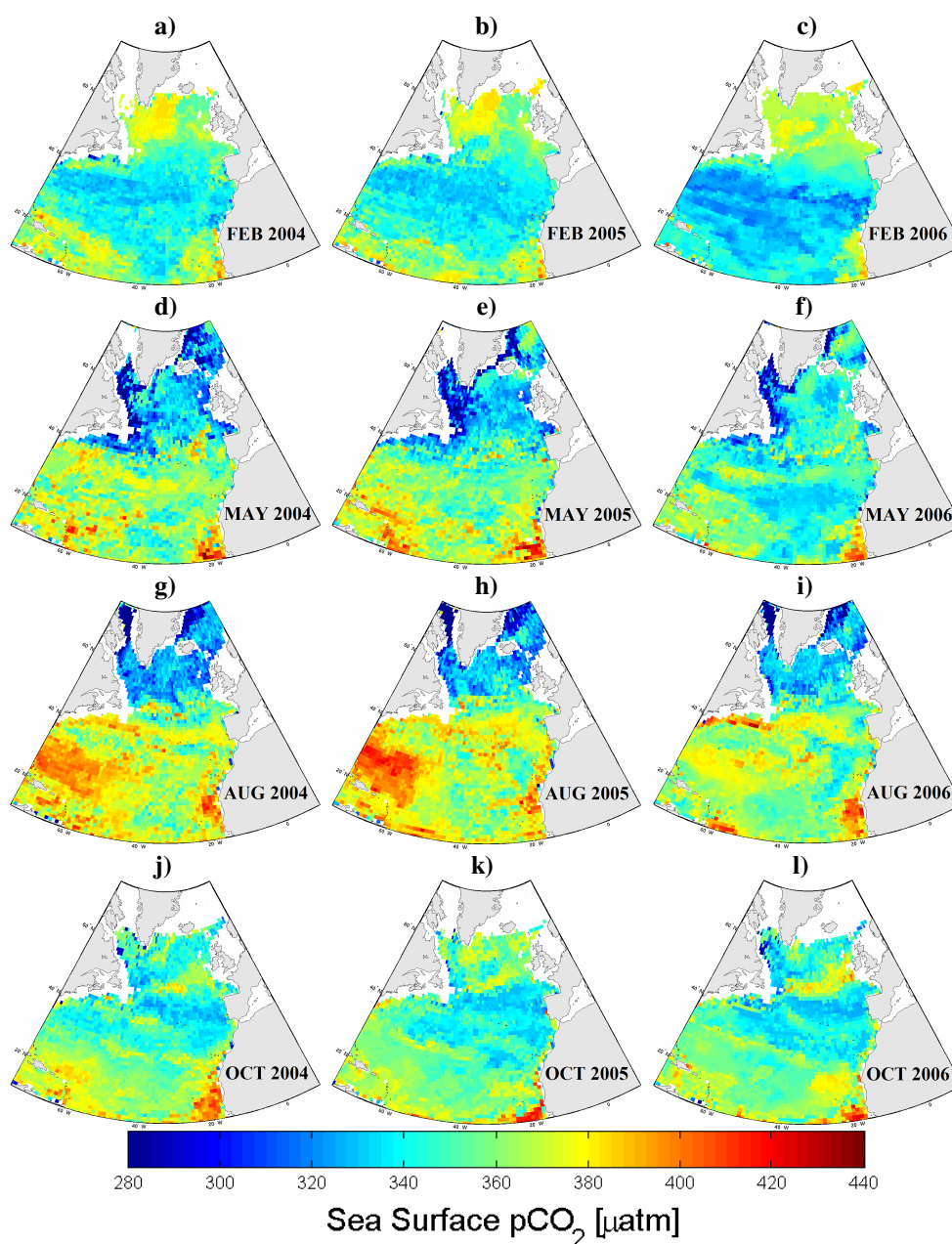


**Fig. 7.** Seasonal (in columns) and interannual (in rows) variability of the sea surface  $p\text{CO}_2$  in the North Atlantic for years 2004 to 2006.

(since it is coming from the model) and therefore, they can report a basin-wide RMSE. Their equivalent of our “along the lines” RMSE equals  $6.3 \mu\text{atm}$  from which they conclude that “along the VOS lines” RMSE is not representative of the basin-wide error (their basin-wide error is around three times higher than “along the lines” error). We suggest that the two RMSE estimates (along the VOS lines and basin-wide) are much more closely related if the training scheme employed in this study is used. The SOM, by definition, cannot reliably estimate output values for input values from outside the training data range, and this is essentially what Friedrich and

Oschlies (2009) tested. This shows that the SOM can be applied to the data in at least two very different ways and careful choice of the training procedure is crucial for successful application.

### 3.2 Monthly $p\text{CO}_2$ maps

Out of the 36 monthly  $p\text{CO}_2$  maps, one representing each season for the three years is shown in Fig. 7. In the columns are three seasonal cycles and in the rows maps for 2004, 2005 and 2006 showing SOM

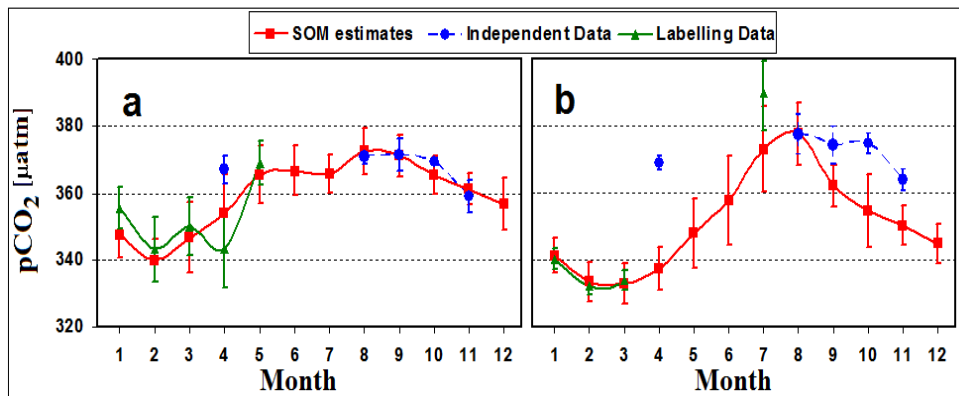


**Fig. 8.** Monthly mean  $p\text{CO}_2$  versus month in 2006 estimated by SOM for two regions where independent (not used in SOM labelling) data from *MV Santa Maria* are available. The regions are well within two biogeochemical provinces: (a) the tropical North Atlantic ( $15^\circ\text{N}$  to  $25^\circ\text{N}$  and  $50^\circ\text{W}$  to  $60^\circ\text{W}$ ) and (b) the western subtropical North Atlantic ( $26^\circ\text{N}$  to  $38^\circ\text{N}$  and  $35^\circ\text{W}$  to  $60^\circ\text{W}$ ). For comparison, monthly means of  $p\text{CO}_2$  from the labelling data in 2006 are also shown. The vertical bars extend from  $-1\sigma$  to  $+1\sigma$  of the area weighted distribution for the given region and month.

estimates of the interannual variability. For the full set of monthly maps see Supplement <http://www.biogeosciences.net/6/1405/2009/bg-6-1405-2009-supplement.pdf>.

Signatures of physical and biological medium-to-large scale processes can be identified in the basin-wide context. In the subtropical gyre ( $\sim 20\text{--}40^\circ\text{N}$ ), high  $p\text{CO}_2$  values are found during spring and summer (Fig. 7d–i), while values are around  $20\ \mu\text{atm}$  lower during fall and winter (Fig. 7a–c and j–l), confirming the mainly temperature driven variability of  $p\text{CO}_2$  in this region (Takahashi et al., 2002; Santana-Casiano et al., 2007).

In the subpolar gyre ( $\sim 40\text{--}60^\circ\text{N}$ ), massive biological  $\text{CO}_2$  drawdown (Takahashi et al., 2002) is reflected in low  $p\text{CO}_2$  levels during spring and summer (Fig. 7d–i). Mixing in the fall counteracts the effect of biological carbon uptake on  $p\text{CO}_2$ , which is visible as strong local maxima and minima in the subpolar waters with values of about  $60\ \mu\text{atm}$  apart (Fig. 7j–l). Relatively high  $p\text{CO}_2$  values in the northern part of the basin in winter (Fig. 7a–c) are attributed to wind driven deepening of the mixed layer (during storms) in fall and winter, which brings  $\text{CO}_2$ -rich waters to the surface (Corbière et al., 2007).

The lack of satellite measurements of chlorophyll-*a* during late fall and winter in the northern ( $>60^\circ\text{N}$ ) North Atlantic (Kaufman, 1989; Moulin et al., 2001) makes it impossible to estimate the  $p\text{CO}_2$  distribution in those regions using the current SOM set up (Fig. 7a–c and j–l). The phytoplankton activity during late fall and winter in the northern part of the basin is low. In order to cover the region with the “missing”  $p\text{CO}_2$  estimates, an additional SOM can be performed where only SST and MLD are used as the training data variables. The  $p\text{CO}_2$ -SST/MLD relationship is strong in regions and periods where the productivity is low (Jamet et al., 2007), therefore  $p\text{CO}_2$  estimates computed using SST/MLD trained

SOM could be used to fill the gaps in the northern North Atlantic with coherent values during fall and winter.

The influence of seasonally changing oceanographic features on the  $p\text{CO}_2$  variability in the North Atlantic can also be distinguished from the maps. Intense upwelling of cold waters along the coast off northwest Africa serves as an example. The main upwelling centre follows the seasonal cycle of the belt of northeast trade winds (Hagen, 2001), reaching its northern-most position in summer and its southern-most position in winter. The increase of  $p\text{CO}_2$  values in this region induced by this upwelling (Pelegrí et al., 2005) is recognized by high  $p\text{CO}_2$  estimates at around  $20^\circ\text{N}$  to  $25^\circ\text{N}$  in summer (Fig. 7g–i), and at around  $10^\circ\text{N}$  to  $15^\circ\text{N}$  in winter (Fig. 7a–c).

### 3.3 Seasonal cycles in the main biogeochemical provinces

In such a heterogeneous basin as the North Atlantic, a coherent interpolation method ought to accurately extract the seasonal cycle of  $p\text{CO}_2$  in its most prominent regions. We first compare SOM estimates in two regions within two biogeochemical provinces (Longhurst, 2007) to an independent in situ data set. We then compare the SOM results to climatological results in five major biogeochemical provinces of the basin.

#### 3.3.1 Comparison to an independent data set

Five months of  $p\text{CO}_2$  data collected between the UK and the Caribbean on board the *MV Santa Maria* during 2006 were not included in the labelling data set. Monthly means of this independent data for two regions are shown in Fig. 8. The data used for labelling the SOM for these regions in 2006 are

also plotted. SOM estimates are the area weighted means for the regions.

In the tropical North Atlantic ( $15^\circ\text{N}$  to  $25^\circ\text{N}$  and  $50^\circ\text{W}$  to  $60^\circ\text{W}$ , Fig. 8a), the RMSE between the SOM estimates and the independent data equals  $6.3\ \mu\text{atm}$ , which relates to RMSE of  $7.9\ \mu\text{atm}$  for all the labelling data in the region. The independent data for one month (April) of the five months falls outside the  $1\text{-}\sigma$  standard deviation of the SOM-predicted values for the region. Given that, based on Gaussian probability distribution, 68% of independent values should fall within such error bars, the SOM performs well in this direct validation exercise. Interestingly, the labelling data for April is on average  $25\ \mu\text{atm}$  lower than the independent data. Both voyages (one in the labelling data set and one in the independent data set) used for calculating averages took place between 18 and 30 April 2006, within the same  $10^\circ$  longitude by  $10^\circ$  latitude region. The tracks crossed (4 days apart) and measured  $p\text{CO}_2$  values differed by around  $20\ \mu\text{atm}$  at the crossing point. Such high spatial and temporal variability complicates comparing a small number of in situ data from a specific sampling region and period to results obtained with interpolation methods designed for a much larger area.

In the western subtropical North Atlantic ( $26^\circ\text{N}$  to  $38^\circ\text{N}$  and  $35^\circ\text{W}$  to  $60^\circ\text{W}$ , Fig. 8b), the RMSE between the SOM estimates and the independent data equals  $19.3\ \mu\text{atm}$ . The RMSE for all the labelling data in this region is also relatively high ( $14.3\ \mu\text{atm}$ ). The SOM tends to underestimate the  $p\text{CO}_2$  values with regards to the independent data in late summer and fall and also fails to reproduce high April values for the region. The sparseness of the in situ data (not shown) in the box may introduce sampling bias and may explain some of these differences. In addition, we suggest that SOM based maps should be used with caution when analyzing fine scale features and processes. Additionally, the RMSE for labelling and independent data in these regions are similar to each other. This confirms our hypothesis that the RMSE which relates the SOM estimates to data points used for labelling is representative of the basin-wide error, providing that sufficient data is available.

### 3.3.2 Comparison to the climatology

The robustness of SOM estimates is further assessed for five biogeochemical regions similar to those proposed by Longhurst (2007), as shown in Fig. 9. The subpolar North Atlantic is represented by two provinces: the first combines the western part of the sub-Arctic (SARC) and the eastern part of the Arctic (ARCT) and stretches from  $58^\circ\text{N}$  to  $66^\circ\text{N}$  and from  $10^\circ\text{W}$  to  $40^\circ\text{W}$ ; the second, the North Atlantic Drift Region (NADR) ranges from  $46^\circ\text{N}$  to  $58^\circ\text{N}$  and from  $10^\circ\text{W}$  to  $40^\circ\text{W}$ . The North Atlantic Subtropical Gyre is divided into a western [NAST(W)] part, between  $26^\circ\text{N}$  and  $38^\circ\text{N}$  and  $35^\circ\text{W}$  and  $70^\circ\text{W}$ , and an eastern [NAST(E)] part between  $26^\circ\text{N}$  and  $42^\circ\text{N}$  and  $10^\circ\text{W}$  and

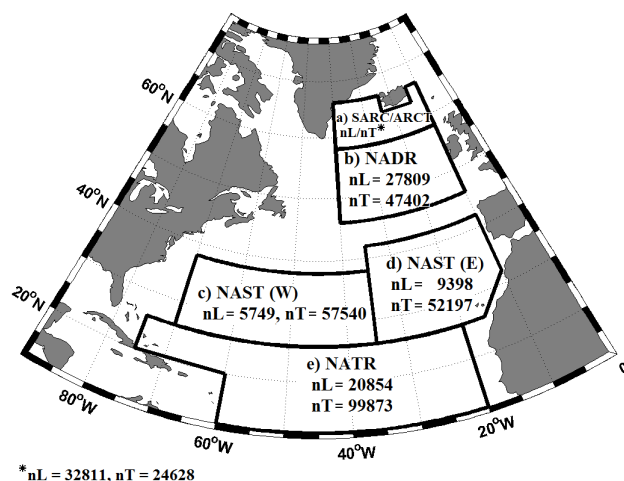


**Fig. 9.** The biogeochemical provinces of the North Atlantic proposed by Longhurst (2007) as used here for an analysis of SOM estimates. nT and nL represent the number of data points available for training and labelling of the SOM respectively.

$35^\circ\text{W}$ . The North Atlantic Tropical Gyre (NATR) stretches from  $10^\circ\text{N}$  to  $26^\circ\text{N}$  and from  $20^\circ\text{W}$  to  $60^\circ\text{W}$  (plus the region from  $20^\circ\text{N}$  to  $26^\circ\text{N}$ , between  $60^\circ\text{W}$  and  $75^\circ\text{W}$ ). For each province we show the number of data points available for training and labelling of the SOM (Fig. 9). The mid-latitude North Atlantic has the smallest number of in situ measurements, whereas the northern provinces were by far the most sampled. The RMS errors for provinces do not correspond to such sampling distributions. The RMSE for the most sampled SARCT/ARCT amounts to  $9.7\ \mu\text{atm}$ , whereas almost four times less sampled NAST(E) has an RMSE of  $7.2\ \mu\text{atm}$ . In situ measurements are not used during the training of the SOM and their spatial distribution is irrelevant to the performance of the method. The number of points in the training data depends mainly on the size of the province. The chosen data sources offer year-round coverage except for the occasional lack of chlorophyll measurements in the SARCT/ARCT region in winter.

In Fig. 10, we compare SOM estimates for a reference year 2005 (mean of the monthly SOM estimates for 2004 to 2006) in these provinces, to a climatological distribution of sea surface  $p\text{CO}_2$  constructed for a reference year 2000 based on in situ  $p\text{CO}_2$  measurements obtained from 1970 to 2006 (Takahashi et al., 2009). For comparison purposes we adjust the climatological distribution of Takahashi et al. (constructed for a reference year 2000) to a reference year 2005 assuming an annual rate of increase of  $1.8\ \mu\text{atm}$  as proposed in Takahashi et al. (2009). The original and adjusted distributions are plotted.

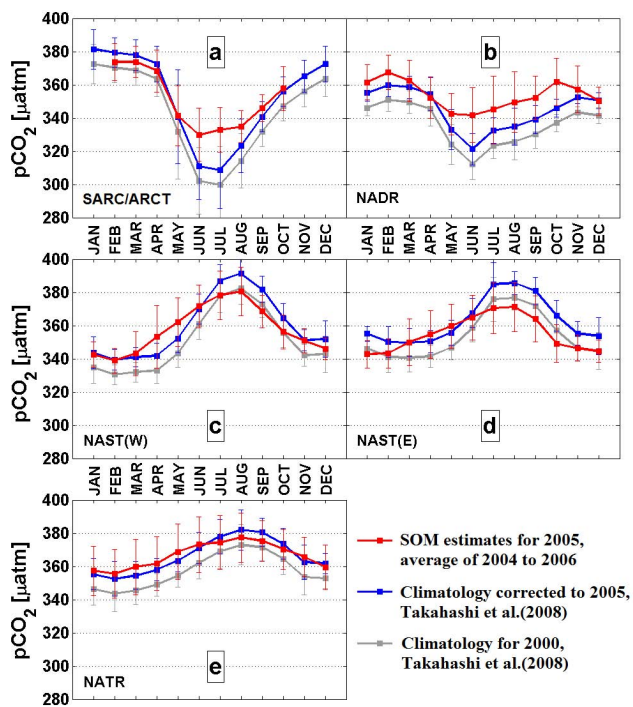


**Fig. 10.** Seasonal cycle of the sea surface  $p\text{CO}_2$  in five biogeochemical provinces of the North Atlantic. The vertical bars extend from  $-\sigma$  to  $+\sigma$  of the area weighted distribution for the given region and month.

### 3.3.3 SARC/ARCT region

In the SARC/ARCT region (Fig. 10a), the SOM estimates  $p\text{CO}_2$  values of  $330\text{--}340\ \mu\text{atm}$  during late spring and summer and of around  $370\ \mu\text{atm}$  during fall and winter. These estimates agree with earlier findings showing that the disequilibrium with the atmospheric  $p\text{CO}_2$  (not shown here) exists throughout most of the year in this region, with the  $\text{CO}_2$  air-sea flux directed into the ocean (Omar and Olsen, 2006; Olsen et al., 2008). Low summer  $p\text{CO}_2$  due to strong biological carbon uptake (Takahashi et al., 2002), and higher winter values (caused by deepening of the mixed layer supplying  $\text{CO}_2$  rich waters to the surface) dominate the seasonal cycle. The SOM estimates resolve such a pattern for the region. SOM values for the summer months are around  $20\ \mu\text{atm}$  higher than the long term climatology (Fig. 10a). However, according to Corbière et al. (2007), who analyzed data from 1993 to 2003 in the western SARC, the seasonal amplitude can be as low as  $20\ \mu\text{atm}$  and as high as around  $60\ \mu\text{atm}$ , depending on the year. A variable intensity of the phytoplankton bloom, generally occurring in June, is given as an explanation by Corbière and co-workers. They also show that, at least for the mid-nineties, the climatological distribution proposed by Takahashi et al. (2002) may overestimate the strength of the biological carbon uptake and thus underestimate the  $p\text{CO}_2$  values in summer.

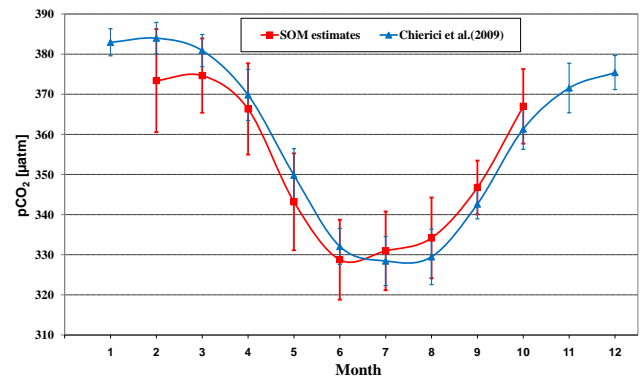


**Fig. 11.** Monthly, area weighted  $p\text{CO}_2$  fields during 2005 in the subpolar North Atlantic ( $58^\circ\text{N}$  to  $63^\circ\text{N}$ ,  $10^\circ\text{W}$  to  $40^\circ\text{W}$ ) estimated by the SOM, compared to the multiple regression estimates for 2005 in the same region after Chierici et al. (2009). Note that this region does not extend as far north as the SARC/ARCT region.

The SOM estimates for the region are consistent with those of Chierici et al. (2009) (Fig. 11). These authors estimated sea surface  $p\text{CO}_2$  for 2005 in a region with a slightly smaller latitudinal extent than our SARC/ARCT region (Fig. 11 shows SOM estimates for the region used by Chierici et al.). Using  $p\text{CO}_2$  measurements obtained on-board *MV Nuka Arctica*, together with remotely sensed data, they applied algorithms based on multiple linear regression. The in situ  $p\text{CO}_2$  measurements used by Chierici and co-workers represent a fraction of the dataset used in this study. The resulting seasonal cycle for 2005 agrees well with the SOM estimates for 2005. Neither method shows  $p\text{CO}_2$  values below  $325\ \mu\text{atm}$  during the 2005 bloom. Both methods also produce an annual amplitude in  $p\text{CO}_2$  of around  $50\ \mu\text{atm}$ . The similar results of the multiple linear regression (designed for regional, high-resolution estimates) and the SOM, increase our confidence in the basin-wide SOM estimates, despite the fact that the  $p\text{CO}_2$  data used have a large overlap.

### 3.3.4 NADR region

In the NADR (Fig. 10b), the SOM estimates a relatively weak seasonal  $p\text{CO}_2$  cycle, with an amplitude of  $26\ \mu\text{atm}$ . This is in line with results from Schuster and Watson (2007). These authors report an average annual amplitude of around  $20\ \mu\text{atm}$  in the eastern temperate region ( $35^\circ\text{N}$  to  $50^\circ\text{N}$  and  $5^\circ\text{W}$  to  $30^\circ\text{W}$ ) for years 2002 to 2005, 50% smaller than the amplitude found for years 1994 to 1995 (Fig. 3b in Schuster and Watson, 2007). This strong decrease in the amplitude over the last decade might also explain the difference in amplitude between the SOM estimates and the climatology in our region, which is shifted slightly to the northwest relative to that in Schuster and Watson (2007).

### 3.3.5 Subtropical North Atlantic

The seasonal cycle in the subtropical North Atlantic, represented here by two provinces (Fig. 10c–d), has an opposite shape to that further north. SOM  $p\text{CO}_2$  estimates in the NAST(W) are characterized by a strong summer maximum in August, which corresponds to the peak of the seasonal temperature cycle in the region (Takahashi et al., 2002; Phillips and Joyce, 2007). The annual amplitude of  $41 \mu\text{atm}$  results from generally low primary production (Bates et al., 2002) having a small counteracting effect on the thermodynamically driven variability in surface water  $p\text{CO}_2$  (Bates, 1998, 2001).

The SOM estimates for the NAST(E) have a relatively low annual amplitude mainly due to an underestimation of the summer maximum in August by  $10\text{--}15 \mu\text{atm}$ . Santana-Casiano et al. (2007) report summer maxima of  $380$  to  $400 \mu\text{atm}$  at the ESTOC station ( $29^\circ 10' \text{ N}$ ,  $15^\circ 30' \text{ W}$ ) for years 1995 to 2004. Also Schuster et al. (2009) report summer maxima of  $400$  and  $390 \mu\text{atm}$  (for years 2005 and 2006, respectively) in a  $5^\circ$  latitude  $\times$   $5^\circ$  longitude grid box centred at  $27.5^\circ \text{ N}$ ,  $17.5^\circ \text{ W}$  (Fig. 2 in Schuster et al., 2009) This is in line with the Takahashi climatology adjusted to 2005, which estimates a summer maximum of  $386 \mu\text{atm}$  (Fig. 10d). The SOM however, estimates a summer maximum of  $371 \mu\text{atm}$ .

The SOM's inability to resolve the full annual amplitude of the  $p\text{CO}_2$  cycle in NAST(E) requires further investigation. Altering the shape of the neighbourhood function during the training phase, slightly increases the ability of the SOM to better mimic the extreme  $p\text{CO}_2$  values. According to sensitivity studies on the choice of neighbourhood function in extracting the known patterns, the Gaussian neighbourhood function (used in this study) returns the smoothest SOM patterns, while the Epanechnikov (ep) neighbourhood function reproduces the most extreme values the most accurately (Liu and Weisberg, 2005; Liu et al., 2006b). However, the real benefit of using "ep" neighbourhood function in the current study, although not negligible, is relatively minor. Our simulations suggest that the monthly  $p\text{CO}_2$  values for July and August in the eastern subtropics increase by  $1\text{--}2 \mu\text{atm}$  when an "ep" neighbourhood function is used instead of the Gaussian neighbourhood function. The SOM estimates are still more than  $10 \mu\text{atm}$  lower than other reports suggest for July through September in the NAST(E), and other causes for the SOM to underestimate the highest values will be investigated. Adding sea surface salinity (SSS) as an additional variable in the training data matrix is suggested to improve SOM estimates, especially in subtropical and tropical North Atlantic (J. Boutin and N. Lefèvre, personal communication, 2008). SSS could act as a water mass tracer and a proxy for water parcel history, which would enable the SOM to account for variability in sea surface  $p\text{CO}_2$  not determined by changes in SST, MLD and CHL. Additionally, an increase in the spatial and temporal resolution of the training data to

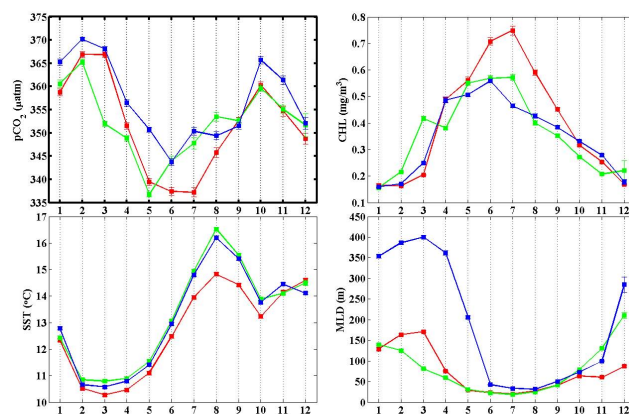


**Fig. 12.** SOM estimates of the interannual variability of  $p\text{CO}_2$  during 2004 (red), 2005 (green) and 2006 (blue) in the NADR province ( $46^\circ \text{ N}$  to  $58^\circ \text{ N}$  and  $10^\circ \text{ W}$  to  $40^\circ \text{ W}$ ) compared to the variability of SST, CHL and MLD.

reduce the effect of averaging on SOM estimates may help overcome this local "smoothing" effect of the SOM.

### 3.3.6 NATR region

In the NATR (Fig. 10e) the SOM estimates a fairly flat seasonal cycle coupled to temperature variability, which agrees well with the climatology. These warm, relatively oligotrophic waters do not support much primary production (Longhurst, 2007), and lack of strong winds reduces mixed layer deepening as a control on the variability of  $p\text{CO}_2$ . Values are relatively high throughout the year and vary between  $355$  and  $380 \mu\text{atm}$ . The West African upwelling brings  $\text{CO}_2$ -rich waters to the surface, thus increasing the sea surface  $p\text{CO}_2$  values, especially during summer.

Overall the SOM proves a robust method for reconstructing seasonal  $p\text{CO}_2$  cycles in a diverse suite of biogeochemical provinces in the North Atlantic.

### 3.4 SOM estimates and the interannual variability of the training data

Medium-to-large scale processes and features of the seasonal  $p\text{CO}_2$  cycle are modified in terms of size, strength and location, by interannual variability. The SOM's basin-wide estimates of such variability for each season are presented in Fig. 7. Visual inspection of this three-year period reveals apparent year-to-year changes. In the western subtropics August values (Fig. 7g–i), are highest for 2005. Also the region of high ( $\sim 400 \mu\text{atm}$ )  $p\text{CO}_2$  values covers a larger area than in either 2004 or 2006. Similarly, in the North Atlantic Drift Region, October  $p\text{CO}_2$  values (Fig. 7j–l) in 2006 are higher and more extensive than in the two previous years.

According to Eq. (1), the SOM predictions are entirely data-based, and therefore the interannual variability in the SOM estimates can only be forced by the interannual

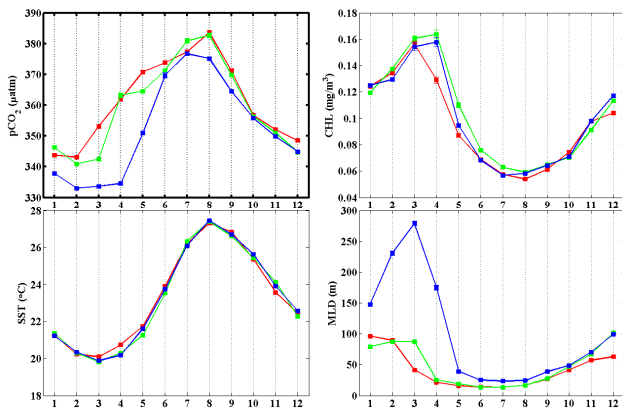


**Fig. 13.** SOM estimates of the interannual variability of  $p\text{CO}_2$  during 2004 (red), 2005 (green) and 2006 (blue) in the NAST(W) province ( $26^\circ\text{N}$  to  $38^\circ\text{N}$  and  $35^\circ\text{W}$  to  $70^\circ\text{W}$ ) compared to the variability of SST, CHL and MLD.

variability of the three training parameters: SST, CHL and MLD. Their variability affects the  $p\text{CO}_2$  distribution in a non-uniform manner, varying with the spatio-temporal dependence of  $p\text{CO}_2$  on the given parameter in each region. Figures 12 and 13 show these relationships for the NADR and NAST(W) respectively. Monthly mean values of estimated  $p\text{CO}_2$  in each province for 2004, 2005 and 2006 are represented by red, green and blue curves, respectively. Error bars represent the standard error of the mean calculated as:

$$\text{SEM} = \frac{\sigma}{\sqrt{n}} \quad (5)$$

where  $\sigma$  represents the standard deviation of the sample, and  $n$  is the sample size.

In the NADR (Fig. 12), the interannual variability of CHL controls the variability in the estimated  $p\text{CO}_2$  field during months with high mean CHL concentrations. High mean CHL values ( $0.55\text{--}0.75\text{ mg/m}^3$ ) during June–August 2004 correspond to  $p\text{CO}_2$  values which are around  $8\text{ }\mu\text{atm}$  lower than during these months in later years; also a comparatively high chlorophyll concentration in March 2005 has decreased the  $p\text{CO}_2$  by  $\sim 15\text{ }\mu\text{atm}$  in comparison to other years. The interannual  $p\text{CO}_2$  variability in the pre- and post-bloom periods appears to be controlled by variations in the MLD. However, significantly higher MLD values during January–May 2006 are not translated into similarly substantial increase in  $p\text{CO}_2$ . This may be explained by the non-linear relationship between sea surface  $p\text{CO}_2$  and MLD in the subpolar North Atlantic proposed by Olsen et al. (2008) and confirmed by our data (not shown). Olsen et al. (2008) found that MLDs deeper than 500m have no or little influence on the sea surface  $p\text{CO}_2$  (their Fig. 9a), whereas an MLD increase between 0 and 200m corresponds to a  $p\text{CO}_2$  increase of up to  $100\text{ }\mu\text{atm}$ . This relationship is influenced by the variability in SST and CHL, but the SOM estimates appear coherent

with findings by Olsen et al. It is also worth noting that the increase in the SST between May and August (almost uniform for 2005 and 2006 and  $1.5^\circ\text{C}$  lower for 2004) does not translate into a corresponding increase in estimated sea surface  $p\text{CO}_2$ . The biological  $\text{CO}_2$  drawdown dominates the thermodynamical effect on  $p\text{CO}_2$  during the bloom period (Olsen et al., 2008), and SOM estimates follow this relationship.

In the NAST(W) (Fig. 13), the estimated interannual variability in  $p\text{CO}_2$  for the years 2004 to 2006 appears to be controlled by the variations in the MLD. The seasonal  $p\text{CO}_2$  cycle in this region is controlled by the combination of SST and MLD. However, for the years 2004–2006 the interannual variability of SST is too weak to contribute to the interannual variability in  $p\text{CO}_2$ . For all three years, the MLD strongly contributes to the parameterization in winter with the mean regression coefficient of  $-0.42$ . It is, however, remarkable that the deep MLD in the winter of 2006 does not translate into a relative change of SST. Also, the lower  $p\text{CO}_2$  for the higher MLD in January–March 2006 is difficult to explain without changes in temperature (despite the negative coefficient for MLD). The non-linear relationship between the sea surface  $p\text{CO}_2$  and MLD found in the subpolar North Atlantic (Olsen et al., 2008), occurring between the deepening of MLD in fall and the beginning of the bloom in spring, is also apparent in the subtropical part of the basin. The SOM estimates resolve this relationship, which can be observed especially during late winter and early spring, when SST and CHL vary relatively little (Fig. 13). During the January–March period of 2004, the MLD was variable and shallow in the subtropics (a decrease from 96 m in January to 41 m in March), and the SOM predicts variable  $p\text{CO}_2$  as a result (an increase of  $9.3\text{ }\mu\text{atm}$ ). During February to April of 2005 the MLD was similarly shallow and variable (62m decrease), and the SOM predicts a  $12.3\text{ }\mu\text{atm}$  increase in the  $p\text{CO}_2$ . Contrary to that, much greater variability of the much deeper MLD during the February–April period of 2006 translates to  $1.5\text{ }\mu\text{atm}$  variability in the predicted  $p\text{CO}_2$ . Changes in deep MLDs result in less  $p\text{CO}_2$  variability than similar or smaller changes in the shallow MLDs.

#### 4 Summary and conclusions

A self organizing neural network has been applied to construct 36 basin-wide, monthly  $p\text{CO}_2$  maps for the North Atlantic for 2004 to 2006. Estimates of three full seasonal cycles and interannual variability between 2004 and 2006 show that the method can account for medium-to-large scale biological and physical processes. The choice of training parameters has resulted in a powerful mapping performance. The estimated seasonal  $p\text{CO}_2$  cycles in five major biogeochemical provinces mostly agree with other data analyses. The distribution of monthly sea surface  $p\text{CO}_2$  for a reference year 2005 in the northern provinces of the North Atlantic suggests



that current  $p\text{CO}_2$  values are 20 to 30  $\mu\text{atm}$  higher than the 35-year climatology (Takahashi et al., 2009) indicates. The difference is especially profound in the June–September phytoplankton bloom period. The lack of estimates in the northern part of the basin in the winter months is a disadvantage of the current SOM set-up for several applications. However, this important issue can be resolved by combining two SOM runs, one with and one without CHL as training parameter, thus covering the missing regions with no-biology predictions.

Discrepancies identified in the eastern subtropics reveal the method's tendency to "smooth" highest and lowest values. This behaviour is to some extent expected from the method which is supposed to robustly estimate basin-wide values. An introduction of basin-wide sea surface salinity field as an additional training parameter is suggested to improve SOM estimates. This will be possible following the launch of ESA's Soil Moisture and Ocean Salinity (SMOS) mission, planned between July and October 2009. However, the influence of the smoothing effect on the overall performance seems to be local and mainly related to the analyses of sub-mesoscale features. Very high spatial and temporal variability of in situ  $p\text{CO}_2$  makes the current SOM estimates too coarse for small-scale analyses and they should only be considered for analyses over larger regions.

The pioneering data-based, basin-wide estimates of the interannual  $p\text{CO}_2$  variability provide confirmation of the SOM's pattern extraction capabilities. There is no need for implementing a mathematical description of governing relationships a priori, as long as sufficient data are available. The method can be used, therefore, to examine the interannual variability in the North Atlantic over the last decade or so, during which the region has weakened as a net  $\text{CO}_2$  sink (Schuster and Watson, 2007). The estimates of the interannual variability could also add significant value to future model predictions. Current models either lack the interannual variability in  $p\text{CO}_2$  or disagree with in situ measurements. The sparse nature of in situ observations is often given as an explanation; therefore monthly basin-wide maps of  $p\text{CO}_2$  as created by the SOM could serve as a better input for models.

Additionally, our SOM maps are a very promising input for monitoring the changing ocean  $\text{CO}_2$  sink and source regions. Watson et al. (2009) use the SOM output together with geostatistical techniques to constrain the  $\text{CO}_2$  uptake by the North Atlantic. They define annual uptake to an unprecedented precision of about 10%. Our future plans include extending their effort to the northern hemisphere and ultimately to provide SOM-based global flux estimates.

As a whole, the SOM approach presented is a major improvement over historical efforts to map the  $p\text{CO}_2$  in the entire basin, eliminating the need to divide the basin into several regions in order to derive individual biogeochemical relationships. The SOM's ability to extract numerous existing

relationships simultaneously provides a good fit to the data and allows for basin-wide analysis over several years.

The continuation of large-scale in situ marine  $p\text{CO}_2$  measurements will improve our understanding of the actual spatial and temporal variability of  $p\text{CO}_2$  in the real ocean, and allow us to assess the quality of  $p\text{CO}_2$  estimates with more confidence. It is our strong recommendation that SOMs be used in conjunction with these measurements during the future oceanic  $p\text{CO}_2$  monitoring programs.

*Acknowledgements.* We thank the captains, officers and crews of the entire commercial and research fleet used during data collection for continuous technical assistance and support on board the ships. We are grateful to three reviewers and Jack J. Middelburg for their constructive and critical comments. Special thanks are for Benjamin Pfeil (Bjerknes Centre for Climate Research, Norway) for data handling and for Laurent Bopp (Laboratoire des Sciences du Climat et de l'Environnement, France) and Corinne Le Quéré (University of East Anglia, UK) for helpful comments and discussions. This work was funded by the European Commission CARBOOCEAN project GOCE 511176-2; the European Commission Marie Curie RTN Greencycles project (MRTN-CT-2004-512464); the Spanish project ICCABA CTM2005-03893/MAR; the Norwegian Research Council through A-CARB (178167) and CARBON-HEAT (185093) and the Swedish National Space Board through RESCUE – II (d.nr 62/07:1).

Edited by: J. Middelburg

## References

- Ali, M. M., Kishtawal, C. M., and Jain, S.: Predicting cyclone tracks in the North Indian Ocean: An artificial neural network approach, *Geophys. Res. Lett.*, 34, L04603, doi:10.1029/2006GL028353, 2007.
- Bates, N. R., Takahashi, T., Chipman, D. W., and Knap, H.: Variability of  $p\text{CO}_2$  on diel to seasonal timescales in the Sargasso Sea, *J. Geophys. Res.*, 103, 15567–15585, 1998.
- Bates, N. R.: Interannual variability of oceanic  $\text{CO}_2$  and biogeochemical properties in the western North Atlantic subtropical gyre, *Deep-Sea Res. Pt. II*, 48, 1507–1528, 2002.
- Bates, N. R., Pequignat, A. C., Johnson, R. J., and Gruber, N.: A short term sink for atmospheric  $\text{CO}_2$  in subtropical mode water of the North Atlantic Ocean, *Nature*, 420, 489–493, 2002.
- Canadell, J. G. Le Quéré, C., Raupach, M. R., Field, C. B., Buitenhuis, E. T., Ciais, P., Conway, T. J., Gillett, N. P., Houghton, R. A., and Marland, G.: Contributions to accelerating atmospheric  $\text{CO}_2$  growth from economic activity, carbon intensity, and efficiency of natural sinks, *P. Natl. Acad. Sci. USA*, 104(24), 10288–10293, 2007.
- Cavazos, T.: Using Self-Organizing Maps to Investigate Extreme Climate Events: An Application to the Wintertime Precipitation in the Balkans, *J. Climate*, 13, 1718–1732, 1999.
- Chierici, M., Olsen, A., Johannessen, T., Trinanes, J., and Wanninkhof, R.: Algorithms to estimate the carbon dioxide uptake in the northern North Atlantic using ship-observations, satellite and

- ocean analysis data, *Deep-Sea Res. Pt. II*, 56(8–10), 630–639, 2009.
- Cooper, D. J., Watson, A. J., and Ling, R. D.: Variation of  $p\text{CO}_2$  along a North Atlantic shipping route (UK to the Caribbean): A year of automated observations, *Mar. Chem.*, 60, 147–164, 1998.
- Corbière, A., Metzl, N., Reverdin, G., Brunet, C., and Takahashi, T.: Interannual and decadal variability of the oceanic carbon sink in the North Atlantic subpolar gyre, *Tellus*, 59B(2), 168–178, 2007.
- Dreyfus, G.: *Neural Networks: Methodology and Applications*, Springer-Verlag, Berlin Heidelberg, New York, Germany, 2005.
- Friedrich, T. and Oschlies, A.: Neural network-based estimates of North Atlantic surface  $p\text{CO}_2$  from satellite data: A methodological study, *J. Geophys. Res.*, 114, C03020, doi:10.1029/2007JC004646, 2009.
- Hagen, E.: Northwest African upwelling scenario, *Oceanol. Acta*, 24, S113–S128, 2001.
- Hewitson, B. C. and Crane, R. G.: Self-organizing maps: applications to synoptic climatology, *Climate Res.*, 22, 13–26, 2002.
- Jamet, C., Moulin, C., and Lefèvre, N.: Estimation of the oceanic  $p\text{CO}_2$  in the North Atlantic from VOS lines in situ measurements: Parameters needed to generate seasonally mean maps, *Ann. Geophys.*, 25, 2247–2257, 2007, <http://www.ann-geophys.net/25/2247/2007/>.
- Kalnay, E., Kanamitsu, M., Kistler, R., Collins, W., Deaven, D., Gandin, L., Redell, M., Saha, S., White, G., Woollen, J., Zhu, Y., Chelliah, M., Ebisuzaki, W., Higgins, W., Janowiak, J., Mo, K. C., Ropelewski, C., Leetmaa, A., Reynolds, R., and Jenne, R.: The NCEP/NCAR Reanalysis Project, *B. Am. Meteorol. Soc.*, 77, 437–471, 1996.
- Kaufman, Y. J.: The atmospheric effect on remote sensing and its correction, pages 336–428, in: *Theory and applications of optical remote sensing*, edited by: Asrar, G., 752 pp., Wiley-Interscience, 1989.
- Kohonen, T.: *Self-Organizing Maps*, Third ed., Springer-Verlag, Berlin Heidelberg New York, 501 pp., 2001.
- Lefèvre, N., Watson, A. J., Cooper, D. J., Weiss, R. F., Takahashi, T., and Sutherland, S. C.: Assessing the seasonality of the oceanic sink for  $\text{CO}_2$  in the northern hemisphere, *Global Biogeochem. Cy.*, 13(2), 273–286, 1999.
- Lefèvre, N., Watson, A. J., Olsen, A., Ríos, A. F., Pérez, F. F., and Johannessen, T.: A decrease in the sink for atmospheric  $\text{CO}_2$  in the North Atlantic, *Geophys. Res. Lett.*, 31, L07306, doi:10.1029/2003GL018957, 2004.
- Lefèvre, N., Watson, A. J., and Watson, A. R.: A comparison of multiple regression and neural network techniques for mapping in situ  $p\text{CO}_2$  data, *Tellus*, 57, 375–384, 2005.
- Liu, Y. and Weisberg, R. H.: Patterns of ocean current variability on the West Florida Shelf using self-organizing map, *J. Geophys. Res.*, 110, C06003, doi:10.1029/2004JC002786, 2005.
- Liu, Y., Weisberg, R. H., and He, R.: Sea Surface Temperature Patterns on the West Florida Shelf Using Growing Hierarchical Self-Organizing Maps, *J. Atmos. Ocean. Tech.*, 23, 325–338, 2006a.
- Liu, Y., Weisberg, R. H., and Mooers, C. N. K.: Performance evaluation of the self-organizing map for feature extraction, *J. Geophys. Res.*, 111, C05018, doi:10.1029/2005JC003117, 2006b.
- Longhurst, A. R.: *Ecological Geography of the Sea*, Second Ed., Academic, Boston, Mass., 542 pp., 2007.
- Lüger, H., Wallace, D. W. R., Körtzinger, A., and Nojiri, Y.: The  $p\text{CO}_2$  variability in the midlatitude North Atlantic Ocean during a full annual cycle, *Global Biogeochem. Cy.*, 18, GB3023, doi:10.1029/2003GB002200, 2004.
- Lüger, H., Wanninkhof, R., Wallace, D. W. R., and Körtzinger, A.:  $\text{CO}_2$  fluxes in the subtropical and subarctic North Atlantic based on measurements from a volunteer observing ship, *J. Geophys. Res.*, 111, C06024, doi:10.1029/2005JC003101, 2006.
- Moulin, C., Gordon, H. R., Chomko, R. M., Banzon, V. F., and Evans, R. H.: Atmospheric correction of ocean color imagery through thick layers of Saharan dust, *Geophys. Res. Lett.*, 28, 5–8, 2001.
- Niang, A., Thiria, S., Badran, F., and Moulin, C.: Automatic neural classification of ocean colour reflectance spectra at the top of the atmosphere with introduction of expert knowledge, *Remote Sens. Environ.*, 86, 257–271, 2003.
- Niang, A., Badran, F., Moulin, C., Crepon, M., and Thiria, S.: Retrieval of aerosol type and optical thickness over the Mediterranean from SeaWiFS images using an automatic neural classification method, *Remote Sens. Environ.*, 100, 82–94, 2006.
- Olsen, A., Bellerby, R. G. J., Johannessen, T., Omar, A. M., and Skjelvan, I.: Interannual variability of the wintertime air-sea flux of carbon dioxide in the northern North Atlantic, 1981–2001, *Deep-Sea Res. Pt. I*, 50, 1323–1338, 2003.
- Olsen, A., Triñanes, J. A., and Wanninkhof, R.: Sea-air flux of  $\text{CO}_2$  in the Caribbean Sea estimated using in situ and remote sensing data, *Remote Sens. Environ.*, 89, 309–325, 2004.
- Olsen, A., Brown, K. R., Chierici, M., Johannessen, T., and Neill, C.: Sea-surface  $\text{CO}_2$  fugacity in the subpolar North Atlantic, *Biogeosciences*, 5, 535–547, 2008, <http://www.biogeosciences.net/5/535/2008/>.
- Omar, A. M. and Olsen, A.: Reconstructing the time history of the air-sea  $\text{CO}_2$  disequilibrium and its rate of change in the eastern subpolar North Atlantic, 1972–1989, *Geophys. Res. Lett.*, 33, L04602, doi:10.1029/2005GL025425, 2006.
- Pelegri, J. L., Aristegui, J., Cana, L., Gonzalez-Davila, M., Hernandez-Guerra, A., Hernandez-Leon, S., Marrero-Diaz, A., Montero, M. F., Sangra, P., and Santana-Casiano, J. M.: Coupling between open ocean and the coastal upwelling region off northwest Africa: water circulation and offshore pumping of organic matter, *J. Marine Syst.*, 54, 3–37, 2005.
- Phillips, H. E. and Joyce, T. M.: Bermuda's tale of two time series: Hydrostation S and BATS, *J. Phys. Oceanogr.*, 37, 554–571, 2007.
- Reusch, D. B., Alley, R. B., Hewitson, B. C.: North Atlantic climate variability from a self-organizing map perspective, *J. Geophys. Res.*, 112, D02104, doi:10.1029/2006JD007460, 2007.
- Richardson, A. J., Risien, C., and Shillington, F. A.: Using self-organizing maps to identify patterns in satellite imagery, *Prog. Oceanogr.*, 59, 223–239, 2003.
- Sabine, C. L., Feely, R. A., Gruber, N., Key, R. M., Lee, K., Bullister, J. L., Wanninkhof, R., Wong, C. S., Wallace, D. W. R., Tilbrook, B., Millero, F. J., Peng, T. H., Kozyr, A., Ono, T., and Rios, A. F.: The oceanic sink for anthropogenic  $\text{CO}_2$ , *Science*, 305(5682), 367–371, 2004.
- Santana-Casiano, J. M., Gonzalez-Davila, M., Rueda, M. J., Llinas, O., and Gonzalez-Davila, E. F.: The interannual variability of oceanic  $\text{CO}_2$  parameters in the northeast Atlantic subtropical gyre at the ESTOC site, *Global Biogeochem. Cy.*, 21, GB1015, doi:10.1029/2006GB002788, 2007.
- Sarmiento, J. L. and Gruber, N.: Sinks for anthropogenic carbon,

- Phys. Today, 55, 30–36, 2002.
- Schuster, U. and Watson, A. J. W.: A variable and decreasing sink for atmospheric  $\text{CO}_2$  in the North Atlantic, *J. Geophys. Res.*, 112, C11006, doi:10.1029/2006JC003941, 2007.
- Schuster, U., Watson, A. J., Bates, N., Corbière, A., Gonzalez-Davila, M., Metzl, N., Pierrot, D., and Santana-Casiano, M.: Trends in North Atlantic sea surface  $f\text{CO}_2$  from 1990 to 2006, *Deep-Sea Res. Pt. II*, 56(8–10), 620–629, 2009.
- Takahashi, T., Feely, R. A., Weiss, R. F., Wanninkhof, R. H., Chipman, D. W., Sutherland, S. C., and Takahashi, T. T.: Global sea-air  $\text{CO}_2$  flux based on climatological surface ocean  $p\text{CO}_2$ , and seasonal biological and temperature effects, *Deep-Sea Res. Pt. II*, 49(9–10), 1601–1622, 2002.
- Takahashi, T., Sutherland, S. C., Wanninkhof, R., Sweeney, C., Feely, R. A., Chipman, D. W., Hales, B., Friederich, G., Chavez, F., Sabine, C., Watson, A. J., Bakker, D. C., Schuster, U., Metzl, N., Yoshikawa-Inoue, H., Ishii, M., Midorikawa, T., Nojiri, Y., Körtzinger, A., Steinhoff, T., Hoppema, M., Olafsson, J., Arnarson, T. S., Tilbrook, B., Johannessen, T., Olsen, A., Bellerby, R., Wong, C. S., Delille, B., Bates, N. R., and de Baar, H. J. W.: Climatological mean and decadal change in surface ocean  $p\text{CO}_2$ , and net sea-air  $\text{CO}_2$  flux over the global oceans, *Deep-Sea Res. Pt. II*, 56(8–10), 554–577, 2009.
- Vesanto, J., Himberg, J., Alhoniemi, E., and Parhankagas, J.: SOM Toolbox for Matlab 5., Libella Oy, Espoo, 59 pp., 2000.
- Watson, A. J., Schuster, U., Bakker, D. C. E., Bates, N., Corbière, A., Friedrich, T., González-Dávila, M., Hauck, J., Heinze, C., Johannessen, T., Körtzinger, A., Metzl, N., Olafsson, J., Olsen, A., Oschlies, A., Padin, X. A., Pfeil, B., Santana-Casiano, M., Steinhoff, T., Telszewski, M., Ríos, A., and Wallace, D. W. R., Wanninkhof, R.: Accurately tracking the variation in the North Atlantic sink for atmospheric  $\text{CO}_2$ , *Science*, in review, 2009.



## 6. Climatological mean and decadal change in surface ocean $p\text{CO}_2$ , and net sea-air $\text{CO}_2$ flux over the global oceans

T. Takahashi, S.C. Sutherland, R. Wanninkhof, C. Sweeney, R.A. Feely, D.W. Chipman, B. Hales, G. Friederich, F. Chavez, C. Sabine, A. Watson, D.C.E. Bakker, U. Schuster, N. Metzl, H. Yoshikawa-Inoue, M. Ishii, T. Midorikawa, Y. Nojiri, A. Körtzinger, **T. Steinhoff**, M. Hoppema, J. Olafsson, T.S. Arnarson, B. Tilbrook, T. Johannessen, A. Olsen, R. Bellerby, C.S. Wong, B. Delille, N.R. Bates, and H.J.W. de Baar (2009), *Deep-Sea Res. II*, 56, 554-577.

My contribution:

- Operating  $p\text{CO}_2$  instrument onboard M/V Falstaff and M/V Atlantic Companion.
- Processing, quality control and evaluation of  $p\text{CO}_2$  data from IFM-GEOMAR VOS line.





Contents lists available at ScienceDirect

## Deep-Sea Research II

journal homepage: [www.elsevier.com/locate/dsr2](http://www.elsevier.com/locate/dsr2)

## Climatological mean and decadal change in surface ocean pCO<sub>2</sub>, and net sea–air CO<sub>2</sub> flux over the global oceans

Taro Takahashi<sup>a,\*</sup>, Stewart C. Sutherland<sup>a</sup>, Rik Wanninkhof<sup>b</sup>, Colm Sweeney<sup>c</sup>, Richard A. Feely<sup>d</sup>, David W. Chipman<sup>e</sup>, Burke Hales<sup>f</sup>, Gernot Friederich<sup>g</sup>, Francisco Chavez<sup>g</sup>, Christopher Sabine<sup>d</sup>, Andrew Watson<sup>h</sup>, Dorothee C.E. Bakker<sup>h</sup>, Ute Schuster<sup>h</sup>, Nicolas Metzl<sup>i</sup>, Hisayuki Yoshikawa-Inoue<sup>j</sup>, Masao Ishii<sup>k</sup>, Takashi Midorikawa<sup>k</sup>, Yukihiro Nojiri<sup>l</sup>, Arne Körtzinger<sup>m</sup>, Tobias Steinhoff<sup>m</sup>, Mario Hoppema<sup>n</sup>, Jon Olafsson<sup>o</sup>, Thorarinn S. Arnarson<sup>o</sup>, Bronte Tilbrook<sup>p</sup>, Truls Johannessen<sup>q</sup>, Are Olsen<sup>q</sup>, Richard Bellerby<sup>q</sup>, C.S. Wong<sup>r</sup>, Bruno Delille<sup>s</sup>, N.R. Bates<sup>t</sup>, Hein J.W. de Baar<sup>u</sup>

<sup>a</sup> Lamont-Doherty Earth Observatory, Columbia University, 61 Route 9W, PO Box 1000, Palisades, NY 10964-8000, USA

<sup>b</sup> Atlantic Oceanographic and Meteorological Laboratory, National Oceanographic and Atmospheric Administration, Miami, FL, USA

<sup>c</sup> Earth System Research Laboratory, National Oceanographic and Atmospheric Administration, Boulder, CO, USA

<sup>d</sup> Pacific Marine Environmental Laboratory, National Oceanographic and Atmospheric Administration, Seattle, WA, USA

<sup>e</sup> 103 Reach Road, Harpswell, ME, USA

<sup>f</sup> College of Oceanic and Atmospheric Sciences, Oregon State University, Corvallis, OR, USA

<sup>g</sup> Monterey Bay Aquarium Research Institute, Moss Landing, CA, USA

<sup>h</sup> School of Environmental Sciences, University of East Anglia, Norwich, UK

<sup>i</sup> Laboratoire d'Océanographie et du Climat, LOCEAN/IPSL, CNRS, Université Pierre et Marie Curie, Paris, France

<sup>j</sup> Graduate School of Environmental Earth Science, Hokkaido University, Sapporo, Japan

<sup>k</sup> Meteorological Research Institute, Tsukuba, Japan

<sup>l</sup> National Institute for Environmental Studies, Tsukuba, Japan

<sup>m</sup> Leibniz Institute of Marine Sciences, Kiel, Germany

<sup>n</sup> Alfred Wegener Institute, Bremerhaven, Germany

<sup>o</sup> Marine Research Institute and University of Iceland, Reykjavik, Iceland

<sup>p</sup> Wealth from Oceans, CSIRO National Research Flagship, and the Antarctic Climate and Ecosystem Cooperative Research Center, Hobart, Australia

<sup>q</sup> Bjerknes Centre for Climate Research, University of Bergen, Norway

<sup>r</sup> Institute of Ocean Sciences, Fisheries and Oceans Canada, Sidney, B.C., Canada

<sup>s</sup> Université de Liege, Liege, Belgium

<sup>t</sup> Bermuda Institute of Ocean Studies, Bermuda

<sup>u</sup> Royal Netherlands Institute of Sea Research, Den Burg, The Netherlands

### ARTICLE INFO

Available online 16 December 2008

#### Keywords:

Carbon dioxide  
Partial pressure  
Surface ocean  
Global ocean  
Sea–air flux

### ABSTRACT

A climatological mean distribution for the surface water pCO<sub>2</sub> over the global oceans in non-El Niño conditions has been constructed with spatial resolution of 4° (latitude) × 5° (longitude) for a reference year 2000 based upon about 3 million measurements of surface water pCO<sub>2</sub> obtained from 1970 to 2007. The database used for this study is about 3 times larger than the 0.94 million used for our earlier paper [Takahashi et al., 2002. Global sea–air CO<sub>2</sub> flux based on climatological surface ocean pCO<sub>2</sub>, and seasonal biological and temperature effects. *Deep-Sea Res. II*, 49, 1601–1622]. A time-trend analysis using deseasonalized surface water pCO<sub>2</sub> data in portions of the North Atlantic, North and South Pacific and Southern Oceans (which cover about 27% of the global ocean areas) indicates that the surface water pCO<sub>2</sub> over these oceanic areas has increased on average at a mean rate of 1.5 μatm y<sup>-1</sup> with basin-specific rates varying between 1.2 ± 0.5 and 2.1 ± 0.4 μatm y<sup>-1</sup>. A global ocean database for a single reference year 2000 is assembled using this mean rate for correcting observations made in different years to the reference year. The observations made during El Niño periods in the equatorial Pacific and those made in coastal zones are excluded from the database.

Seasonal changes in the surface water pCO<sub>2</sub> and the sea–air pCO<sub>2</sub> difference over four climatic zones in the Atlantic, Pacific, Indian and Southern Oceans are presented. Over the Southern Ocean seasonal ice zone, the seasonality is complex. Although it cannot be thoroughly documented due to the limited extent of observations, seasonal changes in pCO<sub>2</sub> are approximated by using the data for under-ice waters during austral winter and those for the marginal ice and ice-free zones.

\* Corresponding author.

E-mail address: [taka@ldeo.columbia.edu](mailto:taka@ldeo.columbia.edu) (T. Takahashi).

The net air–sea CO<sub>2</sub> flux is estimated using the sea–air pCO<sub>2</sub> difference and the air–sea gas transfer rate that is parameterized as a function of (wind speed)<sup>2</sup> with a scaling factor of 0.26. This is estimated by inverting the bomb <sup>14</sup>C data using Ocean General Circulation models and the 1979–2005 NCEP–DOE AMIP-II Reanalysis (R-2) wind speed data. The equatorial Pacific (14°N–14°S) is the major source for atmospheric CO<sub>2</sub>, emitting about +0.48 Pg-Cy<sup>-1</sup>, and the temperate oceans between 14° and 50° in the both hemispheres are the major sink zones with an uptake flux of –0.70 Pg-Cy<sup>-1</sup> for the northern and –1.05 Pg-Cy<sup>-1</sup> for the southern zone. The high-latitude North Atlantic, including the Nordic Seas and portion of the Arctic Sea, is the most intense CO<sub>2</sub> sink area on the basis of per unit area, with a mean of –2.5 tons-Cmonth<sup>-1</sup> km<sup>-2</sup>. This is due to the combination of the low pCO<sub>2</sub> in seawater and high gas exchange rates. In the ice-free zone of the Southern Ocean (50°–62°S), the mean annual flux is small (–0.06 Pg-Cy<sup>-1</sup>) because of a cancellation of the summer uptake CO<sub>2</sub> flux with the winter release of CO<sub>2</sub> caused by deepwater upwelling. The annual mean for the contemporary net CO<sub>2</sub> uptake flux over the global oceans is estimated to be –1.6 ± 0.9 Pg-Cy<sup>-1</sup>, which includes an undersampling correction to the direct estimate of –1.4 ± 0.7 Pg-Cy<sup>-1</sup>. Taking the pre-industrial steady-state ocean source of 0.4 ± 0.2 Pg-Cy<sup>-1</sup> into account, the total ocean uptake flux including the anthropogenic CO<sub>2</sub> is estimated to be –2.0 ± 1.0 Pg-Cy<sup>-1</sup> in 2000.

© 2008 Elsevier Ltd. All rights reserved.

## 1. Introduction

Recent rapid accumulation of CO<sub>2</sub> in the atmosphere is one of the major environmental concerns because of its potential effects on the future global climate. Anticipated warming and associated environmental changes including sea-level rise would adversely affect the socio-economic stability of human society and global terrestrial–marine ecosystems. The results of various independent lines of study show that the present net global ocean CO<sub>2</sub> uptake (not including the pre-industrial steady-state flux) is 1.5–2.0 Pg-Cy<sup>-1</sup> (Pg = Peta grams = 10<sup>15</sup> g = 1 Giga ton), which corresponds to about 25% of the industrial emissions of about 7 Pg-Cy<sup>-1</sup> (Bender et al., 2005; Gloor et al., 2003; Gruber and Sarmiento, 2002; Gurney et al., 2004; Jacobson et al., 2007a,b; Keeling and Garcia, 2002; Mikaloff-Fletcher et al., 2006; Patra et al., 2005; Quay et al., 2003; Sabine et al., 2004; Sarmiento et al., 2000; Takahashi et al., 2002). Accurate assessment of the sea–air CO<sub>2</sub> flux and its time–space variability is important information for the improvement of our understanding of the global carbon cycle and the prognosis for the future atmospheric CO<sub>2</sub> concentration. In this paper, we summarize the measurements of partial pressure of CO<sub>2</sub> in surface waters made 1970–2006 by a large number of international investigators over the global oceans and present estimates for the sea–air CO<sub>2</sub> flux.

The difference between the partial pressure of CO<sub>2</sub> in seawater and that in the overlying air,  $\Delta p\text{CO}_2 = [(p\text{CO}_2)_{\text{sw}} - (p\text{CO}_2)_{\text{air}}]$ , is the thermochemical driving potential for the net transfer of CO<sub>2</sub> across the sea surface. For example, when  $(p\text{CO}_2)_{\text{air}}$  is greater than  $(p\text{CO}_2)_{\text{sw}}$ ,  $\Delta p\text{CO}_2$  is negative and atmospheric CO<sub>2</sub> is taken up by the seawater. The net CO<sub>2</sub> flux across sea surface can be estimated by multiplying the  $\Delta p\text{CO}_2$  by the CO<sub>2</sub> gas transfer coefficient, which depends primarily on the degree of turbulence near the interface. Using this principle, the first set of global surface water pCO<sub>2</sub> data, consisting of about 0.24 million pCO<sub>2</sub> measurements, was assembled and the climatological mean distributions of  $\Delta p\text{CO}_2$  and sea–air CO<sub>2</sub> flux were estimated (Takahashi et al., 1997) using the time–space interpolation method based on a 2-dimensional diffusion–advection transport equation (Takahashi et al., 1995). In the course of the following several years, the database were more than tripled in size to about 0.94 million measurements by 2002, and the second improved version that included the climatological mean monthly distribution of surface water pCO<sub>2</sub> and sea–air flux in the reference year 1995 was published (Takahashi et al., 2002). The database have since been increased by another three-fold to 3 million  $(p\text{CO}_2)_{\text{sw}}$  measurements. As a result, we have been able to obtain a more reliable estimate for interannual changes in surface water pCO<sub>2</sub>. This

paper presents the new results for the climatological mean distribution of surface water pCO<sub>2</sub> and net sea–air CO<sub>2</sub> flux over the global oceans in the reference year of 2000 representing mean non-El Niño conditions.

## 2. Measurements of surface water pCO<sub>2</sub> and database

### 2.1. Data sources and database

The database used for this study consists of about 3.0 million measurements of surface water pCO<sub>2</sub> obtained since the early 1970s. About 0.2 million measurements made in the equatorial Pacific, 10°N–10°S, during the five El Niño periods (1982–1983, 1986–1987, 1991–1994, 1997–1998, 2002–2003 and 2004–2005) and about 0.2 million made in the coastal waters (within about 200 km from the shore) are excluded from the total database of 3.4 million. The remaining 3.0 million  $(p\text{CO}_2)_{\text{sw}}$  values used for the analysis represent open-ocean environments during non-El Niño conditions. This is supplemented by an equal number of other associated data such as SST and salinity. The earlier publications that describe the data are listed in Takahashi et al. (1993, 2002), and the original data files for more recent observations are available from the authors of this paper. Since investigators processed the field observations somewhat differently, we have recomputed all the data using the procedures described below in order to produce a uniform database. The entire database including the coastal and El Niño period equatorial Pacific data (Takahashi et al., 2008) are available at the Carbon Dioxide Information and Analysis Center at the Oak Ridge National Laboratory, Oak Ridge, TN (LDEO database (NDP-088) at <http://cdiac.ornl.gov/oceans/doc.html>).

Although pCO<sub>2</sub> may be computed using TCO<sub>2</sub>, alkalinity and/or pH, it depends on the choice of dissociation constants used. Therefore, we accepted in the database only the pCO<sub>2</sub> values measured directly using the air–water equilibration method, in which two or more standard gas mixtures (not counting pure nitrogen or CO<sub>2</sub>-free air) were used for analyzer calibrations.

### 2.2. Method for measurements

The  $(p\text{CO}_2)_{\text{sw}}$  data used in this study were determined using a turbulent water–air equilibration method modified from the basic designs developed during the 1957–1959 International Geophysical Year (Takahashi, 1961; Keeling et al., 1965; Broecker and Takahashi, 1966), or of the membrane-equilibrator method (Hales et al., 2004). A volume of carrier gas is equilibrated with seawater



(closed or continuously flowing), and the concentration of CO<sub>2</sub> in the equilibrated carrier gas is measured using a CO<sub>2</sub> gas analyzer, either by infrared CO<sub>2</sub> absorption or gas chromatographic analyses. The analyzers are calibrated using two or more reference gas mixtures, of which the CO<sub>2</sub> molar mixing ratios are traceable to either the WMO standards maintained by C.D. Keeling or the reference gases certified by the Earth System Research Laboratory of NOAA. When a dried carrier gas is analyzed, the pCO<sub>2</sub> in seawater at equilibration temperature,  $T_{eq}$ , is computed using

$$(pCO_2)_{sw} = XCO_2(P_{eq} - P_w) \quad (1)$$

where  $XCO_2$  is the mole fraction of CO<sub>2</sub> in dry air;  $P_{eq}$  is the total pressure of carrier gas in the equilibration chamber; and  $P_w$  is the water vapor pressure at the temperature of equilibration,  $T_{eq}$ , and salinity. When the CO<sub>2</sub> mixing ratios in the wet carrier gas is determined,  $P_w$  is set at zero. When an equilibrator is located in an enclosed shipboard laboratory and is open to the room air,  $P_{eq}$  is the ambient pressure in the laboratory. In some data sets,  $P_{eq}$  is not reported for an equilibrator operated in an enclosed space. In such cases,  $P_{eq}$  is assumed to be the reported barometric pressure at sea surface plus 3 mb, that represents an overpressure normally maintained inside a ship. This correction increases the  $(pCO_2)_{sw}$  value by about 1  $\mu$ atm.

To correct the  $(pCO_2)_{sw}$  measured at  $T_{eq}$  to the in situ seawater temperature,  $T_{in situ}$ , a constant-chemistry temperature effect,  $(\partial \ln pCO_2 / \partial T) = 0.0433 - 8.7 \times 10^{-5}T$  ( $^{\circ}C$ ), which was determined for a North Atlantic surface water sample (Takahashi et al., 1993), is used. Eq. (2) is an integrated form of the equation above:

$$(pCO_2)_{sw} \text{ at } T_{in situ} = [(pCO_2)_{sw} \text{ at } T_{eq}] \text{Exp}\{0.0433(T_{in situ} - T_{eq}) - 4.35 \times 10^{-5}[(T_{in situ})^2 - (T_{eq})^2]\} \quad (2)$$

In our previous publication (Takahashi et al., 2002), a mean coefficient of  $0.0423 \text{ }^{\circ}C^{-1}$  (Takahashi et al., 1993) was used instead of Eq. (2). If  $(T_{in situ} - T_{eq})$  is less than 2  $^{\circ}C$ , Eq. (2) yields pCO<sub>2</sub> values virtually indistinguishable from the previous ones. Since temperature changes for continuous underway systems are commonly less than this, the corrections made using the constant coefficient do not require changes. Only those measured for discrete water samples are subject to change up to about 3  $\mu$ atm. For the reasons discussed in Section 2.3, we take the reported “bulk” water temperature as  $T_{in situ}$  to represent the sea-surface condition. The average precision of individual pCO<sub>2</sub> measurements thus obtained is estimated to be  $\pm 3 \mu$ atm at a reported “bulk” water temperature.

Since the data reported by the participating groups had been processed using different computational schemes, all the data are recomputed using Eqs. (1) and (2) in order to remove biases. In the calculation, CO<sub>2</sub> gas is treated as ideal in the range of pressures encountered in this study, and the effects of non-ideal mixing behaviors of CO<sub>2</sub> molecules in air due to CO<sub>2</sub>-H<sub>2</sub>O-N<sub>2</sub>-O<sub>2</sub> molecular interactions are neglected since they are small ( $< 1 \mu$ atm) and are inferred from correlations among the heat of mixing and other thermodynamic parameters for various molecular species (Weiss and Price, 1980).

### 2.3. Temperature of ocean water

The upper several meters of the ocean are thermally stratified depending upon heat balance and turbulence. Since pCO<sub>2</sub> in seawater depends sensitively on temperature, we need to select a  $T_{in situ}$  in Eq. (2), that is critical to the sea-air CO<sub>2</sub> gas transfer. In the skin layer regime ( $< 500 \mu$ m), where conductive and diffusive heat transfer processes are dominant, the layer is cooled due to evaporation; in the sub-skin regime ( $\sim 1$  cm to a few meters), where diffusive and viscous processes are important, the water is

warmed by short-wave solar radiation during the day time; and the bulk mixing layer (a few to several meters) is governed primarily by turbulent mixing. Donlon et al. (2002) compared the bulk water temperatures measured at a depth of 5 m concurrently with the mean skin temperature observations using a shipboard infrared radiometer during six cruises between 50 $^{\circ}$ N and 50 $^{\circ}$ S in the Atlantic and Pacific Oceans. They observed that, at wind speeds exceeding  $6 \text{ m s}^{-1}$ , the skin temperatures were cooler than the bulk water temperatures (measured at 5 m) by  $-0.17 \pm 0.07 \text{ }^{\circ}C$  for both the day- and night-time conditions. At lower wind speeds, skin temperatures of 2  $^{\circ}C$  or more warmer than bulk temperatures were observed during day-time, but not during night-time.

Sarmiento and Sundquist (1992) and Robertson and Watson (1992) proposed that, since skin layer of the oceans is a few tenths of degree cooler than the bulk water, the skin layer pCO<sub>2</sub> should be lower by as much as 1% than that at the bulk water temperature, thus increasing the air-to-sea CO<sub>2</sub> flux by as much as 30% (or 0.1–0.7 Pg-Cy<sup>-1</sup>). On the other hand, McGillis and Wanninkhof (2006) pointed out that, since molecular diffusivities for gases and salt are nearly two orders of magnitude smaller than the thermal diffusivity, the thickness of the diffusive layer for gases should be an order of magnitude smaller than that for the thermal diffusive layer. Hence, the difference between the (CO<sub>2</sub>)<sub>aq</sub> (and hence pCO<sub>2</sub>) in the skin- and sub-skin layers should be an order of magnitude smaller than that estimated on the basis of the thermal skin layer thickness. The effect of skin cooling on pCO<sub>2</sub>, therefore, should be much smaller than previously proposed. Furthermore, Zhang and Cai (2007) consider that, as a result of smaller salt diffusivity than thermal diffusivity in seawater, the skin cooling caused by evaporation may be accompanied with a much thinner salty-skin layer. Since the pCO<sub>2</sub> of seawater decreases with cooling and increases with salinity ( $\partial \ln pCO_2 / \partial \ln Sal = 0.94$ , Takahashi et al., 1993), the effect of skin cooling should be nearly cancelled by that of salty skin. Since the skin layer thickness decreases inversely proportional to wind speed (Saunders, 1967; Fairall et al., 1996), its effect on pCO<sub>2</sub> should be reduced over high wind speed areas of the oceans (such as the southern high wind belt 40–55 $^{\circ}$ S). Therefore, the effect of skin layer cooling on seawater pCO<sub>2</sub> is considered to be negligibly small.

In addition to the effect of skin layer cooling, solar heating affects the temperature of the upper few meters of tropical oceans (Fairall et al., 1996). Satellite-borne microwave measurements show that, over tropical regions under low wind speed conditions, the day-time temperatures of the upper few meters of water exceed the bulk water temperatures (those assembled by Reynolds and Smith (1994)) as much as 2.8  $^{\circ}C$  (Gentemann et al., 2003). The day-time warming would influence the net daily sea-air flux of CO<sub>2</sub> especially in tropical oceans (McNeil and Merlivat, 1996; Ward et al., 2004). On the other hand, for this study, most of the pCO<sub>2</sub> were measured during day and night continuously for a depth range of 1–7 m, and the pCO<sub>2</sub> and bulk water temperature data are averaged over a  $4^{\circ} \times 5^{\circ}$  box area without differentiating the day- and night-time measurements. Hence, the pCO<sub>2</sub> bias resulting from the day-time warming is considered minimal.

As discussed above, the pCO<sub>2</sub> that represents the interface layer with the atmosphere cannot be defined unequivocally on the basis of the measurements in our database. Nevertheless, based on the available information, we judge that the effect of thermal skin layer on pCO<sub>2</sub> is negligibly small, and that the bias due to diurnal temperature changes is minimized by the averaging of large number of day- and night-time measurements. In this study, therefore, the pCO<sub>2</sub> value measured at the “bulk” water temperature is taken as that for the sea-surface value. As the surface-layer effects should become further clarified in the future, they should be taken into consideration in order to reduce systematic errors in sea-air pCO<sub>2</sub> differences.

## 2.4. Atmospheric $p\text{CO}_2$

The atmospheric  $p\text{CO}_2$ ,  $(p\text{CO}_2)_{\text{air}}$ , in the reference year 2000 is computed using:

$$(p\text{CO}_2)_{\text{air}} = X\text{CO}_2(P_{\text{baro}} - P_{\text{sw}}) \quad (3)$$

where  $P_{\text{baro}}$  is the barometric pressure at sea surface, and  $P_{\text{sw}}$  is the water vapor pressure at the temperature and salinity for mixed layer water. The following values are used: the weekly mean  $X\text{CO}_2$  data in dry air from the [GLOBALVIEW—CO<sub>2</sub> Database \(2006\)](#); for  $P_{\text{sw}}$ , 100% humidity at SST (temperature of bulk mixed layer water) and surface water salinity from the NOAA's [Atlas of Surface Marine Data \(1994\)](#); and for  $P_{\text{baro}}$ , the climatological monthly mean barometric pressure at sea surface from the [NCEP Reanalysis data \(2001\)](#). The sea–air  $p\text{CO}_2$  difference,  $\Delta p\text{CO}_2$ , is then computed using

$$\Delta p\text{CO}_2 = [(p\text{CO}_2)_{\text{sw}} \text{ corrected to the year 2000}] - [(p\text{CO}_2)_{\text{air}} \text{ in 2000}] \quad (4)$$

Since  $\text{CO}_2$  is assumed to be an ideal gas for both  $(p\text{CO}_2)_{\text{sw}}$  and  $(p\text{CO}_2)_{\text{air}}$ , the small effects of non-ideality should cancel due to differencing for  $p\text{CO}_2$ . Positive  $\Delta p\text{CO}_2$  values indicate that the sea

is a source for atmospheric  $\text{CO}_2$ , whereas negative values indicate that the sea is a sink.

It should be noted that, while the multi-decadal climatological mean for SST, sea-surface salinity and barometric pressure are nearly steady, the atmospheric and surface ocean  $p\text{CO}_2$  have been changing over the study period due to emissions of anthropogenic  $\text{CO}_2$ . Accordingly, to obtain climatological mean distribution and mean for  $\Delta p\text{CO}_2$ ,  $(p\text{CO}_2)_{\text{sw}}$  values that were measured in different years must be corrected to a single reference year. In this paper, the year 2000 is chosen as the reference year, since it is close to the mean year for the  $p\text{CO}_2$  data. Analytical precision for a single measurement of  $\Delta p\text{CO}_2$  is estimated to be about  $\pm 4 \mu\text{atm}$ . However, since a box area often encompasses various oceanographic features (such as currents, eddies, upwelling and patchy biological activities) (e.g. [Li et al., 2005](#)), the uncertainty in mean  $\Delta p\text{CO}_2$  values is commonly dominated by  $(p\text{CO}_2)_{\text{sw}}$  variations associated with these features.

## 2.5. Distribution of measurements

We choose a  $4^\circ$  (latitude)  $\times$   $5^\circ$  (longitude) spatial resolution for this study based primarily on the time–space density of the

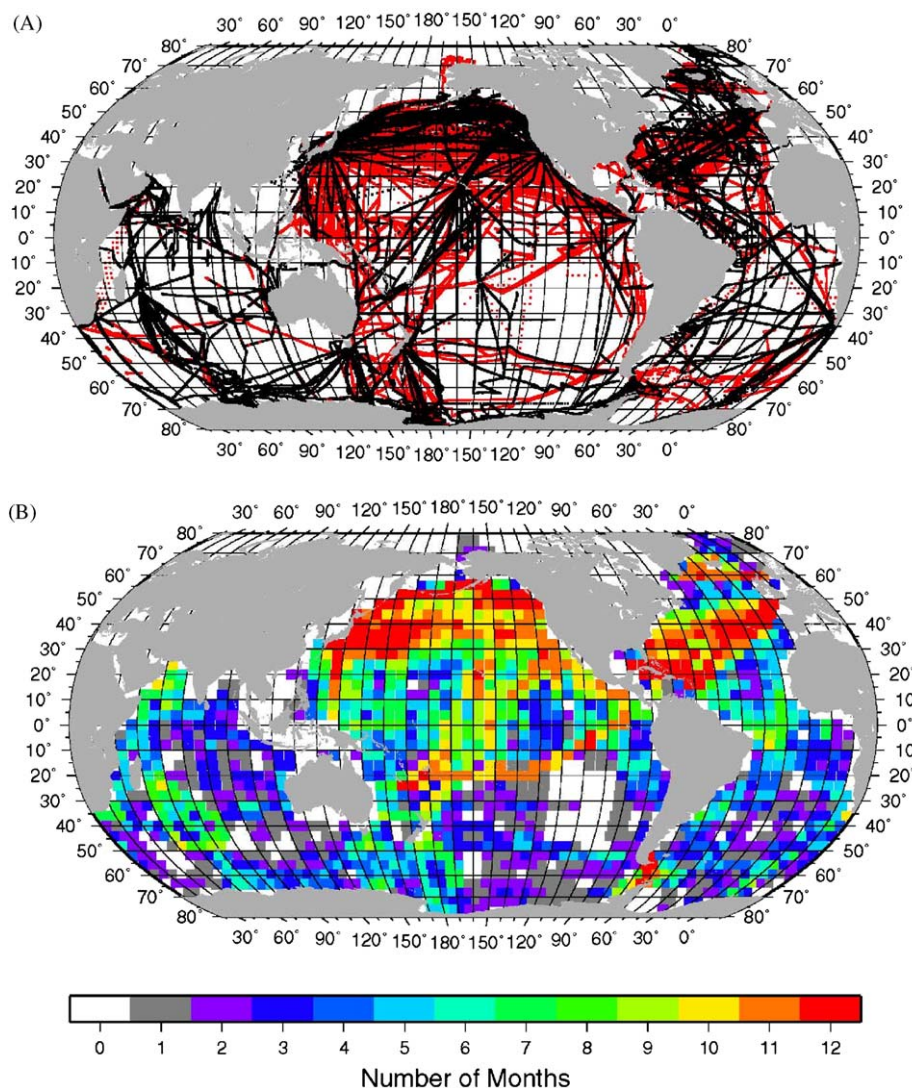


**Fig. 1.** (A) Sampling locations. The black dots indicate the measurements in the 0.94 M database used in Takahashi et al. (2002) and the red dots are new measurements added to the database (3.0 M) used in this study. (B) Number of months in each  $4^\circ \times 5^\circ$  box area where at least one surface water  $p\text{CO}_2$  measurement has been made since the early 1970s. White areas have no measurements.

observations. While smaller box areas would help to resolve narrow oceanographic features such as the Gulf Stream and equatorial currents, they would reduce the number of observations made in a box during different seasons and hence fail to define seasonal variation. Even at this box size, observations made in several years have to be combined to define seasonal variability. Multi-year composite maps summarizing the sampling locations and the number of months, in which at least one measurement was made since 1970 in each box, are shown in Figs. 1A and B. The latter map shows that, of a total of 1759 boxes, about 30% of the boxes have measurements spanning 6 or more months, and 50% of the boxes have measurements spanning 3 or less months. While most boxes in the Northern Hemisphere have observations in 6 or more months, many in the Southern Hemisphere oceans south of 20°S have data only in 3 or less months. The Drake Passage areas that are being investigated as part of the Long Term Ecosystem Research (LTER) program along the Antarctic Peninsula are the only southern high-latitude boxes that have 12-month data.

### 3. Normalization of data to a reference year

The surface water  $p\text{CO}_2$  varies seasonally and from year to year due to changes in biological and physical conditions. In addition, it changes in response to increasing atmospheric  $p\text{CO}_2$ , and over a 30-year period, it could increase as much as 45  $\mu\text{atm}$ , if seawater were equilibrated with the atmosphere. Therefore, the measurements made in different years need to be corrected to a single reference year in order to eliminate biases due to the sampling year and to obtain a climatological mean distribution. In light of the improved observations, the previous procedures used for Takahashi et al. (2002) need to be revised. In this section, the rates of  $p\text{CO}_2$  change in various areas of the global oceans will be examined first, and the new methods that are used to normalize  $p\text{CO}_2$  data to the single reference year 2000 will be presented. The differences between the  $p\text{CO}_2$  values in Takahashi et al. (2002) and this study will be discussed in Section 5.3.

#### 3.1. Method of analysis for mean rate of $p\text{CO}_2$ change in surface waters

Bates (2001) measured the carbonate chemistry parameters at the Bermuda Atlantic Time-Series Study (BATS) station (31°5'N and 64°10'W) over the 10-year period from late 1989 to early 1998. A linear regression of the deseasonalized data yielded a mean rate of  $1.4 \pm 1.1 \mu\text{atm y}^{-1}$ , which is indistinguishable from the mean atmospheric  $p\text{CO}_2$  increase rate of  $1.33 \mu\text{atm y}^{-1}$  (see Bates, 2001, Fig. 3, p. 1514). Following this method, we estimate the mean rate of change for surface water  $p\text{CO}_2$  in selected areas by linearly regressing deseasonalized mean monthly values. Because we do not have sufficient seasonal coverage in a large number of our  $4^\circ \times 5^\circ$  boxes, we expand the scale of the boxes, in some cases to  $5^\circ \times 10^\circ$ , for this analysis.

An example for the deseasonalization procedure is shown in Fig. 2 using the data from an oceanic area 20–25°S and 165–175°E in the South Pacific (hereafter called “Vanuata” zone) on the basis of islands located within this box). The box area is selected to have sufficient number of seasonal measurements, and, at the same time, to avoid geographic and oceanographic features such as the local effects of islands. Using the measurements made during 1993–1996, the seasonal changes are estimated on the basis of the monthly mean values (open circles) computed from the 4-year composite data. Values for months with no measurement (open squares) are estimated by a linear interpolation using adjacent mean monthly values. The difference between a monthly mean and the annual mean represents the correction to be applied for

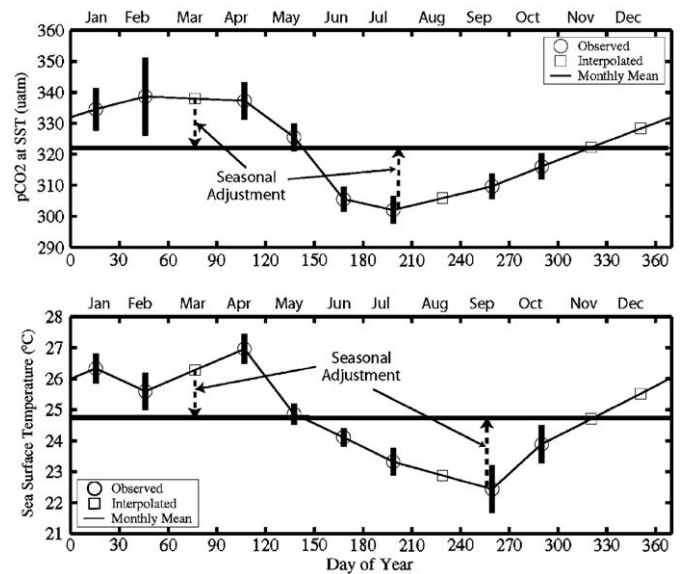


Fig. 2. Surface water  $p\text{CO}_2$  and SST data obtained in the Vanuata area, 20–25°S and 165–175°E in the South Pacific in 1993–1996. The mean seasonal variability for the 4-year period is established assuming that the seasonal variations remained unchanged over this period. The open circles are monthly mean values and the error bars represent one standard deviation of observations. The values for months with no measurements are linearly interpolated using adjacent monthly mean values, and are shown with open squares. The heavy horizontal line indicates the annual mean. The differences between the monthly mean and the annual mean indicate the seasonal corrections used for deseasonalization.

deseasonalization of the monthly mean. Assuming that the seasonal variability and hence the deseasonalization corrections remain unchanged with time, the monthly mean values obtained for years outside the 4-year period are corrected to obtain deseasonalized values.

The deseasonalized mean monthly values thus obtained are regressed linearly against time (year) to obtain the mean rate of change. Uncertainties for the rates of change are computed using

$$\pm[\sigma^2/(\sum(X_i^2) - N(X_{\text{mean}})^2)]^{1/2} \quad (5)$$

where  $\sigma^2 = [(\sum(Y_i - aX_i - b)^2)/(N - 2)]$  is the variance around the fitted equation  $Y = aX + b$ , and  $Y$  is  $(p\text{CO}_2)_{\text{sw}}$  or SST and  $X$  is year. In this study, the amplitude and phase for seasonal changes estimated for each box area are assumed to be unchanged throughout the 30-year period. The magnitude of deseasonalization corrections and hence the rate of  $p\text{CO}_2$  change are affected by interannual changes in the seasonal variability, especially when seasonal amplitudes are large as seen in the high-latitude areas (e.g., the Bering Sea, Fig. 5C). This should introduce an additional uncertainty to the mean rate of  $p\text{CO}_2$  change estimated using the procedures described above. Hence, the uncertainty computed using Eq. (5) should be considered a minimum estimate.

#### 3.2. North Atlantic Ocean

Of the  $5^\circ(\text{latitude}) \times 10^\circ(\text{longitude})$  boxes in the North Atlantic, 37 are found to have a sufficient number of seasonal  $p\text{CO}_2$  measurements over sufficiently long period to allow determination of the decadal mean rate of change. Fig. 3 shows examples for the time-trend data in the three box areas in the North Atlantic: the Irminger Sea, north of the Azores and east of Barbados. The large variability seen in higher latitude areas is attributed largely to large seasonal changes in temperature, intense biological activities and mixing as well as complex current structures such as the Arctic and warm North Atlantic Currents.

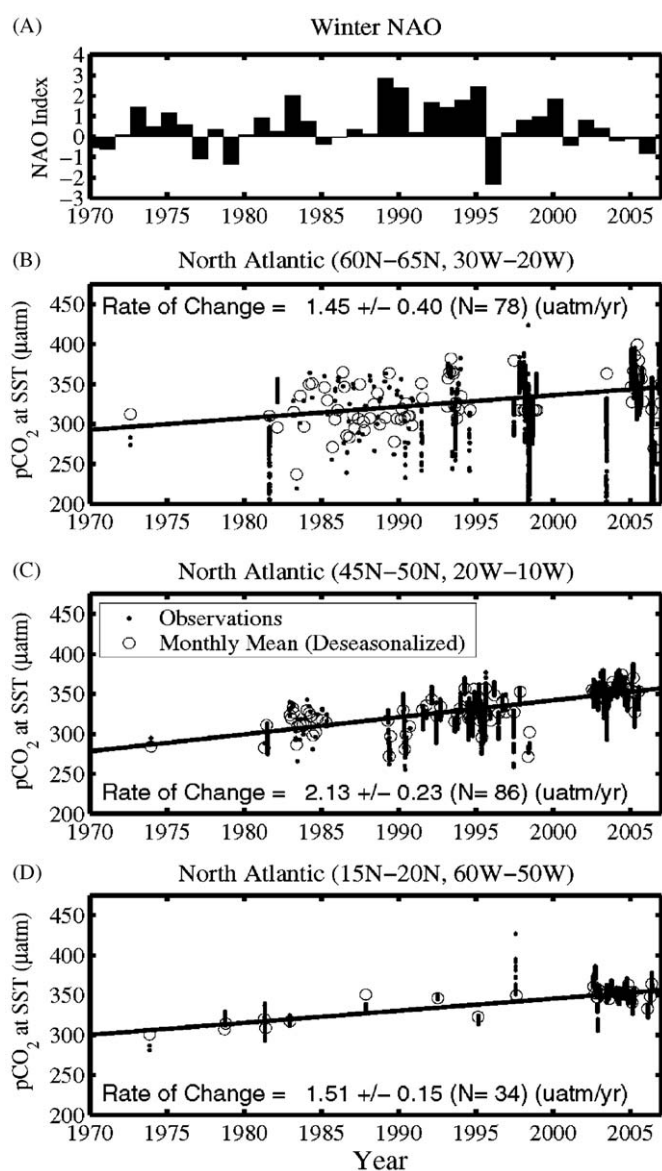


**Fig. 3.** (A) Winter-time NAO index, (B) temporal change in the surface water pCO<sub>2</sub> observed in the Irminger Sea (60–65°N; 30–20°W), (C) north of the Azores (45–50°N; 20–10°W) and (D) east of Barbados (15–20°N; 60–50°W). Black dots indicate the observed values, and the open circles indicate the deseasonalized mean monthly values. The solid line shows a linear regression, and the mean rate of change is shown in each panel. N is the number of monthly mean values used.

Because of uneven time distribution of measurements, it is not possible to detect correlation of the pCO<sub>2</sub> with the winter NAO index (Fig. 3A).

Fig. 4 shows the mean rates of increase in surface water pCO<sub>2</sub> in 37 box areas over the North Atlantic. Regional differences in the rates are not obviously discernible. The mean for the 37 box areas (weighted with the reciprocal of the estimated errors in the mean slope, Eq. (5), and by the area of each box) is  $1.8 \pm 0.4 \mu\text{atm}^{-1}$ .

The mean rates of increase in surface water pCO<sub>2</sub> thus obtained in the North Atlantic and other published values are summarized in Table 1. Observations at BATS by Bates (2001) 1989–1998 and at BATS and Station S by Gruber et al. (2002) and Bates (2007), 1983–2003, constitute the most complete data sets in the western North Atlantic, and give a decadal mean rate of pCO<sub>2</sub> increase ranging from 1.4 to 1.67  $\mu\text{atm}^{-1}$ . Lefèvre et al. (2004) reconstructed pCO<sub>2</sub> values from 1982 to 1998 on a  $1^\circ \times 1^\circ$

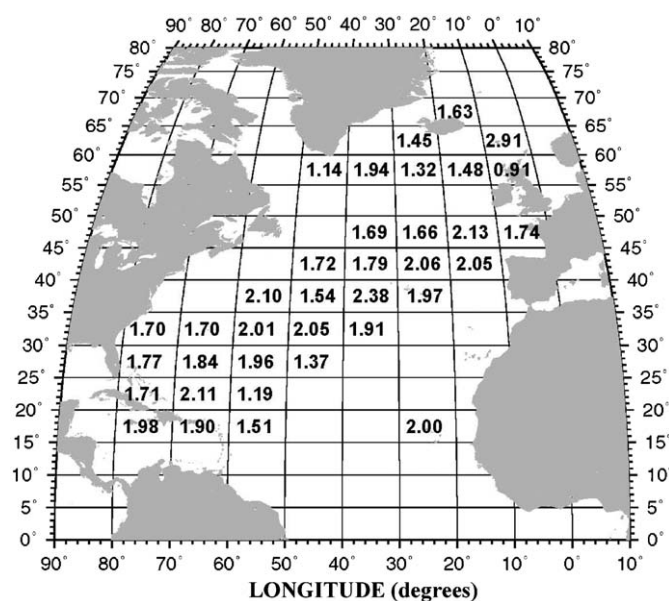


**Fig. 4.** Mean rates of increase during 1970–2007 in surface water pCO<sub>2</sub> in 5° latitude × 10° longitude box areas in the North Atlantic. The number in each box indicates the rates in  $\mu\text{atm}^{-1}$ . Uncertainties for the rates range between  $\pm 0.1$  and  $\pm 0.6 \mu\text{atm}^{-1}$  depending upon the seasonal amplitude and the length of record in each box area.

grid for each month based on the pCO<sub>2</sub> values that were first normalized to a constant temperature and then smoothed and parameterized using latitude, longitude, SST and year of observations. They obtained a mean rate of  $1.8 \mu\text{atm}^{-1}$  (uncertainty not reported in the paper) in the North Atlantic Drift area (50–58°N, 10–38°W) for the 17-year period. They also reported that the rate varied seasonally ranging from  $4 \mu\text{atm}^{-1}$  during summer, when the mixed layer was shallowest and the vertical mixing rate was minimum, to  $0 \mu\text{atm}^{-1}$  during fall, when the mixed layer deepened and deep waters were mixed into the mixed layer. Other estimates (Oudot et al., 1995; Omar et al., 2003; Olsen et al., 2006; Omar and Olsen, 2006; Corbière et al., 2007; Schuster and Watson, 2007) range from 2 to  $4 \mu\text{atm}^{-1}$ , but the sparse spatial and temporal coverage of these studies and the confounding effects of apparently seasonally-varying rates of increase makes direct comparison with this work difficult.

The results of previous studies listed in Table 1 show that the rate of increase in surface water pCO<sub>2</sub> varies geographically as well as within the time periods investigated. In contrast to the objectives of the previous studies, the aim of our analysis is to assess the basin-scale mean rate using 30+ years of observations by smoothing shorter time-scale variation. Hence, the published rates for specific areas and shorter time periods are not inconsistent with the basin-scale mean rate of increase of  $1.8 \pm 0.4 \mu\text{atm}^{-1}$  representing a mean for the three decades. This mean rate is indistinguishable from that for the atmospheric pCO<sub>2</sub> of about  $1.5 \mu\text{atm}^{-1}$  estimated for the 1972–2005 period using the GLOBALVIEW-CO<sub>2</sub> (2006).

### 3.3. North and equatorial Pacific Ocean

Takahashi et al. (2006) analyzed the surface water pCO<sub>2</sub> data obtained between 1970 and 2004 in the North Pacific, and estimated mean decadal rates of pCO<sub>2</sub> increase in 28  $10^\circ \times 10^\circ$  box areas located between 10° and 60°N. These 28 boxes were selected on the basis that the SST values measured concurrently with pCO<sub>2</sub> yielded mean rates of change consistent with those

**Table 1**  
Mean rates of increase of surface water pCO<sub>2</sub> observed in the North Atlantic Ocean.

Locations	Lat. & Long.	pCO <sub>2</sub> rates (µatm y <sup>-1</sup> )	Remarks
Barents Sea	73–80°N 20–58°E	1.4 ± 1	Difference between 1967 and 2000–2001; Omar et al. (2003)
Eastern subpolar North Atlantic	50–64°N 32–10°W	2.25 ± 0.75*	Reconstructed rate between 1972 and 1989; Omar and Olsen (2006)
E. Nordic seas	60–80°N 10°E–15°W	1.6–2.4* ± 0.4	Difference between 1981 and 2003; TA & TCO <sub>2</sub> ; Olsen et al. (2006)
NE Atlantic (Newfoundland to Iceland)	53–62°N 20–45°W	1.8 Summer* 2.8 Winter*	1993–1997 and 2001–2004; TA & TCO <sub>2</sub> ; Corbière et al. (2007)
N. Atlantic Drift	50–58°N 10–38°W	1.8 ± ?	1982–98; pCO <sub>2</sub> ; Lefèvre et al. (2004) 4 µatm y <sup>-1</sup> for May–July; 0 µatm y <sup>-1</sup> for Oct.–Nov.
N. Atlantic (UK to Caribbean)	20°N, 70°W–50°N, 5°W	4.4 ± ?	Mean difference between 1994–95 and 2002–05; pCO <sub>2</sub> ; Schuster and Watson (2007)
BATS	31°N; 64°W	2.7 ± 1.9* 1.4 ± 1.1*	1988–1998; TA & TCO <sub>2</sub> ; linear fit to all data 1988–1998; linear fit to deseasonalized data; Bates (2001)
BATS & Stn. S	31–32°N	1.5 ± 0.1* 1.67 ± 0.28*	1983–2001; TA & TCO <sub>2</sub> ; Gruber et al. (2002) 1983–2003; TA & TCO <sub>2</sub> ; Bates (2007)
Eastern Eq. Atlantic	8°N–5°S 5–35°W	2.5–2.8	Mean difference between 1982 & 1992 French FOCAL pCO <sub>2</sub> data; Oudot et al. (1995)
N. Atlantic Basin	15–70°N 0–75°W	1.8 ± 0.4	1972–2006; pCO <sub>2</sub> ; This study Mean of the rates determined in 37 5°(lat.) × 10° (long.) box areas

“TA & TCO<sub>2</sub>” and \* indicate that pCO<sub>2</sub> in seawater was computed using the total alkalinity and total CO<sub>2</sub> concentration; and “pCO<sub>2</sub>” indicates that it was measured directly.

obtained from the extensive database of Reynolds et al. (2003) for the mixed layer bulk water temperature (SST). The rates range between 0.5 and 2 µatm y<sup>-1</sup> for the open North Pacific. The lower rates (0.5–0.7 µatm y<sup>-1</sup>) that were observed in the Kuroshio Current areas could be due to the outflow from the East China Sea. Although the pCO<sub>2</sub> rates varied geographically, an open-ocean average is 1.2 ± 0.4 µatm y<sup>-1</sup>. Fig. 5 shows the time trends observed in three North Pacific box areas, which include, respectively, the Weather Station “P”, Hawaii Ocean Time Series (HOT) and the southern Bering Sea.

In contrast to the open-ocean areas, the pCO<sub>2</sub> in waters from the southern Bering Sea decreased at a mean rate of  $-1.2 \pm 1.2$  µatm y<sup>-1</sup> (mean of three 10° × 10° boxes), which is estimated using additional data acquired since Takahashi et al. (2006). This estimate (that includes zero change) is subject to a large uncertainty that is caused by large seasonal amplitudes. Nevertheless, the negative trend may be attributed to the combined effects of increased biological production (Gregg et al., 2003) and/or changes in lateral and vertical mixing. The rates of change in (pCO<sub>2</sub>)<sub>sw</sub> reported for the equatorial and North Pacific are summarized in Table 2. At the HOT site (28.8°N, 158°W), Dore et al. (2003) and Keeling et al. (2004) both reported a rate of 2.5 µatm y<sup>-1</sup> for 1988–2002, which is twice as fast as the 1974–2006 mean rate of 1.15 ± 0.17 µatm y<sup>-1</sup> shown in Fig. 5B. As already discussed in Takahashi et al. (2006), the difference may be attributed to the periods represented and sampling frequencies.

The rate of change in the equatorial Pacific belt is complicated by the El Niño events and phase shifts in the Pacific Decadal Oscillation (PDO) as discussed by Feely et al. (2002), Takahashi et al. (2003) and Feely et al. (2006), and varies between  $-0.9$  and 3.4 µatm y<sup>-1</sup> (see Table 2). The 1974–2005 mean for all the observations for the western and central equatorial Pacific is 1.3 ± 0.6 µatm y<sup>-1</sup>.

### 3.4. South Pacific Ocean

Six 5° × 10° areas located between 20° and 55°S have enough observations for the assessment of decadal change in surface

water pCO<sub>2</sub>. Fig. 6 shows the time trends observed in three representative areas in the South Pacific. Since the effects of El Niño (gray dots) are not discernible, the rates of change are computed using all data. The mean rates of change for surface water pCO<sub>2</sub> and SST for the six box areas (Table 3) give a mean rate of change of 1.5 ± 0.3 µatm y<sup>-1</sup>. The rates of change of SST estimated using the temperature data obtained concurrently with pCO<sub>2</sub> measurements are consistent with those based on the more extensive data set of Reynolds et al. (2003).

### 3.5. Subpolar Southern Ocean

The observations made in the Southern Ocean south of 50°S increased significantly not only in numbers from 0.4 M in the database used in Takahashi et al. (2002) to about 1.1 M in this database, but also in geographic coverage (Fig. 1A). On the other hand, based upon a global biogeochemical ocean general circulation model to simulate air–sea flux and sea–air pCO<sub>2</sub> differences over the Southern Ocean (south of 40°S), Lenton et al. (2006) proposed a sampling strategy. They estimated that sampling every 3 months along N–S traverses of 30° apart in longitude and at every 3° in latitude is necessary for obtaining the annual CO<sub>2</sub> uptake flux within ± 0.1 Pg-Cy<sup>-1</sup> (or the mean annual sea–air pCO<sub>2</sub> difference of about ± 2 µatm). As seen in Figs. 1A and B, our N–S traverses with more than 5 months of observations are clustered over five belts over the Southern Ocean and are on the average about 70° apart, which is farther apart than twice the desired intervals of 30°. However, our N–S sampling density appears to be sufficient. Therefore, the climatological mean values reported for the Southern Ocean are subject of errors from this level of undersampling.

Because of the strong zonal structure of the subpolar waters of the Southern Ocean, the surface water pCO<sub>2</sub> data in ice-free areas are examined for decadal changes according to the zonal distribution of SST. In this region the surface water pCO<sub>2</sub> undergoes large seasonal changes (~60 µatm) (Metzl et al., 1995, 1999, 2006) due to deep mixing in winter and photosynthesis in summer (Bakker et al., 1997; Hales and Takahashi, 2004). To minimize the large time–space variability caused by the

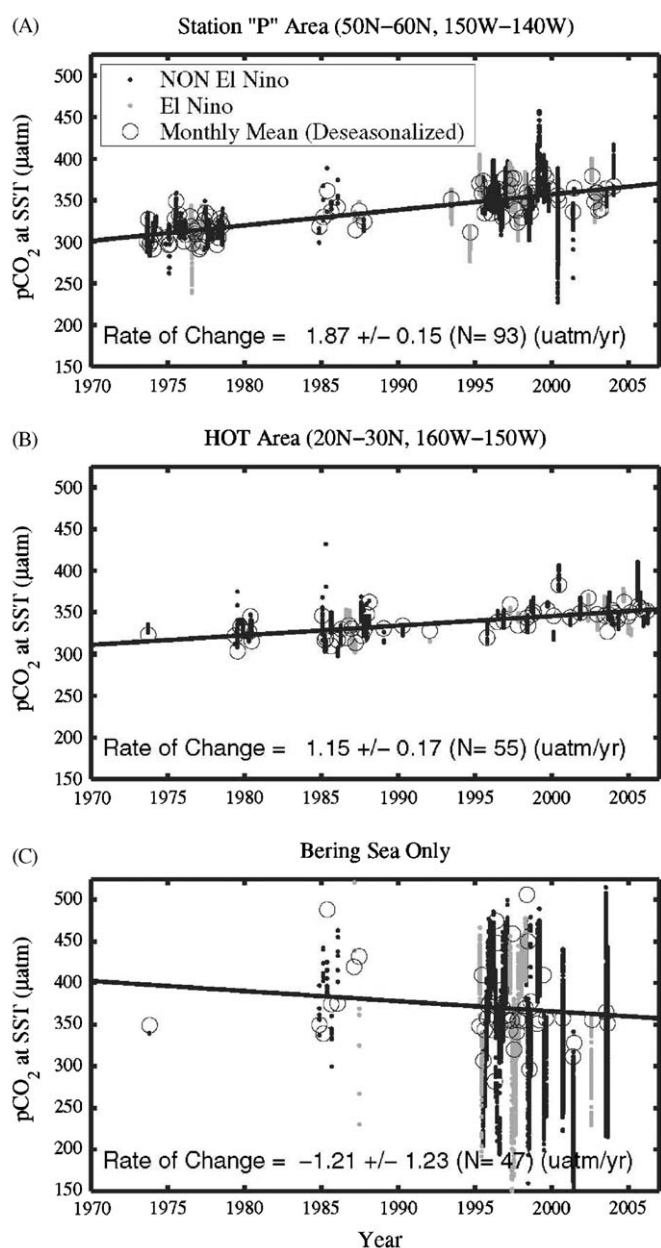


**Fig. 5.** Temporal change in the surface water  $p\text{CO}_2$  (A) in the Station "P" area, (B) HOT area and (C) southern Bering Sea. These plots have been updated using the data obtained since Takahashi et al. (2006). Black dots indicate the observed values during non-El Niño periods, and gray dots those during El Niño periods. Open circles indicate the deseasonalized mean monthly values, and the solid line shows a linear regression computed using the mean monthly values. The mean rate of change is shown at the bottom of each panel.  $N$  is the number of monthly mean values used. The El Niño values are indistinguishable from the non-El Niño values.

photosynthetic drawdown of  $p\text{CO}_2$ , only the data obtained south of  $50^\circ\text{S}$  during the austral winter months (days of year from 172 to 326 between the two solstices) are analyzed in order to detect decadal change in the surface water  $p\text{CO}_2$ . The austral winter observations span the 20-year period from 1986 to 2006, and are from all around the continent (see Fig. 1A), although they are more frequent in the Kerguelen, Drake Passage and New Zealand-Ross Sea areas. The data are binned into six  $1^\circ\text{C}$ -wide circumpolar SST zones ranging from  $0.8$  to  $6.5^\circ\text{C}$ , and the mean rate of  $p\text{CO}_2$  change in each zone is computed by linearly regressing monthly mean values (Fig. 7 and Table 4). Since all data used were observed in the winter months in various years, deseasonalization

corrections are not necessary. The data in three of the six SST zones are shown in Fig. 7. Although variability in ocean circulations and ice fields in the Southern Ocean are related to the El Niño/Southern Oscillation (ENSO) (e.g., Simmonds and Jacka, 1995; Yuan and Martinson, 2000), no discernible differences in ocean  $p\text{CO}_2$  are observed for El Niño periods. An overall mean rate for the circumpolar sub-Antarctic surface waters is estimated to be  $2.1 \pm 0.6 \mu\text{atm y}^{-1}$ . Three zones with temperatures between  $1.5$  and  $4.5^\circ\text{C}$ , which straddle the Antarctic Convergence Zone, tend to have higher rates than the atmospheric increase rate of  $1.5 \mu\text{atm y}^{-1}$ . We speculate that these high values may reflect an increase in vertical mixing rates of high- $\text{CO}_2$  subsurface waters.

### 3.6. Seasonal ice zone around Antarctica

An increasing number of  $p\text{CO}_2$  observations have become available as a result of improved ice-field capabilities of research icebreakers. Twelve thousand observations made in ice-field waters ( $\text{SST} \leq -1.75^\circ\text{C}$ ) south of about  $60^\circ\text{S}$  within seasonal ice fields during the austral winter months (June–September in various years) are summarized in Fig. 8, and show a steady increase from about  $340 \mu\text{atm}$  in early June to about  $410 \mu\text{atm}$  in the end of September, far exceeding the atmospheric  $p\text{CO}_2$  of about  $357 \mu\text{atm}$ . A similar trend has been observed during the winter months of 1993–1995 at the Prydz Bay station ( $68^\circ34'\text{S}$ ,  $78^\circ55'\text{E}$ ) by Gibson and Trull (1999), although their  $p\text{CO}_2$  values were systematically lower than ours by about  $50 \mu\text{atm}$ . The difference may reflect the waters at their location, and/or may be attributed to their  $p\text{CO}_2$  values that were calculated using  $\text{TCO}_2$  and pH measurements.

These data in Fig. 8 represent the under-ice waters, which may be exposed to the air and exchange  $\text{CO}_2$  through polynyas, leads and cracks in the ice fields. The increasing  $p\text{CO}_2$  suggests that, as the winter season progresses, the water chemistry is increasingly affected by mixing with deeper waters and/or respiration within the under-ice mixed layer. This is consistent with the low oxygen concentrations observed in the ice-field waters of the Weddell Sea (Gordon et al., 1984), the Prydz Bay (Gibson and Trull, 1999) and the Ross Sea (Sweeney, 2003). Brine rejection during ice formation may also contribute some high  $\text{CO}_2$  waters (Nomura et al., 2006). Therefore, the seasonal ice fields surrounding Antarctica are considered to be a potential source for atmospheric  $\text{CO}_2$  as indicated by positive  $\Delta p\text{CO}_2$  observed by Bakker et al. (1997), Bakker et al. (2008) and Bellerby et al., (2004) in the Weddell gyre and by Rubin et al. (1998) in the Amundsen–Bellingshausen Seas shortly after the retreat of the ice. In contrast, Stoll et al. (1999) observed that the ice-field waters in the Weddell Sea had negative  $\Delta p\text{CO}_2$  ( $30 \mu\text{atm}$  below the atmospheric) in early winter of April–May 1996, and proposed that the Weddell Sea could be a significant  $\text{CO}_2$  sink throughout the winter. The observations presented in Fig. 8 (i. e.  $p\text{CO}_2 > 360 \mu\text{atm}$  after June) as well as the work cited above do not support their extrapolation of the early winter observations into the peak winter months. We speculate that the observations of Stoll et al. (1999) may represent a remnant of the low  $p\text{CO}_2$  water formed during earlier seasons (Sweeney et al., 2000; Sweeney, 2003; Hales and Takahashi, 2004; Metzler et al., 2006).

The data shown in Fig. 8, however, include observations made only along several N–S transects ( $65 \pm 5^\circ\text{W}$ ,  $170 \pm 10^\circ\text{W}$ ,  $20 \pm 10^\circ\text{E}$ ,  $90 \pm 30^\circ\text{E}$  and  $120 \pm 20^\circ\text{E}$ ) over a 10-year period, and, by no means reflect the time–space variability of  $p\text{CO}_2$  in ice-field waters occurred during the decade. Nevertheless, because of the limited observations, we assume that the observed relationship applies universally for the ice-field waters around the continent, and estimate the  $p\text{CO}_2$  in ice-field waters as a function of time of year

**Table 2**  
Mean rates of change in surface water pCO<sub>2</sub> in the North and Equatorial Pacific.

Oceans	Locations (μatm y <sup>-1</sup> )	Rates	Remarks & References
S. Bering & Okhotsk Seas	Subarctic marginal seas	-1.1 ± 0.6	1974–2002 mean of four 10° × 10° boxes; Takahashi et al. (2006)
S. Bering Sea	Bering Sea south of 58°N	-1.2 ± 1.2	1974–2004 mean of three 10° × 10° boxes; This study
N. Pacific Basin	Open N. Pacific	1.2 ± 0.5	1970–2004 mean of 28 10° × 10° boxes; Takahashi et al. (2006)
	North of 10°N		
Western	7–33°N	1.2 ± 0.9	1984–1993; Inoue et al. (1995)
North Pacific	137°E	1.6 ± 0.2	1983–2003; Midorikawa et al. (2005)
N. Central Pacific	28.8°N, 158°W	2.5 ± 0.3*	1989–2001; Dore et al. (2003)
HOT Time Series		2.5 ± 0.1*	1988–2002; Keeling et al. (2004)
Central Eq. Pacific	5°N–5°S	-0.9 ± 1.3	1979–1990, non-El Niño periods
Nino 3.4 area	120–170°W	1.3 ± 0.9	1990–2001, non-El Niño periods; the 1990 change may reflect a phase shift in Pacific Decadal Oscillation; Takahashi et al. (2003)
		1.7 ± 1.4	1985–1998, El Niño periods; Takahashi et al. (2003)
Central Eq. Pacific	5°N–5°S	1.1 ± 0.3	1974–2005; non-El Niño periods;
Nino 3.4 area	120–170°W	2.5 ± 0.9	1974–2005; El Niño periods; Feely et al., (2006)
Western Eq. Pacific	5°N–5°S	0.5 ± 0.3	1980–1990; non-El Niño periods;
Warm Water Pool	180°W–175°E	3.4 ± 0.4	1990–2001, non-El Niño periods; Takahashi et al. (2003)
Western Eq. Pacific	5°N–5°S	2.2 ± 0.3	1981–2005; non-El Niño periods;
Warm Water Pool	180°W–175°E	0.9 ± 0.4	1983–2003; El-Niño periods; Feely et al. (2006)
Eq. Pacific	10°N–5°S	2.0 ± 0.2	1990–2003; El Niño included;
Divergence Zone	95°W–150°E		S ≥ 34.8; Ishii et al. (2004)
Western Eq. Pacific	10°N–5°S	1.2 ± 0.1	1990–2003; El Niño included;
Warm Water Pool	160°W–135°E		S < 34.8; Ishii et al. (2004)

The rates with \* are estimated using the total alkalinity and TCO<sub>2</sub> data, and all other are based on direct measurements of pCO<sub>2</sub> in seawater. Uncertainties are defined by Eq. (5) in Section 3.1.

regardless of location, when observations are not available. Obviously, this approximation needs to be improved in the future as more observations are accumulated.

### 3.7. South Atlantic and Indian Oceans

As shown in Fig. 1, not enough pCO<sub>2</sub> measurements are available in the South Atlantic and Indian Oceans for estimating the multi-decadal mean rates.

### 3.8. Global summary

On the basis of the surface water pCO<sub>2</sub> data measured during the past three decades, the mean rate of increase in about 27% of the global ocean areas is estimated to be in a range of 1.26 (±0.55) to 2.13 (±0.64) μatm y<sup>-1</sup> (Table 5). Because of insufficient sampling, the rate for the Indian and South Atlantic Oceans as well as for large areas of the South Pacific cannot be assessed satisfactorily as yet. The mean rate for the North Atlantic (1.80 ± 0.37 μatm y<sup>-1</sup>) appears to be somewhat higher than that for the North Pacific (1.28 ± 0.46 μatm y<sup>-1</sup>), although they overlap within respective standard deviations. On the other hand, since the rate of change depends not only on the air–sea CO<sub>2</sub> flux but also on the lateral and vertical transport of waters, regional differences in the rate are expected. On the basis of the available database, the difference between these two ocean basins cannot be firmly established.

The area-weighted mean for the rates for the 78 box areas (27% of the ocean area including the Southern Ocean) determined in this study is 1.69 ± 0.51 μatm y<sup>-1</sup>, and that for 72 box areas (17% of the ocean area excluding the Southern Ocean) is 1.45 ± 0.47 μatm y<sup>-1</sup> (Table 5). These two mean values are given since the rate for the Southern Ocean represents only for the winter months, whereas the rates for other ocean basins are for all seasons. In addition, as a result of various degrees of undersampling in time and space, including the assumed time-independent seasonal variability in each box area, the uncertainties for mean rates of surface water pCO<sub>2</sub> change are

minimum estimates. Furthermore, the rates for the remaining 73% of the ocean areas are not available. Therefore, a global ocean mean rate of increase is taken to be 1.5 μatm y<sup>-1</sup>, the mean of these two mean values. This rate is used throughout this study to normalize the pCO<sub>2</sub> data to a reference year 2000, with the exception of the Bering Sea where the observed rate of -1.2 μatm y<sup>-1</sup> is used. In Section 6.3, the sensitivity of the sea–air CO<sub>2</sub> flux to various pCO<sub>2</sub> increase rate will be discussed. However, until the rates of pCO<sub>2</sub> increase in regional scales are more firmly established in the future, use of regionally specific increase rates is not justified.

The mean annual rate of atmospheric CO<sub>2</sub> increase fluctuated between about 0.8 and 2.9 μatm y<sup>-1</sup> (or ppm y<sup>-1</sup>) in 1970–2006, whereas the corresponding annual changes for surface water pCO<sub>2</sub> cannot be computed reliably due to its large seasonal variation and small annual increases (Figs. 3, 5 and 6). Because of the differences between processes and time-scales regulating the atmospheric and oceanic pCO<sub>2</sub>, the individual annual rates cannot be compared. On the three-decade average, however, the rate of oceanic pCO<sub>2</sub> increase, appears to be similar to that for the atmospheric pCO<sub>2</sub> increase. This suggests that the sea–air CO<sub>2</sub> exchange is a dominant process for regulating the surface water CO<sub>2</sub>.

## 4. Method for time–space interpolation

Using the procedures explained in Section 3, all observations are corrected to the single reference year 2000. For the interpolation scheme used for this study, the pCO<sub>2</sub> values must be binned into 642,000 space–time pixels that represent a 4° × 5° computational grid for each day in the single reference year (= 1759 box areas × 365 days). In the northern and equatorial ocean areas north of 12°S, there are observations in many of these pixels (Fig. 1), and hence the daily mean value in each pixel is used. On the other hand, fewer observations are available in the Southern Hemisphere, and many pixels have no data. Since this makes our interpolation solutions unstable for the areas south of 12°S, available observations were propagated to neighboring pixels

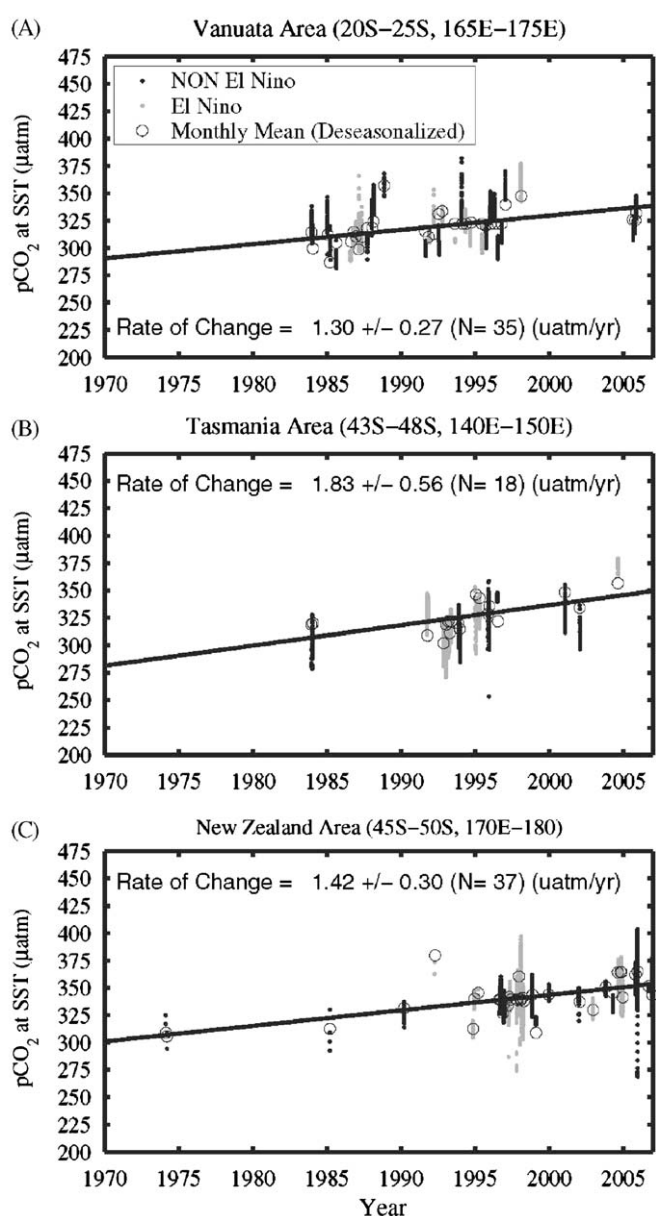


**Fig. 6.** Rates of increase in surface water  $p\text{CO}_2$  in three areas in the temperate South Pacific: (A) Vanuata area, (B) Tasmania area and (C) New Zealand area. Solid dots (black for non-El Niño periods and gray for El Niño periods) indicate individual measurements, and open circles are the deseasonalized monthly mean values. The effects of El Niño events are not discernible. The mean annual rate of change is computed using a linear regression for the deseasonalized mean monthly values.

with no observations by including the values in neighboring areas for  $\pm 4^\circ$  latitude,  $\pm 5^\circ$  longitude and  $\pm 1$  day from the center of a pixel. The mean is computed by weighting a measured value inversely proportional to its time-space distance from the pixel center. This procedure is equivalent of increasing the size of pixels to four neighboring pixels over 3 days (past, present and future by 1 day). After the above procedures are applied, about 50% of the space–time pixels over the global oceans have measured values.

To estimate  $p\text{CO}_2$  values in the boxes without observations, an interpolation equation based on 2-D diffusion–advection transport equation for surface waters is used:

$$dS/dt = K\nabla^2 S - (\partial S/\partial x V_x + \partial S/\partial y V_y) \quad (6)$$

where  $\nabla^2 S = \partial^2 S/\partial x^2 + \partial^2 S/\partial y^2$ .

$S$  is a scalar quantity,  $K$  is lateral eddy diffusivity set at a canonical value of  $2000 \text{ m}^2/\text{s}$  for surface waters (Thiele et al., 1986), and  $V_x$  and  $V_y$  are monthly mean advective velocities for surface waters. For the advective flow field, the monthly mean of Toggweiler et al. (1989) is used. This equation is discretized onto a  $5^\circ$  longitude by  $4^\circ$  latitude spatial grid over the globe, and solved iteratively using a finite difference algorithm (Takahashi et al., 1995, 1997). Material transport across the sea–land interface is assumed to be negligibly small:  $\partial S/\partial x = 0$  and  $\partial S/\partial y = 0$ . Singularities at the poles are avoided by the presence of Antarctica in the south and by treating the Arctic ice field as land in the north. The surface water  $p\text{CO}_2$  values are the solutions obtained after 500 iterations. This is determined on the basis of behaviors of the temperature values that are interpolated using the same method described above.

In this interpolation scheme, the observations are satisfied explicitly, and those in pixels that have no observations are computed by the continuity equation. The effects of internal sources and sinks of  $\text{CO}_2$ , exchange with atmosphere and upwelling of deep waters are considered imbedded in the observed data, and accordingly, terms for internal source and sink and exchange fluxes are neglected in Eq. (6). While the interpolation scheme yields daily values, the monthly mean values for each box area are presented in this paper.

## 5. Climatological mean distribution of surface water $p\text{CO}_2$

### 5.1. Global distribution

The climatological mean distribution of  $\Delta p\text{CO}_2$  in each month for the reference year 2000 (Fig. 9) is computed using the monthly mean surface water  $p\text{CO}_2$  values over the global ocean and the mean monthly atmospheric  $p\text{CO}_2$  values for the year 2000 as described in Section 2. It should be pointed out that any differences between the new and the previous maps for the reference years 1990 (Takahashi et al., 1997) and 1995 (Takahashi et al., 2002) do not indicate changes occurred in the oceans from 1990 to 2000, but rather reflect primarily the improved database as well as the improvements in the normalization method for the reference year as described in Section 3.

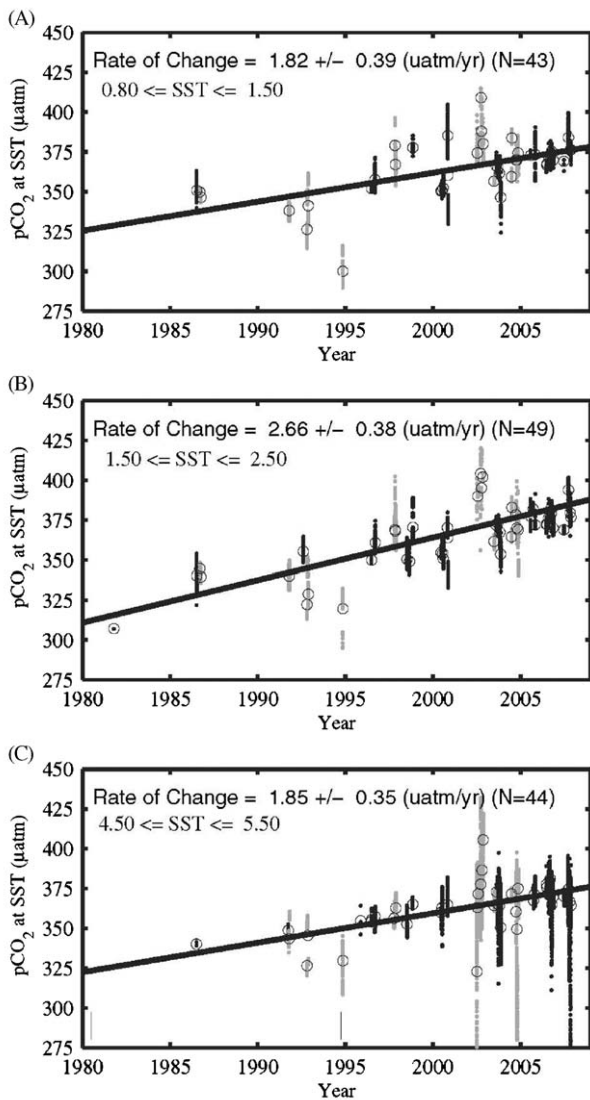
### 5.2. Regional distribution

To show the seasonal and regional changes in  $\Delta p\text{CO}_2$  more clearly, monthly mean  $\Delta p\text{CO}_2$  data are plotted in Fig. 10 for six climatic zones in the four ocean basins. The tropical belt ( $14^\circ\text{N}$ – $14^\circ\text{S}$ ) of the oceans has high positive values with little seasonal variability, indicating that the area is a strong source for  $\text{CO}_2$  year around. The tropical Pacific (Fig. 10B) has the highest positive  $\Delta p\text{CO}_2$  values (annual mean of  $27 \mu\text{atm}$ ), the tropical Atlantic (Fig. 10A, annual mean of  $18 \mu\text{atm}$ ) next, and the tropical Indian (Fig. 10C, annual mean of  $15 \mu\text{atm}$ ) the lowest. The temperate Atlantic and Pacific ( $14$ – $50^\circ$  in the both hemispheres) exhibit large seasonal changes, positive  $\Delta p\text{CO}_2$  in warm summer months and negative values in colder winter months reflecting the dominant effect on  $(p\text{CO}_2)_{\text{sw}}$  of seasonal SST changes. However, the peak-to-peak amplitude for the temperate North Atlantic is about  $42 \mu\text{atm}$ , and is somewhat larger than  $37 \mu\text{atm}$  for the temperate North Pacific. Since the mean seasonal amplitudes for SST are similar in these two ocean areas ( $5.7$  and  $5.8^\circ\text{C}$ ), the difference in  $\Delta p\text{CO}_2$  amplitudes cannot be attributed to SST, and may reflect differences in biological environments such as a greater supply of nitrate by the nitrification of atmospheric nitrogen in the North Atlantic (Capone et al., 2005). Seasonal

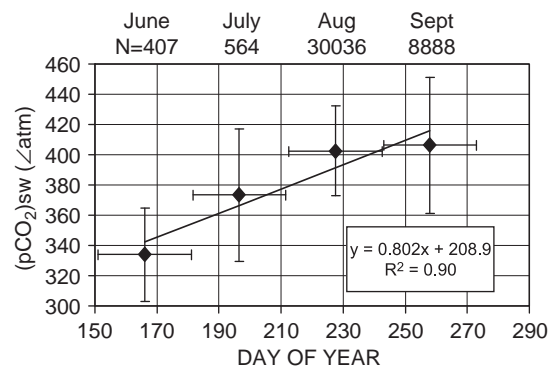


**Table 3**Mean rates of change in surface water pCO<sub>2</sub> and bulk water temperature of mixed layer (SST) estimated in six areas in the temperate South Pacific Ocean.

Locations	Lat.	Long.	Data period	Rate of change		No. of MOS.	Rate of change	
				pCO <sub>2</sub> @SST (µatm y <sup>-1</sup> )	±σ (µatm y <sup>-1</sup> )		SST (°C y <sup>-1</sup> )	±σ (°C y <sup>-1</sup> )
Tahiti	15–20°S	135–145°W	1974–1997	2.00	0.39	16	0.033	0.034
Vanuata	20–25°S	165–175°E	1984–2006	1.30	0.27	35	–0.048	0.018
New Caledonia	25–30°S	170–180°W	1974–2005	1.05	0.09	17	–0.033	0.020
Tasmania	43–48°S	140–150°E	1984–2004	1.83	0.56	18	–0.051	0.062
New Zealand	45–50°S	170–180°E	1974–2006	1.42	0.30	37	0.001	0.027
S. of Tasmania	50–55°S	140–150°E	1984–2002	1.61	0.20	12	–0.044	0.064
Mean				1.5 ± 0.3	0.30	–	–0.02 ± 0.05	0.04

The rates are computed using mean monthly values. The temperatures are measured concurrently with pCO<sub>2</sub>.**Fig. 7.** Rates of increase in surface water pCO<sub>2</sub> in the subpolar region (south of 50°S) of the Southern Ocean in the austral winter months (day of year from 172 to 326) during the period from 1986 to 2007: (A) SST between 0.80 and 1.50 °C, (B) SST between 1.50 and 2.50 °C, and (C) SST between 4.50 and 5.50 °C. Black dots indicate measurements made in non-El Niño periods; and gray dots indicate those made in El Niño periods. No discernible differences are seen between these periods. The mean rates are estimated by linearly regressing the monthly mean values (open circles); and *N* is the number of monthly mean values.**Table 4**Mean rate of increase for pCO<sub>2</sub> in winter-time surface waters (Year dates 172–326) in various SST bands over the subpolar Southern Oceans for the period 1986–2007.

Temperature range (°C)	Rate of pCO <sub>2</sub> Change (µatm y <sup>-1</sup> )	No. months (N)	Data counts
0.80–1.50	1.82 ± 0.39	43	3915
1.50–2.50	2.66 ± 0.38	49	7733
2.50–3.50	2.80 ± 0.39	43	8084
3.50–4.50	2.61 ± 0.58	43	13,968
4.50–5.50	1.85 ± 0.35	44	15,463
5.50–6.50	1.18 ± 0.40	42	17,077
0.80–6.50	Mean 2.1 ± 0.6	264	66,240

The rates are estimated by a linear regression of monthly mean values made during the winter months within each SST band. *N* is the number of months used for the regression, and ± uncertainties are computed using Eq. (5). The area-weighted mean rate for the circumpolar zone is 2.1 ± 0.6 µatm y<sup>-1</sup>, where ± uncertainty is one standard deviation of the six zonal mean values.**Fig. 8.** Multi-year pCO<sub>2</sub> data observed in ice field waters with temperatures less than –1.75 °C in the Southern Ocean south of 60°S during the austral winter months, June–September. The pCO<sub>2</sub> increases with progressing seasons. The values are not corrected for the reference year; and *N* indicates the number of pCO<sub>2</sub> measurements. When these waters are exposed to the air, they are a source for CO<sub>2</sub> since they have pCO<sub>2</sub> values greater than those in the overlying atmosphere by as much as 40 ± 20 µatm during the late winter months (August–September).

changes in the northern temperate oceans are about 6 months out of phase from the southern temperate oceans.

The annual mean ΔpCO<sub>2</sub> for the southern temperate Atlantic (–10 µatm, 14–50°S) is similar to that for the southern Pacific of –10 µatm, while the southern temperate Indian has more negative ΔpCO<sub>2</sub> values with a mean of –17 µatm (Fig. 10C). The regional mean SST for the temperate South Indian (18.6 °C) is

**Table 5**Summary of mean rates of increase in surface water pCO<sub>2</sub>.

	No. of box areas	Ocean area <sup>a</sup> (10 <sup>6</sup> km <sup>2</sup> )	Annual <sup>b</sup> rate (μatm y <sup>-1</sup> )	Standard deviation (μatm y <sup>-1</sup> )	References
N. Pacific (10–60°N) <sup>c</sup>	28	28.9	1.28	0.46	Takahashi et al. (2006)
Equatorial Pacific (5–5°S) <sup>d</sup>	2	7.4	1.26	0.55	Feely et al. (2006)
N. Atlantic (15–70°N) <sup>e</sup>	36	16.8	1.80	0.37	This study
S. Pacific (15–55°S) <sup>e</sup>	6	2.9	1.53	0.35	This study
Southern O. (50–60°S) <sup>f</sup>	6	30.6	2.13	0.64	This study
Global with Southern Ocean	78	86.6 (27%)	1.69	0.51	
Global without Southern Ocean	72	56.0 (17%)	1.45	0.47	

While the rate for the Southern Ocean is estimated for the winter months only, all other rates represent seasonal mean.

<sup>a</sup> Global ocean area = 326.5 × 10<sup>6</sup> km<sup>2</sup>.

<sup>b</sup> Area-weighted mean.

<sup>c</sup> 10°(lat.) × 10° (long) boxes, excluding the Bering Sea.

<sup>d</sup> Nino 3.4 (120–170°W) and Western Warm Pool (165–175°E) areas.

<sup>e</sup> 5°(lat.) × 10°(long.) boxes.

<sup>f</sup> Winter data only for circumpolar 2° (lat.) wide bands.

similar to that for the South Pacific (18.9 °C) and somewhat higher than the South Atlantic (17.4 °C), and the mean annual surface water salinity values are also similar (35.0 for the South Indian, 35.4 for the South Atlantic and 35.1 for the South Pacific). Hence, the low pCO<sub>2</sub> in the South Indian Ocean cannot be attributed to differences in SST or salinity. Primary productions estimated from the SeaWiFS observations (Gregg et al., 2003) suggest that the mean annual productivity in the South Indian is higher than in the South Pacific, but lower than the South Atlantic. Hence, the biological production data cannot account for the ΔpCO<sub>2</sub> data. It is possible that the ΔpCO<sub>2</sub> data and hence the fluxes could be biased because of undersampling in the Southern Hemisphere oceans (see Fig. 1).

A strong negative ΔpCO<sub>2</sub> observed in the spring–summer months in the sub-arctic Atlantic (Körtzinger et al., 2008) and Pacific (Fig. 10A and B) are due to the effect of biological drawdown of CO<sub>2</sub>, in strongly stratified shallow mixed layers. The seasonal ΔpCO<sub>2</sub> change in subpolar regions is about 4 months out of phase from that for the adjacent temperate region.

The positive ΔpCO<sub>2</sub> values observed in July–September in the northern Indian Ocean (north of 14°N, Fig. 10C) is due to the seasonal upwelling of deep waters caused by the Southwest Monsoon winds. The positive peak observed in July–October in the seasonal ice zone of the Southern Ocean (south of 62°S, Fig. 10D) represents the under-ice mixed water layer that is enriched with CO<sub>2</sub> and nutrients primarily by the vertical mixing of deep waters. During the austral spring–summer months, phytoplankton blooms occurring near ice margins and within polynyas reduce ΔpCO<sub>2</sub> values as low as –100 μatm. However, extent and duration of bloom areas that form a strong sink for atmospheric CO<sub>2</sub> may vary geographically and have not been well documented.

### 5.3. Comparison with the 2002 results

Takahashi et al. (2002) used the following procedures for correcting the pCO<sub>2</sub> data to a reference year 1995. They considered that the surface water values in tropical and temperate oceans (45°N–50°S in the Atlantic, north of 50°S in the Indian Ocean and 40°N–50°S in the western Pacific west of the date line and 40°N–60°S in the eastern Pacific east of the date line) were increasing at the same rate as the atmospheric pCO<sub>2</sub>. As done for this study, they corrected the observed values to the reference year using a mean atmospheric CO<sub>2</sub> increase rate of 1.5 μatm. On the other hand, on the basis of a limited number of the pCO<sub>2</sub> observations in high latitudes, they considered that CO<sub>2</sub> proper-

ties in surface waters in subpolar and polar regions remained unchanged year to year due to the dilution by vertical mixing of deep waters that were little affected by the atmospheric CO<sub>2</sub> increase. Accordingly, they made no correction for the time of pCO<sub>2</sub> observations. In contrast, we have demonstrated in this study that the surface water pCO<sub>2</sub> over the subpolar oceans has been also increasing at a mean rate of 1.5 μatm y<sup>-1</sup> (ranging between 1.3 and 2.0, see Table 5), and used this mean rate for normalizing the multi-year data to a reference year of 2000 for the entire oceanic areas with the exception of the Bering Sea, where the observed rate of –1.2 μatm y<sup>-1</sup> is used.

The difference maps between the surface water pCO<sub>2</sub> values from this study (3.0 M) and the 2002 study (0.94 M) are shown in Fig. 11: (A) February and (B) August. To make these two studies comparable, the 2002 values, which were normalized to a reference year 1995, are corrected by adding 7.5 μatm (= 1.5 μatm y<sup>-1</sup> × 5 y) to adjust them to the reference year 2000. Reflecting the assumptions made in the 2002 study, larger differences are found in the subpolar to polar regions. Differences in the temperate and tropical areas are less than 5 μatm on the average. In the seasonal ice zone of the Southern Ocean south of about 62°S, the results of this study are found as much as 100 μatm greater than those of 2002 (Fig. 11B). This is attributed to the high pCO<sub>2</sub> values revealed by new measurements for under-ice waters during austral winter (Fig. 8). In the Arctic Chukchi Sea, the values for this study are found to be lower than those for the 2002 study by as much as 100 μatm both in February and August. Although this is attributed to new measurements, the time–space coverage of the Arctic waters is highly limited presently.

## 6. Net sea–air CO<sub>2</sub> flux

### 6.1. Computational method

The net sea–air CO<sub>2</sub> flux ( $F$ ) is estimated using

$$F = k \alpha \Delta pCO_2 = Tr \Delta pCO_2 \quad (7)$$

where  $k$  is the CO<sub>2</sub> gas transfer velocity;  $\alpha$  is the solubility of CO<sub>2</sub> in seawater;  $Tr$  is the sea–air gas transfer coefficient; and  $\Delta pCO_2$  is the sea–air pCO<sub>2</sub> difference in the reference year 2000 as defined by Eq. (4). The gas transfer velocity ( $k$ ) is typically expressed as a power function of wind speed ( $U$ ):  $k \propto U^n$  at a given temperature and salinity. The value of exponent,  $n$ , has been suggested to be between 1 (Liss and Merlivat, 1986) and 3 (Wanninkhof and McGillis, 1999). Ho et al. (2006), on the basis of the <sup>3</sup>He/SF<sub>6</sub> double tracer data obtained over high wind speed conditions (up to

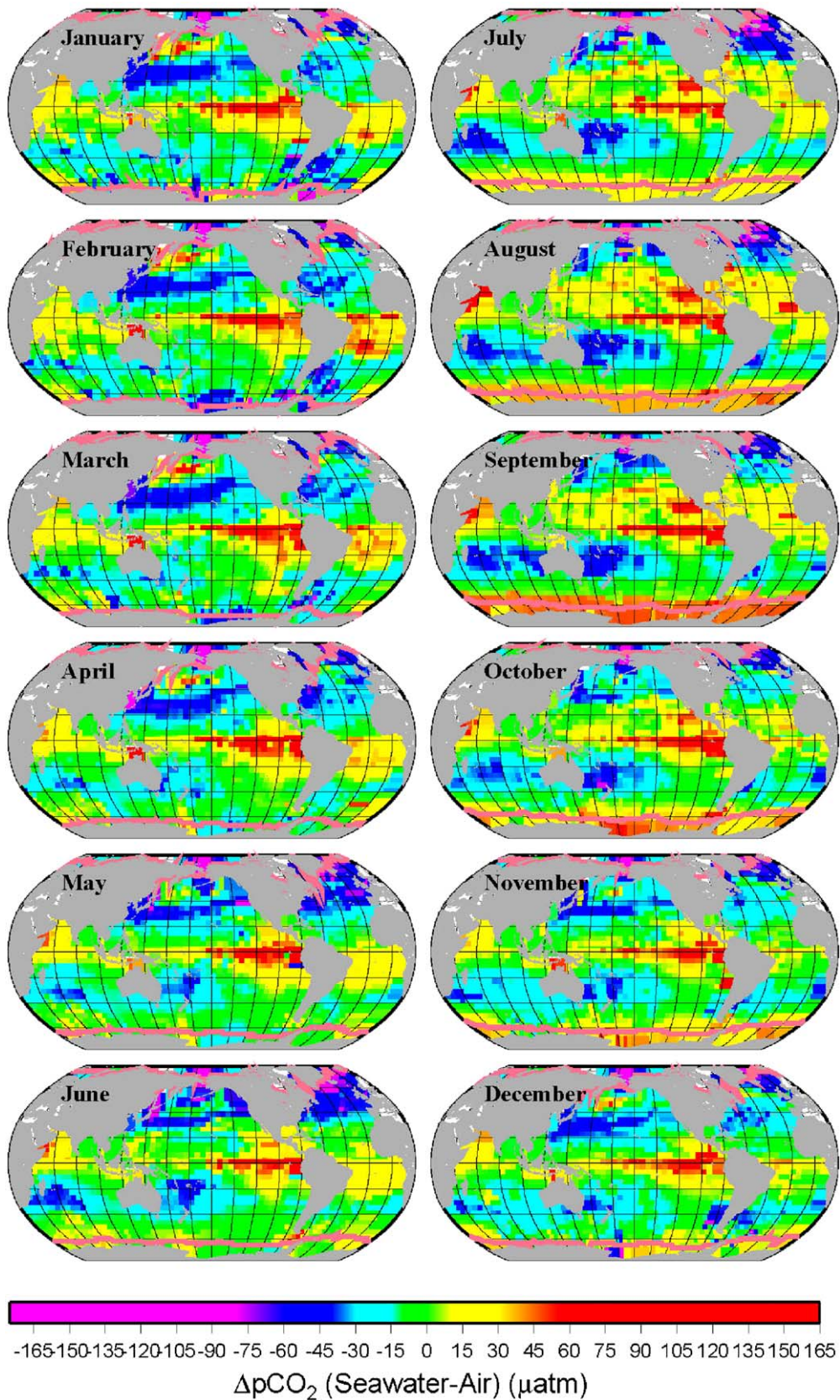


**Fig. 9.** The monthly mean values for sea–air  $p\text{CO}_2$  differences in the global ocean. The values represent climatological mean for non-El Niño conditions adjusted to a reference year 2000. Orange–yellow colors indicate positive  $\Delta p\text{CO}_2$  (sea is a source for atmospheric  $\text{CO}_2$ ), green indicates near zero  $\Delta p\text{CO}_2$ , and cyan–blue colors indicate negative  $\Delta p\text{CO}_2$  (sea is a  $\text{CO}_2$  sink). Heavy pink curves indicate the mean position for the northerly extent of 90% ice cover. Waters under the Southern Ocean ice-field have high positive  $\Delta p\text{CO}_2$ . Whenever measurements are lacking for ice field waters, the values are estimated using the equation in Fig. 8. (For interpretation of the references to color in this figure legend, the reader is referred to the web version of this article.)

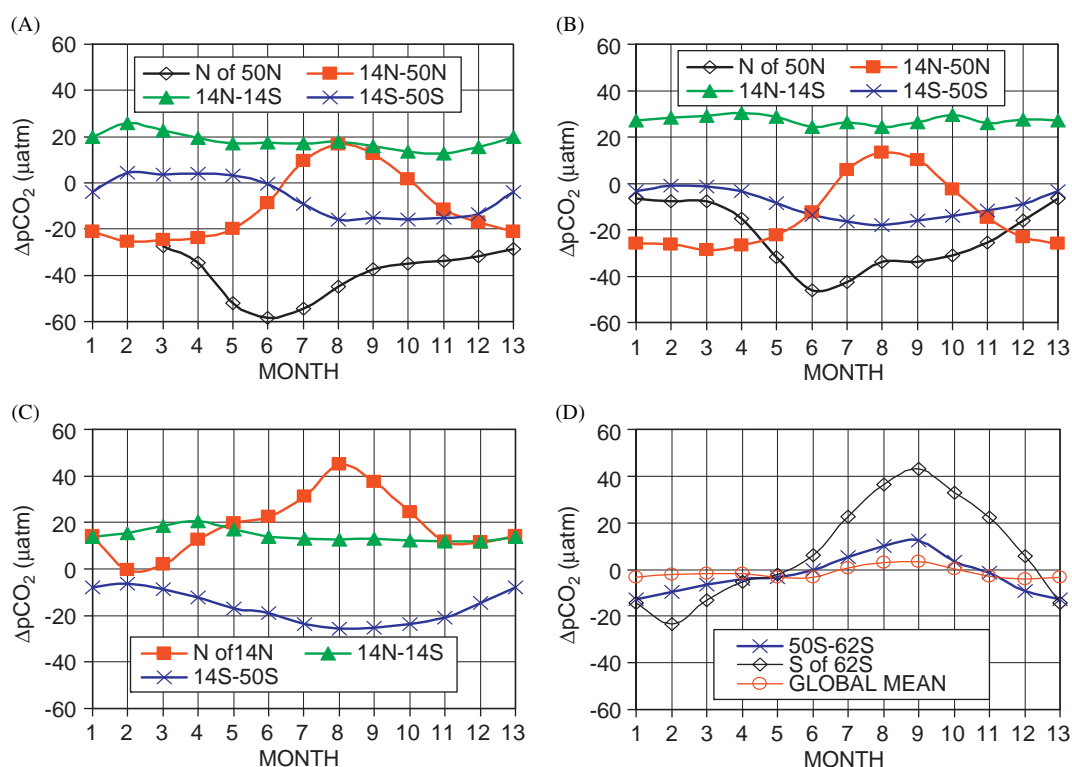


**Fig. 10.** The monthly mean values for sea-air  $p\text{CO}_2$  differences in the four major ocean basins: (A) Atlantic, (B) Pacific, (C) Indian, (D) Southern and Global Oceans. Average values in each climatic zone are plotted against month (1 = January, 2 = February, ..., 12 = December and 13 = January). The zones “50S–62S” and “S of 62S” in the Southern Ocean represent, respectively the open water zone and the seasonal ice zone.

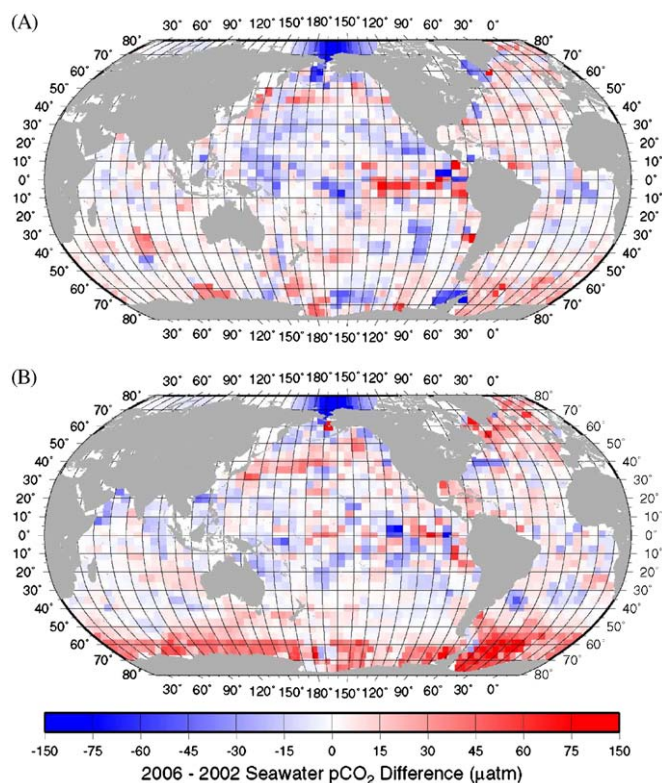


**Fig. 11.** Difference maps for the surface water  $p\text{CO}_2$  values for this study and Takahashi et al. (2002): (A) February and (B) August. In order to make the results of these two studies comparable, the 2002 values, which were normalized to a reference year 1995, are corrected by adding  $7.5 \mu\text{atm}$  ( $= 1.5 \mu\text{atm y}^{-1} \times 5 \text{ y}$ ) to adjust to the reference year 2000 used for this study.

$16 \text{ m s}^{-1}$ ) in the Southern Ocean, suggested a square dependence of wind speed. Considering various studies including Wanninkhof (1992), Nightingale et al. (2000) and Wanninkhof et al. (2004), we choose a formulation:  $k \text{ (cm h}^{-1}\text{)} = \Gamma (U_{10})^2 (Sc/660)^{-1/2}$ , where  $U_{10}$  is wind speed at 10 m above sea surface, and  $Sc$  is Schmidt number [ $= (\text{kinematic viscosity of water})/(\text{diffusion coefficient of CO}_2 \text{ in water})$ ]. The value for a scaling factor,  $\Gamma$ , is evaluated according to the following procedures.

Wanninkhof (1992) used  $^{14}\text{C}$  as a diagnostic for sea–air  $\text{CO}_2$  gas transfer, and estimated the scaling factor,  $\Gamma$ , of 0.39 based on a mean global wind speed of  $7.4 \text{ m s}^{-1}$ , and a mean gas invasion rate of  $21 \text{ cm h}^{-1}$  derived from a simple box model to fit the global ocean bomb- $^{14}\text{C}$  inventory of  $2.89 \times 10^{28}$  atoms that was estimated by Broecker et al. (1985). In our previous publication (Takahashi et al., 2002), this value for  $\Gamma$  was used. Improvements in the wind speed and  $^{14}\text{C}$  data have resulted in smaller values for  $\Gamma$  as reviewed by Wanninkhof (2007). Naegler et al. (2006) pointed out that  $\Gamma$  depends on the  $^{14}\text{C}$  inventory and wind speed field used, and that it must be evaluated for the same wind speed data used for the  $\text{CO}_2$  flux calculations. Sweeney et al. (2007) have further extended this approach and inverted bomb- $^{14}\text{C}$  data for ocean waters using three Ocean General Circulation Models, in which the global oceans are divided into 29 discrete surface areas. By their method, the time-space distribution of  $^{14}\text{C}$  in surface waters, hence the gas transfer rates, is taken into account. To simplify computations, they assumed that the flux into each of the 29 areas has a time history proportional to the observed  $^{14}\text{C}$  values in the atmosphere. Assuming a quadratic dependence of piston velocity on wind speed, they obtained a  $\Gamma$  value of 0.27 (for long-time average) using the 1954–2000 NCEP Reanalysis-I wind speeds (Kalnay et al., 1996) over the ice-free global oceans and the bomb- $^{14}\text{C}$  inventory of  $3.43 \pm 0.40 \times 10^{28}$  atoms as of 1994. This formulation yields not only piston velocity values consistent

with those obtained from some small-scale deliberate tracer studies (e.g. Nightingale et al., 2000), but also with the total bomb- $^{14}\text{C}$  inventory obtained for the strato- and troposphere.

For this study, a  $\Gamma$  value of 0.26 has been computed using the 1979–2005 NCEP-DOE AMIP-II Reanalysis 6-h wind speed data (Kanamitsu et al., 2002), which is recast onto the same  $4^\circ \times 5^\circ$  grid as used for this study. The value includes the effect of dilution of ocean water  $^{14}\text{CO}_2$  by the uptake of fossil fuel  $\text{CO}_2$  (free of  $^{14}\text{C}$ ). The wind speed data have a mean speed  $\langle U_{10} \rangle$  of  $8.06 \text{ m s}^{-1}$  and  $\langle U_{10}^2 \rangle / \langle U_{10} \rangle^2$  of 1.20 for ice-free oceans using the 6-h wind to calculate  $\langle U_{10}^2 \rangle$ . The overall error in  $\Gamma$  is estimated to be  $\pm 30\%$  that includes uncertainties in the  $^{14}\text{C}$  inventory, ocean models and  $p^{14}\text{CO}_2$  (Sweeney et al., 2007).

## 6.2. Distribution of the sea–air $\text{CO}_2$ gas transfer coefficient

The product of the first two terms in Eq. (7) represents a sea–air  $\text{CO}_2$  gas transfer rate constant (hereafter called gas transfer coefficient). When monthly mean wind speeds ( $U_{10}$  in the unit of meters  $\text{s}^{-1}$ ) and  $\alpha$  in ( $\text{mol liter}^{-1} \text{ atm}^{-1}$ ) (Weiss, 1974) are used, Eq. (8) gives the transfer coefficient (Tr):

$$\text{Tr}(\text{g-C m}^{-2} \text{ month}^{-1} \mu\text{atm}^{-1}) = 0.585 \cdot \alpha \cdot (\text{Sc})^{-1/2} \cdot (U_{10})^2 \quad (8)$$

where 0.585 is a unit conversion factor taking into account the scaling factor for the gas transfer rate (0.26), ( $\text{mol liter}^{-1} \text{ atm}^{-1}$ ) to ( $\text{g-C m}^{-3} \mu\text{atm}^{-1}$ ), ( $\text{cm h}^{-1}$ ) to ( $\text{m month}^{-1}$ ) ( $= 10^{-2} \times 24 \times 365/12$ ), and a reference Schmidt number ( $660^{1/2}$ ). The Schmidt number (Sc) and the solubility of  $\text{CO}_2$  in seawater depend sensitively on

the temperature: from  $0^\circ$  to  $30^\circ \text{C}$ , Sc for  $\text{CO}_2$  decreases by a factor of 5 and  $\alpha$  also decreases by a factor of 2.5. Accordingly, the product  $\alpha \cdot (\text{Sc})^{-1/2}$  is nearly constant and changes by less than 10% over the temperature range of global surface ocean waters. Hence, the transfer rate coefficient, Tr, is primarily a function of wind speed. Since a product of Tr with  $\Delta p\text{CO}_2$  gives the net sea–air  $\text{CO}_2$  flux, the seasonal and geographical variation of Tr is of interest.

In Fig. 12, the monthly mean Tr values in six climatic zones are summarized for the four major ocean basins and the global ocean. The subpolar regions of the North Atlantic (Fig. 12A, north of  $50^\circ \text{N}$ ) and the Southern Ocean (Fig. 12D,  $50\text{--}2^\circ \text{S}$ ) have the highest values for the transfer rate coefficient reaching as high as  $0.12 \text{ g-C m}^{-2} \text{ month}^{-1} \mu\text{atm}^{-1}$  (hereafter the unit is omitted) due to persistent high winds during the regions' respective winter months. During the summer months, however, the Tr values decrease to as low as 0.03 in the sub-arctic Atlantic (Fig. 12A) and to 0.08 in the Southern Ocean (Fig. 12D). In contrast, winter-maximum Tr values reach only to 0.09 in the sub-arctic Pacific. The Antarctic zone (south of  $62^\circ \text{S}$ , Fig. 12D) has much lower wind speeds and hence shows lower Tr values ranging between 0.07 in winter and 0.05 in summer. In the temperate zones of the Atlantic and Pacific, the Tr values vary from summer values of about 0.03 to winter values of 0.07 (Fig. 12A and B); and the seasonal changes in the northern oceans are 6 months out of phase from the Southern Hemisphere oceans. The tropical Atlantic and Pacific (Fig. 12A and B,  $14^\circ \text{N}\text{--}14^\circ \text{S}$ ) have Tr values of about 0.03, and show very small seasonal variability. The northern Indian Ocean is significantly different from the Atlantic and Pacific. Tr values peak in June–August due to southwest monsoon winds in the tropical

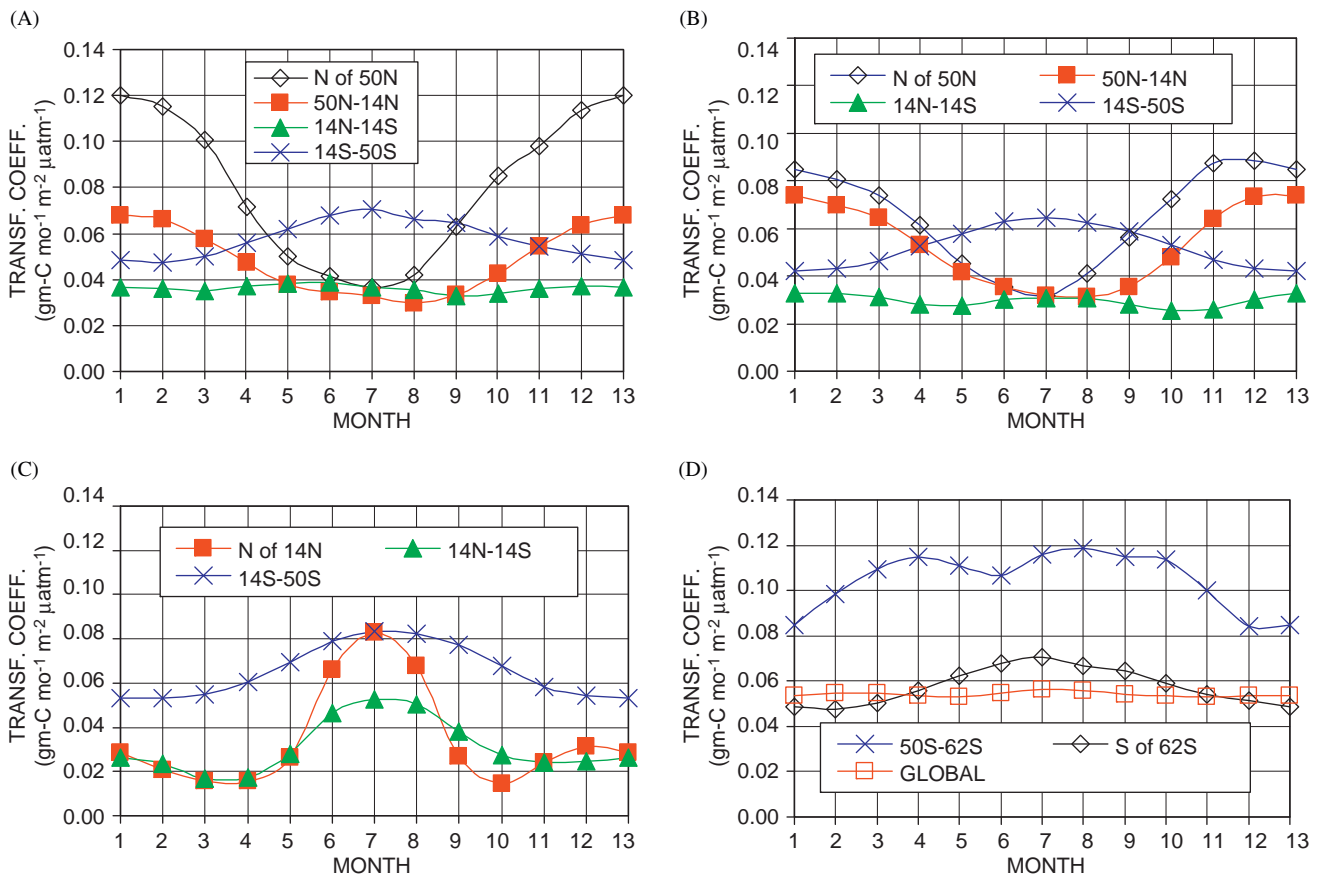


**Fig. 12.** Monthly mean values for the  $\text{CO}_2$  gas transfer rate coefficient, Tr, in ( $\text{g-carbon m}^{-2} \text{ month}^{-1} \mu\text{atm}^{-1}$ ) computed using Eq. (8). The monthly mean values for  $U_{10}$  in each  $4^\circ \times 5^\circ$  box were computed using the 1979–2005 NCEP-DOE AMIP-II Reanalysis data (updated version of Kanamitsu et al., 2002). The monthly mean values for each zone shown in the plots are area-weighted mean values of the box areas within each zone. Months are expressed as 1 = January, 2 = February, ..., 12 = December and 13 = January.

zone and especially in the zone north of 14°N (Fig. 12C). The high wind speeds induce not only intense upwelling in the western Arabian Sea, but also cause high rates of sea–air gas exchange. The southern temperate Indian Ocean also has higher wind speeds than the southern Pacific and Atlantic, and hence higher  $Tr$  values ranging between 0.05 in summer and 0.08 in winter. The mean monthly values (area weighted) for the global ocean are nearly constant around  $0.05 \text{ g-C month}^{-1} \text{ m}^{-2} \mu\text{atm}^{-1}$  (Fig. 12D).

### 6.3. Global distribution of the net sea–air $\text{CO}_2$ flux

The climatological mean sea–air  $\text{CO}_2$  flux in each box area for each month is computed by multiplying monthly mean values for  $Tr$  (Eq. (8)) and  $\Delta p\text{CO}_2$  (Eq. (4)) in each box. Since no significant correlation of individual  $\Delta p\text{CO}_2$  values with 6-h mean wind speed data is found in a single month, the product of monthly mean values is considered as a valid approximation for the  $\text{CO}_2$  flux. Over the polar regions, where sea-ice fields form seasonally, the following assumptions are made for computing the sea–air  $\text{CO}_2$  flux. When the ice cover is less than 10%, a box area is assumed to be all water. For ice covers between 10% and 90%, the flux is assumed to be proportional to open water area. Since ice fields have leads and polynyas due to dynamic motions of sea ice as evidenced by “sea smoke”, we accept the estimates by Saunders and Ackley (personal communication) that 10% of fields is open water at any given time even in areas where satellite observations indicate 100% ice cover. The ice cover values used in this study are based on the NCEP/DOE 2 Reanalysis data (2005) (provided by the NOAA/OAR/ESRL PSD). The original data given in a Gaussian grid for 1970–2005 are re-gridded to our  $4^\circ \times 5^\circ$  grid, and the ice cover values in each pixel are averaged for each month (30.5 days).

#### 6.3.1. Mean annual distribution

Fig. 13 shows the climatological mean annual sea–air  $\text{CO}_2$  flux ( $\text{g-C m}^{-2} \text{ yr}^{-1}$ ) for the reference year 2000, and Fig. 14 shows  $4^\circ$  zonal aggregates for the flux in the major ocean basins and the global oceans. The annual fluxes in six climatic zones in each ocean basin are summarized in Table 6. The equatorial Pacific is the most prominent source area for atmospheric  $\text{CO}_2$  with a seasonally persistent sea-to-air flux of  $0.48 \text{ Pg-C yr}^{-1}$ . Together with the tropical Atlantic and Indian Oceans, the global tropical oceans emit  $0.69 \text{ Pg-C yr}^{-1}$  to the atmosphere. A belt of  $\text{CO}_2$  sink zone is located in  $20\text{--}50^\circ$  latitudes in the both hemispheres (Fig. 14). This is attributed primarily to strong winds between  $40^\circ$  and  $50^\circ\text{S}$ , and the low  $p\text{CO}_2$  values produced along the subtropical convergence zone, where the cooled subtropical gyre waters with low  $p\text{CO}_2$  meet the subpolar waters with biologically-lowered  $p\text{CO}_2$ . Together, the mid-high latitude northern ( $22\text{--}50^\circ\text{N}$ ) and southern ( $22\text{--}50^\circ\text{S}$ ) oceans constitute a sink of  $-0.70$  and  $-1.05 \text{ Pg-C yr}^{-1}$ . A sink area ( $-0.27 \text{ Pg-C yr}^{-1}$ ) is seen also in the North Atlantic north of  $50^\circ\text{N}$ , including the Nordic Seas and portion of the Arctic. This is attributed to strong phytoplankton blooms in spring and strong cooling in winter. The annual  $\text{CO}_2$  flux over the Southern Ocean seasonal ice zone is small due to the ice cover that reduces sea–air gas transfer in winter and by the cancellation of the seasonal source and sink fluxes.

The mean annual sea–air  $\text{CO}_2$  flux values for the four major ocean basins are compared in Table 6. While the Atlantic has only 23% of the global ocean area, it takes up 41% of the annual global ocean flux of  $-1.42 \text{ Pg-C yr}^{-1}$ . On the other hand, while the Pacific has the largest area (47%), twice as large as the Atlantic, it takes up only 33% of the global flux. This is due to the large  $\text{CO}_2$  source

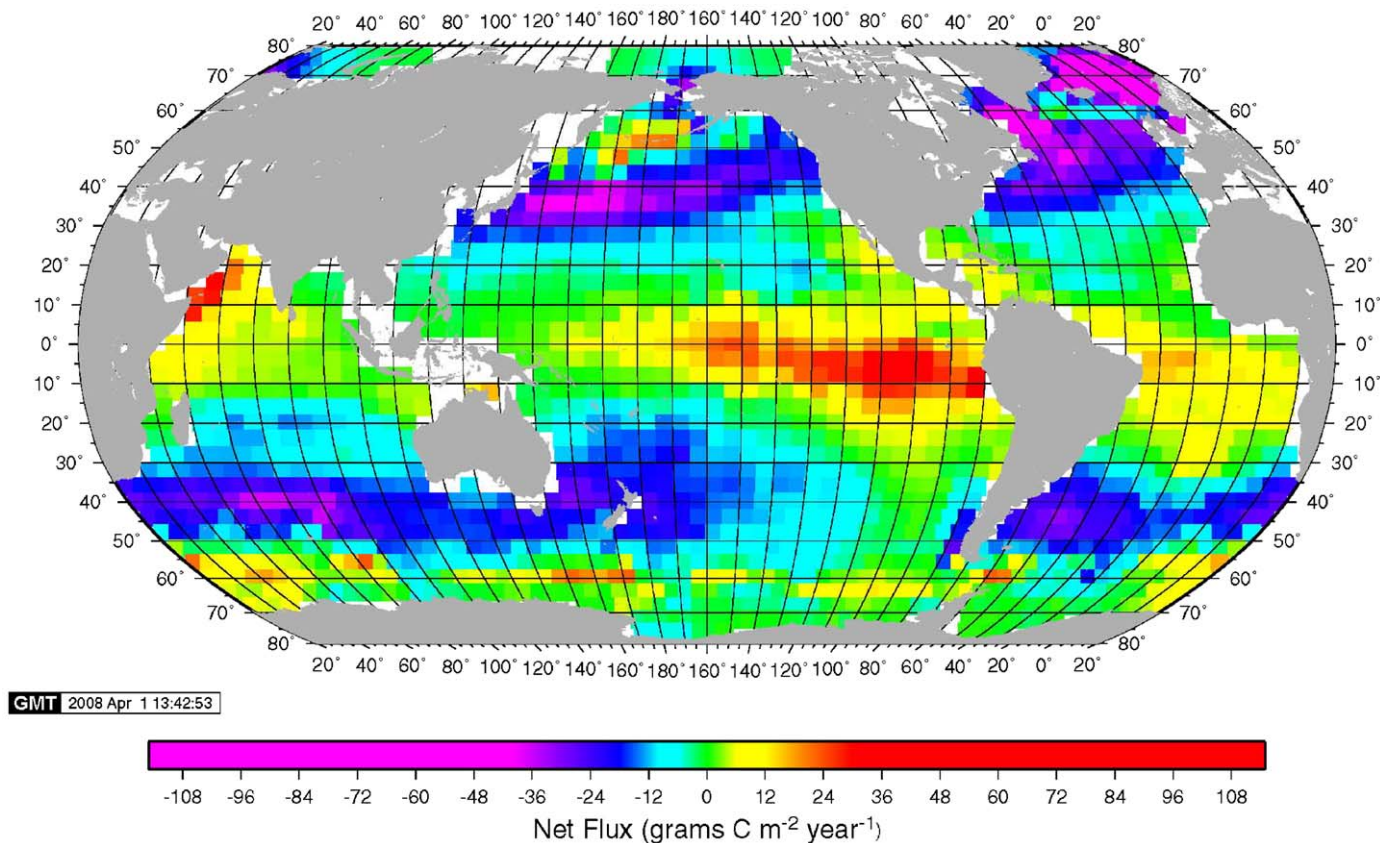


**Fig. 13.** Climatological mean annual sea–air  $\text{CO}_2$  flux ( $\text{g-C m}^{-2} \text{ yr}^{-1}$ ) for the reference year 2000 (non-El Niño conditions). The map is based on 3.0 million surface water  $p\text{CO}_2$  measurements obtained since 1970. Wind speed data from the 1979–2005 NCEP–DOE AMIP-II Reanalysis (R-2) and the gas transfer coefficient with a scaling factor of 0.26 (Eq. (8)) are used. This yields a net global air-to-sea flux of  $1.42 \text{ Pg-C yr}^{-1}$ .

(+0.48 Pg-Cy<sup>-1</sup>) located along the equatorial Pacific. Since this source is reduced significantly due to the El Niño events (Feely et al., 2006), the net uptake by the Pacific would be increased during these periods. The sink over the Southern Ocean is small due mainly to large seasonal ice cover that reduces gas exchange rates.

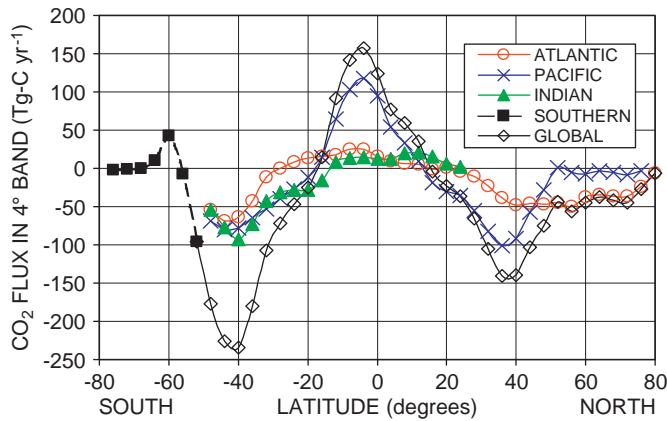


**Fig. 14.** Zonal mean sea-air CO<sub>2</sub> flux in the four major ocean basins. The flux values are expressed in Tg-Cy<sup>-1</sup> (Tg = 10<sup>12</sup> g) for each 4°-wide zonal band across each ocean basin. This plot gives a total global air-to-sea flux of 1.42 Pg-Cy<sup>-1</sup>. The wind speed data are from the 1979–2005 NCEP-DOE AMIP-II Reanalysis, and the gas transfer coefficient is computed using Eq. (8).

The climatological mean value for the net air-to-sea flux for the reference year 2000 is estimated to be  $-1.42 \text{ Pg-Cy}^{-1}$  for the global oceans (Table 6). Errors for these estimates are discussed in Section 6.4.

### 6.3.2. Seasonal variation of the global ocean sea-air CO<sub>2</sub> flux

Fig. 15 shows the distribution of monthly mean flux in February and August in a reference year 2000. Seasonal changes in the flux field are clearly seen in the figures, and they are attributed to a combination of the effects of seasonal changes in water temperatures, biological utilization of CO<sub>2</sub> and water mixing as well as changes in wind speeds (Takahashi et al., 2002). The mid-latitude regions of the Atlantic, Indian and Pacific Oceans all change from a near-zero or weak source in the respective summer seasons to a strong sink in the respective winter seasons. This is due to the winter cooling of waters transported poleward by eastern boundary currents. In spring and summer, biological drawdown of CO<sub>2</sub> is to some extent offset by increase in pCO<sub>2</sub> due to warming. Subtropical gyres move from weak sinks in the winter seasons to weak sources in the summer seasons, consistent with the seasonal SST cycles, confirming the dominance of heating and cooling effects in controlling the seasonal variability in the pCO<sub>2</sub> and sea-air fluxes. At tropical latitudes, seasonality is most evident in the northwestern Indian Ocean, where the summer monsoon winds force upwelling of CO<sub>2</sub>-rich subsurface waters coincident with high gas transfer rate (Tr) (Chen et al., 1998; Takahashi et al., 2002). The equatorial Pacific and Atlantic show little seasonal variability in CO<sub>2</sub> flux (Feely et al., 2002).

**Table 6**

Mean annual sea-air CO<sub>2</sub> fluxes (Pg-Cy<sup>-1</sup>) in the four major ocean basins and the global oceans for the reference year 2000 based on the 3.0 million pCO<sub>2</sub> measurements, the wind speed data from the 1979–2005 NCEP-DOE AMIP-II Reanalysis (rows marked 3.0 M and values in bold letters).

Zones	Areas 10 <sup>6</sup> km <sup>2</sup>	Data (M)	Sea-air CO <sub>2</sub> flux (Pg-Cy <sup>-1</sup> )				
			Atlantic Ocean	Pacific Ocean	Indian Ocean	Southern Ocean	Zone sum
N of 50°N	16.2	<b>3.0</b>	<b>-0.27</b>	<b>-0.03</b>	-	-	<b>-0.30</b>
		0.94	-0.31	+0.01	-	-	-0.30
50–14°N	69.1	<b>3.0</b>	<b>-0.22</b>	<b>-0.50</b>	<b>+0.02</b>	-	<b>-0.70</b>
		0.94	-0.25	-0.47	+0.04	-	-0.68
14°N–14°S	86.7	3.0	<b>+0.10</b>	<b>+0.48</b>	<b>+0.10</b>	-	<b>+0.69</b>
		0.94	+0.11	+0.52	+0.13	-	+0.76
14–50°S	109.6	<b>3.0</b>	<b>-0.20</b>	<b>-0.41</b>	<b>-0.44</b>	-	<b>-1.05</b>
		0.94	-0.23	-0.37	-0.46	-	-1.06
50–62°S	29.7	3.0	-	-	-	<b>-0.06</b>	<b>-0.06</b>
		0.94	-	-	-	-0.34	-0.34
S of 62°S	15.3	3.0	-	-	-	<b>+0.01</b>	<b>+0.01</b>
		0.94	-	-	-	-0.04	-0.04
Basin/global % of flux		<b>3.0</b>	<b>-0.58</b>	<b>-0.46</b>	<b>-0.32</b>	<b>-0.05</b>	<b>-1.42</b>
		<b>3.0</b>	<b>41%</b>	<b>32%</b>	<b>23%</b>	<b>4%</b>	<b>100%</b>
		0.94	-0.66	-0.31	-0.29	-0.39	-1.65
		0.94	-40%	19%	18%	24%	100%
Area (10 <sup>6</sup> km <sup>2</sup> )	326.5		74.8	153.8	53.0	44.9	
			23	47	16	14	

The gas transfer coefficient is computed using Eq. (8). The + values indicate sea-to-air fluxes; and the - values air-to-sea fluxes. The results for this study are compared with those for the reference year 1995 based on the 0.94 million measurements (marked 0.94 M with light letters) used by Takahashi et al. (2002). These fluxes are recomputed using the same wind speed data and gas transfer coefficients as used for this study. Hence the differences between these sets of flux values reflect the differences in the sea-air pCO<sub>2</sub> difference discussed in Section 5.3. The sink flux for the open Southern Ocean waters, 50–62°S, estimated by this study (3.0 M) is significantly smaller than that estimated on the basis of the earlier database of 0.94 M. This is attributed primarily to the improved database.

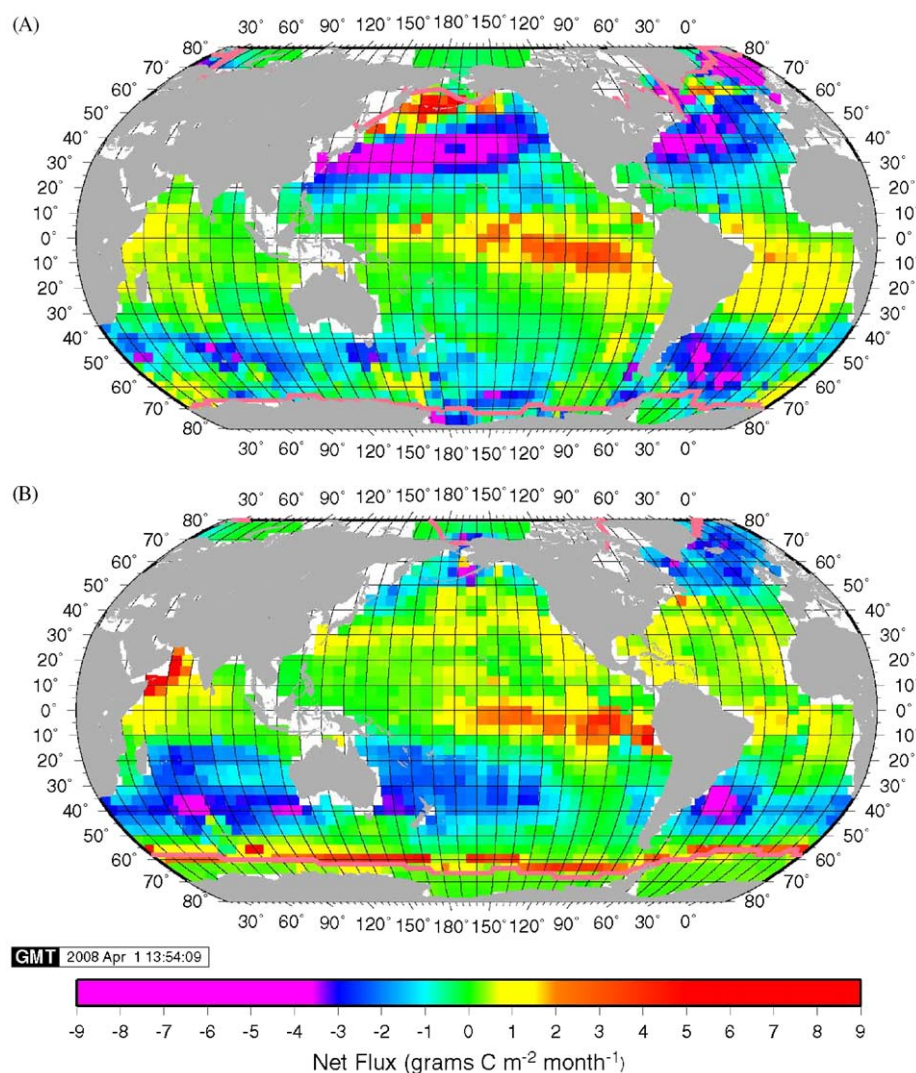


**Fig. 15.** Climatological mean sea–air  $\text{CO}_2$  flux ( $\text{g}\cdot\text{C}\cdot\text{m}^{-2}\cdot\text{month}^{-1}$ ) in February (A) and August (B) in the reference year 2000. The wind speed data are from the 1979–2005 NCEP–DOE AMIP-II Reanalysis, and the gas transfer coefficient is computed using Eq. (8). Positive values (yellow–orange–red) indicate sea-to-air fluxes, and negative values (blue–magenta) indicate air-to-sea fluxes. Ice field data are from NCEP/DOE 2 Reanalysis (2005). (For interpretation of the references to color in this figure legend, the reader is referred to the web version of this article.)

Another striking seasonal feature is the band of moderate source waters (yellow–orange) located along the northern margins for the Antarctic sea-ice field in the vicinity of  $60^\circ\text{S}$  in August. This represents release of  $\text{CO}_2$  from the high  $\text{pCO}_2$  under-ice waters (see Fig. 8) along the ice-field edges. In the areas southward of the edge lines, the open water areas are small, hence the sea–air  $\text{CO}_2$  flux is reduced significantly as indicated by the green areas in Fig. 15B. As the ice field recedes with the arrival of spring, photosynthesis draws down  $\text{pCO}_2$  below the atmospheric level, and the open water areas become a  $\text{CO}_2$  sink as shown in the February map (Fig. 15A).

### 6.3.3. Sea–air $\text{CO}_2$ flux differences in the ocean basins

The sea–air  $\text{CO}_2$  flux is governed by the complex interactions of various oceanographic and meteorological processes. In order to gain insight in regional differences in the influences of these processes, the mean flux per unit area ( $\text{t}\cdot\text{C}\cdot\text{month}^{-1}\cdot\text{km}^{-2} = \text{g}\cdot\text{C}\cdot\text{month}^{-1}\cdot\text{m}^{-2}$ ;  $1\text{t} = 10^6\text{g}$ ) is computed by dividing the total flux with the area for the six climatic zones in each ocean basin (Fig. 16).

The high-latitude North Atlantic (north of  $50^\circ\text{N}$ , Fig. 16A) is clearly the most intense  $\text{CO}_2$  sink area on the per unit area basis.

Cold temperature, strong photosynthesis, high wind speeds and high alkalinity in Arctic waters contribute at various levels over the course of the year to the intense sink.

The tropical zone  $14^\circ\text{N}$ – $14^\circ\text{S}$  for all oceans is a  $\text{CO}_2$  source with fluxes ranging between 0.3 and  $0.9\text{t}\cdot\text{C}\cdot\text{month}^{-1}\cdot\text{km}^{-2}$  with small seasonal variability. The Pacific tropical zone (Fig. 16B) has the highest mean flux of  $0.8\text{t}\cdot\text{C}\cdot\text{month}^{-1}\cdot\text{km}^{-2}$ , the Atlantic next at 0.6 (Fig. 16A) and the Indian the lowest at 0.5 (Fig. 16C). The high Pacific flux is due primarily to an intense upwelling of  $\text{CO}_2$ -rich deep waters in the eastern half of the zone during non-El Niño periods, however, it is about 1/5 of the flux in the Arabian Sea during the peak upwelling time (July–August) (north of  $14^\circ\text{N}$ , Fig. 16C). This is because (a) upwelled deep waters in the northwestern Arabian Sea have much higher  $\text{pCO}_2$  than those in the equatorial Pacific (Figs. 10B and C); (b) the gas transfer coefficient for the Arabian Sea is three times as great as that for the equatorial Pacific (Fig. 12) due to the high monsoon winds; and (c) the Pacific value is averaged over large areas including the western Warm Water zone with weak fluxes (Figs. 13 and 15).

The magnitude and seasonal amplitude of the mean area fluxes for the temperate North and South Atlantic (Fig. 16A) are similar to those for the North and South Pacific (Fig. 16B), respectively.



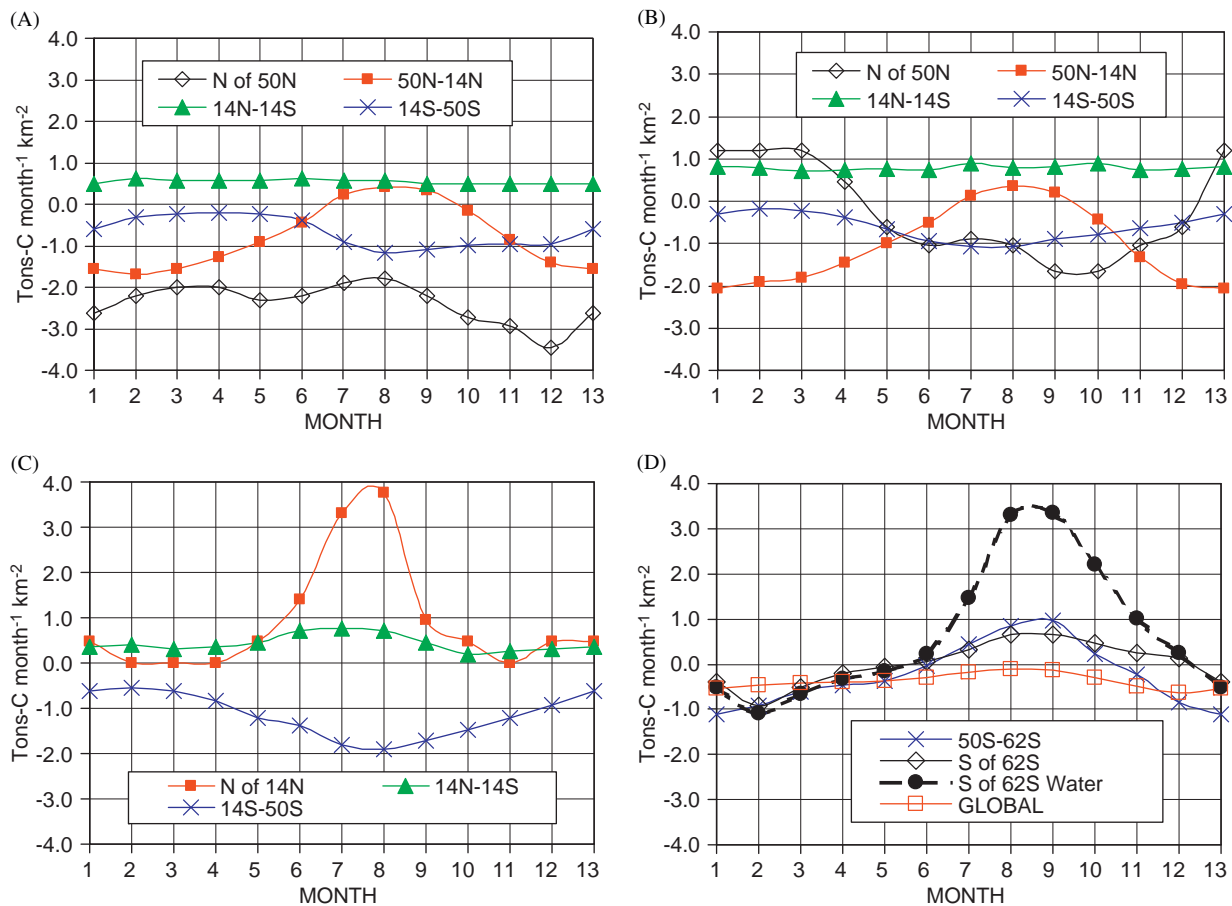


**Fig. 16.** Monthly mean sea-air CO<sub>2</sub> flux per unit area for the four major ocean basins and the global oceans in the unit of tons-carbon month<sup>-1</sup> km<sup>-2</sup> (1 ton = 10<sup>6</sup> g): (A) Atlantic, (B) Pacific, (C) Indian, and (D) Southern and Global Oceans. Month numbers 1 and 13 are January, and Month number 12 is December. For the region "South of 62°S" in panel D, the black solid curve with open diamonds indicates the flux per km<sup>2</sup> of geographic area including ice cover; and the black dashed curve with solid circles indicates the flux per km<sup>2</sup> of water exposed to the air in leads and polynyas in the ice fields. Positive values indicate sea-to-air fluxes, and negative values air-to-sea fluxes.

This suggests that the processes governing the sea-air CO<sub>2</sub> transfer are similar. On the other hand, the area mean air-to-sea CO<sub>2</sub> flux over the temperate South Indian Ocean (annual mean of  $-1.0 \text{ t-C month}^{-1} \text{ km}^{-2}$  for 14–50°S, Fig. 16C) is twice as intense as the corresponding regions of the Atlantic ( $-0.61$  for 14–50°S, Fig. 16A) and Pacific ( $-0.56$  for 14–50°S, Fig. 16B). A number of reasons may be considered. Wind speeds are higher over the South Indian Ocean (annual mean of  $9.04 \text{ m s}^{-1}$ ) than the South Atlantic (annual mean of  $8.48 \text{ m s}^{-1}$ ) and Pacific (annual mean speed of  $8.15 \text{ m s}^{-1}$ ). Seawater pCO<sub>2</sub> is also lower for the South Indian Ocean (annual mean  $\Delta\text{pCO}_2$  of  $-16 \mu\text{atm}$ ) than that for the South Atlantic ( $-6 \mu\text{atm}$ ) and the South Pacific ( $-9 \mu\text{atm}$ ). However, the stronger negative  $\Delta\text{pCO}_2$  in the South Indian is not well understood as discussed in Section 5.2.

The subpolar Southern Ocean between 50° and 62°S (Fig. 16D) has a sea-to-air CO<sub>2</sub> flux in winter and an air-to-sea flux in summer. In this zone,  $\Delta\text{pCO}_2$  is small in magnitude (Fig. 10D) ranging between  $+12 \mu\text{atm}$  in winter (enhanced vertical mixing) and  $-12 \mu\text{atm}$  in summer (biological drawdown). Although this region is mostly within the high wind speed zone (40–60°S), the flux is moderate ranging between  $+1$  (winter) and  $-1 \text{ t-C month}^{-1} \text{ km}^{-2}$  (summer) because of the small  $\Delta\text{pCO}_2$  values.

The "S of 62°S" region represents the seasonal ice-field zone. Although the winter ice field extends as far north as 55°S in the Atlantic sector in some years, the northern extent of the winter sea-ice field may be located around 62°S on the average around Antarctica. Two curves are presented in Fig. 16D for this region:

the black solid curve with open diamonds indicates the flux per km<sup>2</sup> of geographic area including ice covered areas (marked "S of 62S"); and the black dashed curve with solid circles indicates the flux per km<sup>2</sup> of water area exposed to the air in leads and polynyas (marked "S of 62S Water"). Water areas exposed to the air in the monthly mean ice field have been estimated using the ice cover data from the NCEP/DOE AMIP-II Reanalysis (2005). High pCO<sub>2</sub> in sub-ice waters ( $\Delta\text{pCO}_2$  as high as  $+40 \mu\text{atm}$ , Fig. 10D) accounts for the high fluxes. The differences between these curves indicate the effect of the ice cover on the flux. The high potential for CO<sub>2</sub> fluxes estimated for the ice field waters during Antarctic winter is similar to those for the Arabian Sea region in the North Indian Ocean during the Southwest Monsoon months. The global ocean mean uptake flux (Fig. 16D) is about  $0.5 \text{ t-C month}^{-1} \text{ km}^{-2}$  with small seasonal variability.

#### 6.3.4. Comparison with other studies for the Southern Ocean

The sea-air CO<sub>2</sub> flux and  $\Delta\text{pCO}_2$  reported for the Southern Ocean vary over a wide range due primarily to the limited number of seasonal observations over oceanographically complex areas. As discussed in Section 5.3, the larger database used for this study accounts mostly for the differences from Takahashi et al. (2002). In Table 6, the fluxes computed using the earlier database (light numbers marked 0.94M) and the same wind speeds and gas transfer coefficients as used in this study are compared with the flux values (bold numbers marked 3.0M). The Southern Ocean

(50–62°S) sink flux of  $-0.34 \text{ Pg-Cy}^{-1}$  obtained from the 0.94 M database is about six times larger than  $-0.06 \text{ Pg-Cy}^{-1}$  from the 3.0 M database, and this is accounted for by the improved database for  $\Delta p\text{CO}_2$ .

The flux obtained in this paper is smaller than  $-0.17 \text{ Pg-Cy}^{-1}$  estimated by Metzl et al. (2006). Since the 3.0 M database used in this study includes the data used by Metzl et al., the flux difference is primarily attributed to the choice of the gas transfer coefficients and wind speeds. For the gas transfer coefficients, they used a scaling factor of 0.39 (Wanninkhof, 1992), while we used 0.26 (see Section 6.1). If this scaling factor is used, their flux would be reduced to about  $-0.1 \text{ Pg-Cy}^{-1}$ . Differences in wind speed fields used for the respective studies may account for the rest.

McNeil et al. (2007) computed seawater  $p\text{CO}_2$  using the alkalinity (TA) and the total  $\text{CO}_2$  concentration ( $\text{TCO}_2$ ) in seawater, that were parameterized separately as a function of temperature, salinity and nutrients for each of the summer and winter seasons. They reported a  $\text{CO}_2$  sink flux of  $-0.4 \pm 0.25 \text{ Pg-Cy}^{-1}$  over the areas south of 50°S. The large sink flux is a result of negative  $\Delta p\text{CO}_2$ , seasonally averaging about  $-12 \mu\text{atm}$  (seasonal range from +3 to  $-20 \mu\text{atm}$ ) between 50° and 60°S. In contrast, our study gives a mean  $\Delta p\text{CO}_2$  of  $-5 \mu\text{atm}$  (seasonal range from +12 to  $-15 \mu\text{atm}$ ) for the same zone. The discrepancy may be attributed to several reasons. First, the computed  $p\text{CO}_2$  values depends sensitively on the accuracy of estimated values for  $\text{TCO}_2$  and TA: in the sub-Antarctic surface waters,  $(\partial \ln p\text{CO}_2 / \partial \ln \text{TCO}_2)$  ranges from 12 to 15 and  $(\partial \ln p\text{CO}_2 / \partial \ln \text{TA})$  from  $-10$  to  $-13$ . The standard errors of  $\pm 8.5 \mu\text{mol kg}^{-1}$  and  $\pm 8.1 \mu\text{eq kg}^{-1}$  estimated by McNeil et al. for  $\text{TCO}_2$  and TA, respectively should introduce a  $p\text{CO}_2$  error of about 5% or  $\pm 15 \mu\text{atm}$  for each, and a combined error of  $\pm 20 \mu\text{atm}$  if errors in  $\text{TCO}_2$  and TA are uncorrelated. The differences between their  $p\text{CO}_2$  values and ours appear to be within the estimated error limit. Second, the parameterization equation for TA derived by McNeil et al. (2007) shows that TA increases with increasing nitrate concentration. On the other hand, since TA is a representation of ionic charge balance in aqueous solutions, the charge balance requires that TA should decrease with increasing nitrate concentration. Since their parameterization for TA is not consistent with the principle of ionic charge balance, it may yield biased TA values.

Le Quèrè et al. (2007) estimated the time trend of the Southern Ocean  $\text{CO}_2$  sink intensity using an atmospheric transport model for an inversion of the atmospheric  $\text{CO}_2$  concentration data from the Southern Ocean area. They reported that the Southern Ocean sink south of 45°S decreased significantly after 1990, and attributed this to increasing wind speeds that may cause a rise in surface water  $p\text{CO}_2$  due to enhanced vertical mixing of deep waters as well as other associated changes in ocean biogeochemistry. Their flux trend implies that the surface water  $p\text{CO}_2$  increased at a similar or a slightly faster rate than the mean atmospheric rate during the past 15 years. Our winter-month  $p\text{CO}_2$  data for the Southern Ocean surface waters show an increase somewhat faster than the atmospheric  $p\text{CO}_2$  increase rate (Table 5). The results of our analysis for the winter  $p\text{CO}_2$  data are qualitatively consistent with their results.

#### 6.4. Error analysis and the global sea–air $\text{CO}_2$ flux

The reliability of the sea–air  $\text{CO}_2$  flux thus computed depends on the accuracy of the sea–air  $p\text{CO}_2$  difference ( $\Delta p\text{CO}_2$ ) and that of the parameterization for the gas transfer coefficient and the wind speed used in it.

##### 6.4.1. Error estimate for $\Delta p\text{CO}_2$

One standard deviation around a mean  $\Delta p\text{CO}_2$  for  $4^\circ \times 5^\circ$  box is about  $\pm 10 \mu\text{atm}$  on the average over the global oceans. Since

$3 \times 10^6$  measurements were made in 1630 boxes (out of a total of 1759 box areas with a  $4^\circ \times 5^\circ$  grid) over 12 months, the average number of measurements in each box is about 153 per month, although actual numbers vary over a wide range from one box to another. Hence, the average error for monthly mean values for seawater  $p\text{CO}_2$  is about  $\pm 0.8 \mu\text{atm}$  ( $= 10 / (153)^{1/2}$ ). The average error for the atmospheric  $p\text{CO}_2$  (including the effect of barometric pressure) is estimated to be about  $\pm 0.2 \mu\text{atm}$ . We, therefore, estimate that the mean error for  $\Delta p\text{CO}_2$  is about  $\pm 0.9 \mu\text{atm}$  ( $= (0.8^2 + 0.2^2)^{1/2}$ ). On the other hand, the gas transfer coefficient,  $\text{Tr}$ , varies from 0.03 to  $0.12 \text{ g-C}\mu\text{atm}^{-1} \text{ month}^{-1} \text{ m}^{-2}$  with an area-weighted global mean of  $0.05 \text{ g-C}\mu\text{atm}^{-1} \text{ month}^{-1} \text{ m}^{-2}$ . Using the global ocean area of  $326.5 \times 10^6 \text{ km}^2$ , the random error for the global flux is estimated to be about  $\pm 0.2 \text{ Pg-Cy}^{-1}$  ( $= 0.05 \times 0.9 (\mu\text{atm}) \times 12 (\text{months}) \times 326.5 \times 10^{12} (\text{m}^2)$ ). This corresponds to about  $\pm 13\%$  of the net global ocean uptake flux of  $1.4 \text{ Pg-Cy}^{-1}$  estimated by this study.

##### 6.4.2. Error estimate for the sea–air gas transfer coefficient

The sea–air gas transfer piston velocity ( $k$ ) and the transfer coefficient ( $\text{Tr}$ ) (Eq. (8)) depends on the errors for the wind speed and the scaling factor ( $\Gamma$ ). Although the errors in wind speeds are not well quantified, we assume a random error of  $\pm 10\%$  for the wind speeds used in this study. The error for  $\Gamma$  has been estimated to be  $\pm 30\%$  (Sweeney et al., 2007), which affects the  $\text{CO}_2$  flux proportionally. If  $\Gamma$  is set at a constant value, a systematic increase in the wind speed by 10% would increase the global  $\text{CO}_2$  flux by 20% due to the (wind speed)<sup>2</sup> dependence of  $k$  and  $\text{Tr}$ . Since Naegler et al. (2006) pointed out that the product  $\{\Gamma \times [\text{mean of (wind speed)}^2]\}$  is nearly independent of the wind speed fields used, a systematic error of +10% in wind speeds (or +20% in (wind speed)<sup>2</sup>) should be compensated by a reduction of 20% in  $\Gamma$ . Therefore, the effects of systematic errors in wind speeds on the  $\text{CO}_2$  flux are largely cancelled by corresponding changes in  $\Gamma$ . On the other hand,  $\Gamma$  is fixed at 0.26 in our study, and its  $\pm 30\%$  ( $\pm 0.42 \text{ Pg-Cy}^{-1}$ ) uncertainty is largely from sources other than wind speeds. Hence, the error in  $\Gamma$  is considered to be uncorrelated with random errors in wind speeds.

##### 6.4.3. Effects of the seawater $p\text{CO}_2$ rate of change

The sea–air  $p\text{CO}_2$  difference and the  $\text{CO}_2$  flux are affected by the uncertainty in the mean rate of change for surface water  $p\text{CO}_2$  used for normalization of the data to a reference year of 2000. Since the magnitude of corrections is greater for measurements taken longer years away from the reference year, the magnitude of the effects depends on the age distribution of measurements. As seen in Table 5, while a global mean value of  $1.5 \mu\text{atm y}^{-1}$  is used for the normalization of the data to a reference year 2000, the rate appears to be lower in the North Pacific and higher in the North Atlantic than the global mean by  $0.3 \mu\text{atm y}^{-1}$ . Table 7 shows the sensitivity of the regional and global sea–air  $\text{CO}_2$  flux computed for three rates of increase. For a decrease of  $0.1 \mu\text{atm y}^{-1}$  for the entire global ocean, the global sea–air  $\text{CO}_2$  flux increases by about  $0.1 \text{ Pg-Cy}^{-1}$ . However, if a rate of  $1.2 \mu\text{atm y}^{-1}$  is used for the Pacific and  $1.8 \mu\text{atm y}^{-1}$  is used for the Atlantic, the Pacific sink flux increases by  $0.1 \text{ Pg-Cy}^{-1}$  and the Atlantic sink flux decreases by  $0.1 \text{ Pg-Cy}^{-1}$ . Hence the effects cancel each other and the global flux remains unaffected.

Although the geographic coverage is limited for the rate, the results in Table 5 suggest an area-weighted mean of  $1.5 \pm 0.5 \mu\text{atm y}^{-1}$  for the global mean. Taking this as the uncertainty for the global mean rate, we estimate an error of  $\pm 0.5 \text{ Pg-Cy}^{-1}$  (or  $\pm 35\%$ ) for the global ocean sea–air flux.

**Table 7**  
Sensitivity of the rate of increase in surface ocean pCO<sub>2</sub> to the sea–air CO<sub>2</sub> flux.

		Flux (Pg-Cy <sup>-1</sup> )				
		Pacific <sup>a</sup>	Atlantic	Indian	Southern	Global <sup>a</sup>
Change rate 1.2 μatm y <sup>-1</sup>	N of 50°N	-0.03	-0.28			-0.32
	50–14°N	-0.52	-0.24	0.02		-0.74
	14°N–14°S	0.45	0.08	0.09		0.62
	14–50°S	-0.46	-0.25	-0.48		-1.19
	50–62°S				-0.10	-0.10
	S of 62°S				0.00	0.00
Total		-0.56	-0.69	-0.37	-0.09	-1.71
Change rate 1.5 μatm y <sup>-1</sup>	N of 50°N	-0.03	-0.27			-0.30
	50–14°N	-0.51	-0.22	0.02		-0.69
	14–14°S	0.48	0.10	0.10		0.69
	14–50°S	-0.41	-0.29	-0.44		-1.05
	50–62°S				-0.06	-0.06
	S of 62°S				0.01	0.01
Total		-0.46	-0.58	-0.32	-0.05	-1.41
Change rate 1.8 μatm y <sup>-1</sup>	N of 50°N	-0.03	-0.26			-0.28
	50–14°N	-0.48	-0.20	0.03		-0.65
	14°N–14°S	0.51	0.12	0.12		0.75
	14°S–50°S	-0.36	-0.15	-0.41		-0.92
	50–62°S				-0.03	-0.03
	S of 62°S				0.01	0.01
Total		-0.36	-0.48	-0.26	-0.01	-1.12

Each of these rates is used to normalize the data to the reference year 2000: 1.5 μatm y<sup>-1</sup> representing the global mean, and 1.2 and 1.8 μatm y<sup>-1</sup> representing the mean rates observed in the North Pacific and North Atlantic, respectively. The scaling factor of 0.26 for the gas transfer rate and the NCEP-DOE-AMIP II wind speeds are used for the calculation.

<sup>a</sup> Exclude the Bering Sea areas where negative rates are observed.

#### 6.4.4. Error due to undersampling

Systematic biases in surface water pCO<sub>2</sub> and global flux arise from undersampling and our interpolation method. This may be evaluated on the basis of a comparison of the SST values measured in this study with the extensive climatological SST data of Shea et al. (1992). The SST values measured concurrently with seawater pCO<sub>2</sub> are processed using the same space–time interpolation method as used for the seawater pCO<sub>2</sub> data. The differences between our values with the climatological mean for the corresponding months and locations are computed in a SST range from -1.9 to 30 °C and averaged (see Fig. 3 of Takahashi et al., 1997, as an example). For 21,108 pairs of comparison for monthly mean values, that include those for boxes with measurements as well as those interpolated (due to no measurements), the mean difference for (interpolated–climatological mean) is found to be +0.08 °C with a standard deviation of mean of ±0.01 °C (= (1.4 °C standard deviation)/(21,108)<sup>1/2</sup>). For the interpolated boxes only (N = 10,708), the mean difference is +0.13 °C with a standard deviation of mean of ±0.02 °C (standard deviation = ±1.7 °C); and for the boxes with at least one observation (N = 10,400), the mean difference is +0.03 ± 0.01 °C (standard deviation = ±1.0 °C). Assuming that the SST biases reflect biases in calculated surface water pCO<sub>2</sub>, and using an isochemical temperature dependence (∂ln pCO<sub>2</sub>/∂T) of 4.23% °C<sup>-1</sup> (Takahashi et al., 1993), we estimate that the global mean surface water pCO<sub>2</sub> obtained in this study may be biased by about +1.3 μatm (= 350 μatm × 0.0423 °C<sup>-1</sup> × 0.08 °C). This corresponds to a flux bias of 20% (or 0.25 Pg-Cy<sup>-1</sup>) when a global mean transfer coefficient of 0.05 g-C m<sup>-2</sup> μatm<sup>-1</sup> month<sup>-1</sup> is used. Accordingly, our global ocean uptake flux of -1.42 Pg-Cy<sup>-1</sup> may be biased low by about 20%, and could be as large as -1.7 Pg-Cy<sup>-1</sup>.

#### 6.4.5. Error summary

In summary, the net global sea–air flux may be subject to random errors of ±0.18 Pg-Cy<sup>-1</sup> (±13%) from the ΔpCO<sub>2</sub> measurements, ±0.42 Pg-Cy<sup>-1</sup> (±30%) in the scaling factor for the gas transfer piston velocity parameterization, ±0.28 Pg-Cy<sup>-1</sup> (±20%) in wind speeds and ±0.5 Pg-Cy<sup>-1</sup> (±35%) for the mean rate of change in ocean water pCO<sub>2</sub>. A combined precision for the flux is estimated to be ±0.7 Pg-Cy<sup>-1</sup> (= (0.18<sup>2</sup>+0.42<sup>2</sup>+0.28<sup>2</sup>+0.50<sup>2</sup>)<sup>1/2</sup>) or ±53%. Additionally, the net global ocean uptake flux is subject to systematic biases caused by undersampling and the interpolation method used, and may be as large as -1.7 Pg-Cy<sup>-1</sup>. Thus, the best estimate for the climatological mean for the net CO<sub>2</sub> uptake by the global ocean in the reference year 2000 is -1.6 ± 0.9 Pg-Cy<sup>-1</sup>, which includes a possible undersampling correction applied to our direct estimate of -1.4 ± 0.7 Pg-Cy<sup>-1</sup>. Counting the pre-industrial steady-state sea–air CO<sub>2</sub> flux of 0.4 ± 0.2 Pg-Cy<sup>-1</sup> (Sarmiento and Sundquist, 1992; Aumont et al., 2001; Gloor et al., 2003; Bender et al., 2005; Jacobson et al., 2007a), the oceanic uptake flux of CO<sub>2</sub> including anthropogenic CO<sub>2</sub> is -2.0 ± 1.0 Pg-Cy<sup>-1</sup>. In this study, the dependence for the gas transfer rates is taken to be proportional to (wind speed)<sup>2</sup> and only one wind speed product is used. However, the estimated flux depends on the choice of this information.

## 7. Summary and conclusion

A climatological mean distribution for the surface water pCO<sub>2</sub> over the global oceans has been constructed based upon about 3 million measurements for surface water pCO<sub>2</sub> obtained from 1970 to 2007. The observations made in the El Niño periods over the equatorial zone of the Pacific (5°N–5°S) and in coastal waters are excluded from the analysis. The database used for this study is about three times as large as the 0.94 million used for our earlier paper (Takahashi et al., 2002). Since the surface water pCO<sub>2</sub> changed with time and the measurements were made over many years, the global data observed in different years have been corrected to a single virtual reference year 2000 using a mean rate of increase of 1.5 μatm y<sup>-1</sup>, which is consistent with the decadal mean rate of increase in the atmospheric pCO<sub>2</sub>. This is estimated on the basis of a time-trend analysis using deseasonalized surface water pCO<sub>2</sub> data in the North Atlantic, North and South Pacific and Southern Oceans. The pCO<sub>2</sub> values thus corrected to the reference year 2000 are binned into a 4° (latitude) × 5° (longitude) grid and interpolated in space and time using a lateral two-dimensional diffusion–advection equation (Takahashi et al., 1995, 1997), and monthly mean values for the pixels are presented. Thus, the distributions presented in this paper represent the mean non-El Niño conditions adjusted to a reference year 2000. Outside the equatorial Pacific, the effects on pCO<sub>2</sub> of El Niño and the Pacific Decadal Oscillations cannot be identified.

The sea–air pCO<sub>2</sub> difference, ΔpCO<sub>2</sub> is computed as [(climatological mean surface water pCO<sub>2</sub> for each month)–(monthly mean atmospheric pCO<sub>2</sub> in the year 2000)] in each box area. The atmospheric pCO<sub>2</sub> values are computed using the dry-air mol fraction for the year 2000 (GLOBALVIEW–CO<sub>2</sub>, 2006) and the climatological mean values for monthly barometric pressures and sea-surface temperatures. The monthly distributions over the global oceans are presented in Figs. 9 and 10.

The rate constant for the air–sea gas transfer is parameterized as a function of (wind speed)<sup>2</sup>. The scaling factor of 0.26 for long-term (month) mean gas transfer piston velocity is estimated by inverting the bomb <sup>14</sup>C data using Ocean General Circulation models and the 1979–2005 NCEP-DOE AMIP-II Reanalysis (R-2) wind speed data (Sweeney et al., 2007). The net sea–air CO<sub>2</sub> flux is

computed by multiplying the  $\Delta p\text{CO}_2$  and the gas transfer coefficient. Regional mean sea–air flux per unit area varies among the ocean basins (Fig. 16). The high-latitude North Atlantic, including the Nordic seas and portion of the Arctic Sea, is the most intense  $\text{CO}_2$  sink area on the basis of per unit area, with an annual mean of  $-2.5 \text{ t-C month}^{-1} \text{ km}^{-2}$  as a result of the highly negative  $\Delta p\text{CO}_2$  (Fig. 10) and strong winds (Fig. 12). The temperate South Indian Ocean  $14\text{--}50^\circ\text{S}$  has an annual mean of  $-1.1 \text{ t-C month}^{-1} \text{ km}^{-2}$ , which is twice as intense as the corresponding regions of the Atlantic ( $-0.61$  for  $14\text{--}50^\circ\text{S}$ ) and Pacific ( $-0.56$  for  $14\text{--}50^\circ\text{S}$ ). The ice-free sub-Antarctic zone ( $50^\circ\text{S}\text{--}62^\circ\text{S}$ ) has a small mean annual flux as a result of the summer sink flux canceling with the winter source flux. In the seasonal ice-field zone, south of  $62^\circ\text{S}$ , the sea-to-air  $\text{CO}_2$  flux is very high per unit area of waters exposed to the air, but is small for the ice field area as a whole because of the ice cover. As ice fields retreat in springtime, surface waters become a strong sink due to locally intense phytoplankton blooms caused by increased sunlight and abundant nutrients in shallow, low salinity mixed layer. The mean air-to-sea flux for the global oceans is about  $0.4 \text{ t-C month}^{-1} \text{ km}^{-2}$ .

The annual mean for the net sea–air  $\text{CO}_2$  flux over the global oceans and the geographic distribution are summarized in Figs. 13–16 and in Table 5. Of the major ocean basins, the Southern Hemisphere oceans, south of  $14^\circ\text{S}$  to Antarctica, is the largest  $\text{CO}_2$  sink taking up about  $-1.1 \text{ Pg-Cy}^{-1}$ , while the northern oceans north of  $14^\circ\text{N}$  take up about  $-0.7 \text{ Pg-Cy}^{-1}$ . The equatorial oceans,  $14^\circ\text{N}\text{--}14^\circ\text{S}$ , emit  $+0.7 \text{ Pg-Cy}^{-1}$  to the atmosphere. The net uptake flux for the global oceans is estimated to be  $-1.6 \pm 0.9 \text{ Pg-Cy}^{-1}$  counting uncertainties in the  $\Delta p\text{CO}_2$ , scaling factor, wind speeds and rates of change in surface water  $p\text{CO}_2$  as well as errors due to undersampling and interpolation method. Taking the pre-industrial steady-state flux value of  $0.4 \pm 0.2 \text{ Pg-Cy}^{-1}$  into account, the total ocean uptake flux for anthropogenic  $\text{CO}_2$  emissions is estimated to be  $-2.0 \pm 1.0 \text{ Pg-Cy}^{-1}$  in a reference year 2000.

## Acknowledgments

We thank valuable advice and suggestions from Steve Ackley, Nikki Gruber, Doug Martinson, John Shepherd and Christopher Zappa; and constructive suggestions from two anonymous reviewers. Tobias Naegler pointed out the effect of dilution of  $^{14}\text{CO}_2$  by the uptake of fossil fuel  $\text{CO}_2$ . This study has been supported by grants from many national and international government agencies and private foundations. We gratefully acknowledge for the support and encouragements from the US National Science Foundation, National Oceanographic Atmospheric Administration, Department of Energy, National Aeronautical and Space Administration, EXXON Research & Engineering Company, Ford Motor Company and David Packard Foundation, and Raytheon Antarctic Service (the United States); the European Commission (CARBOOCEAN GOCE-511176-1); The Natural Environment Research Council (the United Kingdom); the Australian Climate Change Science Program; and various government agencies and foundations of Belgium, Canada, France, Germany, Iceland, Japan, Norway and The Netherlands. Without the dedication of the sea-going staff from the participating institutions, this study would not be possible. This is a LDEO Contribution no. 7062.

## References

Atlas of Surface Marine Data, 1994. CD-ROM NODC-56, Ocean Climate Laboratory. NOAA, Washington, DC.  
 Aumont, O., Orr, J.C., Monfray, P., Ludwig, W., Amiotte-Suchet, P., Probst, J.-L., 2001. Riverine-driven interhemispheric transport of carbon. *Glob. Biogeochem. Cycles* 15 (2), 393–406.

Bakker, D.C.E., de Baar, H.J.W., Bathmann, U.V., 1997. Changes of carbon dioxide in surface waters during spring in the Southern Ocean. *Deep-Sea Res.* II 44, 91–128.  
 Bakker, D.C.E., Hoppema, M., Schröder, M., Geibert, W., de Baar, H.J.W., 2008. A rapid transition from ice covered  $\text{CO}_2$ -rich waters to a biologically mediated  $\text{CO}_2$  sink in the eastern Weddell Gyre. *Biogeosci. Discuss.* 5, 1205–1235 <[http://www.biogeosciences-discuss.net/papers\\_in\\_open\\_discussion.html](http://www.biogeosciences-discuss.net/papers_in_open_discussion.html)>.  
 Bates, N.R., 2001. Interannual variability of oceanic  $\text{O}_2/\text{N}_2$  changes and biogeochemical properties in the Western North Atlantic subtropical gyre. *Deep-Sea Res.* II 48 (8–9), 1507–1528.  
 Bates, N.R., 2007. Interannual variability of the oceanic  $\text{CO}_2$  sink on the subtropical gyre of the North Atlantic Ocean over the last 2 decades. *J. Geophys. Res.* 112.  
 Bellerby, R.G.J., Hoppema, M., Fahrback, E., De Baar, H.J.W., Stoll, M.H.C., 2004. Interannual controls on Weddell Sea surface water  $f\text{CO}_2$  during the autumn–winter transition phase. *Deep-Sea Res.* I 51, 793–808.  
 Bender, M.L., Ho, D.T., Hendricks, M.B., Mika, R., Bazttle, M.O., Tans, P.P., Conway, T.J., Sturtevant, B., Cassar, N., 2005. Atmospheric  $\text{O}_2/\text{N}_2$  changes, 1993–2002: implications for the partitioning of fossil fuel  $\text{CO}_2$  sequestration. *Glob. Biogeochem. Cycles* 19, GB4017.  
 Broecker, W.S., Takahashi, T., 1966. Calcium carbonate precipitation on the Bahama Banks. *J. Geophys. Res.* 71, 1575–1602.  
 Broecker, W.S., Peng, T.-H., Ostlund, G., Stuiver, M., 1985. The distribution of bomb radiocarbon in the ocean. *J. Geophys. Res.* 90, 6953–6970.  
 Capone, D.G., Burns, J.A., Michaels, A.F., Montoya, J.P., Subramaniam, A., Carpenter, E.J., 2005. Nitrogen fixation by *Trichodesmium* spp.: an important source of new nitrogen to the tropical and subtropical North Atlantic Ocean. *Glob. Biogeochem. Cycles* 19.  
 Chen, G.L., Peng, J.H., Xu, W.X., Goyet, C., Millero, F.J., O'Sullivan, D.W., Eiseheid, G., McCue, S.J., Bellerby, R.G.J., 1998. Temporal variations of  $p\text{CO}_2$  in surface seawater of the Arabian Sea in 1995. *Deep-Sea Res.* I 45, 609–623.  
 Corbière, A., Metzl, N., Reverdin, G., Brunet, C., Takahashi, T., 2007. Interannual and decadal variability of the carbon dioxide and air–sea  $\text{CO}_2$  fluxes in the North Atlantic subpolar gyre. *Tellus B* 59, 168–179.  
 Donlon, C.J., Minnett, P.J., Gentemann, C., Nightingale, T.J., Barton, I.J., Ward, B., Murray, M., 2002. Toward improved validation of satellite sea surface skin temperature measurements for climate research. *J. Clim.* 15, 353–369.  
 Dore, J.E., Lukas, R., Sadler, D.W., Karl, D.M., 2003. Climate-driven changes to the atmospheric  $\text{CO}_2$  sink in the subtropical North Pacific Ocean. *Nature* 424, 754–757.  
 Fairall, C.W., Bradley, E.F., Godfrey, J.S., Wick, G.A., Edson, J.B., Young, G.S., 1996. Cool-skin and warm layer effects on sea surface temperature. *J. Geophys. Res.* 101, 1295–1308.  
 Feely, R.A., Boutin, J., Cosca, C.E., Dandonneau, Y., Etcheto, J., Inoue, H., Ishii, M., LeQuéré, C., Mackey, D.J., McPhaden, M., Metzl, N., Poisson, A., Wanninkhof, R., 2002. Seasonal and interannual variability of  $\text{CO}_2$  in the equatorial Pacific. *Deep-Sea Res.* II 49, 2443–2469.  
 Feely, R.A., Takahashi, T., Wanninkhof, R., McPhaden, M.J., Cosca, C.E., Sutherland, S.C., Carr, M.-E., 2006. Decadal variability of the air–sea  $\text{CO}_2$  fluxes in the equatorial Pacific Ocean. *J. Geophys. Res.* 111, C07S03.  
 Gentemann, C.L., Donlon, C., Stuart-Menteth, A., Wentz, F.J., 2003. Diurnal signals in satellite sea surface temperature measurements. *Geophys. Res. Lett.* 30, 1140.  
 Gibson, J.A.E., Trull, T., 1999. Annual cycle of  $f\text{CO}_2$  under sea-ice and in open ocean water in Prydz Bay, East Antarctica. *Mar. Chem.* 66, 187–200.  
 GLOBALVIEW- $\text{CO}_2$ , 2006. Cooperative atmospheric data integration project—carbon dioxide. CD-ROM, NOAA CMDL, Boulder, CO. [Also available on Internet via anonymous FTP to <ftp.cmdl.noaa.gov>, Path: <ccg/co2/GLOBALVIEW>].  
 Gloor, M., Gruber, N., Sarmiento, J., Sabine, C.L., Feely, R.A., Rodenbeck, C., 2003. A first estimate of present and preindustrial air–sea  $\text{CO}_2$  flux patterns based on ocean interior carbon measurements and models. *Geophys. Res. Lett.* 30.  
 Gibson, J.A.E., Trull, T., 1999. Annual cycle of  $f\text{CO}_2$  under sea-ice and in open ocean water in Prydz Bay, East Antarctica. *Mar. Chem.* 66, 187–200.  
 Gordon, A.L., Chen, C.T.A., Metcalf, 1984. Winter mixed layer entrainment of Weddell deep water. *J. Geophys. Res.* 89, 637–640.  
 Gregg, W.W., Conkright, M.E., Ginoux, P., O'Reilly, J.E., Casey, N.W., 2003. Ocean primary production and climate: global decadal changes. *Geophys. Res. Lett.* 30.  
 Gruber, N., Sarmiento, J.L., 2002. Large-scale biogeochemical–physical interactions in elemental cycles. In: Robinson, A.R., McCarthy, J., Rothschild, B.J. (Eds.), *The Sea*, vol. 12. Wiley, New York, pp. 337–399.  
 Gruber, N., Keeling, C.D., Bates, N.R., 2002. Interannual variability in the North Atlantic Ocean carbon sink. *Science* 298, 2374–2378.  
 Gurney, K.R., Law, R.M., Denning, A.S., Rayner, P.J., Pak, B., the TransCom-3L2 modelers, 2004. TransCom-3 inversion intercomparison: control results for the estimation of seasonal carbon sources and sinks. *Glob. Biogeochem. Cycles* 18, GB1010.  
 Hales, B., Chipman, D.W., Takahashi, T., 2004. High-frequency measurement of partial pressure and total concentration of carbon dioxide in seawater using microporous hydrophobic membrane contactors. *Limnol. Oceanogr. Methods* 2, 356–364.  
 Hales, B., Takahashi, T., 2004. High-resolution biogeochemical investigation of the Ross Sea, Antarctica, during the AESOPS (US JGOFS) Program. *Glob. Biogeochem. Cycles* 18 (3), GB3006.  
 Ho, D.T., Law, C.S., Smith, M.J., Schlosser, P., Harvey, M., Hill, P., 2006. Measurements of air–sea gas exchange at high wind speeds in the Southern Ocean: implications for global parameterization. *Geophys. Res. Lett.* 33, L16611.



- (Version 1.0). ORNL/CDIAC-152, NDP-088. Carbon Dioxide Information Analysis Center, Oak Ridge National Laboratory, US Department of Energy, Oak Ridge, TN, 20pp.
- Thiele, G., Roether, W., Schlosser, P., Kuntz, R., Siedler, G., Stramma, L., 1986. Baroclinic flow and transient-tracer fields in the Canary-Cape Verde Basin. *J. Phys. Ocean.* 16, 814–826.
- Toggweiler, J.R., Dixon, K., Bryan, K., 1989. Simulations of radiocarbon in a coarse resolution world ocean model I: steady state pre-bomb distributions. *J. Geophys. Res.* 94, 8217–8242.
- Wanninkhof, R., 1992. Relationship between wind speed and gas exchange. *J. Geophys. Res.* 97, 7373–7382.
- Wanninkhof, R., McGillis, W.M., 1999. A cubic relationship between gas transfer and wind speed. *Geophys. Res. Lett.* 26, 1889–1892.
- Wanninkhof, R.H., Sullivan, K.F., Top, Z., 2004. Air–sea gas transfer in the Southern Ocean. *J. Geophys. Res.* 109 (C8), C08S19.
- Wanninkhof, R., 2007. The impact of different gas exchange formulations and wind speed products on global air–sea CO<sub>2</sub> fluxes. In: Garbe, C.S., Handler, R.A., Jähne, B. (Eds.), *Transport at the Air Sea Interface: Measurements, Models and Parameterizations*. Springer, Heidelberg, p. 320.
- Ward, B., Wanninkhof, R., McGillis, W.R., Jessup, A.T., DeGrandpre, M.D., Hare, J.E., Edson, J.B., 2004. Biases in the air–sea flux of CO<sub>2</sub> resulting from ocean surface temperature gradients. *J. Geophys. Res.* 109, C8S08.
- Weiss, R.F., 1974. Carbon dioxide in water and seawater: the solubility of a non-ideal gas. *Mar. Chem.* 2, 203–215.
- Weiss, R.F., Price, B.A., 1980. Nitrous oxide solubility in water and seawater. *Mar. Chem.* 8, 347–359.
- Yuan, X., Martinson, D.G., 2000. Antarctic sea ice extent variability and its global connectivity. *J. Clim.* 13, 1697–1717.
- Zhang, X., Cai, W.-J., 2007. On some biases of estimating the global distribution of air–sea CO<sub>2</sub> flux by bulk parameterization. *Geophys. Res. Lett.* 34, L01608.

## 7. Estimating mixed layer nitrate in the North Atlantic Ocean

**T. Steinhoff**, T. Friedrich, S.E. Hartman, A. Oschlies, D.W.R. Wallace, and A. Körtzinger (2009). *Biogeosciences*, 7, 795-807.

My contribution:

- Operating instruments onboard M/V Falstaff and M/V Atlantic Companion.
- Data evaluation and all calculations except calculations regarding the neural network and model data.
- Writing the paper.





## Estimating mixed layer nitrate in the North Atlantic Ocean

T. Steinhoff<sup>1</sup>, T. Friedrich<sup>2</sup>, S. E. Hartman<sup>3</sup>, A. Oschlies<sup>1</sup>, D. W. R. Wallace<sup>1</sup>, and A. Körtzinger<sup>1</sup>

<sup>1</sup>Leibniz Institut für Meereswissenschaften (IFM-GEOMAR), Kiel, Germany

<sup>2</sup>International Pacific Research Center, School of Ocean and Earth Science and Technology, University of Hawaii at Manoa, Honolulu, Hawaii, USA

<sup>3</sup>National Oceanography Centre, Southampton, UK

Received: 29 July 2009 – Published in Biogeosciences Discuss.: 3 September 2009

Revised: 27 January 2010 – Accepted: 23 February 2010 – Published: 1 March 2010

**Abstract.** Here we present an equation for the estimation of nitrate in surface waters of the North Atlantic Ocean (40° N to 52° N, 10° W to 60° W). The equation was derived by multiple linear regression (MLR) from nitrate, sea surface temperature (SST) observational data and model mixed layer depth (MLD) data. The observational data were taken from merchant vessels that have crossed the North Atlantic on a regular basis in 2002/2003 and from 2005 to the present. It is important to find a robust and realistic estimate of MLD because the deepening of the mixed layer is crucial for nitrate supply to the surface. We compared model data from two models (FOAM and Mercator) with MLD derived from float data (using various criteria). The Mercator model gives a MLD estimate that is close to the MLD derived from floats. MLR was established using SST, MLD from Mercator, time and latitude as predictors. Additionally a neural network was trained with the same dataset and the results were validated against both model data as a “ground truth” and an independent observational dataset. This validation produced RMS errors of the same order for MLR and the neural network approach. We conclude that it is possible to estimate nitrate concentrations with an uncertainty of  $\pm 1.4 \mu\text{mol L}^{-1}$  in the North Atlantic.

### 1 Introduction

Estimating seasonal new production is fundamental for our understanding of the global carbon cycle. Especially in regions where nitrate is depleted during summer the amount of nitrate that is available at the onset of the productive season

is essential for further production estimates. Inter-annual changes of the nitrate availability will directly influence new production and carbon drawdown (Koeve, 2001). But estimating nutrient fluxes into the upper ocean and their subsequent utilisation by marine primary production is still a big challenge in oceanography. Even though there are continuous sampling programs at Bermuda Atlantic Time Series (BATS, Bates, 2007) station in the western North Atlantic and European Station for Time Series in the Ocean, Canary Islands (ESTOC, González-Dávila et al., 2007) in the eastern part of the subtropical North Atlantic, it is impossible to map nutrient variability for the whole basin. The mechanism of nutrient supply is very different at the two stations: at BATS it is mainly driven by eddies and at ESTOC by winter convection (Cianca et al., 2007). Furthermore these two stations are located in the subtropical gyre where seasonality is low. In the temperate North Atlantic, between 30° N and 60° N, the coverage of surface nutrient data is sparse especially because of very few wintertime observations. Körtzinger et al. (2008) and Hartman et al. (2010) reported the seasonal cycle of nutrient data for the years 2003/2004 with data from a single location, the Porcupine Abyssal Plain site (PAP), located in the temperate North East Atlantic Ocean (49° N, 16.5° W).

Some work has been done to estimate winter nitrate concentrations from nitrate-density relationships (Garside and Garside, 1995), nitrate-temperature/density relationships (Kamykowski and Zentara, 1986; Sherlock et al., 2007) or to estimate nutrient fields from remotely sensed data (Goes et al., 2000; Kamykowski et al., 2002; Switzer et al., 2003). Several other attempts were made to estimate wintertime nitrate concentration (e.g. Takahashi et al., 1985; Glover and Brewer, 1988; Körtzinger et al., 2001; Koeve, 2001) as the values at the onset of the productive season are crucial to assess new production (Minas and Codespoti, 1993).



Correspondence to: T. Steinhoff  
(tsteinhoff@ifm-geomar.de)

Another possible application of predicting seasonal nutrient cycles, that are not based on climatology, is the parameterization of  $\text{CO}_2$  partial pressure in seawater ( $p\text{CO}_2$ ). Studies have been performed to relate the  $p\text{CO}_2$  in the North Atlantic to remotely sensed data (Lefèvre et al., 2005; Jamet et al., 2007; Lüger et al., 2008; Chierici et al., 2009; Friedrich and Oschlies, 2009a,b; Telszewski et al., 2009) as it is driven by many factors: thermodynamics, biology, mixing and air-sea gas exchange. Chlorophyll *a* (chl-*a*) concentrations are often employed to estimate the biological driver of the  $p\text{CO}_2$ , but the utility of chl-*a* for this purpose is rather limited (Ono et al., 2004; Lüger et al., 2008). Given that nitrate changes are directly related to new production we believe that estimation of the entire seasonal cycle of nitrate could also improve  $p\text{CO}_2$  predictions.

Here we present (and compare) two methods using observational data to estimate mixed-layer nitrate in the North Atlantic between  $40^\circ\text{N}$  and  $52^\circ\text{N}$  and  $10^\circ\text{W}$  and  $60^\circ\text{W}$ . The first method is a multi linear regression (MLR) and the second method used the same data to train a neural network.

However, the quality of any prediction depends on the quality of the predictors. Therefore we chose the variables to be used in the prediction, sea surface temperature (SST) and MLD, very carefully. Reliable and well tested SST products are available (e.g. the Advanced Microwave Scanning Radiometer-EOS (AMSR-E) on NASA EOS Aqua satellite, Emery et al., 2006). The situation is more complicated for MLD because there is no uniform criterion for its estimation. Numerous criteria for the estimation of MLD can be found in the literature (e.g. Kara et al., 2003; de Boyer Montégut et al., 2004) and often the criteria need to be adjusted regionally. The proposed criteria vary from simple temperature difference criteria to advanced methods such as the curvature criterion of Lorbacher et al. (2006) that uses the shape of vertical profiles (temperature or density). For all these criteria temperature/density profiles are required for the MLD estimation. Alternatively, MLD climatologies or MLD estimates from models can be used. In this study we compare MLD calculated from in-situ measured profiles (i.e. by ARGO floats), MLD climatology of Monterey and Levitus (1997), and MLD estimates from two different models (FOAM and Mercator).

## 2 Data and calculations

### 2.1 Discrete water samples

We used data from water samples taken on “Volunteer Observing Ships” (VOS) along a trans-Atlantic route between Europe and North America (Fig. 1a). The studies were part of two European research projects: Carbon Variability Studies by Ships Of Opportunity (CAVASSOO) and CARBOOCEAN. During CAVASSOO (2002/2003) samples were collected from the merchant vessel M/V Falstaff (Wallenius

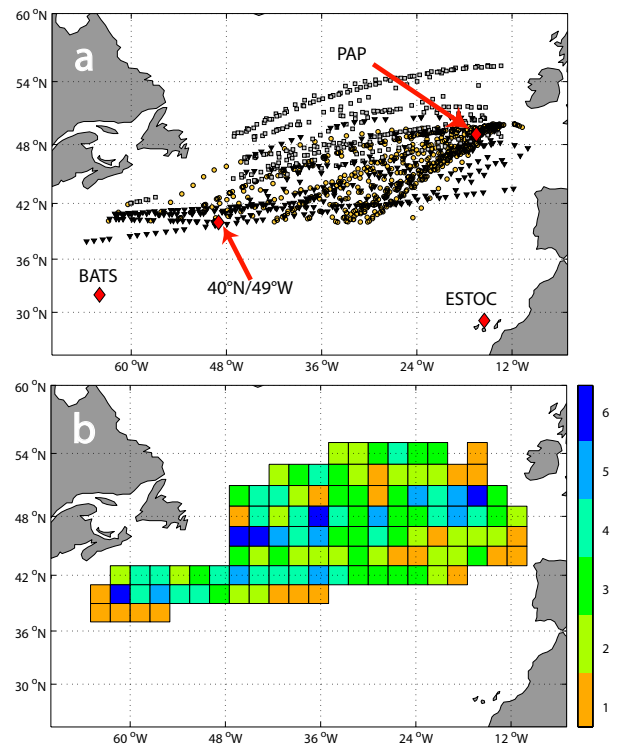


**Fig. 1.** (a) Location of samples used in this study. Triangles denote samples taken in 2002 and 2003 and squares denote samples taken since 2005. For validation purpose we also used data from another VOS line (UK-Caribbean), that was sampled in 2002/2003 by the National Oceanographic Center (NOC), Southampton (circles). The diamonds denote the position of the three time series stations BATS, ESTOC and PAP, as well as one location that is used for demonstration (refer to Fig. 5). (b) Number of month sampled within a  $2^\circ$  Latitude  $\times$   $2.5^\circ$  Longitude box.

Lines, Stockholm, Sweden). The M/V Falstaff was also used at the onset of CARBOOCEAN in 2005 but was changed to a new ship, the M/V Atlantic Companion (Atlantic Container Lines, New Jersey, USA), in 2006. Both ships were outfitted with autonomous instruments that measure  $p\text{CO}_2$  (Lüger et al., 2004). At the same time sea surface temperature (SST) and salinity (SSS) were measured using Seabird thermosalinographs (SBE21 or SBE45) with external SBE38 temperature sensors that were located near the seawater intake. The setup of the sampling line were different on both ships. Onboard M/V Falstaff a 4 m insulated pipe was connected to the small starboard side sea chest, used for the evaporator of the ship, leading to the SBE21. The manifold of the SBE21 was used to divide the water and one line was used for discrete water samples (i.e. nutrients). During CAVASSOO the water flowed to the manifold just by hydrostatic pressure. During CARBOOCEAN a torque-flow pump was installed before the SBE21. Onboard M/V Atlantic Companion a 15 m insulated pipe was connected to a rear starboard

side seachest, that was used only by us. A torque-flow pump was installed near the seachest to pump the water to the sampling site. The water depth of both seachests varied between 4 and 8 m depending on the draught of the ship.

On both ships samples were taken by trained IFM-GEOMAR personnel and we employed the same sampling procedure for the nitrate samples: seawater was drawn into 60 mL plastic bottles that were immediately frozen at  $-18^{\circ}\text{C}$ . The storage and transportation of the samples was no problem because the freezer was next to the sampling point and samples were removed when the ships stopped in Germany. They were transported in cooling boxes to the laboratory and analyzed at the IFM-GEOMAR, Kiel, following the method of Hansen and Koroleff (1999). The overall accuracy of these samples is  $\pm 3\%$  in the range of  $0\text{--}10\ \mu\text{mol L}^{-1}$ . The data were manually inspected for each cruise separately and data were flagged (good, suspicious or bad). In this study we used only data that were flagged “good” and that were taken at water depths deeper than 1000 m, in order to exclude any influence by shelf waters. We used 413 samples (spread over 4 years) from 28 different cruises for our calculation. Figure 1a shows the positions of the samples. The earlier data taken on the M/V Falstaff (black triangles) are located closer to the southern end of the study region, covering a latitudinal band between  $40^{\circ}\text{N}$  and  $50^{\circ}\text{N}$ . The data from the M/V Atlantic Companion (grey squares) are located further to the north between  $45^{\circ}\text{N}$  and  $55^{\circ}\text{N}$ . Figure 1b shows the number of month where data were available in  $2^{\circ}\text{Latitude} \times 2.5^{\circ}\text{Longitude}$  boxes. The maximum number of month with samples per pixel is 6. The cruises are equally distributed over the seasons, so that the linear interpolation approach is an adequate method to fill the gaps between the measured locations.

## 2.2 Mixed layer depth

We compared MLD estimations from the climatology of Monterey and Levitus (1997), the output of two ocean models, and calculated by applying different criteria on vertical temperature profiles measured by the ARGO float network in order to identify the most suitable MLD estimate. The data from the ARGO floats were collected and made freely available by the Coriolis project and programmes that contribute to it (<http://www.coriolis.eu.org>).

### 2.2.1 MLD calculated from ARGO data

We downloaded all profile data available for the time period 2002–2007 in our study region from the ARGO website. All profiles were linearly interpolated onto 5 m depth intervals. MLD was calculated only from temperature profiles for this comparison, because the number of profiles including both temperature and salinity is less than the number of temperature profiles. We note that calculations based on a temperature criterion represent the iso-thermal layer (ILD) which

can be different from the MLD (Kara et al., 2003), but we assume this difference to be negligible for our comparison study. Thomson and Fine (2002) have shown that using temperature related MLD estimates are preferable for biological applications. We used only profiles with at least 10 data points, with the uppermost data points shallower than 15 m. For the specified time period we found more than 23 000 profiles. The MLD was calculated using the commonly used threshold difference method with various  $\Delta T$  ( $\Delta T = 0.2^{\circ}\text{C}$ ,  $0.5^{\circ}\text{C}$  and  $1^{\circ}\text{C}$ ). We used the uppermost data point of each profile ( $\leq 15\text{ m}$ ) as the surface reference temperature. In addition to these simple difference criteria, we also applied the curvature criterion of Lorbacher et al. (2006) that defines the MLD by the curvature of the given profile (temperature or density). We used a Matlab<sup>®</sup> routine that was provided by the authors for the calculation.

### 2.2.2 Climatological MLD

The MLD climatology of Monterey and Levitus (1997) contains monthly MLD fields on a  $1^{\circ} \times 1^{\circ}$  grid for the global ocean. MLD is calculated based on three different criteria: a temperature difference, a density difference, and a variable density change. As previous stated, we used only the data calculated with the temperature difference criterion, which employs a surface-to-depth difference of  $0.5^{\circ}\text{C}$ .

### 2.2.3 Modelled MLD

For the modelled MLD we chose the output from two models: (a) Forecasting Ocean Assimilation Model (FOAM) from the Met Office, UK (<http://www.ncof.co.uk/FOAM-System-Description.html>) and (b) Mercator Project, France ([www.mercator-ocean.fr](http://www.mercator-ocean.fr)). The two models provide daily MLD from 2002 with a spatial resolution of  $1/8^{\circ} \times 1/8^{\circ}$  and  $1/6^{\circ} \times 1/6^{\circ}$ , for FOAM and Mercator, respectively. A difference criterion of  $1^{\circ}\text{C}$  for temperature and  $0.05\ \text{kg m}^{-3}$  for density is used in the FOAM model while difference criteria of  $0.2^{\circ}\text{C}$  and  $0.01\ \text{kg m}^{-3}$  are used for Mercator.

### 2.2.4 Comparison of MLD estimates

We randomly chose 31 temperature profiles from ARGO floats for the comparison, for which we calculated the MLD using the different criteria mentioned above. Figure 2 shows two typical examples of temperature profiles with the various MLD estimates. We also tried to manually identify a best MLD estimate as a reference point by the “eyeball” method, i.e. a phenomenological identification of the MLD. We determined the climatological value and the model data for this specific time and position and calculated the difference between the various MLD estimates and the “eyeball” reference MLD. The mean values for these 31 profiles are shown in Fig. 3. Although the criterion of Lorbacher et al. (2006) appears to yield the best MLD estimate, we decided to use the MLD output from a model for further calculations for the

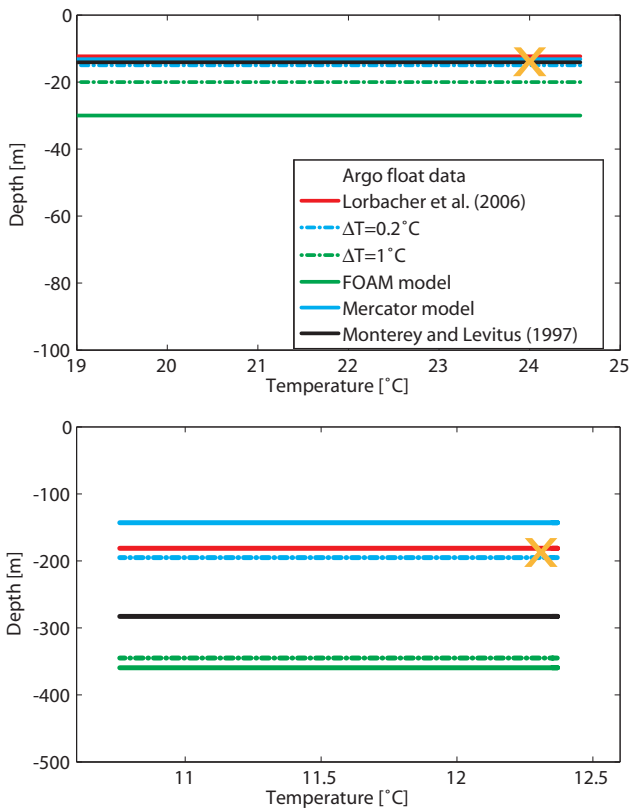


**Fig. 2.** Two examples of vertical temperature profiles from ARGO floats with the MLD assigned using various techniques or sources. The orange Xs denote the eyeball reference MLD. Top: summer temperature profile. Bottom: winter temperature profile.

following reasons: 1) despite the huge number of floats in the ocean (3190 floats in October 2008) the coverage is spatially and temporally sparse compared to the model, 2) existence of a diel cycle in the MLD (Price et al., 1986) may bias MLD estimation when using real profiles. We calculated the difference between the MLD computed with the Lorbacher criterion and the MLD estimations from Mercator and FOAM, respectively ( $\Delta\text{MLD} = \text{MLD}_{\text{Lorb.}} - \text{MLD}_{\text{Model}}$ ). The mean difference was  $-24.2 \pm 104.2$  m (RMSE) for Mercator and  $117.5 \pm 405.2$  m (RMSE) for FOAM and therefore we opted for the MLD from Mercator.

### 2.3 Multiple Linear Regression (MLR)

Our ultimate goal was to develop a predictive equation for mixed layer nitrate on the basis of a minimum number of variables that are publicly available. Our initial list of predictors were the following parameters: SST, MLD, latitude (Lat), longitude (Lon) and time ( $t$ ), where  $t$  is the day of the year. To take into account that the first and the last day of a year have nearly the same influence on our dataset we performed a sinusoidal transformation to the actual day of the year analogous to Nojiri et al. (1999).

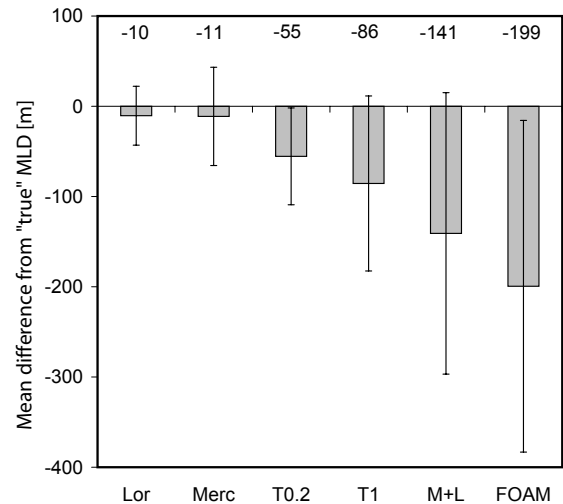


**Fig. 3.** Comparison of MLD estimates. The bars denote the mean difference between the eyeball defined MLD and the respective estimated MLD for 31 profiles. The exact mean differences are shown above each bar. Negative values indicate that the product defines a deeper MLD than the eyeball reference and vice versa. The error bars are the standard deviation ( $1\sigma$ ). Abbreviations: Lor: criterion of Lorbacher et al. (2006), Merc: data from Mercator model, T0.2: temperature difference criterion with  $\Delta T=0.2$  °C, T1: temperature difference criterion with  $\Delta T=1$  °C, M+L: data from Monterey and Levitus (1997) climatology, FOAM: data from FOAM model.

We employed a common logarithmic expression of SST–nitrate relationship because SST shows rather large variability when the nitrate concentration is low (i.e. during summer time). The logarithmic formulation results in a decrease of this non-linear character of the SST. We explicitly used in situ SST and not remotely sensed data to keep the errors associated with the establishment of the algorithm as small as possible. The use of different SST products derived for example from satellites is discussed below.

All MLRs were calculated using the STATISTICA<sup>®</sup> software package (StatSoft, Tulsa, USA). In the first step we used all variables for the MLR (Lat, Lon,  $\log(\text{SST})$ , MLD and  $t$ ). The longitudinal information turned out to be statistically insignificant and we repeated the MLR without longitude. Now all residing variables turned out to be statistically significant. This procedure ensured that the resulting equation includes only a minimum of the available parameters that are necessary to estimate the nitrate cycle. Our set of predictive variables results in the following best-fit equation:

$$\text{NO}_3 = 0.274 \times \text{Lat} - 5.445 \times \log(\text{SST}) + 0.006 \times \text{MLD} + 3.142 \times \sin\left(2\pi \frac{t}{365}\right) + 1.110 \times \cos\left(2\pi \frac{t}{365}\right) - 3.345 \quad (1)$$

where nitrate is in  $\mu\text{mol L}^{-1}$ , SST in °C, MLD in m and  $t$  denotes the day of the year. The MLR used 413 datapoints and the adjusted  $R^2$  value is 0.82.

To study possible improvements by adding chl-*a* data from SeaWifs (<http://oceancolor.gsfc.nasa.gov>) to the initial dataset we performed a MLR with SST, MLD, Lat, Lon, time and chl-*a* as predictors. The chl-*a* data were 8 day composites with 9km resolution (at the equator). The adjusted  $R^2$  value of the resulting equation is also 0.82. A major drawback of adding chl-*a* is the reduction of datapoints for the MLR. Due to the typical clouds above the North Atlantic the cases where we had data for nitrate, MLD and chl-*a* were reduced to 230. Therefore we did not include chl-*a* in the algorithm.

## 2.4 Self-Organizing Map (SOM)

The regression coefficients provide information about physical relationships between nitrate and SST or MLD, respectively, if the predictors of a MLR are independent. The drawback of this method is the limitation to a linear relation and (even for a polynomial regression) the fitting to a predefined function. Therefore, a neural network approach was additionally employed using a self-organizing map. SOMs were introduced to science by Kohonen (1982) and successfully applied to oceanographic data by Lefèvre et al. (2005), Friedrich and Oschlies (2009a,b) and Telszewski et al. (2009). SOMs are able to estimate a target value (e.g. nitrate) from related parameters (e.g. MLD, SST) without fitting to a predefined function by recognizing relationships in the observational data during the training process. The same predictive parameters used in the MLR (Eq. 1) were employed in the SOM.

## 2.5 Algorithm validation

### 2.5.1 Validation against observational data

We performed several tests to evaluate the predictive power of the algorithm for mixed layer nitrate (Eq. 1) and for the SOM estimations. Figure 4 shows that the calculated data (MLR) are generally in good agreement with the measurements, although there are obvious differences in spring and autumn. Negative nitrate values are predicted during the summer when nitrate is depleted but for a simple linear approach allowing for random error the prediction of negative values is the only way to produce a period of zero nitrate. All predicted negative values were set to zero for further calculations. The higher deviations in spring and autumn may arise from small scale variability (patchiness) and cannot be reproduced through our simple MLR approach. By comparing the measured training data with the estimated data it results in a mean underestimation of nitrate of  $0.1 \pm 1.4 \mu\text{mol L}^{-1}$  (RMSE). The same comparison with the algorithm that includes the chl-*a* term leads to an overestimation of  $8.2 \pm 8.3 \mu\text{mol L}^{-1}$  (RMSE), which might be due to the sparse data coverage.

In addition, we randomly chose 100 data points to exclude from the entire dataset and performed a MLR with

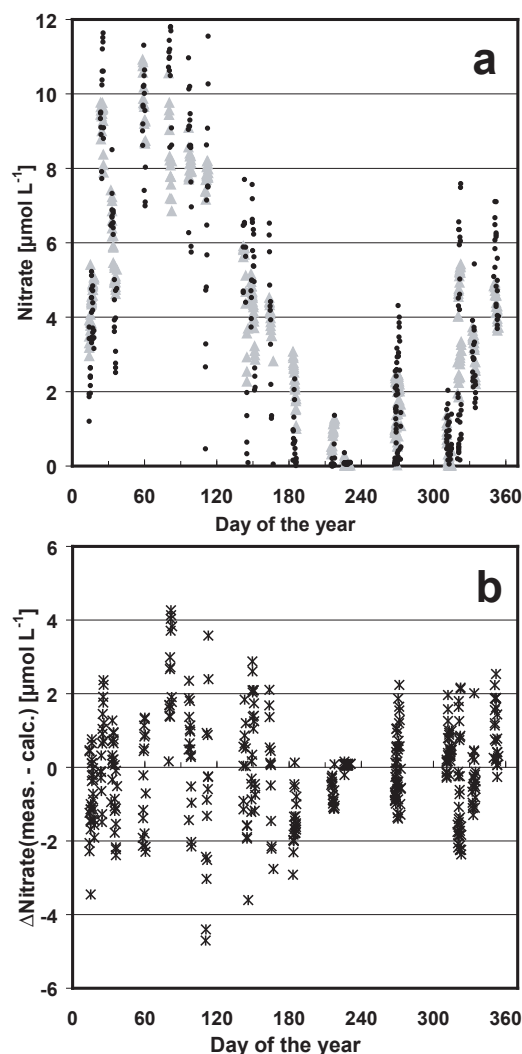


**Fig. 4.** (a) Surface nitrate concentration versus day of the year for all data taken between 2002 and 2007. Black dots are the measured concentrations and grey triangles denote predicted concentrations. (b) Difference between measured and calculated nitrate data. Negative values show overestimation of the MLR with respect to the measured nitrate and vice versa.

the remaining data. The coefficients of the resulting equation were of the same order as the ones in Eq. (1). We used this equation to estimate the nitrate concentration for the 100 data points we deleted for the MLR. We performed this test three times and calculated the mean deviation for the chosen data points each time. The resulting deviations were between  $-0.4 \mu\text{mol L}^{-1}$  and  $0.0 \mu\text{mol L}^{-1}$  with an RMSE of  $1.4 \mu\text{mol L}^{-1}$  for all runs.

We also employed a completely independent data set for comparison. During CAVASSOO the National Oceanography Center, Southampton, UK (NOC) took nitrate samples onboard the VOS M/V Santa Lucia and M/V Santa

Maria, respectively. Both ships were sailing between the UK and Caribbean (Fig. 1) and produced more than 600 nitrate samples between May 2002 and December 2003 in the area north of 40° N. We used the SST from their dataset and the matching MLD from Mercator to estimate corresponding nitrate data with both methods: SOM and MLR. Since we do not have the MLD for all 2002 dates we included only 344 datapoints. In average nitrate was underestimated by  $0.6 \pm 1.2 \mu\text{mol L}^{-1}$  (RMSE) with the MLR and overestimated by  $0.4 \pm 1.5 \mu\text{mol L}^{-1}$  (RMSE) with the SOM. Using only data between 10° W and 50° W (the SOM was trained only in this region) the MLR underestimates nitrate by  $0.5 \pm 1.1 \mu\text{mol L}^{-1}$  (RMSE) and the SOM overestimates it by  $0.3 \pm 1.3 \mu\text{mol L}^{-1}$  (RMSE).

Figure 5 shows the intra and interannual variability of SST, MLD and nitrate concentration for the time period between 2002 and 2007 for two example locations: eastern (49° N, 16.5° W, PAP) and western (40° N, 49° W) North Atlantic. SST and nitrate are also available for a whole annual cycle in 2002/2003 at the PAP site (Körtzinger et al., 2008), resulting in another independent dataset. The West Atlantic location was chosen to illustrate the limitations of a MLR approach because the Labrador current may introduce short term variability on a daily timescale. The corresponding SST and nitrate values measured onboard one of the VOS lines mentioned above were added to the plot if one of the VOS line crossed an area of  $1^\circ \times 1^\circ$  ( $2^\circ \times 2^\circ$ ) latitude/longitude around the location within one day. The annual amplitude of SST is more pronounced in the western region and the short term variability is also higher. The VOS SST measurements are in good agreement with AMSR-E in the eastern region. Deviations can be seen in the westerly region due to the high short term variability there, especially if data are from a  $2^\circ \times 2^\circ$  grid cell. This short term variability at the westerly location also results in deviation of the VOS measured nitrate data from the predicted concentrations.

The MLD amplitude is slightly higher at PAP station. The instruments at PAP were deployed in approximately 30 m depth and Körtzinger et al. (2008) excluded data that were measured below the thermocline. The SST data measured at PAP and from the VOS lines agree with the data from AMSR-E. This results in good agreement between measurements and predicted values of nitrate. In contrast to the measured and SOM estimated nitrate data the (MLR) calculated nitrate data show a smooth seasonality. A comparison of the latter two results in a RMS error of  $0.9 \mu\text{mol L}^{-1}$ . A comparison of the SOM calculated data and the measured values at PAP results in a RMS error of  $1.4 \mu\text{mol L}^{-1}$ . However, the SOM estimates in the western part are in better agreement with the measured data. Figure 5 (second row) shows the difference between MRL estimated nitrate and the other nitrate products. The SOM estimates and the VOS measurements deviate mostly in the same order and direction.

## 2.5.2 Validation using a biogeochemical model

Predicted nitrate concentrations were also validated against nitrate concentrations predicted by a high-resolution nitrogen-based nitrate-phytoplankton-zooplankton-detritus model of the North Atlantic. All model details are described in Oschlies et al. (2000) and Eden and Oschlies (2006). The advantage of this model-based validation is that the model produces daily nitrate fields with a horizontal resolution of  $1/12^\circ \times 1/12^\circ$  latitude/longitude which can be used as a basin wide “ground-truth” to assess the accuracy of the nitrate estimates generated by the MLR and the SOM, respectively. The model output of SST, MLD and nitrate was sampled according to the time (day of the year) and position of the actual nitrate measurements during the period of June 2002 to May 2003, where error of nitrate measurements was not considered. This model-generated data set was then used to calculate a MLR and to train a SOM. The input parameters for both approaches were the same as for the observational data: Lat, SST, MLD and time (day of the year). Monthly mean model outputs of SST and MLD were used to generate nitrate estimates from both methods. Figure 6i shows the annual cycle of nitrate simulated by the model in the domain covered by the nitrate sampling (40° N to 52° N, 10° W to 50° W) and the annual cycle of the nitrate estimates derived from the model-generated data set by the MLR and the SOM, respectively. The general pattern of the annual cycle can be reproduced by the estimates. High winter nitrate concentrations are underestimated. The SOM estimate has a higher accuracy in reproducing the late summer nitrate minimum. It is apparent that the mapping fails in the north-western part of the basin because of the spatial and temporal distribution of the nitrate mapping error (Fig. 6a–d (MLR) and 6e–h (SOM)). This applies for both the MLR and for the SOM. High nitrate values occurring in the Labrador current cannot be reproduced by either estimate. This disparity may be due to the sparse observational coverage of the considered region or to the highly variable current system in this region. The basin wide RMS-error for our model-based validation amounts to  $2.1 \mu\text{mol L}^{-1}$  for the SOM estimate and  $2.2 \mu\text{mol L}^{-1}$  for the MLR estimate which is significantly higher than the error derived from the validation against independent observational data.

## 2.5.3 Error estimation

The uncertainty in nitrate estimation of  $1.4 \mu\text{mol L}^{-1}$  appears for different validation approaches. Therefore we speculate that this is the uncertainty within the training dataset itself that arises for instance from sampling/measurement errors or problems in the water supply (e.g. biofouling). Thus it is impossible to estimate nitrate with an uncertainty better than  $\pm 1.4 \mu\text{mol L}^{-1}$  with the presented algorithm. Another error source can be small scale variability that can not be covered with a simple MLR approach, whereas mesoscale variability

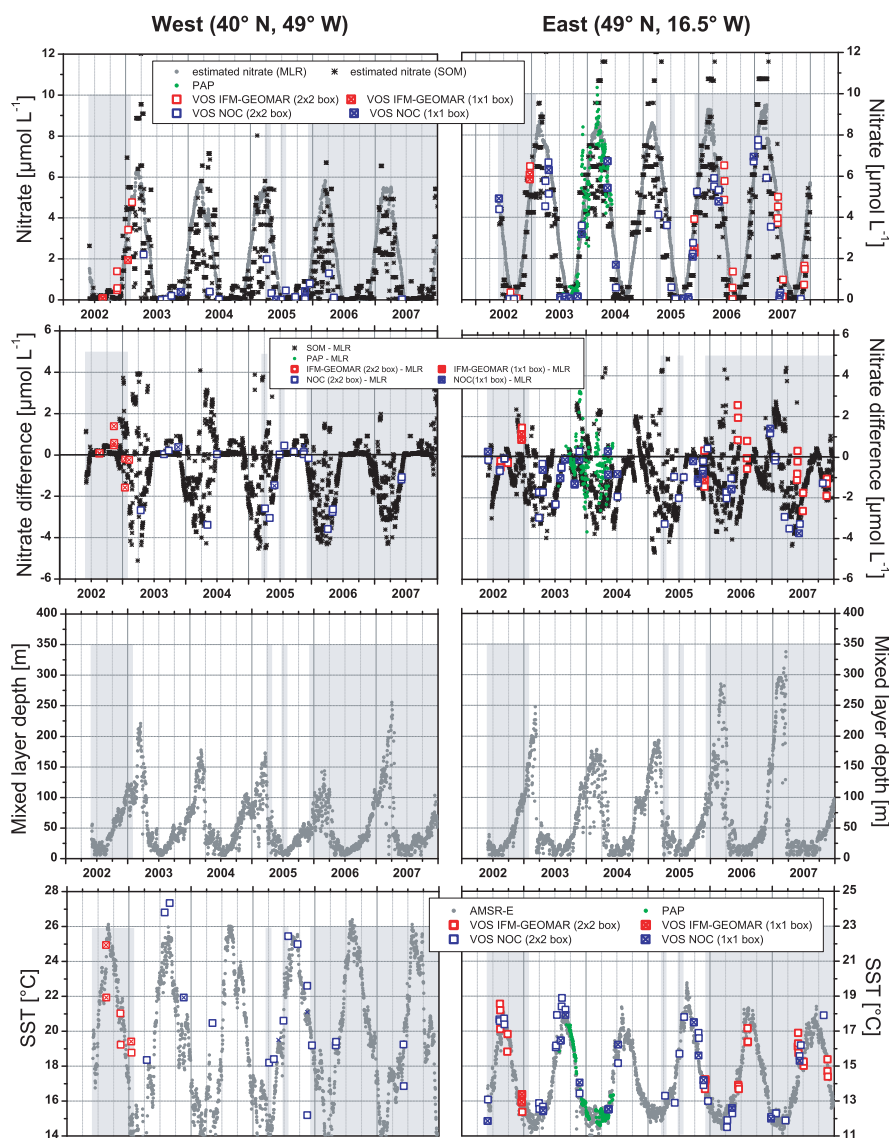


**Fig. 5.** Seasonality of nitrate, MLD and SST for the time period between 2002 and 2007 for a single location in the western and eastern parts (PAP site) of the North Atlantic, respectively. The panels in the first row show the nitrate concentration calculated with the MLR and SOM, respectively. Nitrate measurements from PAP mooring and VOS lines that passed within a  $1^{\circ} \times 1^{\circ}$  and  $2^{\circ} \times 2^{\circ}$  grid cell, respectively, are shown. The panels in the second row show the difference between measured and estimated nitrate using the same data as in the upper panels. Negative values show overestimation of the MLR and vice versa. The panels in the third row show the MLD taken from Mercator (mean value of  $\pm 0.5^{\circ}$  Lat/Lon around the location). The lower two panels show the SST from AMSR-E (mean value of  $\pm 0.5^{\circ}$  Lat/Lon around the location) and measured SST from VOS lines. Also shown are the SST measurements from the PAP site in the eastern part.

should only add random noise to the data. The effect could be seen when we tried to estimate nitrate in the area of the Labrador current (Fig. 6): the uncertainty of the estimates increases rapidly. A minor drawback of a MLR is the linear correlation of the predictors itself. So it is clear that SST is corellated to Lat or time. In oceanography it is a general problem that variables are correlated, but given that each variable influences the result in a different way it was acceptable to use variables that are somehow correlated.

Olsen et al. (2004) analysed the deviation between satellite derived SST and in situ measured SST. They found differences of up to  $1^{\circ}\text{C}$ . The minimum and maximum SST within our dataset is  $5.9^{\circ}\text{C}$  and  $25.6^{\circ}\text{C}$ , respectively. The maximum error would be between 4% and 20%. An error of 20% (4%) in SST would result in an error in nitrate of  $0.4\ \mu\text{mol L}^{-1}$  ( $0.1\ \mu\text{mol L}^{-1}$ ). In contrast, Emery et al. (2006) showed that the Advanced Microwave Scanning Radiometer-EOS (AMSR-E) on NASA EOS Aqua satellite produces SST

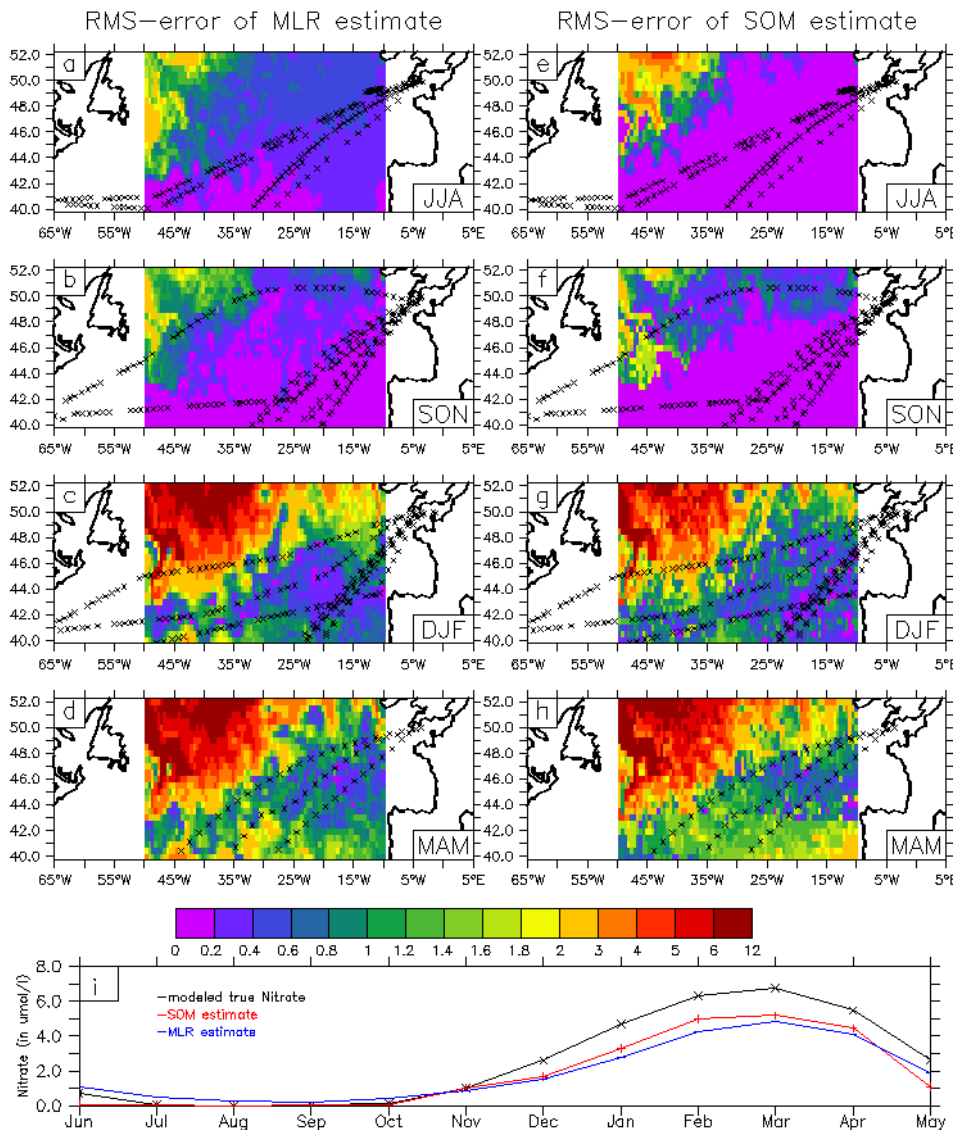


**Fig. 6.** RMS errors for nitrate estimates in  $\mu\text{mol L}^{-1}$  using a MLR (a–d) or SOM (e–h) technique in summer, fall, winter and spring, respectively. (i) Annual cycle of simulated “true” nitrate (black), and nitrate estimates using the SOM (red) or MLR (blue) technique for the region shown in (a–h). RMS errors and annual cycles were calculated using a biogeochemical model.

data that are in good agreement with the in situ measured SST. We suggest that using the temperature from AMSR-E (<http://www.ssmi.com/amr>) will introduce only a small error.

The choice of MLD can lead to huge over- or underestimations of MLD. To assess the influence of over/underestimation of MLD, we calculated the error in nitrate that will arise from an uncertainty of 50 m in the MLD. The resulting error is approximately  $0.3 \mu\text{mol L}^{-1}$ .

### 3 Discussion

#### 3.1 MLD estimations and variability

Our results indicate that it is possible to find a robust MLD estimate with a good temporal and spatial resolution. Although using in-situ profiles results in the best estimation of the MLD at a specific position and time the resolution of the ARGO network is too sparse for reflecting an annual cycle of MLD on the scale of the entire North Atlantic Ocean. In contrast, climatological MLD estimates (e.g. Monterey and Levitus, 1997; de Boyer Montégut et al., 2004) have uniform resolution but do not reflect interannual changes and show



considerable deviations from observations (e.g. tend to significantly overpredict MLD). Using MLD generated by models could be a compromise: data are produced on a daily basis, on a regular grid, and can be in good agreement with observations. Here we compare results from two models since the model dependent differences are large.

For in-situ profiles, such as those measured by floats, the curvature criterion of Lorbacher et al. (2006) results in MLD that are closest to those which are eyeball-defined (Fig. 3). The model output from FOAM yields MLD that are significantly deeper than in-situ observations. This finding is in good agreement with de Boyer Montégut et al. (2004) who, among others, showed that a temperature criterion of 1 °C (see Fig. 2.2.3) is too large for the subpolar North Atlantic. We chose the model output of the Mercator project, as this provides high resolution and MLD that are close to the eyeball-defined MLD.

We examined the variability in the reliably estimated MLD during the entire time period to understand the dynamics in the region. The mixed layer in the subpolar North Atlantic shows a clear seasonality (Fig. 5): during summer the MLD may be only a few tens of meters while, in wintertime, depths greater than 350 m can be reached. We carefully inspected the dynamics of the winter MLD since its deepening supplies nutrients to the sea surface (Oschlies, 2002). This makes the MLD one of the main forcing features in this region's biogeochemistry (Oschlies, 2002). It is well known that the maximum winter MLD increases with latitude and numerous studies have shown that a local maximum in the winter MLD exists between 45° N and 50° N in the North Atlantic (e.g. Koeve, 2001; de Coëtlogon and Frankignoul, 2003). The region of occurrence of the maximum MLD is known to be a region of most intense wintertime ocean heat loss (Marshall, 2005). Due to this rapid cooling at the surface the density rapidly increases and the surface waters along the North Atlantic Drift (NAD) are mixed much deeper than to the north and south of this region. Figure 7 shows the MLD as calculated by Mercator for 10 March, 2006. The maximum MLD along the NAD is clearly visible.

### 3.2 Nitrate estimations

The nitrate data show a clear seasonality (Fig. 4a), with nitrate depletion during summer and the highest values in spring (8–12  $\mu\text{mol L}^{-1}$ ). The data during summer show low variability due to depletion of nitrate in the whole study area. Higher scatter can be observed in the data during the rest of the year. This is probably due to small scale variability of the sampled surface water (patchiness) as well as to the large latitudinal range of the cruise tracks (Fig. 1a).

The validation of the presented algorithm shows that 82% of the nitrate variability is explained by Eq. (1). It turned out that it was a reasonable approach to use a MLR for the 413 datapoints that are spread over 4 years, because the data that were used for the algorithm are distributed over the whole

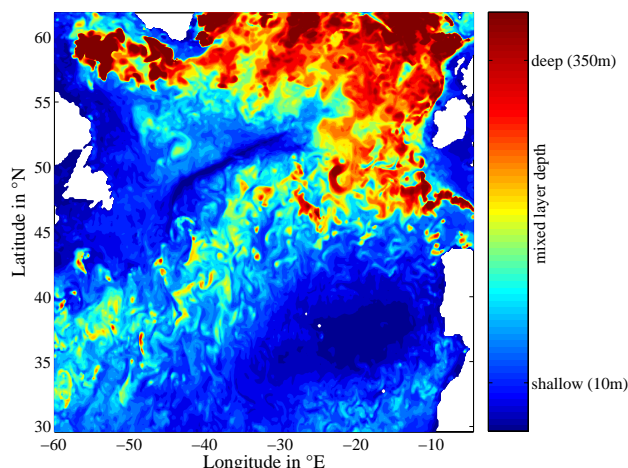
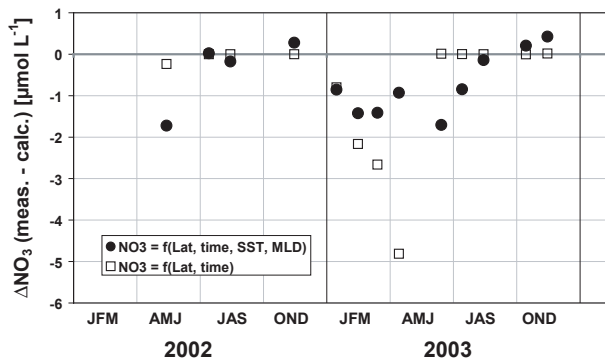


Fig. 7. MLD for 10 March 2006 as calculated by Mercator.

range of the predicting variables (Lat, day of the year, SST and MLD).

As expected, the latitude and time in the MLR-algorithm explain most of the nitrate variability (Garcia et al., 2006). The latitudinal dependence was mentioned in various studies (e.g. Koeve, 2001; Kamykowski et al., 2002) and, together with time, it represents nearly a climatological annual nitrate cycle that is very stable within our study area.

The algorithm can be adjusted to capture the interannually varying conditions by adding SST and MLD (provided they are not taken from climatologies). They reflect the actual conditions that can drive biological production and can change from year to year as well as from one place to another. The MLD appears to be a good indicator of the variable vertical supply of nitrate. Figure 8 shows the difference between measured nitrate and nitrate estimations that were calculated from an equation that uses only Lat and time and from Eq. (1). For this purpose we performed a MLR with the same dataset using only Lat and time as predictors. Then the difference between the measured nitrate concentrations of the independent dataset of the NOC and estimations from the climatological approach and from Eq. (1) were calculated. During most of the year the difference between the algorithm that uses only Lat and time and the one that uses also SST and MLD as predictors is small. But the most interesting time are the winter months (February–March) when MLD reaches its maximum and fresh nitrate is mixed into the surface. Figure 8 shows clearly that both algorithms overestimate the winter nitrate concentration, but the error with the climatological approach is bigger compared to Eq. (1). So we can state that inclusion of SST and MLD shows an improvement that is of the order of the interannual variability. This variability in the nitrate supply that is linked to variability in MLD will result in interannual variations in biological production that will therefore influence the carbon drawdown.



**Fig. 8.** Monthly mean difference between measured and estimated nitrate. The nitrate estimations were made (1) only from Lat and time and (2) with Eq. (1). The measured nitrate data are from the NOC dataset that was not used for the establishment of the algorithm.

The increase in winter time mixed layer between 2004 and 2007 (Fig. 5, third row) in both basins, east and west, results in an increase in nitrate concentrations. Figure 9a–c shows averaged values of the February/March data of MLD, SST and estimated MLR nitrate concentration at PAP site.

Adding chl-*a* to the algorithm did not lead to improvements of the result what might be caused by two factors: (i) the reduction of number of samples from 413 to 230; and (ii) The ratio of converted nitrate to chl-*a* is not a constant ratio (e.g. Hydes et al., 2001; Kähler and Koeve, 2001). At the onset of a bloom where nitrate is high and chl-*a* is low the nitrate consumption is high and particulate organic material has low C/N values (Körtzinger et al., 2001). During the bloom this conversion factor will change due to the reduced availability of nitrate and this change can not be covered by an easy algorithm like the presented one.

The small interannual variations of ca.  $1.5 \mu\text{mol L}^{-1}$  (e.g. Fig. 5) can be explained by the fact that the data fall in nearly one biogeographic province as defined by Oliver and Irwin (2008). Following the classification of Longhurst (2007), our sampling area covers three provinces (Gulf Stream (GFST), North Atlantic drift (NADR) and North Atlantic subtropical gyre (NAST(E)) province). There are certain differences between these provinces, but the ecological processes are primarily driven by the same physical processes. Longhurst (2007) defined 6 cases of physical control, of which GFST and NADR are assigned to the same case: “nutrient-limited spring production peak”. NAST(E) is assigned to another case (“winter-spring production with nutrient limitation”) but these samples contribute only 5% of our dataset and are located at the northern border of the NAST(E) province. As the borders between the certain provinces are not very strict, we can state that our dataset also fits in one biogeographical province as defined by Longhurst (2007).

The overall uncertainty in predicting nitrate with the presented MLR-algorithm and SOM is  $1.4 \mu\text{mol L}^{-1}$ . As this uncertainty appears by different validation approaches we believe that this is the internal uncertainty of the presented dataset. Initially this does not appear to be better than algorithms presented in former studies (e.g. Kamykowski and Zentara, 1986; Garside and Garside, 1995; Goes et al., 2000; Kamykowski et al., 2002; Switzer et al., 2003). But some of them are presenting algorithms only for other regions than the North Atlantic (Goes et al., 2000; Kamykowski and Zentara, 1986) or present gridded estimations on  $10^\circ \times 10^\circ$  grid (Switzer et al., 2003). The algorithm presented by Garside and Garside (1995) is based only on SST and they report a RMSE of  $1.1 \mu\text{mol L}^{-1}$  for their North Atlantic dataset. Applying their equation to our dataset leads to an overestimation of  $1.4 \pm 2.9 \mu\text{mol L}^{-1}$  (RMSE). The algorithm used in this study estimates nitrate with an uncertainty of  $1.4 \mu\text{mol L}^{-1}$ , both for the reproduction of the training dataset itself and for the independent dataset from NOC. This gives confidence in the presented equation. However, here we present one simple algorithm for a whole region that is easy to use and the desired input data (MLD, SST) can be accessed easily. As an example we calculated the annual new production for 2004 at PAP station and compared it with the calculations from Körtzinger et al. (2008). Using the same MLD and C/N ratio as Körtzinger et al. (2008) we calculated the new production to be  $6.5 \pm 2.7 \text{ mol C m}^{-2} \text{ yr}^{-1}$  (their result from measurements was  $6.4 \pm 1.1 \text{ mol C m}^{-2} \text{ yr}^{-1}$ ). Using the MLD estimates from Mercator (the same as used for nitrate estimation) the new production is estimated to be  $2.6 \pm 1.3 \text{ mol C m}^{-2} \text{ yr}^{-1}$ . Note, that the difference between this two calculations is only due to the different MLD estimations. A predictive accuracy of  $1.4 \mu\text{mol L}^{-1}$  is not better than the measurements itself but it offers the potential to estimate nitrate with a sufficient accuracy within the whole study area.

In this study, the SOM predicted nitrate data are not better than the MLR estimates, despite in the regions that were influenced by the Labrador current. This is a clear limitation of an easy MLR approach, as the MLR was trained with data from a different biogeographic province and is not possible to extrapolate the presented equation to different regions. This is the advantage of the SOM as it recognizes the relationship of the predictors at the specific position. We speculate that taking full advantage of the benefits of SOM would require better data coverage. The basinscale validation of the MLR and the SOM against a biogeochemical model produced RMS errors of  $2.1 \mu\text{mol L}^{-1}$  (SOM) and  $2.2 \mu\text{mol L}^{-1}$  (MLR) respectively. These errors are considerably larger than those obtained from the validation against independent observational data. In particular high nitrate values in winter and spring in the Labrador Current region could not have been reproduced by our estimation techniques. This clearly shows the temporal and spatial limitations of the presented method. The predictive potential of both techniques is mostly

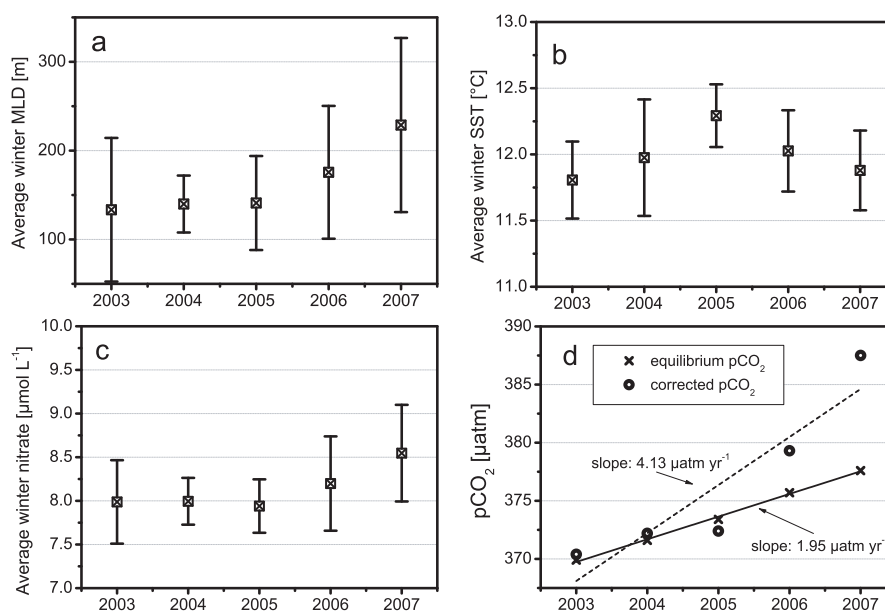


**Fig. 9.** (a–c) Average values of wintertime (February, March) MLD, SST and nitrate estimates from MLR at the location of PAP site. Error bars are standard deviations ( $1\sigma$ ). (d) Seawater  $p\text{CO}_2$  that is in equilibrium with the atmosphere and corrected for the extra amount of DIC associated with the extra nitrate.

restricted to interpolation between lines of observations. For the water masses that could be classified as nearly the same biogeochemical province the interpolations works well, because the training dataset contains data from all seasons in different years. This enabled us to find good estimation results with an easy MLR approach. An extrapolation to water masses not or barely covered by the variability range of the measurements suffers from larger estimation errors. Thus we can state that an extrapolation in time might work sufficiently well, but an extrapolation in space will not work, because of different dependencies (e.g. main nutrient supply in the study region by convection).

### 3.3 Implications of nitrate estimation to $p\text{CO}_2$

We calculated the increase in  $p\text{CO}_2$  that should result from increased nitrate concentration as mentioned above (Fig. 9b): we assume that the nitrate concentration until 2005 constitutes a baseline and that the associated dissolved inorganic carbon (DIC) supply will result in  $p\text{CO}_2$  values that are in equilibrium with the atmosphere. We found that the increased nitrate and the associated increased DIC (calculated from C/N ratio of 7.2, Körtzinger et al., 2001) will result in  $p\text{CO}_2$  values that are increasing faster than in the atmosphere (Fig. 9d). Both rates of  $p\text{CO}_2$  increase are within the range of previous observations (Corbière et al., 2007; Takahashi et al., 2009, and references herein) and we speculate that the observed changes in rates of  $p\text{CO}_2$  increase may be due to the variable winter MLD and, thus, the nitrate supply.

As mentioned above a lot of effort is being made to predict seawater  $p\text{CO}_2$  in the North Atlantic Ocean very precisely using remotely sensed data. One important driving force of the  $p\text{CO}_2$  is the SST due to the thermodynamic effect, that is well known (e.g. Takahashi et al., 1993). But the  $p\text{CO}_2$  is also affected by high biological activity (Watson et al., 1991; Lüger et al., 2004; Körtzinger et al., 2008) especially in the temperate North Atlantic which is hard to assess by remote sensing (Ono et al., 2004; Lüger et al., 2008, and references herein) as satellite chlorophyll data proved to be rather useless as a predictor in their study. As the biological production in the world oceans follows a nearly constant stoichiometry (Redfield et al., 1963) it is easy to calculate the change in DIC from a known nitrate change and subsequently the effect on  $p\text{CO}_2$  can be calculated. Following the MLR approach of other studies but substituting satellite chlorophyll with calculated nitrate using the algorithm presented above has the potential to obtain better  $p\text{CO}_2$  estimates. A residual error of  $1.4 \mu\text{mol L}^{-1}$  in nitrate would still translate, however, into a  $p\text{CO}_2$  error of  $\geq 18 \mu\text{atm}$  what is comparable to the RMSE of the parameterization used by Corbière et al. (2007) ( $17.4 \mu\text{atm}$ ). One could argue in favour of using the MLD and SST twice (first for the nitrate estimation and second for the  $p\text{CO}_2$  estimation) as the SST dependence of  $p\text{CO}_2$  is different from the dependence of nitrate.

This hypothesis has to be tested in future work and also the ongoing research onboard VOS lines will produce more nitrate data that could support and/or improve the presented algorithm and especially the SOM approach will become more important with a larger dataset.

**Acknowledgements.** We thank the captains and crews of M/V Falstaff, M/V Atlantic Companion, M/V Santa Maria and M/V Santa Lucia for their support. We would also like to thank all the people involved in taking/measuring the nitrate samples. Mooring data and support for this research were provided by the European research projects ANIMATE (Atlantic Network of Interdisciplinary Moorings and Time-Series for Europe), MERSEA (Marine Environment and Security for the European Sea) and EUR-OCEANS (European Network of Excellence for Ocean Ecosystems Analysis). This route of M/V Santa Maria and M/V Santa Lucia is used by the CAVASSOO (Carbon Variability Studies by Ships Of Opportunity) project to investigate seasonal and year-to-year variations in carbon fluxes in the North Atlantic. More information on CAVASSOO (EC funded between Nov 2000 and Nov 2003, EC grant number EVK2-CT-2000-00088) is available on: <http://tracer.env.uea.ac.uk/e072/>. This work was supported by the European Commission under the CARBOOCEAN project GOCE 511176-2. The authors thank the Ocean Biology Processing Group (Code 614.2) at the GSFC, Greenbelt, MD 20771, for the production and distribution of the ocean color data. Two anonymous reviewer provided helpful comments.

Edited by: S. W. A. Naqvi

## References

- Bates, N. R.: Interannual variability of the oceanic CO<sub>2</sub> sink in the subtropical gyre of the North Atlantic Ocean over the last 2 decades, *J. Geophys. Res.*, 112, C09013, doi:10.1029/2006JC003759, 2007.
- Chierici, M., Olsen, A., Johannessen, T., Trinañes, J., and Wanninkhof, R.: Algorithms to estimate the carbon dioxide uptake in the northern North Atlantic using shipboard observations, satellite and ocean analysis data, *Deep-Sea Res. II*, 56, 630–639, 2009.
- Cianca, A., Helmke, P., Mouriño, B., Rueda, M. J., Llinás, O., and Neuer, S.: Decadal analysis of hydrography and in situ nutrient budgets in the western and eastern North Atlantic subtropical gyre, *J. Geophys. Res.*, 112, C07025, doi:10.1029/2006JC003788, 2007.
- Corbière, A., Metzl, N., Reverdin, G., Brunet, C., and Takahashi, T.: Interannual and decadal variability of the oceanic carbon sink in the North Atlantic subpolar gyre, *Tellus*, 59B, 168–178, 2007.
- de Boyer Montégut, C., Madec, G., Fischer, A. S., Lazar, A., and Iudicone, D.: Mixed layer depth over the global ocean: An examination of profile data and profile-based climatology, *J. Geophys. Res.*, 109, C12003, doi:10.1029/2004JC002378, 2004.
- de Coëtlogon, G. and Frankignoul, C.: The persistence of Winter Sea Surface Temperature in the North Atlantic, *J. Climate*, 16, 1364–1377, 2003.
- Eden, C. and Oschlies, A.: Adiabatic reduction of circulation-related CO<sub>2</sub> air-sea flux biases in a North Atlantic carbon-cycle model, *Global Biogeochem. Cy.*, 20, GB2008, doi:10.1029/2005GB002521, 2006.
- Emery, W., Brandt, P., Funk, A., and Böning, C.: A comparison of sea surface temperatures from microwave remote sensing of the Labrador Sea with in situ measurements and model simulations, *J. Geophys. Res.*, 111, C12013, doi:10.1029/2006JC003578, 2006.
- Friedrich, T. and Oschlies, A.: Neural network-based estimates of North Atlantic surface pCO<sub>2</sub> from satellite data: A methodological study, *J. Geophys. Res.*, 114, C03020, doi:10.1029/2007JC004646, 2009a.
- Friedrich, T. and Oschlies, A.: Basin-scale pCO<sub>2</sub> maps estimated from ARGO float data – a model study, *J. Geophys. Res.*, 114, C10012, doi:10.1029/2009JC005322, 2009b.
- Garcia, H., Locarnini, R., Boyer, T., and Antonov, J.: Volume 4: Nutrients (phosphate, nitrate, silicate), in: *World Ocean Atlas 2005*, edited by: Ed. NOAA Atlas NESDIS 64, U. G. P. O., S. Levitus, 2006.
- Garside, C. and Garside, J. C.: Euphotic-zone nutrient algorithms for the NABE and EqPac study site, *Deep-Sea Res. II*, 42, 335–347, 1995.
- Glover, D. M. and Brewer, P. G.: Estimates of wintertime mixed layer nutrient concentration in the North Atlantic, *Deep-Sea Res.*, 35, 1525–1546, 1988.
- Goes, J. I., Saino, T., Oaku, H., Ishizaka, J., Wong, C. S., and Nojiri, Y.: Basin scale estimates of sea surface nitrate and new production from remotely sensed sea surface temperature and chlorophyll, *Geophys. Res. Lett.*, 27, 1263–1266, 2000.
- González-Dávila, M., Santana-Casiano, J. M., and González-Dávila, E. F.: Interannual variability of the upper ocean carbon cycle in the northeast Atlantic Ocean, *Geophys. Res. Lett.*, 34, L07608, doi:10.1029/2006GL028145, 2007.
- Hansen, H. and Koroleff, F.: Determination of nutrients, in: *Methods of seawater analysis*, edited by: Grasshoff, K., Kremling, K., and Erhardt, M., Verlag Chemie, Weinheim, Germany, 159–228, 1999.
- Hartman, S. E., Larkin, K. E., Lampitt, R. S., Lankhorst, M., and Hydes, D. J.: Seasonal and inter-annual biogeochemical variations in the Porcupine Abyssal Plain 2003–2005 associated with winter mixing and surface circulation, *Deep Sea Res. II*, In Press, doi: 10.1016/j.dsr2.2010.01.007, 2010.
- Hydes, D., Gall, A. L., Miller, A., Brockmann, U., Raabe, T., Holley, S., Alvarez-Salgado, X., Antia, A., Balzer, W., L.Chou, Elskens, M., Helder, W., Joint, I., and Orren, M.: Supply and demand of nutrients and dissolved organic matter at and across the NW European shelf break in relation to hydrography and biogeochemical activity, *Deep-Sea Res. II*, 48, 3023–3047, 2001.
- Jamet, C., Moulin, C., and Lefèvre, N.: Estimation of the oceanic pCO<sub>2</sub> in the North Atlantic from VOS lines in-situ measurements: parameters needed to generate seasonally mean maps, *Ann. Geophys.*, 25, 2247–2257, 2007, <http://www.ann-geophys.net/25/2247/2007/>.
- Kähler, P. and Koeve, W.: Marine dissolved organic matter: can its C:N Ratio explain carbon overconsumption?, *Deep Sea Res. I*, 48, 49–62, 2001.
- Kamykowski, D. and Zentara, S.-J.: Predicting plant nutrient concentration from temperature and sigma-*t* in the upper Kilometer of the world ocean, *Deep-Sea Res. A*, 33, 89–105, 1986.
- Kamykowski, D., Zentara, S.-J., Morrison, J. M., and Switzer, A. C.: Dynamic global patterns of nitrate, phosphate, silicate, and iron, *Global Biogeochem. Cy.*, 16(4), 1077, doi:10.1029/2001GB001640, 2002.
- Kara, A. B., Rochford, P. A., and Hurlburt, H. E.: Mixed layer depth variability over the global ocean, *J. Geophys. Res.*, 108(C3), 3079, doi:10.1029/2000JC000736, 2003.
- Koeve, W.: Wintertime nutrients in the North Atlantic – new ap-

- proaches and implications for new production estimates, *Mar. Chem.*, 74, 245–260, 2001.
- Kohonen, T.: Self-Organized Formation of Topologically Correct Feature Maps, *Biol. Cybern.*, 43, 59–69, 1982.
- Körtzinger, A., Koeve, W., Kähler, P., and Mintrop, L.: C:N ratios in the mixed layer during the productive season in the northeast Atlantic Ocean, *Deep-sea Res. I*, 48, 661–688, 2001.
- Körtzinger, A., Send, U., Lampitt, R. S., Hartman, S., Wallace, D. W. R., Karstensen, J., Villagarcia, M. G., Llinás, O., and DeGrandpre, M. D.: The seasonal  $p\text{CO}_2$  cycle at 49° N/16.5° W in the northeastern Atlantic Ocean and what it tells us about biological productivity, *J. Geophys. Res.*, 113, C04020, doi:10.1029/2007JC004347, 2008.
- Lefèvre, N., Watson, A. J., and Watson, A. R.: A comparison of multiple regression and neural network techniques for mapping *in situ*  $p\text{CO}_2$  data, *Tellus*, 57B, 375–384, 2005.
- Longhurst, A. R.: *Ecological geography of the sea*, Academic Press, Boston, 2nd edn., 2007.
- Lorbacher, K., Dommenges, D., Niiler, P., and Köhl, A.: Ocean mixed layer depth: A subsurface proxy of ocean-atmosphere variability, *J. Geophys. Res.*, 111, C07010, doi:10.1029/2003JC002157, 2006.
- Lüger, H., Wallace, D. W. R., Körtzinger, A., and Nojiri, Y.: The  $p\text{CO}_2$  variability in the midlatitude North Atlantic Ocean during a full annual cycle, *Global Biochem. Cy.*, 18, GB3023, doi:10.1029/2003GB002200, 2004.
- Lüger, H., Wanninkhof, R., Olsen, A., Trinañes, J., Johannessen, T., Wallace, D., and Körtzinger, A.: The sea-air  $\text{CO}_2$  flux in the North Atlantic estimated from satellite and ARGO profiling data, Tech. rep., NOAA, OAR AOML-96, 2008.
- Marshall, J.: CLIMODE: a mode water dynamics experiment in support of CLIVAR, *Clivar Variations*, 3, No. 2, 8–14, 2005.
- Minas, H. J. and Codespoti, L. A.: Estimates of primary production by observation of changes in the mesoscale nitrate field, *ICES Mar. Sci. Symp.*, 197, 215–235, 1993.
- Monterey, G. and Levitus, S.: *Seasonal Variability of the Mixed Layer Depth for the World Ocean*, in: NOAA Atlas NESDIS 14, US Gov. Printing Office, Wash., DC, 1997.
- Nojiri, Y., Fujinuma, Y., Zeng, J., and Wong, C.: Monitoring of  $p\text{CO}_2$  with complete seasonal coverage utilizing a cargo ship M/S Skaugran between Japan and Canada/US, in: *Proceedings of the 2nd International Symposium  $\text{CO}_2$  in the Oceans*, CGER/NIES, 1999.
- Oliver, M. J. and Irwin, A. J.: Objective global ocean biogeographic provinces, *Geoph. Res. Lett.*, 35, L15601, doi:10.1029/2008/GL034238, 2008.
- Olsen, A., Trinañes, J. A., and Wanninkhof, R.: Sea-air flux of  $\text{CO}_2$  in the Caribbean Sea estimated using *in situ* and remote sensing data, *Remote Sens. Environ.*, 89, 309–325, 2004.
- Ono, T., Saino, T., Kurita, N., and Sasaki, K.: Basin-scale extrapolation of shipboard  $p\text{CO}_2$  data by using satellite SST and  $\text{Chl}_a$ , *Int. J. Remote. Sens.*, 25(19), 3803–3815, 2004.
- Oschlies, A.: Nutrient supply to the surface waters of the North Atlantic: A model study, *J. Geophys. Res.*, 107, 3046, doi:10.1029/2000JC000275, 2002.
- Oschlies, A., Koeve, W., and Garçon, V.: An eddy-permitting coupled physical-biological model of the North Atlantic. Part 2: Ecosystem dynamics and comparison with satellite and JGOFS local studies data, *Global Biogeochem. Cy.*, 14, 499–523, 2000.
- Price, J. F., Weller, R. A., and Pinkel, R.: Diurnal Cycling: Observations and Models of the Upper Ocean Response to, *J. Geophys. Res.*, 91, 8411–8427, 1986.
- Redfield, A. C., Ketchum, B. H., and Richards, F. A.: The influence of organisms on the composition of seawater, in: *The Sea*, Vol. 2, edited by: Hill, M., vol. 2, 26–77, Interscience, New York, 1963.
- Sherlock, V., Pickmere, S., Currie, K., Hadfield, M., Nodder, S., and Boyd, P. W.: Predictive accuracy of temperature-nitrate relationships for the oceanic mixed layer of the New Zealand region, *J. Geophys. Res.*, 112, C06010, doi:10.1029/2006JC003562, 2007.
- Switzer, A. C., Kamykowski, D., and Zentara, S.-J.: Mapping nitrate in the global ocean using remotely sensed sea surface temperature, *J. Geophys. Res.*, 108(C8), 3280, doi:10.1029/2000JC000444, 2003.
- Takahashi, T., Broecker, W. S., and Langer, S.: Redfield Ratio Based on Chemical Data from Isopycnal Surfaces, *J. Geophys. Res.*, 90, 6907–6924, 1985.
- Takahashi, T., Olafsson, J., Goddard, J. G., Chipman, D. W., and Sutherland, S. C.: Seasonal Variation of  $\text{CO}_2$  and Nutrients in the High-Latitude Surface Oceans: a comparative study, *Global Biogeochem. Cy.*, 7, 843–878, 1993.
- Takahashi, T., Sutherland, S. C., Wanninkhof, R., Sweeney, C., Feely, R. A., Chipman, D. W., Hales, B., Friederich, G., Chavez, F., Sabine, C., Watson, A., Bakker, D. C., Schuster, U., Metzl, N., Yoshikawa-Inoue, H., Ishii, M., Midorikawa, T., Nojiri, Y., Körtzinger, A., Steinhoff, T., Hoppema, M., Olafsson, J., Arnarson, T. S., Tilbrook, B., Johannessen, T., Olsen, A., Bellerby, R., Wong, C., Delille, B., Bates, N., and de Baar, H. J.: Climatological mean and decadal change in surface ocean  $p\text{CO}_2$ , and net sea-air  $\text{CO}_2$  flux over the global oceans, *Deep Sea Res. II*, 56, 554–577, doi:10.1016/j.dsr2.2008.12.009, http://www.sciencedirect.com/science/article/B6VGC-4V59VVH-1/2/6c157bd4052048ac211736c038787a3a, surface Ocean  $\text{CO}_2$  Variability and Vulnerabilities, 2009.
- Telszewski, M., Chazottes, A., Schuster, U., Watson, A. J., Moulin, C., Bakker, D. C. E., González-Dávila, M., Johannessen, T., Körtzinger, A., Lüger, H., Olsen, A., Omar, A., Padin, X. A., Ríos, A. F., Steinhoff, T., Santana-Casiano, M., Wallace, D. W. R., and Wanninkhof, R.: Estimating the monthly  $p\text{CO}_2$  distribution in the North Atlantic using a self-organizing neural network, *Biogeosciences*, 6, 1405–1421, 2009, http://www.biogeosciences.net/6/1405/2009/.
- Thomson, R. E. and Fine, I. V.: Estimating Mixed Layer Depth from Oceanic Profile Data, *J. Atmos. Ocean. Tech.*, 20, 319–329, 2002.
- Watson, A. J., Robinson, C., Robinson, J., Williams, P., and Fasham, M.: Spatial variability in the sink for atmospheric carbon dioxide in the North Atlantic, *Nature*, 350, 50–53, 1991.



## 8. Production estimates in the Mauritanian upwelling from gas measurements of CO<sub>2</sub> and N<sub>2</sub>O

### 8.1. Methods

In addition to the  $p\text{CO}_2$  measurements (described in Chapter 2) N<sub>2</sub>O measurements were used for this study. Table 8.1 shows all data and their measurements frequency. Nitrous oxide was determined via a gas chromatograph (GC) with an electron capture detector. A detailed description of the method is given in Walter *et al.* (2004) and Bange *et al.* (1996). N<sub>2</sub>O<sub>sw</sub> was measured using a shower head equilibrator, and with the same GC the atmospheric N<sub>2</sub>O<sub>equ</sub> was determined. The accuracy of the underway measurements was determined to  $\pm 1\%$ .

For the present study additional data sources were employed for parameters such as chl-a, MLD, upwelling index (UI) and atmospheric CO<sub>2</sub> concentration.

Chl-a data were derived from SeaWiFS 8-Day Global 9-km Product (<http://reason.gsfc.nasa.gov/Giovanni/>).

For MLD estimates the model output of the Mercator project (<http://www.mercator-ocean.fr>) was used since it has been shown to be in good agreement with MLD estimates derived by accepted standard criteria applied on profile data (Steinhoff *et al.*, 2010). The model derived MLD was compared with MLD estimated from measured profile data using the criterion of Lorbacher *et al.* (2006) and they are in good agreement. The model output yield one MLD estimate based on a temperature criterion and one based on a density criterion. The mean MLD value of these two was used for each grid cell ( $1/6^\circ$ latitude x  $1/6^\circ$  longitude).

The Pacific Fisheries Environmental Laboratory (PFEL) provides 6-hourly upwelling indices on a  $1^\circ \times 1^\circ$  grid for coastal regions, that are derived from wind stress data ([www.http://www.pfel.noaa.gov/products/PFEL/modeled/indices/upwelling/upwelling.html](http://www.pfel.noaa.gov/products/PFEL/modeled/indices/upwelling/upwelling.html)). The

Parameter	discrete	underway	sampling interval (underway)
Seawater $p\text{CO}_2$		X	1 min
Atmospheric $p\text{CO}_2$		X	5 h
Seawater $\text{N}_2\text{O}$		X	40 min
Equilibrium $\text{N}_2\text{O}$		X	40 min
Dissolved oxygen		X	1 min
SST		X	1 min
SSS		X	1 min
Wind speed		X	1 min
Atmospheric pressure		X	1 min
DIC	X		
$A_T$	X		
Nitrate	X		

Table 8.1.: Measured data that were used in this study. For details please refer to text.

data along  $16.5^\circ\text{W}$  and between  $17.5^\circ\text{N}$  and  $20.5^\circ\text{N}$  were averaged. The data show high fluctuations and an asymmetric running mean of 21 days (19 days back, 1 day ahead) was used. For the calculation of atmospheric  $p\text{CO}_2$   $x\text{CO}_2$  data from GLOBALVIEW- $\text{CO}_2$  (2009) were used. They are in good agreement with our own measurements but do not contain short term fluctuations associated with air mass trajectories that do not significantly influence  $p\text{CO}_{2,\text{sw}}$  because of the longer ASE time scale.  $x\text{CO}_2$  data from two stations were chosen and linearly interpolated between them ( $x\text{CO}_2 = f(\text{Latitude})$ ): Azores (AZR:  $38.77^\circ\text{N}$ ,  $-27.38^\circ\text{W}$ ) and Barbados (RPB:  $13.17^\circ\text{N}$ ,  $59.43^\circ\text{W}$ ).

SSS- $A_T$  relationships were calculated for every cruise using  $A_T$  measurements from discrete samples of the upper 8 m. These relationships were used to calculate  $A_T$  to match the underway dataset. From the calculated  $A_T$  and the measured  $p\text{CO}_{2,\text{sw}}$   $\text{DIC}_{\text{sw}}$  was calculated for every datapoint using the  $\text{CO}_2\text{sys}$  program by van Heuven *et al.* (2009) and observed SST and SSS. A theoretical equilibrium DIC ( $\text{DIC}_{\text{equ}}$ ) was calculated analogously by replacing  $p\text{CO}_{2,\text{sw}}$  with  $p\text{CO}_{2,\text{atm}}$ .

Transfer velocities  $k$  were calculated for  $\text{N}_2\text{O}$  and  $\text{CO}_2$  using the parameterization of Wanninkhof and McGillis (1999).

We used the  $\text{N}_2\text{O}$  data to estimate the time  $\tau$  that has passed since a water parcel had upwelled, i.e. highest observed  $\text{N}_2\text{O}_{\text{sw}}$  concentrations denote freshly upwelled water and thus the origin of the time axis ( $\tau=0$ ).

Furthermore  $\text{N}_2\text{O}$  serves as a central variable for the NCP calculations and the relationships be-



	<b>P320</b>		<b>M68-3</b>		<b>P399-2</b>	
	$r^2$	RMSE	$r^2$	RMSE	$r^2$	RMSE
<b>regression parameters</b>						
$N_2O_{\text{equ}}$ [nmol L <sup>-1</sup> ]	0.91	0.09	0.81	0.11	0.96	0.26
Equilibrium DIC [ $\mu\text{mol kg}^{-1}$ ]	0.87	3.6	0.76	5.1	0.27	14.06
$A_T$ [ $\mu\text{mol kg}^{-1}$ ]	0.52	1.53	0.76	1.16	0.54	1.82
Salinity	0.52	0.01	0.76	0.03	0.54	0.04
SST [°C]	0.91	0.37	0.84	0.53	0.70	1.15
<b>mean values</b>						
MLD [m]	25 ( $\pm 10$ )		13 ( $\pm 5$ )		18 ( $\pm 6$ )	
$k_{N_2O}$ [cm h <sup>-1</sup> ]	14.7 ( $\pm 5.8$ )		3.5 ( $\pm 6.3$ )		14.2 ( $\pm 8.1$ )	
$k_{CO_2}$ [cm h <sup>-1</sup> ]	15.0 ( $\pm 6.0$ )		3.6 ( $\pm 6.5$ )		14.5 ( $\pm 8.3$ )	

Table 8.2.: Regression parameters and root mean square errors (RMSE) for parameters that were estimated from  $N_2O_{\text{sw}}$  concentrations. Note that there is no biogeochemical reason for the fits and they were exclusively used to match  $N_2O_{\text{sw}}$  values with corresponding values of regressed variables. The lower part shows mean values of the parameters that couldn't be parameterized and had to be taken as averages. The values in parentheses are the standard deviations.

tween  $N_2O$  and various variables that were needed for our calculation were determined:  $N_2O_{\text{equ}}$ ,  $DIC_{\text{equ}}$ ,  $A_T$ , SSS, SST,  $k_{N_2O}$ ,  $k_{CO_2}$  and MLD (cf. Table 8.2). Linear relationships were used where suitable otherwise the mean value was used. Fig. 8.1 shows the relationship and the regression lines exemplary for SST.

Relating  $N_2O_{\text{equ}}$  to  $N_2O_{\text{sw}}$  is a sort of circular argument, when calculating ASE. But all found relationships have no biogeochemical meaning and were only used for the following calculation.

**Calculation of NCP** To perform the following calculation three major assumptions had to be made: (1) Vertical mixing is neglected as it is assumed to be small compared to ASE and biological drawdown. (2) The highest  $N_2O_{\text{sw}}$  concentration and the associated  $pCO_{2,\text{sw}}$  are taken as representative for freshly upwelled water for the whole study area (i.e. all sampled surface waters are assumed to have started with these values). (3) The observed decrease in  $N_2O_{\text{sw}}$  is only due to ASE while  $pCO_{2,\text{sw}}$  is influenced by ASE and biology, i.e once in the mixed layer  $N_2O$  is chemically inert.

Fig. 8.2 illustrates the calculations that were performed to derive NCP for every cruise:

**(a) Iterative calculation of  $N_2O$  air-sea equilibration time scale**

The dataset was searched for highest  $N_2O_{\text{sw}}$  concentration (red marker) and it was confirmed that the location of this point was indeed in the upwelling region. Using the average MLD the

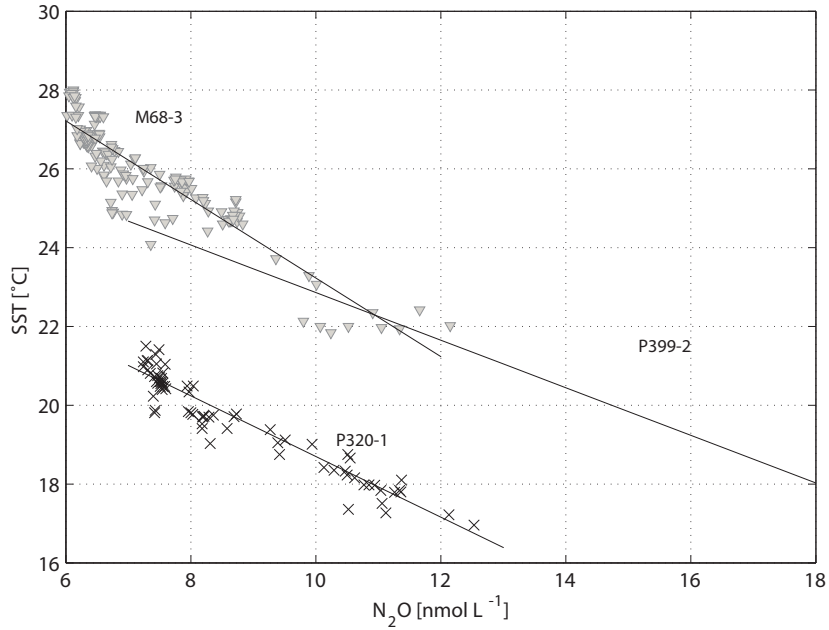


Figure 8.1.: SST- $N_2O$  relationships for the different cruises.

concentration was converted into a mixed layer inventory (Eqn. 8.1):

$$N_2O_{inv} = N_2O_{sw} \times MLD \quad (8.1)$$

Next, the daily ASE fluxes for  $N_2O$  were calculated based on  $\Delta N_2O$  ( $N_2O_{sw} - N_2O_{equ}$ ):

$$F_{N_2O} = k_{N_2O} \times \Delta N_2O \quad (8.2)$$

where  $k_{N_2O}$  is the transfer coefficient for  $N_2O$  at SST (Table 8.2). SST and  $N_2O_{equ}$  were calculated from  $N_2O_{sw}$  as described in the "Calculated data"-section. Subtracting the daily loss of  $N_2O$  due to ASE from the inventory resulted in a new inventory which was converted back into  $N_2O_{sw}$  concentration using MLD. These daily inventory/flux cycle calculations were performed until the time  $\tau_{max}$  when  $\Delta N_2O$  was less than  $0.1 \text{ nmol L}^{-1}$ , i.e.  $N_2O$  air-sea equilibrium was practically reached. The resulting temporal evolution of the  $N_2O_{sw}$  concentrations are shown in Fig. 8.2(a). A function was fitted to these  $N_2O$  data and a value for  $\tau$  was assigned to each measured  $N_2O_{sw}$  value.

### (b) Application of time stamp to DIC data

With the results from (a)  $\tau$  was assigned to each  $DIC_{sw}$  value where both,  $DIC_{sw}$  and  $N_2O_{sw}$ , measurements were available. An exponential function was then fitted to the data (Fig. 8.2(b)).

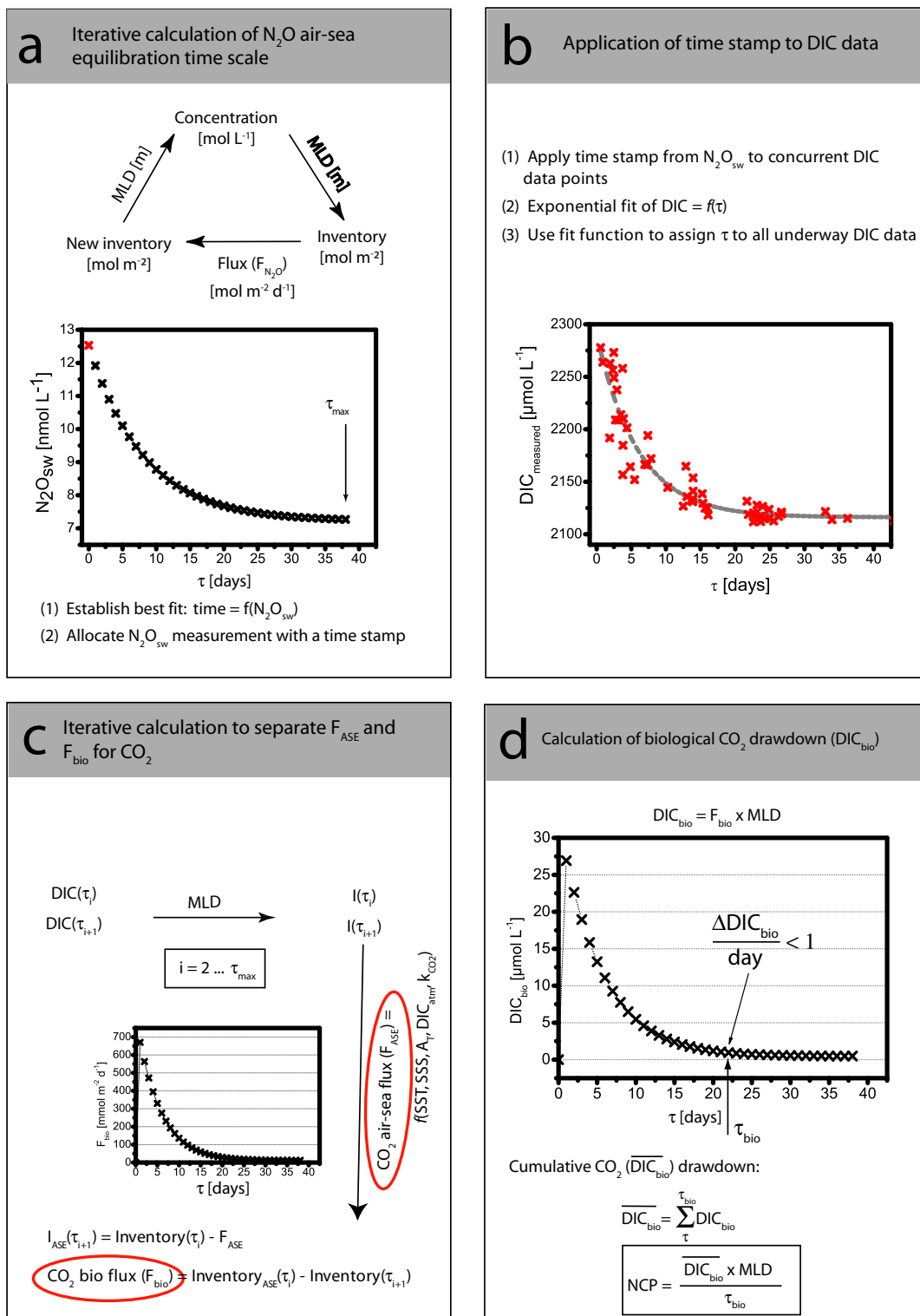


Figure 8.2.: Calculation scheme to obtain NCP. The red marked values are measured data, the black ones were calculated. For details please refer to text. The data were from P320/1.

With this function a value of  $\tau$  was assigned to every  $\text{DIC}_{\text{sw}}$  value even when no concurrent  $\text{N}_2\text{O}_{\text{sw}}$  value was available.

**(c) Iterative calculation to separate  $F_{\text{ASE}}$  and  $F_{\text{bio}}$  for  $\text{CO}_2$**

With the results from (a) and (b) the  $\text{CO}_2$  ASE flux per day was calculated: Starting with  $\text{DIC}_{\text{sw}}$  values at day 1 and 2 (i.e.  $\tau_1$  and  $\tau_2$ ) these values were converted into inventories  $I$  ( $I(\tau_1)$  and  $I(\tau_2)$ ). Matching values for  $\text{DIC}_{\text{equ}}$ ,  $A_{\text{T}}$ , SSS and SST were calculated from  $\text{N}_2\text{O}_{\text{sw}}$  at  $\tau_1$  (cf. Table 8.2) and the  $\text{CO}_2$  ASE flux  $F_{\text{ASE}}$  was calculated. A new inventory was calculated that was influenced only by air sea gas exchange (Eqn. 8.3):

$$I_{\text{ASE}}(\tau_2) = I(\tau_1) - F_{\text{ASE}} \quad (8.3)$$

The difference between  $I_{\text{ASE}}(\tau_2)$  and  $I(\tau_2)$  is the amount of  $\text{CO}_2$  that was consumed by biology (8.4) during this time step:

$$F_{\text{bio}} = I_{\text{ASE}}(\tau_2) - I(\tau_2) \quad (8.4)$$

This cycle was repeated for every one day time step until reaching  $\tau_{\text{max}}$ . The resulting daily biological flux,  $F_{\text{bio}}$ , is shown in Fig. 8.2(c).

**(d) Calculation of biological  $\text{CO}_2$  drawdown ( $\text{DIC}_{\text{bio}}$ )**

MLD was used to calculate the amount of biological  $\text{CO}_2$  drawdown (Fig. 8.2):

$$\text{DIC}_{\text{bio}} = \frac{F_{\text{bio}}}{\text{MLD}} \quad (8.5)$$

When the change of  $\text{DIC}_{\text{bio}}$  per day was less than  $1 \mu\text{mol L}^{-1}$  this day was defined as the end of the upwelling mediated productive period  $\tau_{\text{bio}}$ . The overall amount of  $\text{CO}_2$  that was consumed by biology is the sum of all daily estimates of  $\text{DIC}_{\text{bio}}$  until  $\tau_{\text{bio}}$ :

$$\overline{\text{DIC}_{\text{bio}}} = \sum_{\tau=1}^{\tau_{\text{bio}}} \text{DIC}_{\text{bio}}(\tau) \quad (8.6)$$

NCP was calculated:

$$\text{NCP} = \overline{\text{DIC}_{\text{bio}}} \times \text{MLD} \times \frac{1}{\tau_{\text{bio}}} \times 0.012 \quad (8.7)$$

where NCP is in  $\text{g C m}^{-2} \text{d}^{-1}$ ,  $\overline{\text{DIC}_{\text{bio}}}$  in  $\text{mmol m}^{-3}$ , MLD in m and  $\tau_{\text{bio}}$  in days. The factor 0.012 converts to gravimetric units of carbon. The resulting NCP values and corresponding values for

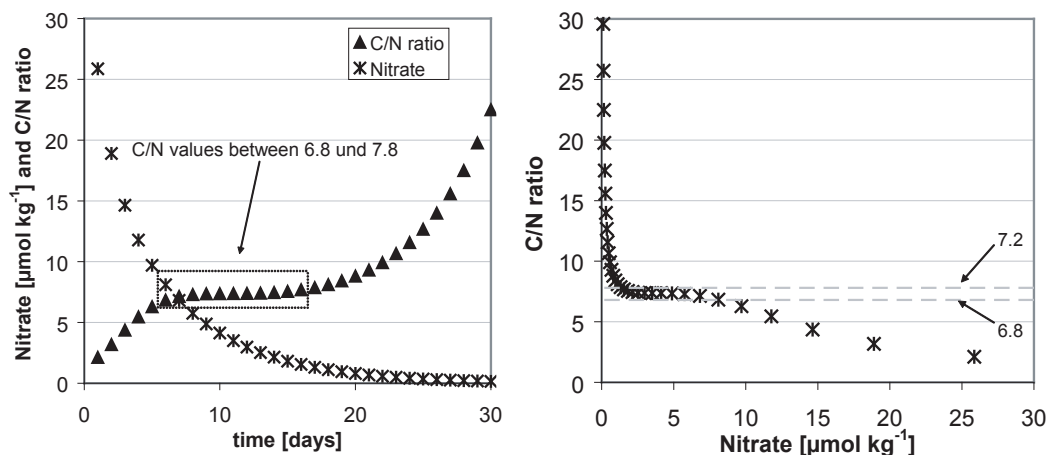


Figure 8.3.: Nitrate drawdown during P320/1. The data were calculated by an exponential fit that was applied to the measured data. Also shown are the C/N values of the daily decrease of nitrate and CO<sub>2</sub>.

$\tau_{\text{bio}}$  for the different cruises are shown in Table 8.3.

	P320-1	M68-3	P399-2
duration of biological drawdown [d]	18 ± 6	28 ± 9	11 ± 4
NCP [g C m <sup>-2</sup> d <sup>-1</sup> ]	2.8 ± 0.9	0.4 ± 0.1	2.0 ± 0.6

Table 8.3.: Duration of the biological drawdown and the resulting NCP.

**Carbon-to-nitrogen ratios of NCP** The observed nitrate concentrations were regressed on  $N_2O_{\text{sw}}$  and  $N_2O_{\text{sw}} = f(\tau)$  was used to attach a time stamp to the nitrate data. By comparison with  $\text{DIC}_{\text{bio}}$  we could estimate the C/N ratio of the biological uptake as a function of time (Eqn. 8.8, Fig. 8.3):

$$\text{C/N} = \frac{\Delta \text{DIC}}{\Delta \text{NO}_3^-} \quad (8.8)$$

$\Delta \text{DIC}$  and  $\Delta \text{NO}_3^-$  are the daily concentration changes of DIC and nitrate, respectively.

**Error assessment** Due to the complex calculation scheme it is hard to assess a single error estimate for each calculation step. However, the RMS errors that arise from the fitting functions were studied and they turned out to be small (< 5%). Larger uncertainties are introduced by the estimation of transfer velocity  $k$ . Therefore a sensitivity test was performed where we calculated

NCP with extreme values of  $k$  (i.e. for P320-1 we used a  $k_{\text{N}_2\text{O}}$  ( $k_{\text{CO}_2}$ ) of 8.9 (9)  $\text{cm h}^{-1}$  and 20.5 (21)  $\text{cm h}^{-1}$ ). This resulted in an uncertainty of 23% for the NCP estimates and of 32% for the estimate of the duration of biological drawdown (Table 8.3).

## 8.2. Results and Discussion

The different upwelling patterns can be seen clearly in Fig. 8.4. The colorscale for each variable was kept unchanged between panels. During P320/1 and P399/2 which took place in late winter and late spring, respectively, low SST ( $<20^\circ\text{C}$ ) along the coast of Mauritania indicates upwelled water masses. As the water moves away from the coast it warms and approaches SST typical for open ocean waters in the region. During M68/3, which took place in summer, i.e during the non-upwelling period, SST is nearly uniformly high ( $26\text{--}28^\circ\text{C}$ ) throughout the entire study area except in a small coastal stretch in the north-eastern part of the cruise track. This part is located at the northern end of the study region, off Cape Blanc. These observations are in good agreement with the study of Schemainda *et al.* (1975) and Wooster *et al.* (1976), who report constant upwelling in this region throughout the year. The upwelled water masses display elevated concentration of  $\text{CO}_2$  and  $\text{N}_2\text{O}$  with respect to atmospheric levels. Both  $p\text{CO}_{2,\text{sw}}$  and  $\text{N}_2\text{O}_{\text{sw}}$  show intensive supersaturation along the coast during P320/1 and P399/2 and nearly equilibrated waters during M68/3. Especially the southern part of the coastal upwelling shows a strong seasonality (Wooster *et al.*, 1976) and we speculate that P399/2 took place while the upwelling shifts to the south.

Fig. 8.5 shows the deconvoluted  $\text{CO}_2$  fluxes exemplary for P320/1 and M68/3. As expected, the fluxes both due to ASE and NCP, are larger during P320/1 (intense upwelling) than during M68/3 (weak or near absent upwelling).

In both cases the biologically mediated  $\text{CO}_2$ -flux is an order of magnitude greater than the ASE flux. As soon as the upwelled water masses reach the euphotic zone, strong biological production starts and maintains these large biological  $\text{CO}_2$  fluxes.

The biological signal is reflected also in the nitrate data: During P320/1 nitrate concentrations were up to  $18 \mu\text{mol L}^{-1}$  near the coast in the upwelling band. Fig. 8.3 illustrate that as long as nitrate is replete the C/N ratio is lower than the canonical Redfield ratio of 6.6 (Redfield *et al.*, 1963) to 7.3 (Anderson and Sarmiento, 1994), a situation that can be characterized as nitrogen overconsumption. The C/N ratio increases with time until nitrate concentration reach moderate levels between 2 and  $8 \mu\text{mol L}^{-1}$ . During this time the C/N ratio reaches a plateau

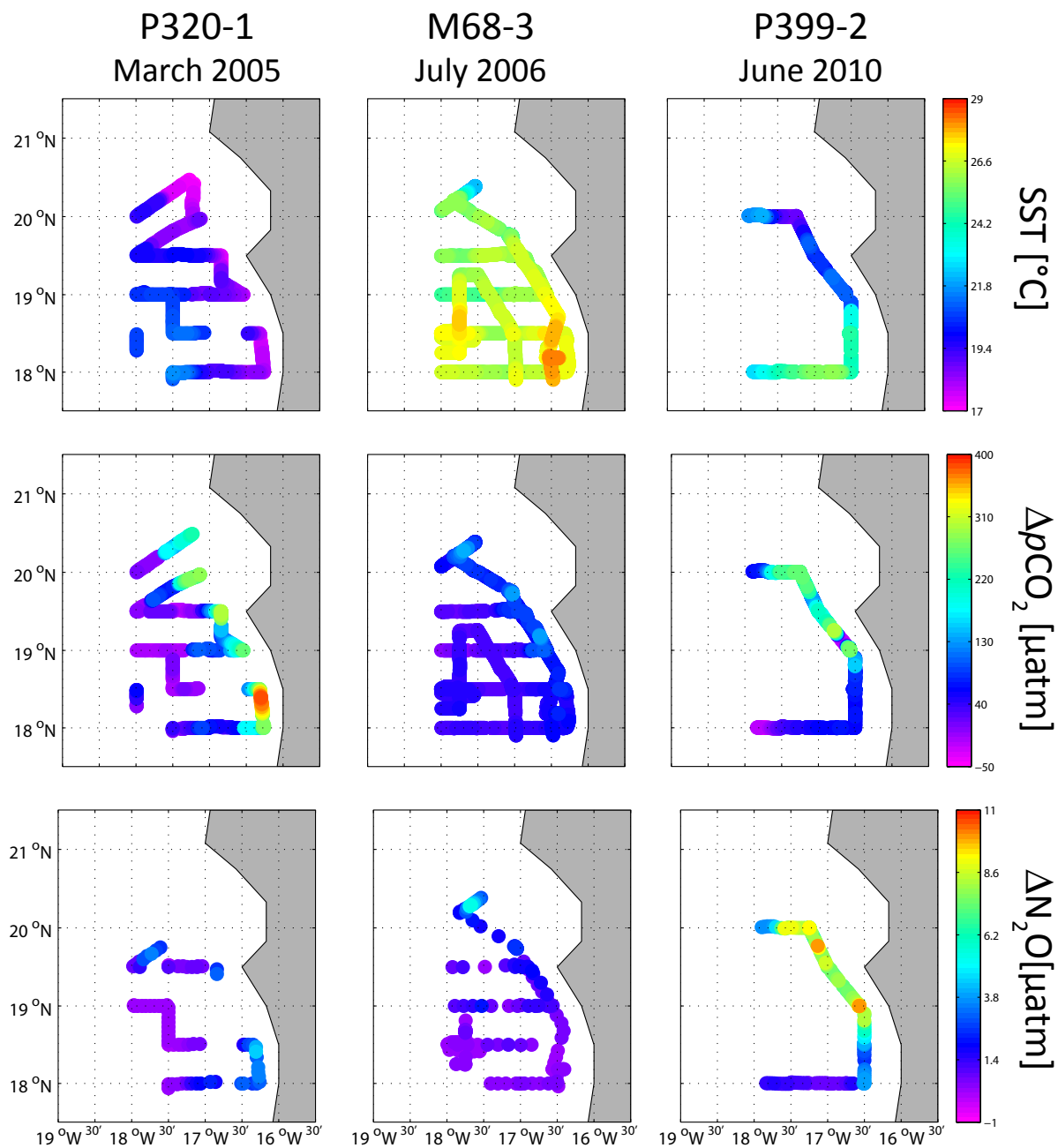


Figure 8.4.: Surface data of SST,  $\Delta p\text{CO}_2$  and  $\Delta \text{N}_2\text{O}$ . For better comparison the color range of each parameter is the same for all three cruises.

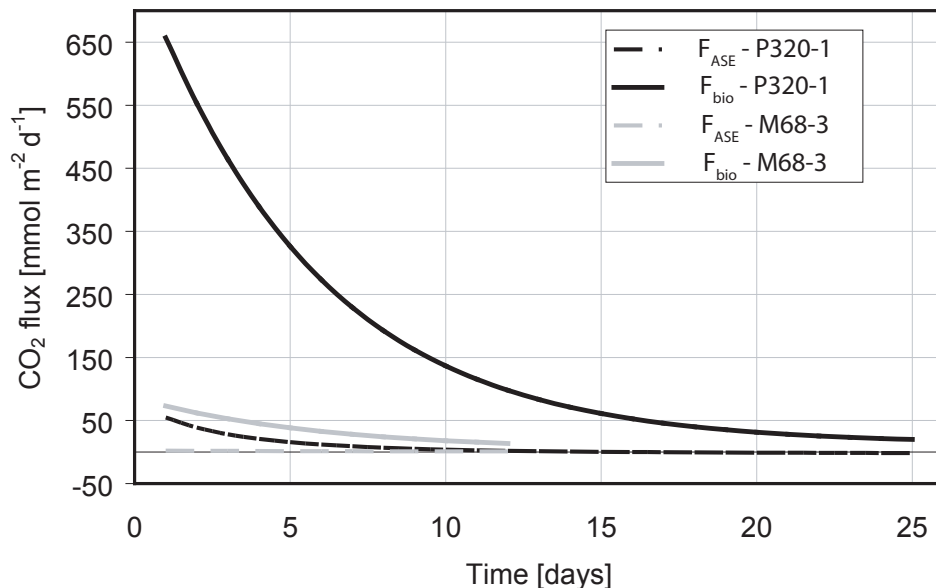


Figure 8.5.: CO<sub>2</sub> flux due to ASE and biological production during P320/1 and M68/3. Due to intense upwelling during P320/1 both flux components are an order of magnitude greater than during M68/3. Data were derived from the NCP calculation.

and stays nearly constant with values around 7.3. This is similar to a situation reported by Körtzinger *et al.* (2001) for the North Atlantic where a ratio of 7.2 was found. When nitrate concentration fall below  $2 \mu\text{molL}^{-1}$  the C/N ratio starts to increase towards levels around 20. This observation is in good agreement with findings of Körtzinger *et al.* (2001), who report low C/N ratios during production and high ratios when nitrate is depleted. The variable C/N ratios suggest that (under sufficient light conditions) as long as nitrate is replete it might be "stored" (e.g. amino acids, proteins, nucleic acids) in the cells and when the system becomes depleted in nitrate carbon overconsumption as described by Toggweiler (1993) leads to the observed high C/N ratios.

Fig. 8.6a shows the wind-derived upwelling index for the time period of this study and for the years 1974 and 1983 when studies of Minas *et al.* (1986) and Hoepffner *et al.* (1999) took place. Hoepffner *et al.* (1999) estimated the seasonal net primary production (NPP) along the coast of Northwest Africa from satellite data, while Minas *et al.* (1986) used measured nitrate data to estimate NCP. Even if NCP and NPP are different quantities (NPP excludes heterotrophic respiration) we find it useful to compare our NCP estimates with other productivity estimates. We used NPP estimates from the Vertical Generalized Production Model (VGPM) presented by Behrenfeld and Falkowski (1997) and a more recent Carbon Based Production Model (CBPM) (Behrenfeld *et al.*, 2005). NPP data from both models did not show any relationship with our



data but show a high scatter. Since the study region is known for high dust deposition in the atmosphere this will affect the atmospheric correction of satellites (Chavez and Messié, 2009) which might be the reason for the observed scatter.

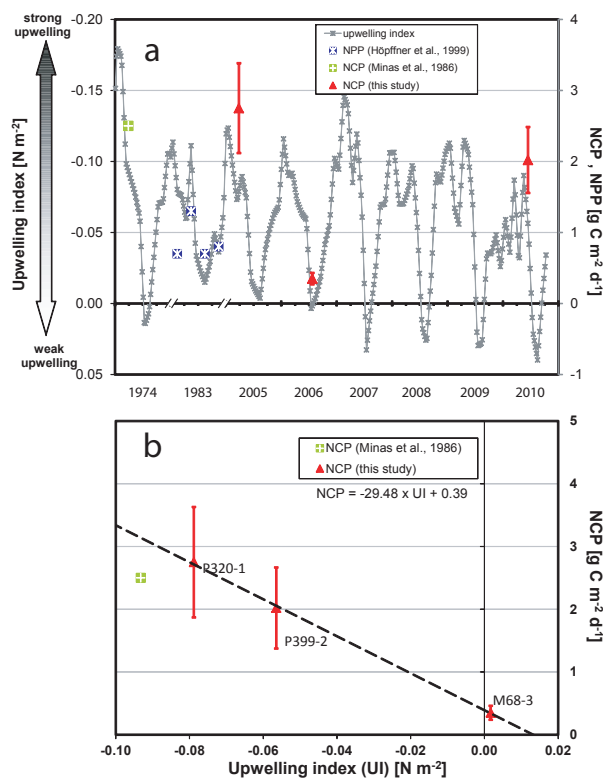


Figure 8.6.: (a) Upwelling index derived from wind stress for the period 2005-2010 and two single years (1974, 1983), in which comparable studies took place. Also shown are the NCP estimates of this study as well as NCP and NPP estimates from former studies. (b) Relation between NCP (of this study) and upwelling index. For the regression line only data from this study were used. The NCP estimate from Minas *et al.* (1986) is shown for comparison.

The estimates of Hoepffner *et al.* (1999) and Minas *et al.* (1986) are also shown in Fig. 8.6. It is clearly visible that P320/1 took place during intensive upwelling, M68/3 during the time with the lowest upwelling and P399/2 at the end of an upwelling season. This corresponds very well with the NCP and NPP values: highest production during intense upwelling and lowest production during weak upwelling. The maximum values of Hoepffner *et al.* (1999) are lower than the maximum NCP estimates of this study. This might be due to the fact that they calculated mean values for an entire season but the intensity of the upwelling varies on shorter timescales (i.e. days to weeks, Fig. 8.6a). In Fig. 8.6b we related the NCP values of this study to the upwelling index, which was averaged over the time of each cruise. There is a strong linear relationship for the three datapoints ( $r^2 > 0.9$ ). We are fully aware that this relationship

year	NCP budget [g C m <sup>-2</sup> yr <sup>-1</sup> ]
1974	960±218
1983	762±176
2005	776±178
2006	790±182
2007	931±214
2008	801±184
2009	691±159

Table 8.4.: Annual NCP budgets calculated from the equation derived in Fig. 8.6(b).

found between the upwelling index and NCP needs further evaluation before it can be used for extrapolation. However, we used the shown relationship to calculate NCP from the upwelling index for the period 2002 - 2009 and for the years 1974 and 1983. Integrating over the entire year results in annual NCP budgets (Table 8.4). The NCP budgets increased between 2005 and 2007 analogous to the increased upwelling. This observation is in good agreement with the findings of Messié *et al.* (2009) who have shown the relationship between intensified upwelling and elevated production. McGregor *et al.* (2007) showed that the intensified upwelling might be consequence of global warming which has significant ramification for the future development of the productivity of the EBUE. Messié *et al.* (2009) report a mean value for potential new production of 539 g C m<sup>-2</sup>yr<sup>-1</sup> for the North West African coast (12 - 22°N). They used the termination of potential new production instead of new production due to their assumption that all supplied nutrients are consumed by phytoplankton. Note that their value is a climatological value based on observations from 1999 - 2008. Given that their study region covers a larger area, their findings compare with our observations of increasing NCP. This might explain that the value of 539 g C m<sup>-2</sup> yr<sup>-1</sup> is below the range of our observations.

Minas *et al.* (1986) calculated a NCP value of 2.5 g C m<sup>-2</sup> d<sup>-1</sup> using the nitrate decrease of fresh upwelled water. Similar to our approach employing N<sub>2</sub>O loss, they used the heat loss of the upwelled water as a tracer for time. Their calculations are based on data from a cruise that took place in March/April 1974 slightly north of P320-1. Also, the strength of upwelling is comparable to that of 2005 (Fig. 8.6 a). For comparison their value and the upwelling index at the time of their measurements are shown in Fig 8.6 b. Given that there are uncertainties (i) in the estimation of the upwelling index and (ii) in both NCP calculation the data match rather well. With the presented method more information can be obtained about the variability of NCP with respect to the strength of upwelling. This will increase our knowledge about upwelling systems

and their influence on global new production. We have shown that the annual variability is large and so a better quantification of this variability should lead to improved estimations of the global ocean productivity estimates.

### 8.3. Conclusions

It was shown that in the Mauritanian upwelling the CO<sub>2</sub> drawdown by biology is an order of magnitude larger than CO<sub>2</sub> uptake due to ASE (Fig. 8.5). This applies to both, periods with intense upwelling and periods with weak upwelling. However, during weak upwelling the overall flux is an order of magnitude lower than during intense upwelling.

The estimated NCP values are between  $0.4 \pm 0.1 \text{ g C m}^{-2} \text{ d}^{-1}$  during weak upwelling and  $2.8 \pm 0.9 \text{ g C m}^{-2} \text{ d}^{-1}$  during intense upwelling. NCP appears to be well correlated to the upwelling index. Assuming that the found relationship holds for the complete annual cycle we estimated an annual NCP between  $762 \text{ g C m}^{-2} \text{ yr}^{-1}$  in years with weak upwelling and values up to  $960 \text{ g C m}^{-2} \text{ yr}^{-1}$  in years of more intense upwelling.

Our findings indicate that the NPP products based on remotely sensed chlorophyll concentrations are rather inaccurate in this region of (seasonally) high atmosphere dust loading.



## 9. Conclusions and future outlook

- The  $p\text{CO}_{2,\text{sw}}$  data obtained during this thesis onboard a volunteer observing ship (VOS) were compared with data from another VOS plying on a similar route across the North Atlantic in 2002/2003. The seawater  $p\text{CO}_2$  between  $40^\circ$  and  $50^\circ\text{N}$  is highly variable both in time and space where the western part (west of  $30^\circ\text{W}$ ) shows higher interannual variability than the eastern part. This difference is mostly due to the influence of the LC in the western part.
- The results indicate that the non-thermal component of  $p\text{CO}_{2,\text{sw}}$  is mainly driven by biological  $\text{CO}_2$  drawdown which is most pronounced in the eastern part of the study region.
- As a consequence of the variable  $p\text{CO}_2$  pattern the resulting  $\text{CO}_2$  flux is also variable in space and time. For the western part of the study area an air-to-sea  $\text{CO}_2$  flux of  $48.4 \text{ g C m}^{-2} \text{ yr}^{-1}$  for 2002/2003 and  $26.4 \text{ g C m}^{-2} \text{ yr}^{-1}$  for 2006/2007 was calculated. For the eastern part  $32.0 \text{ g C m}^{-2} \text{ yr}^{-1}$  for 2002/2003 and  $28.9 \text{ g C m}^{-2} \text{ yr}^{-1}$  for 2006/2007 was calculated which shows the high interannual variability in the western part. Also a comparison with the climatology from Takahashi *et al.* (2009) shows better agreement in the eastern than in the western part which indicates the interannual variability.
- $\text{CO}_2$  fluxes are most intense in the region between  $35^\circ$  and  $40^\circ\text{W}$  in both datasets (2002/2003 and 2006/2007). The reason for the intense fluxes are high wind speeds during winter (up to  $15 \text{ m s}^{-1}$ ) occurring in this area.
- In 2005 a coordinated network of different VOS was used to measure  $p\text{CO}_2$  in the surface waters of the North Atlantic. They recorded approximately 125,000 datapoints during the whole year. These data were used to estimate the  $\text{CO}_2$  flux with a multiple linear regression (MLR) and a neural network (NN) approach using mixed layer depth (MLD) and sea surface temperature (SST) as predictive variables. The mean annual flux (average of MLR and NN) was estimated to be  $-0.25 \pm 0.05 \text{ Pg C yr}^{-1}$  what is lower than the flux

calculated with  $\Delta p\text{CO}_2$  values from the climatology of Takahashi *et al.* (2009).

Using data from the VOS network lead to an uncertainty in the  $\Delta p\text{CO}_2$  data of 10% but the uncertainty arising from the parameterization of  $k$  is estimated to be 20%. Hence, annual  $\text{CO}_2$  fluxes from different years can be compared with a precision of 10% (providing the same parameterization of  $k$  is used).

- The NN technique was applied to the  $p\text{CO}_2$  data of various VOS between 2004 and 2006 in the North Atlantic in order to produce basinwide monthly maps. Using SST, MLD and chl-a as predictive variables the uncertainty of the  $p\text{CO}_2$  predictions was estimated to be  $\pm 11.6 \mu\text{atm}$  (2004:  $\pm 8.1 \mu\text{atm}$ ; 2005:  $\pm 12.6 \mu\text{atm}$ ; 2006:  $\pm 12.5 \mu\text{atm}$ ). The NN suggests that the  $p\text{CO}_2$  between  $20^\circ$  and  $40^\circ\text{N}$  is driven mainly by temperature changes while north of  $40^\circ\text{N}$  massive biological carbon drawdown plays an important role.
- The major  $\text{CO}_2$  sink area between  $20^\circ$  and  $50^\circ\text{N}$  migrates northward during summer with a maximal flux into the ocean in March/April. Consequently the subtropical gyre acts as a sink during winter and as a source during summer.
- Part of the data of this thesis were used for the climatology of Takahashi *et al.* (2009) which includes more than 3 million  $p\text{CO}_{2,\text{sw}}$  measurements between 1974 and 2007. The North Atlantic north of  $50^\circ\text{N}$  shows the highest  $\text{CO}_2$  flux into the ocean per area of the global ocean due to cold SST, strong photosynthesis and high wind speeds.
- The dataset of Takahashi *et al.* (2009) allowed to estimate the mean  $p\text{CO}_{2,\text{sw}}$  increase in regions where data were available for a sufficient period. The mean increase of the North Atlantic ( $15^\circ$ -  $65^\circ\text{N}$ ) is estimated to be  $1.5 \pm 0.4 \mu\text{atm yr}^{-1}$ . The value varies for different part of the North Atlantic and it is  $2.1 \pm 0.2 \mu\text{atm yr}^{-1}$  for the region between  $45^\circ\text{N}$  and  $50^\circ\text{N}$ .
- Several methods to estimate MLD in the North Atlantic were compared: profile based calculations, model data and climatological data. If temperature data from a measured profile are available the calculation method developed from Lorbacher *et al.* (2006) achieved results that were closest to an "eyeball" defined reference MLD. For a basinwide estimation of MLD the modeled data from Mercator-project yield the best results compared to the "eyeball" defined reference.
- A highly variable winter MLD was observed during 2002 and 2006. Values varied between 150 and 250m at a certain location in the western part and between 175 and 350 m in the

eastern part. At the eastern location a steady increase of the winter MLD is observed since 2004.

- An equation to predict nitrate concentration in the mixed layer of the North Atlantic between 40°N and 55°N was employed. The equation was derived by MLR using latitude, time (day of the year), SST and MLD as predictive variables. About 82% of the observed nitrate variability can be explained by the algorithm with an uncertainty of  $\pm 1.4 \mu\text{mol L}^{-1}$ . In addition the training dataset was used to train a NN. The nitrate data estimated by the NN were not significantly better than the estimations from the MLR. Taking full advantage of the NN needs a better data coverage.
- The estimated nitrate data were used to examine the biological driven impact on  $p\text{CO}_{2,\text{sw}}$  in the North Atlantic. Due to the increasing winter MLD the nitrate concentration in the mixed layer increased and the corresponding respired dissolved inorganic carbon (DIC) is also increasing. These findings could explain the observed increase of  $p\text{CO}_{2,\text{sw}}$  (e.g. Corbière *et al.*, 2007).
- During three research cruises in the Mauritanian upwelling region measurements of  $p\text{CO}_2$  and  $\text{N}_2\text{O}$  in the surface water were conducted. The combined dataset was used to separate the  $\text{CO}_2$  gas exchange from the biological mediated drawdown and to estimate NCP in the upwelling region in different seasons (spring and summer). During strong upwelling (spring) NCP was estimated to be  $2.8 \pm 0.9 \text{ g C m}^{-2} \text{ d}^{-1}$  and  $0.4 \pm 0.1 \text{ g C m}^{-2} \text{ d}^{-1}$  during weak upwelling in summer. The corresponding duration of the biological mediated carbon drawdown was estimated to be  $28 \pm 9$  and  $11 \pm 4$  days, respectively.

We found a strong relationship between the NCP estimates from the three cruises and a wind derived upwelling index. Using this (speculative) relationship lead to annual NCP estimations for the upwelling region off Mauritania.

- The  $\text{CO}_2$  fluxes (biological and ASE) were an order of magnitude higher during strong upwelling than during weak upwelling. The biological mediated  $\text{CO}_2$  flux was an order of magnitude higher than the flux driven by ASE.
- Using discrete nitrate samples from the surface carbon to nitrogen ratios were calculated for one of the cruises that took place during spring (R/V Poseidon cruise P320-1). As long as nitrate was available in excess ( $> 8 \mu\text{mol kg}^{-1}$ ) C/N values were lower than the canonical Redfield ratio. When nitrate concentration reached moderate levels between 2 and  $8 \mu\text{mol}$

$\text{kg}^{-1}$  the C/N values were nearly constant around 7.3. As soon nitrate concentration falls under  $2 \mu\text{mol kg}^{-1}$  the C/N ratio increased rapidly to values exceeding 15 (carbon overconsumption).

In Chapter 2.3 it was shown that it is crucial for underway observations of  $p\text{CO}_{2,\text{sw}}$  to accurately estimate the time difference between intake and equilibrator. This time difference is strongly correlated to the water flow. The newer systems that were used for the data obtained during this study have nearly constant water flow and a fixed time difference is sufficient to correct the whole dataset. For systems with a higher (and often more variable) water flow a variable time difference has to be applied in order to achieve accurate results (Fig. 2.5). The accurate determination of the time difference influences also the determination of the temperature difference between equilibration and intake. In regions where sharp temperature gradients are observed (e.g. Labrador current) a faulty time difference will lead to faulty temperature difference estimates, even with the opposite sign (i.e. cooling of seawater on its way from the inlet to the equilibrator). This will consequently influence the temperature correction of  $p\text{CO}_2$  measurements, what is  $14 \mu\text{atm}$  per  $1^\circ\text{C}$  temperature correction at  $350 \mu\text{atm}$ .

In Chapter 4 it was shown that a concerted network of VOS based underway measurements is able to produce accurate basin wide estimations of  $p\text{CO}_{2,\text{sw}}$  using high quality  $p\text{CO}_{2,\text{sw}}$  measurements and adequate interpolation methods (NN, MLR). The advantage of NN over MLR is that a NN recognizes different patterns of the training dataset and consequently it is more flexible. But it needs more knowledge to set up a NN than an "easy" MLR. In Chapter 5 it is shown that with the present coverage of the North Atlantic  $p\text{CO}_{2,\text{sw}}$  can be estimate with an uncertainty of  $\pm 11.6 \mu\text{atm}$  (average, calculated over three years). But the capability of each interpolation method increases with sufficient data coverage. Presently a good spatial coverage is given in the North Atlantic and North Pacific. Even if it was shown that the uncertainty ( $1\sigma$ ) of the annual mean  $p\text{CO}_{2,\text{sw}}$  between  $10^\circ$  and  $65^\circ\text{N}$  is about 10% the determination of basinwide  $\text{CO}_2$  fluxes poses another problem: a precise determination of the gas transfer coefficient  $k$ . The resulting uncertainty for basinwide flux estimations is about 20% and reducing the combined uncertainty is a challenging task for the future.

The multi-year comparison shows that long-term monitoring of an ocean basin is crucial to develop a dataset that can be used for further applications (e.g. interpolation methods, models,...). Comparing two annual cycles as done in Chapter 3 helps to understand the biogeochemical processes that drive the observed patterns of  $p\text{CO}_{2,\text{sw}}$ . But the information has to be put into a



broader context as the interannual variability of  $p\text{CO}_{2,\text{sw}}$  in the North Atlantic is high and the annual flux can vary by a factor of two from one year to another.

The main driving forces of  $p\text{CO}_{2,\text{sw}}$  are temperature and biological production/respiration. The production of biomass needs nutrients and thus the estimation of basinwide nutrients helps to improve  $p\text{CO}_{2,\text{sw}}$  predictions. The availability of nutrients in the North Atlantic is mainly driven by winter convection and thus it turned out that MLD (together with SST) is a good predictor for nitrate in the mixed layer. The variability of available nitrate (due to MLD variations) can explain observed increase/decrease of  $p\text{CO}_{2,\text{sw}}$ .

An important task for future oceanic  $\text{CO}_2$  flux observations is to develop an efficient infrastructure for  $p\text{CO}_{2,\text{sw}}$  measurements. Together with other parameter (e.g. SST, SSS, chl-a, nitrate, organic carbon) it will help to better understand the driving forces and constrain the data fundamental for future climate predictions. Within the framework of the planned "Integrated Carbon Observation System" (ICOS; [www.icos-infrastructure.eu](http://www.icos-infrastructure.eu)) of the EU such an infrastructure might be developed. Also the follow up of CARBOOCEAN (Carbochange) will help to improve the measurement network. The development of small, submersible  $p\text{CO}_2$  sensors (or for other parameters of the  $\text{CO}_2$  system) will also help to improve the data base, but some work is to do before these sensors achieve the desired accuracy (Byrne *et al.*, 2010).

Furthermore another application of shipboard measurements in the surface ocean were presented in Chapter 8. Onboard research vessels it was possible to study the small scale dynamic of  $\text{CO}_2$  in the Mauritanian upwelling region, which is characterized by high  $p\text{CO}_{2,\text{sw}}$  values of about  $750 \mu\text{atm}$  during strong upwelling. Using the parallel measurements of  $\text{N}_2\text{O}$  and  $p\text{CO}_{2,\text{sw}}$  NCP was estimated for the upwelling region and it was shown that NCP varies with the strength of upwelling. If the intensity of upwelling increases further with climate change as proposed by McGregor *et al.* (2007) this may influence the productivity of "Eastern Boundary Upwelling Ecosystems" (EBUE). Consequently the impact of EBUE's on global productivity will increase. To constrain the proposed relationship between upwelling and productivity in the Mauritanian upwelling area more cruises especially in other seasons than spring or summer should be conducted. Furthermore the diurnal cycle in the high productivity regions has to be quantified to better estimate NCP.



# Acknowledgements

I would like to thank Prof. Dr. Arne Körtzinger and Prof. Dr. Doug Wallace for making this thesis possible. I appreciate the encouraging discussions with Arne and that he always took the time for trying to answer all my questions.

Thanks to the shipping companies Wallenius Wilhemsen in Sweden and Atlantic Container Lines in USA, who provided the platform for the results of this thesis. Special thanks to Mats, who made the installations onboard M/V Atlantic Companion much easier.

There are numerous people I would like to thank: Björn, who was always willing to assist me in the installations/maintenance onboard the VOS and who spend days driving with me through Europe.

Craig Neill, who gave me support for the  $p\text{CO}_2$  instrument also during night time.

Anke, for discussions about the carbonate system (and the meaning of life in science). Thanks for the essential support in the day-to-day business and great training events ("Mexico!!!").

Alina, who knew a solution for nearly every problem in Matlab and for numerous discussions about statistical problems.

Thanks to the people of FB2-CH, I enjoyed working with you. I would like to thank numerous people that provided their help for cruises and measurements: Karoline Streidt, Tim Kalvelage, Sebastian Göseke, Evelyn Draus, Lars Ebner, Heiko Brenner, Mario Wriedt, Kathrin Wuttig, Philip Nuß, Imke Grefe, Lena Hübner, Marion Meyer, Jan Harlaß, Thomas Homburg, Frank and Susann Malien and Hergen Johannsen.

AMSR-E data are produced by Remote Sensing Systems and sponsored by the NASA Earth Science MEaSUREs DISCOVER Project and the AMSR-E Science Team. Data are available at [www.remss.com](http://www.remss.com).

Analyses and visualizations used in this study were produced with the Giovanni online data system, developed and maintained by the NASA Goddard Earth Sciences (GES) Data and Information Services Center (DISC). I also thank Robert O'Malley (Department of Botany and Plant Pathology, Oregon State University, Corvallis) for providing the VGPM and CbPM pro-

ductivity estimates.

Last but not least I thank Bianca, Jone, Lasse and Lotta for accepting my changes in mood and for bringing me back down to earth. Thanks for tolerating all the cruises and special thank to my Mom who spent in total more than a year in Kiel to take care of the kids when I was abroad.

# Bibliography

- Anderson, L. A. and Sarmiento, J. L. (1994). Redfield ratios of remineralization determined by nutrient data analysis. *Global Biogeochem. Cycl.*, **8**(1), 65–80.
- Antonov, J. I., Locarnini, R. A., Boyer, T. P., Mishonov, A. V., and Garcia, H. E. (2006). *World Ocean Atlas 2005, Volume 2: Salinity*. S. Levitus, Ed. NOAA Atlas NESDIS 62, U.S. Government Printing Office, Washington, D.C.
- Bange, H. W., Rapsomanikis, S., and Andreae, M. O. (1996). The aegean sea as a source of atmospheric nitrous oxide and methane. *Mar. Chem.*, **53**, 41–49.
- Bates, N. R. (2007). Interannual variability of the oceanic CO<sub>2</sub> sink in the subtropical gyre of the North Atlantic Ocean over the last 2 decades. *J. Geophys. Res.*, **112**, C09013.
- Behrenfeld, M. J. and Falkowski, P. F. (1997). Photosynthetic rates derived from satellite-based chlorophyll concentration. *Limnol. Oceanogr.*, **42**(1), 1–20.
- Behrenfeld, M. J., Boss, E., Siegel, D. A., and Shea, D. M. (2005). Carbon-based ocean productivity and phytoplankton physiology from space. *Global Biogeochem. Cycl.*, **19**, GB1006.
- Broecker, W. S. (1991). The great ocean conveyor. *Oceanography*, **4**(2), 79–89.
- Byrne, R. H., DeGrandpre, M. D., Short, R. T., Martz, T. R., Merlivat, L., McNeil, C., Sayles, F. L., Bell, R., and Fietzek, P. (2010). Sensors and systems for in situ observations of marine carbon dioxide system variables. In J. Hall, D. Harrison, and D. Stammer, editors, *Proceedings of OceanObs'09: Sustained Ocean Observations and Information for Society (Vol.2)*, Venice, Italy, 21-25 September 2009. ESA Publication WPP-306.
- Carr, M.-E. and Kearns, E. J. (2003). Production regimes in four eastern boundary current systems. *Deep-Sea Res. II*, **50**, 3199–3221.
- Chavez, F. P. and Messié, M. (2009). A comparison of eastern boundary upwelling ecosystems. *Progr. Oceanogr.*, **83**, 80–96.
- Chavez, F. P. and Toggweiler, J. R. (1995). Physical estimates of global new production: the upwelling contribution. In C. Summerhayes, K. Emeis, M. Angel, R. Smith, and B. Zeitzschel, editors, *Upwelling in the Ocean: Modern Processes and Ancient Records*, pages 313–320. Wiley, Chichester, UK.
- Cianca, A., Helmke, P., Mouriño, B., Rueda, M. J., Llinás, O., and Neuer, S. (2007). Decadal analysis of hydrography and in situ nutrient budgets in the western and eastern North Atlantic subtropical gyre. *J. Geophys. Res.*, **112**, C07025, doi:10.1029/2006JC003788.
- Corbière, A., Metzl, N., Reverdin, G., Brunet, C., and Takahashi, T. (2007). Interannual and decadal variability of the oceanic carbon sink in the North Atlantic subpolar gyre. *Tellus*, **59B**, 168–178.

- Demarcq, H. (2009). Trends in primary production, sea surface temperature and wind in upwelling systems (1998-2007). *Progr. Oceanogr.*, **83**, 376–385.
- Denman, K., Brasseur, G., Chidthaisong, A., P. Ciais, P. C., Dickinson, R., Hauglustaine, D., Heinze, C., Holland, E., Jacob, D., Lohmann, U., Ramachandran, S., da Silva Dias, P., Wofsy, S., and Zhang, X. (2007). Couplings between changes in the climate system and biogeochemistry. In S. Solomon, D. Qin, M. Manning, Z. Chen, M. Marquis, K. Averyt, M. Tignor, and H. Miller, editors, *Climate Change 2007: The Physical Science Basis. Contribution of Working Group I to the Fourth Assessment Report of the Intergovernmental Panel on Climate Change*, chapter 7, pages 499–588. Cambridge University Press, Cambridge, United Kingdom and New York, NY, USA.
- Dickson, A. (1981). An exact definition of total alkalinity and a procedure for the estimation of alkalinity and total inorganic carbon from titration data. *Deep-Sea Res. Part A*, **28**(6), 609–623.
- Dickson, A. (2001). Reference materials for oceanic CO<sub>2</sub> measurements. *Oceanography*, **14**(4), 21–22.
- Dickson, A. G., Sabine, C. L., and Christian, J. R. E. (2007). *Guide to Best Practices for Ocean CO<sub>2</sub> Measurements*. PICES Special Publication 3.
- Dugdale, R. and Goering, J. (1967). Uptake of new and regenerated forms of nitrogen in primary productivity. *Limnol. Oceanogr.*, **12**(2), 196–206.
- Emery, W. and Meincke, J. (1986). Global water masses - summary and review. *Oceanol. Acta*, **9**(4), 383–391.
- Forster, P., Ramaswamy, V., Artaxo, P., Berntsen, T., Betts, R., Fahey, D., Haywood, J., Lean, J., Lowe, D., Myhre, G., Nganga, J., Prinn, R., Raga, G., Schulz, M., and Van Dorland, R. (2007). Changes in atmospheric constituents and in radiative forcing. In S. Solomon, D. Qin, M. Manning, Z. Chen, M. Marquis, K. Averyt, M. Tignor, and H. Miller, editors, *Climate Change 2007: The Physical Science Basis. Contribution of Working Group I to the Fourth Assessment Report of the Intergovernmental Panel on Climate Change*, chapter 2, pages 129–234. Cambridge University Press, Cambridge, United Kingdom and New York, NY, USA.
- Freon, P., Barange, M., and Aristegui, J. (2009). Eastern boundary upwelling ecosystems: Integrative and comparative approaches. *Progr. in Oceanogr.*, **83**, 1–14.
- Friedrich, T. and Oschlies, A. (2009). Neural network-based estimates of North Atlantic surface pCO<sub>2</sub> from satellite data: A methodological study. *J. Geophys. Res.*, **114**, C03020, doi:10.1029/2007JC004646.
- GLOBALVIEW-CO<sub>2</sub> (2009). Cooperative atmospheric data integration project - carbon dioxide. CD-ROM, NOAA ESRL, Boulder, Colorado [Also available on Internet via anonymous FTP to ftp.cmdl.noaa.gov, Path: ccg/co2/GLOBALVIEW].
- Gloor, M., Gruber, N., Sarmiento, J., C.L.Sabine, Feely, R., and Rödenbeck, C. (2003). A first estimate of present and preindustrial air-sea CO<sub>2</sub> flux patterns based on ocean interior carbon measurements and models. *Geophys. Res. Lett.*, **30**(1), 1010.
- Goni, G., Roemmich, D., Molinari, R., Meyers, G., Sun, C., Boyer, T., Baringer, M., Gouretski, V., DiNezio, P., Reseghetti, F., Vissan, G., Swart, S., Keeley, R., Garzoli, S., Rossby, T.,

- Maes, C., and Reverdin, G. (2010). The ship of opportunity program. In J. Hall, D. Harrison, and D. Stammer, editors, *Proceedings of OceanObs'09: Sustained Ocean Observations and Information for Society (Vol.2)*, Venice, Italy, 21-25 September 2009. ESA Publication WPP-306.
- Goyet, C. and Poisson, A. (1989). New determination of carbonic acid dissociation constants in seawater as a function of temperature and salinity. *Deep-Sea Res. A*, **36**(11), 1635–1654.
- Gruber, N., Keeling, C. D., and Bates, N. R. (2002). Interannual variability in the North Atlantic Ocean Carbon Sink. *Science*, **298**, 2374–2378.
- Gruber, N., Gloor, M., Fletcher, S. E. M., Doney, S. C., Dutkiewicz, S., Follows, M. J., Gerber, M., Jacobson, A. R., Joos, F., Lindsay, K., Menemenlis, D., Mouchet, A., Mueller, S. A., Sarmiento, J. L., and Takahashi, T. (2009). Oceanic sources, sinks, and transport of atmospheric CO<sub>2</sub>. *Global Biogeochem. Cycl.*, **23**, GB1005.
- Hansen, H. and Koroleff, F. (1999). Determination of nutrients. In K. Grasshoff, K. Kremling, and M. Erhardt, editors, *Methods of seawater analysis*, pages 159–228. Verlag Chemie, Weinheim, Germany.
- Hansson, I. (1973). A new set of acidity constants for carbonic acid and boric acid in sea water. *Deep-Sea Res.*, **20**(5), 461–478.
- Hegerl, G., Zwiers, F. W., Braconnot, P., Gillett, N., Luo, Y., Orsini, J. M., Nicholls, N., Penner, J., and Stott, P. (2007). Understanding and attributing climate change. In S. Solomon, D. Qin, M. Manning, Z. Chen, M. Marquis, K. Averyt, M. Tignor, and H. Miller, editors, *Climate Change 2007: The Physical Science Basis. Contribution of Working Group I to the Fourth Assessment Report of the Intergovernmental Panel on Climate Change*, chapter 9, pages 663–746. Cambridge University Press, Cambridge, United Kingdom and New York, NY, USA.
- Hoepffner, N., Sturm, B., Finenko, Z., and Larkin, D. (1999). Depth-integrated primary production in the eastern tropical and subtropical North Atlantic basin from ocean colour imagery. *Int. J. Remote Sensing*, **20**(7), 1435–1456.
- Horrigan, S., Carlucci, A., and Williams, P. (1981). Light inhibition of nitrification in sea-surface films. *J. Mar. Research*, **39**(3), 557–565.
- Hydes, D. J., Kelly-Gerreyn, B. A., Colijn, F., Petersen, W., Schroeder, F., Mills, D., Dur, D., Wehde, H., Sørensen, K., and Morrison, G. (2009). The way forward in developing and integrating ferrybox technologies. In J. Hall, D. Harrison, and D. Stammer, editors, *Proceedings of OceanObs'09: Sustained Ocean Observations and Information for Society (Vol.2)*, Venice, Italy, 21-25 September 2009. ESA Publication WPP-306.
- Jamet, C., Moulin, C., and Lefèvre, N. (2007). Estimation of the oceanic pCO<sub>2</sub> in the North Atlantic from VOS lines in-situ measurements : Parameters needed to generate seasonally mean maps. *Ann. Geophys.*, **25**, 2247–2257.
- Johnson, K., Wills, K., Butler, D., Johnson, W., and Wong, C. (1993). Coulometric total carbon dioxide analysis for marine studies: maximizing the performance of an automated gas extraction system and coulometric detector. *Mar. Chem.*, **44**, 167–187.
- Johnson, K. M., Dickson, A. G., Eiseid, G., Goyet, C., Guenther, P., Key, R. M., Millero, F. J., Purkerson, D., Sabine, C. L., Schottle, R. G., Wallace, D. W. R., Wilke, R. J., and

- Winn, C. D. (1998). Coulometric total carbon dioxide analysis for marine studies: assessment of the quality of total inorganic carbon measurements made during the US Indian Ocean CO<sub>2</sub> Survey 1994-1996. *Mar. Chem.*, **63**, 21–37.
- Kent, E. C., Ball, G., Berry, D. I., Fletcher, J., Hall, A., North, S., and Woodruff, S. D. (2010). The Voluntary Observing Ship (VOS) scheme. In J. Hall, D. Harrison, and D. Stammer, editors, *Proceedings of OceanObs'09: Sustained Ocean Observations and Information for Society (Vol.2)*, Venice, Italy, 21-25 September 2009. ESA Publication WPP-306.
- Kitzis, D. and Zhao, C. (1999). CMDL/Carbon Cycle Greenhouse Gases Group standards preparation and stability. NOAA TM ERL CMDL-14, Environ. Res. Labs., Boulder, CO,.
- Körtzinger, A., Thomas, H., Schneider, B., Gronau, N., Mintrop, L., and Duinker, J. C. (1996). At-sea intercomparison of two newly designed underway *p*CO<sub>2</sub> systems - encouraging results. *Mar. Chem.*, **52**, 133–145.
- Körtzinger, A., Koeve, W., Kähler, P., and Mintrop, L. (2001). C:N ratios in the mixed layer during the productive season in the Northeast Atlantic Ocean. *Deep-Sea Res. I*, **48**, 661–688.
- Le Quéré, C., Raupach, M. R., Canadell, J. G., Marland, G., Bopp, L., Ciais, P., Conway, T. J., Doney, S. C., Feely, R. A., Foster, P., Friedlingstein, P., Gurney, K., Houghton, R. A., House, J. I., Huntingford, C., Levy, P. E., Lomas, M. R., Majkut, J., Metzl, N., Ometto, J. P., Peters, G. P., Prentice, I. C., Randerson, J. T., Running, S. W., Sarmiento, J. L., Schuster, U., Sitch, S., Takahashi, T., Viovy, N., van der Werf, G. R., and Woodward, F. I. (2009). Trends in the sources and sinks of carbon dioxide. *Nat. Geosci.*, **2**(12), 831–836.
- Lefèvre, N., Watson, A., Olsen, A., A.F.Ríos, Pérez, F., and Johannessen, T. (2004). A decrease in the sink for atmospheric CO<sub>2</sub> in the North Atlantic. *Geophys. Res. Lett.*, **31**, L07306,.
- Lefèvre, N., Watson, A. J., and Watson, A. R. (2005). A comparison of multiple regression and neural network techniques for mapping *in situ* *p*CO<sub>2</sub> data. *Tellus*, **57B**, 375–384.
- Liss, P. S. (1983). Gas transfer: experiments and geochemical implications. In P. Liss and W. Slinn, editors, *Air-Sea exchange of gases and particles*, volume C 108, pages 241–298. NATO ASI Series.
- Liss, P. S. and Merlivat, L. (1986). Air-sea gas exchange rates: introduction and synthesis. In P. Buat-Ménard, editor, *The Role of Air-Sea Exchange in Geochemical Cycling*, volume C 185, pages 113–127. NATO ASI Series.
- Longhurst, A. R. (2007). *Ecological geography of the sea*. Academic Press, Boston, 2nd edition.
- Lorbacher, K., Dommenges, D., Niiler, P., and Köhl, A. (2006). Ocean mixed layer depth: A subsurface proxy of ocean-atmosphere variability. *J. Geophys. Res.*, **111**, C07010.
- Lueker, T. J., Dickson, A. G., and Keeling, C. D. (2000). Ocean *p*CO<sub>2</sub> calculated from dissolved inorganic carbon, alkalinity, and equations for  $K_1$  and  $K_2$  : validation based on laboratory measurements of CO<sub>2</sub> in gas and seawater at equilibrium. *Mar. Chem.*, **70**, 105–119.
- Lueker, T. J., Walker, S. J., Vollmer, M. K., Keeling, R. F., Nevison, C. D., Weiss, R. F., and Garcia, H. E. (2003). Coastal upwelling air-sea fluxes revealed in atmospheric observations of O<sub>2</sub>/N<sub>2</sub>, CO<sub>2</sub> and N<sub>2</sub>O. *Geophys. Res. Lett.*, **30**(6), 1292.



- Lüger, H., Wallace, D. W. R., Körtzinger, A., and Nojiri, Y. (2004). The  $p\text{CO}_2$  variability in the midlatitude North Atlantic Ocean during a full annual cycle. *Global Biochem. Cycles*, **18**, GB3023.
- Lüger, H., Wanninkhof, R., Wallace, D., and Körtzinger, A. (2006).  $\text{CO}_2$  fluxes in the subtropical and subarctic North Atlantic based on measurements from a volunteer observing ship. *J. Geophys. Res.*, **111**, C06024.
- McGregor, H. V., Dima, M., Fischer, H. W., and Mulitza, S. (2007). Rapid 20th-century increase in coastal upwelling off Northwest Africa. *Science*, **315**, 637–639.
- Mehrbach, C., Culbertson, C. H., Hawley, J. E., , and Pytkowicz, R. M. (1973). Measurement of the apparent dissociation constants of carbonic acid in seawater at atmospheric pressure. *Limnol. Oceanogr.*, **18**(6), 897–907.
- Messié, M., Ledesma, J., Kolber, D. D., Michisaki, R. P., Foley, D. G., and Chavez, F. P. (2009). Potential new production estimates in four eastern boundary upwelling ecosystems. *Progr. Oceanogr.*, **83**, 151–158.
- Minas, H. J., Minas, M., and Packard, T. T. (1986). Productivity in upwelling areas deduced from hydrographic and chemical fields. *Limnol. Oceanogr.*, **31**(6), 1182–1206.
- Mintrop, L., Perez, F., Gonzales-Davila, M., Santana-Casiano, J., and Körtzinger, A. (2000). Alkalinity determination by potentiometric titration: intercalibration using three different methods. *Ciencias Marinas*, **26**(1), 23–37.
- Mojica Prieto, F. J. and Millero, F. J. (2002). The values of  $\text{pk}_1 + \text{pk}_2$  for the dissociation of carbonic acid in seawater. *Geochimica et Cosmochimica Acta*, **66**(14), 2529–2540.
- Monteiro, P. M., Schuster, U., Hood, M., Lenton, A., Metzl, N., Olsen, A., Rogers, K., Sabine, C., Takahashi, T., Tilbrook, B., Yoder, J., Wanninkhof, R., and Watson, A. J. (2010). A global sea surface carbon observing system: assessment of changing sea surface  $\text{CO}_2$  and air-sea  $\text{CO}_2$  fluxes. In J. Hall, D. Harrison, and D. Stammer, editors, *Proceedings of OceanObs'09: Sustained Ocean Observations and Information for Society (Vol.2)*, Venice, Italy, 21-25 September 2009. ESA Publication WPP-306.
- Nightingale, P., Malin, G., Law, C., Watson, A., Liss, P., Liddicoat, M., Boutin, J., and Upstill-Goddard, R. (2000). In situ evaluation of air-sea gas exchange parameterizations using novel conservative and volatile tracers. *Global Biogeochem. Cycl.*, **14**(1), 373–387.
- Olsen, A., Bellerby, R. G., Johannessen, T., Omar, A. M., and Skjelvan, I. (2003). Interannual variability in the wintertime air-sea flux of carbon dioxide in the northern North Atlantic, 1981-2001. *Deep-Sea Res. I*, **50**, 1323–1338.
- Olsen, A., Trinañes, J. A., and Wanninkhof, R. (2004). Sea-air flux of  $\text{CO}_2$  in the Caribbean Sea estimated using in situ and remote sensing data. *Rem. Sens. Environ.*, **89**, 309–325.
- Omar, A. M. and Olsen, A. (2006). Reconstructing the time history of the air-sea  $\text{CO}_2$  disequilibrium and its rate of change in the eastern subpolar North Atlantic, 1972-1989. *Geophys. Res. Lett.*, **33**, L04602.
- Pierrot, D., Neill, C., Sullivan, K., Castle, R., Wanninkhof, R., Lüger, H., Johannessen, T., Olsen, A., Feely, R. A., and Cosca, C. E. (2009). Recommendations for autonomous underway  $p\text{CO}_2$  measuring systems and data reduction routines. *Deep-Sea Res. II*, **56**, 512–522.

- Redfield, A. C., Ketchum, B. H., and Richards, F. A. (1963). The influence of organisms on the composition of seawater. In M. Hill, editor, *The Sea, Vol.2*, volume 2, pages 26–77. Interscience, New York.
- Roy, R. N., Roy, L. N., Vogel, K. M., Porter-Moore, C., Pearson, T., Good, C. E., Millero, F. J., and Campbell, D. M. (1993). The dissociation constants of carbonic acid in seawater at salinities 5 to 45 and temperatures 0 to 45°C. *Mar. Chem.*, **44**, 249–267.
- Sabine, C., Feely, R., Gruber, N., Key, R., Lee, K., Bulister, J., Wanninkhof, R., Wong, C., Wallace, D. R., Tilbrook, B., Millero, F., Peng, T., Kozyr, A., Ono, T., and Rios, A. (2004). The oceanic sink for anthropogenic CO<sub>2</sub>. *Science*, **305**, 367–371.
- Sarmiento, J. L. and Gruber, N. (2006). *Ocean Biogeochemical dynamics*. Princeton University Press, 41 William Street, Princeton, New Jersey.
- Schemainda, R., Nehring, D., and Schulz, S. (1975). Ozeanologische Untersuchungen zum Produktionspotential der nordwestafrikanischen Wasserauftriebsregionen. *Geodätische und Geophysikalische Veröffentlichungen, Reihe IV*, 1–88.
- Schuster, U. and Watson, A. (2007). A variable and decreasing sink for atmospheric CO<sub>2</sub> in the North Atlantic. *J. Geophys. Res.*, **112**, C11006.
- Schuster, U., Watson, A. J., Bates, N. R., Corbiere, A., Gonzalez-Davila, M., Metzl, N., Pierrot, D., and Santana-Casiano, M. (2009). Trends in North Atlantic sea-surface *f*CO<sub>2</sub> from 1990 to 2006. *Deep-Sea Res. II*, **56**, 620–629.
- Service, S. K., Rice, J. A., and Chavez, F. P. (1998). Relationship between physical and biological variables during the upwelling period in Monterey Bay, CA. *Deep-Sea Res. II*, **45**, 1669 – 1685.
- Siegel, D. A., Doney, S. C., and Yoder, J. A. (2002). The North Atlantic spring phytoplankton bloom and Sverdrup’s critical depth hypothesis. *Science*, **296**, 730–733.
- Steinhoff, T., Friedrich, T., Hartman, S. E., Oshlies, A., Wallace, D. W. R., and Körtzinger, A. (2010). Estimating mixed layer nitrate in the North Atlantic Ocean. *Biogeosciences*, **7**, 795–807.
- Takahashi, T., Olafsson, J., Goddard, J. G., Chipman, D. W., and Sutherland, S. C. (1993). Seasonal variation of CO<sub>2</sub> and nutrients in the high-latitude surface oceans: a comparative study. *Global Biogeochem. Cycl.*, **7**(4), 843–878.
- Takahashi, T., Sutherland, S. C., Sweeney, C., Poisson, A., Metzl, N., Tilbrook, B., Bates, N., Wanninkhof, R., Feely, R. A., Sabine, C., Olafsson, J., and Nojiri, Y. (2002). Global sea-air CO<sub>2</sub> flux based on climatological surface ocean *p*CO<sub>2</sub>, and seasonal biological and temperature effects. *Deep-Sea Res. II*, **49**, 1601–1622.
- Takahashi, T., Sutherland, S. C., Wanninkhof, R., Sweeney, C., Feely, R. A., Chipman, D. W., Hales, B., Friederich, G., Chavez, F., Sabine, C., Watson, A., Bakker, D. C., Schuster, U., Metzl, N., Yoshikawa-Inoue, H., Ishii, M., Midorikawa, T., Nojiri, Y., Körtzinger, A., Steinhoff, T., Hoppema, M., Olafsson, J., Arnarson, T. S., Tilbrook, B., Johannessen, T., Olsen, A., Bellerby, R., Wong, C., Delille, B., Bates, N., and de Baar, H. J. (2009). Climatological mean and decadal change in surface ocean *p*CO<sub>2</sub>, and net sea-air CO<sub>2</sub> flux over the global oceans. *Deep-Sea Res. II*, **56**(8-10), 554 – 577.

- Telszewski, M., Chazottes, A., Schuster, U., Watson, A. J., Moulin, C., Bakker, D. C. E., González-Dávila, M., Johannessen, T., Körtzinger, A., Lüger, H., Olsen, A., Omar, A., Pérez, F., Ríos, A., Steinhoff, T., Santana-Casiano, M., Wallace, D. W. R., and Wanninkhof, R. (2009). Estimating the monthly  $p\text{CO}_2$  distribution in the North Atlantic using a self-organizing neural network. *Biogeosci.*, **6**, 1405–1421.
- Toggweiler, J. R. (1993). Carbon overconsumption. *Nature*, **363**, 210–211.
- Tomczak, M. and Godfrey, J. (2002). *Regional Oceanography: An Introduction*, chapter 14. Matthias Tomczak and J. Stuart Godfrey.
- van Heuven, S., Pierrot, D., Lewis, E., and Wallace, D. W. R. (2009). Matlab program developed for  $\text{CO}_2$  system calculations. ORNL/CDIAC-105b. Technical report, Carbon Dioxide Information Analysis Center, Oak Ridge National Laboratory, U.S. Department of Energy, Oak Ridge, Tennessee.
- Walter, S., Bange, H. W., and Wallace, D. W. (2004). Nitrous oxide in the surface layer of the tropical North Atlantic Ocean along a west to east transect. *Geophys. Res. Lett.*, **31**, L23S07.
- Wanninkhof, R. (1992). Relationship between wind speed and gas exchange over the ocean. *J. Geophys. Res.*, **97**(C5), 7373–7382.
- Wanninkhof, R. and McGillis, W. R. (1999). A cubic relationship between air-sea  $\text{CO}_2$  gas exchange and wind speed. *Geophys. Res. Lett.*, **26**, 1889–1892.
- Wanninkhof, R., Asher, W. E., Ho, D. T., Sweeney, C., and McGillis, W. R. (2009). Advances in quantifying air-sea gas exchange and environmental forcing. *Ann. Rev. Mar. Sci.*, **1**, 213–244.
- Watson, A. J., Schuster, U., Bakker, D. C. E., Bates, N. R., Corbiere, A., Gonzalez-Davila, M., Friedrich, T., Hauck, J., Heinze, C., Johannessen, T., Kortzinger, A., Metzl, N., Olafsson, J., Olsen, A., Oschlies, A., Padin, X. A., Pfeil, B., Santana-Casiano, J. M., Steinhoff, T., Telszewski, M., Rios, A. F., Wallace, D. W. R., and Wanninkhof, R. (2009). Tracking the variable North Atlantic sink for atmospheric  $\text{CO}_2$ . *Science*, **326**(5958), 1391–1393.
- Weiss, R. (1974). Carbon dioxide in water and seawater: The solubility of a non-ideal gas. *Mar. Chem.*, **2**, 203–251.
- Wooster, W. S., Bakun, A., and McLain, D. R. (1976). The seasonal upwelling cycle along the eastern boundary of the North Atlantic. *J. Mar. Res.*, **34**(2), 131–141.
- Wright, W. R. and Worthington, L. (1970). *The Water Masses of the North Atlantic Ocean: A Volumetric Census of Temperature and Salinity*, volume 19, page 8 pp. Am. Geogr. Soc., New York.
- Zeng, J., Nojiri, Y., Murphy, P. P., Wong, C., and Fujinuma, Y. (2002). A comparison of  $\Delta p\text{CO}_2$  distributions in the northern North Pacific using results from a commercial vessel in 1995–1999. *Deep-Sea Res. II*, **49**, 5303–5315.

## A. Abbreviations

AMSRE	Advanced Microwave Scanning Radiometer-EOS
ASE	Air-sea gas exchange
$A_T$	Total alkalinity
CAVASSOO	CARbon VARIability Studies by Ships Of Opportunity
$c_d$	Drag coefficient
chl-a	Chlorophyll-a concentration
$\Delta\text{DIC}_{\text{bio}}$	DIC drawdown mediated by biological activity
DIC	Dissolved inorganic carbon
$\text{DIC}_{\text{bio}}$	DIC component of DIC that resulted from biological production
$\overline{\text{DIC}}_{\text{bio}}$	Cumulative amount of $\text{CO}_2$ that was consumed by biological production
$\text{DIC}_{\text{equ}}$	DIC concentration of a seawater sample that is in equilibrium with the atmosphere
$\text{DIC}_{\text{sw}}$	Seawater DIC
$\overline{dp\text{CO}_2}$	Annual increase of seawater $p\text{CO}_2$
EBUE	Eastern Boundary Upwelling Ecosystem
ENACW	Eastern North Atlantic Central Water
$F_{\text{ASE}}$	Flux of $\text{CO}_2$ due to ASE
$F_{\text{bio}}$	Flux component of $\text{CO}_2$ flux that is mediated by biology
$F_{\text{CO}_2}$	$\text{CO}_2$ flux between ocean and atmosphere
$F_{\text{N}_2\text{O}}$	Flux of $\text{N}_2\text{O}$
GFST	Gulf Stream
GTD	Gas tension device; instrument that measures the total gas pressure of all gases dissolved in seawater
$I$	Column inventory of $\text{CO}_2$
$I_{\text{ASE}}$	Column inventory of $\text{CO}_2$ that resulted from ASE
$k_{\text{N}_2\text{O}}$	Gas transfer velocity of $\text{N}_2\text{O}$
$k_{\text{CO}_2}$	Gas transfer velocity of $\text{CO}_2$
$\kappa$	Kármán constant, a dimensionless constant describing the logarithmic velocity profile of a turbulent fluid flow near a boundary
LC	Labrador Current
MLD	Mixed layer depth
MLR	Multiple linear regression
$\text{N}_2\text{O}_{\text{equ}}$	$\text{N}_2\text{O}$ concentration of a seawater sample that is in equilibrium with the atmosphere
$\text{N}_2\text{O}_{\text{inv}}$	Column inventory of $\text{N}_2\text{O}$
$\text{N}_2\text{O}_{\text{sw}}$	Seawater $\text{N}_2\text{O}$ concentration
NADR	North Atlantic Drift Region
NAST	North Atlantic Subtropical Gyre
NCP	Net community production
NN	Neural network
NPP	Net primary production
$p_{\text{atm}}$	Observed atmospheric pressure

$p\text{CO}_{2,\text{AMSR-E}}$	Seawater $p\text{CO}_2$ corrected to $\overline{\text{SST}_{\text{AMSR-E}}}$
$p\text{CO}_{2,\text{atm}}$	Atmospheric $p\text{CO}_2$
$p\text{CO}_{2,\text{clim-00}}$	Seawater $p\text{CO}_2$ from climatology (Takahashi <i>et al.</i> , 2009) at the reference year 2000
$p\text{CO}_{2,\text{clim-00,SST}}$	Seawater $p\text{CO}_2$ from climatology (Takahashi <i>et al.</i> , 2009) at the reference year 2000 corrected to the actual SST
$p\text{CO}_{2,\text{clim-act}}$	Seawater $p\text{CO}_2$ from climatology (Takahashi <i>et al.</i> , 2009) corrected to the actual year
$p\text{CO}_{2,\text{is}}$	Seawater $p\text{CO}_2$ measured at SST
$p\text{CO}_{2,\text{is},2000}$	Seawater $p\text{CO}_2$ measured at SST and corrected to the year 2000
$p\text{CO}_{2,\text{non-t}}$	Non-thermal component of observed seawater $p\text{CO}_2$
$p\text{CO}_{2,\text{sw}}$	seawater $p\text{CO}_2$
$p\text{CO}_{2,\text{t}}$	Thermal component of observed seawater $p\text{CO}_2$
RF	Revelle factor
SSS	Sea surface salinity
SST	Sea surface temperature
$\text{SST}_{\text{AMSR-E}}$	SST derived Advanced Microwave Scanning Radiometer (AMSR-E)
$\overline{\text{SST}_{\text{AMSR-E}}}$	Monthly mean $\text{SST}_{\text{AMSR-E}}$
$\tau$	Time since upwelled water reached the surface
$\tau_{\text{bio}}$	Duration of biological carbon draw down
$T_{\text{EQU}}$	Equilibrator temperature
UI	Upwelling index
VOS	Volunteer Observing Ship
WNAC	Western North Atlantic Central Water
$z$	Height about sea surface where wind speed was measured
$z_0$	Roughness length



## B. Cruises

cruise name	ship	area	time
Fal01	M/V Falstaff	North Atlantic	February 2002
Fal02	M/V Falstaff	North Atlantic	March 2002
Fal03	M/V Falstaff	North Atlantic	April 2002
Fal04	M/V Falstaff	North Atlantic	May 2002
Fal05	M/V Falstaff	North Atlantic	May 2002
Fal06	M/V Falstaff	North Atlantic	June 2002
Fal07	M/V Falstaff	North Atlantic	June 2002
Fal08	M/V Falstaff	North Atlantic	July 2002
Fal09	M/V Falstaff	North Atlantic	August 2002
Fal11	M/V Falstaff	North Atlantic	September 2002
Fal12	M/V Falstaff	North Atlantic	October 2002
Fal13	M/V Falstaff	North Atlantic	November 2002
Fal14	M/V Falstaff	North Atlantic	November 2002
Fal15	M/V Falstaff	North Atlantic	December 2002
Fal16	M/V Falstaff	North Atlantic	January 2003
Fal17	M/V Falstaff	North Atlantic	February 2003
Fal18	M/V Falstaff	North Atlantic	April 2003
FALCO-01	M/V Falstaff	North Atlantic	April 2005
FALCO-02	M/V Falstaff	North Atlantic	July 2005
COM09	M/V Atlantic Companion	North Atlantic	June 2006
COM10	M/V Atlantic Companion	North Atlantic	June 2006
COM11	M/V Atlantic Companion	North Atlantic	July 2006
COM15	M/V Atlantic Companion	North Atlantic	September 2006
COM16	M/V Atlantic Companion	North Atlantic	October 2006
COM18	M/V Atlantic Companion	North Atlantic	November 2006
COM21	M/V Atlantic Companion	North Atlantic	January 2007
COM22	M/V Atlantic Companion	North Atlantic	January 2007
COM23	M/V Atlantic Companion	North Atlantic	February 2007
COM25	M/V Atlantic Companion	North Atlantic	March 2007
COM26	M/V Atlantic Companion	North Atlantic	April 2007
COM27	M/V Atlantic Companion	North Atlantic	April 2007
COM28	M/V Atlantic Companion	North Atlantic	May 2007
COM29	M/V Atlantic Companion	North Atlantic	May 2007
COM30	M/V Atlantic Companion	North Atlantic	June 2007
COM32	M/V Atlantic Companion	North Atlantic	July 2007
COM35	M/V Atlantic Companion	North Atlantic	September 2007
COM36	M/V Atlantic Companion	North Atlantic	October 2007
COM37	M/V Atlantic Companion	North Atlantic	November 2007
P320-1	R/V Poseidon	Mauritanian upwelling	March 2005
M68-3	R/V Meteor	Mauritanian upwelling	July 2006
ATA3	R/V L'Atalante	Mauritanian upwelling	February 2008

# Eidesstattliche Versicherung

Ich versichere an Eides statt, dass ich die von mir vorgelegte Dissertation - abgesehen von der Beratung durch meinen Betreuer - selbstständig und ohne unerlaubte Hilfe angefertigt habe und alle benutzten Quellen und Hilfsmittel vollständig angegeben habe. Die Zusammenarbeit mit anderen Wissenschaftlern habe ich kenntlich gemacht. Die Arbeit ist unter Einhaltung der Regeln guter wissenschaftlicher Praxis der Deutschen Forschungsgemeinschaft entstanden. Ferner habe ich weder diese noch eine ähnliche Arbeit an einer anderen Abteilung oder Hochschule im Rahmen eines Prüfungsverfahrens vorgelegt, veröffentlicht oder zur Veröffentlichung vorgelegt.

Kiel, 09. Dezember 2010

.....  
Tobias Steinhoff



# Curriculum Vitae

Tobias Steinhoff

born 09. August 1973 in Wolfsburg

German

## Presentations:

Steinhoff, T., A. Körtzinger, F. Schroeder, W. Petersen und M. Hoppema. September 2008: Southampton, UK, FerryBox and Ship of Opportunity meeting: Inter-comparison of  $p\text{CO}_2$  instruments - classical versus new methods.

Steinhoff, T., A. Körtzinger, F. Schroeder und M. Hoppema. September 2008: OCEANET meeting, Geesthacht, Germany:  $p\text{CO}_2$  measurements during ANTXXIV-4.

Steinhoff, T., A. Körtzinger und D.W.R. Wallace. Dezember 2007: CARBOOCEAN annual meeting, Bremen, Germany: The nitrate versus mixed layer depth relationship and its implication for  $p\text{CO}_2$  measurements.

## Publications:

Steinhoff, T., T. Friedrich, S.E. Hartman, A. Oschlies, D.W.R. Wallace und A. Körtzinger (2010). Estimating mixed layer nitrate in the North Atlantic Ocean. *Biogeosciences*, 7, 795-807.

Watson, A.J., U. Schuster, D.C.E. Bakker, N.R. Bates, A. Corbière, M. González-Dávila, T. Friedrich, J. Hauck, C. Heinze, T. Johannessen, A. Körtzinger, N. Metzl, J. Olafsson, A. Olsen, A. Oschlies, X. A. Padin, B. Pfeil, J.M. Santana-Casiano, T. Steinhoff, M. Telszewski, A.F. Rios, D.W.R. Wallace, R. Wanninkhof (2009). Tracking the Variable North Atlantic Sink for Atmospheric  $\text{CO}_2$ . *Science*, 326 (5958), doi:10.1126/science.1177394.

Telszewski, M., Chazottes, A., Schuster, U., Watson, A. J., Moulin, C., Bakker, D. C. E., González-Dávila, M., Johannessen, T., Körtzinger, A., Lüger, H., Olsen, A., Omar, A., Padin, X. A., Ríos, A. F., Steinhoff, T., Santana-Casiano, M., Wallace, D. W. R., and Wanninkhof, R. (2009). Estimating the monthly  $p\text{CO}_2$  distribution in the North Atlantic using a self-organizing neural network. *Biogeosciences*, 6, 1405-1421.

Takahashi, T, S.C. Sutherland, R. Wanninkhof, C. Sweeney, R.A. Feely, D.W. Chipman, B.

Hales, G. Friederich, F. Chavez, C. Sabine, A. Watson, D.C.E. Bakker, U. Schuster, N. Metzl, H. Yoshikawa-Inoue, M. Ishii, T. Midorikawa, Y. Nojiri, A. Körtzinger, T. Steinhoff, M. Hoppema, J. Olafsson, T.S. Arnarson, B. Tilbrook, T. Johannessen, A. Olsen, R. Bellerby, C.S. Wong, B. Delille, N.R. Bates und H.J.W. de Baar (2009). Climatological mean and decadal change in surface ocean  $p\text{CO}_2$ , and net sea-air  $\text{CO}_2$  flux over the global oceans. *Deep-Sea Res. II*, 56, 554-577.

#### Research cruises:

- 1999 Meteor 45-3, North Atlantic
- 2001 Meteor 50-1 und -4, North Atlantic
- 2002 Falstaff, North Atlantic
- 2003 Meteor 59-2, North Atlantic
- 2005 Poseidon 320-1, tropical Atlantic  
Falstaff, North Atlantic
- 2006 Atlantic Companion, North Atlantic  
Meteor 68-3, tropical Atlantic
- 2008 Polarstern ANTXXIV-4, Atlantic  
Polarstern ANTXXV-1, Atlantic
- 2009 Meteor 80-1, tropical Atlantic
- 2010 Polarstern ANTXXVII-1, Atlantic

#### Summer Schools:

- July 2007 Eur-Oceans/CarboOcean Summer School "Combining data and models - statistical analysis and data assimilation in biogeochemical oceanography", Kiel.

#### Education:

- since 03/05 Postgraduate studies at the Leibniz-Institute of Marine Sciences (IFM-GEOMAR) at the University of Kiel
- 04/00-12/04 Undergraduate studies of Chemistry at the University of Kiel (Degree: Diplom)
- 10/95 - 03/00 Undergraduate studies of Mathematics/Chemistry pursuing teaching certification
- 08/84 - 07/93 Secondary school, Ratsgymnasium in Wolfsburg
- 08/80 - 07/84 Primary school Wolfsburg